Applications of X-ray Instrumentation for Dark Matter Searches with Cosmic Antiparticles

by

Field Rose Rogers

B.S., Yale University (2015)

Submitted to the Department of Physics
in partial fulfillment of the requirements for the degree of

Doctor of Philosophy in Physics

at the

MASSACHUSETTS INSTITUTE OF TECHNOLOGY

June 2022

Author .....
Department of Physics
May 13, 2022

Certified by .....
Kerstin Perez
Associate Professor of Physics
Thesis Supervisor

Accepted by .....
Deepto Chakrabarty
Associate Department Head of Physics

Applications of X-ray Instrumentation for Dark Matter Searches with Cosmic Antiparticles

by

Field Rose Rogers

Submitted to the Department of Physics
on May 13, 2022, in partial fulfillment of the
requirements for the degree of
Doctor of Philosophy in Physics

Abstract

Approximately 85% of the mass in the Universe is composed of dark matter. Scientific consensus is that this dark matter is comprised of some unidentified fundamental particle, but despite compelling evidence of abundant dark matter and precise observation of its gravitational effects, the nature of this material remains a mystery. The effort to reveal the fundamental properties of the dark matter is a central and and unifying theme of modern particle and astrophysics. Indirect dark matter detection centers on cosmic-ray signatures of possible dark matter annihilation or decay to Standard Model particles in the Galaxy. Relative to terrestrial experiments, such indirect dark matter searches benefit from the large size of the Galaxy and can probe broad classes of dark matter models including those that, due to low cross sections, evade both production at colliders and direct detection. The challenge for indirect dark matter detection lies in disentangling possible dark matter signatures from the large and often uncertain cosmic-ray fluxes arising from other astrophysical sources. At the same time, cosmic-ray particles, which are themselves agents of Galactic evolution, provide unparalleled probes of the Galactic environment and dynamics. This dissertation describes two complementary approaches to the interconnected worlds of indirect dark matter detection and cosmic-ray physics: first, searching for rare cosmic-ray species local to Earth, and second, using astrophysical techniques to observe the effects of cosmic-ray particles in remote regions of the Galaxy.

The General Antiparticle Spectrometer (GAPS) is an upcoming balloon mission to search for signatures of dark matter annihilation or decay in low-energy ($<0.25\,\mathrm{GeV}/n$) cosmic-ray antinucleus fluxes. The goal of GAPS is to deliver 1) a precision cosmic antiproton spectrum in an unexplored low-energy region; 2) a first detection of cosmic antideuterons, a signature of new physics essentially free of astrophysical background; and 3) leading sensitivity to cosmic antihelium-3. To identify rare antinuclei out of the trillions of particles expected in flight, GAPS pioneers a novel exotic atom-based particle identification technique, which relies on $>10\,\mathrm{m}^2$ of lithium-drifted silicon (Si(Li)) detectors to capture an incoming antinucleus into an exotic atom and measure the resulting X-ray and nuclear annihilation products. This

dissertation details the development, noise performance, and tracking capabilities of the large-area, high-temperature Si(Li) detectors developed for the GAPS mission. Their performance is precisely characterized using a semiconductor noise model and has been shown to be stable over time. In addition, the GAPS sensitivity to cosmic-ray antiprotons is demonstrated in this work using a full instrument simulation, event reconstruction, and models of solar and atmospheric effects. With its large geometric acceptance, GAPS will detect $\sim$500 cosmic antiprotons per flight, producing a precision spectrum extending to lower energies than any previous measurement. This measurement will be sensitive to models of dark matter, evaporating primordial black holes, and cosmic ray propagation. It will also validate the exotic atom particle identification technique prior to the other GAPS analyses.

Beyond local detection in high-altitude particle detectors, cosmic ray populations can be probed remotely via the electromagnetic radiation they produce as they propagate through the Galaxy. Recent evidence points to enhanced particle populations of uncertain origin in the Galactic Center region. These unexplained particles challenge the conventional models of cosmic ray propagation used to predict the local fluxes critical for dark matter detection. Using X-ray observations of the giant molecular cloud Sagittarius B2, new upper limits are set on low-energy cosmic ray populations near the Galactic center. The limits are comparable to predictions from hydrogen ionization measurements, supporting the observation of elevated Galactic Center cosmic ray populations.

Thesis Supervisor: Kerstin Perez
Title: Associate Professor of Physics

Acknowledgments

First, I thank my thesis advisor, Kerstin Perez, for her mentorship and guidance during my six years at MIT. Thank you for scaffolding my scientific training – for letting me make mistakes and helping me learn from them so I could become my own scientist. Thank you for teaching me how science is about stories and for repeatedly helping me develop and share scientific narratives. Thank you for showing up to check in every week, for years. I admire your fundamentally interdisciplinary approach, the care and intention with which you deviate from the mold, your dedication to doing the reading, and your bravery in asking questions until everyone is on the same page. I could not be more proud to have been trained by you.

I would also like to thank the two other professors on my thesis committee. Lindley Winslow has looked out for me as one of her own, shared professional advice as only she could, supervised my first teaching experience, and never failed to brighten my day. Tracy Slatyer completely re-shaped my perspective on dark matter and cosmic rays, taught my favorite class at MIT, shared their enthusiasm for gardens and plants, and, together with Rebecca Leane, supervised a project that kept me engaged during an otherwise difficult period. It meant a lot to defend my thesis to a panel of faculty whom I respect and admire so deeply and who have demonstrated such true care for me both as a scientist and as a person.

I am grateful to the members of the Perez Lab for their research insights and friendship. Tyler Erjavec and I began together with an empty lab – thank your fearlessness and for sharing both the frustrations and the breakthroughs. Rachel Carr has been an inspiration for her humility and persistence in pursuit of original ideas. Many thanks to Shuo Zhang for her mentorship, care, and support, and the grace with which she has shared them. Brandon Roach was always there to remind me how bizarre physics is and and has taught me far more than he may have realized – I'll miss our discussions. Mengjiao Xiao's detector wizardry is unparalleled – thank you for all your help and for taking the lab to the next level. Kelsey Yee, I look forward to seeing you take the torch!

GAPS is an interdisciplinary and international collaboration of >50 scientists and engineers, and this work would not have happened without all of their contributions. I am particularly grateful to the GAPS people for welcoming me and building a truly collaborative team. The Si(Li) development and characterization would not have been possible without Chuck Hailey's knowledge and experience, and my own development as a scientist has been far richer thanks to his support, critical feedback, and encouragement over the years. Philip von Doetinchem directly supervised my work with the antiproton sensitivity study, taught me everything I know about working with big data sets, and has become a trusted scientific mentor. Lorenzo Fabris, Brent Mochizuki, and Alex Lowell went above and beyond to welcome me into technical spaces. Rene Ong, Mirko Boezio, and Hide Fuke have consistently provided insightful feedback that has tightened my language and broadened my perspective. I would like to thank Achim Stoessl for maintaining the GAPS software, for his singular patience teaching me how to use a computer, and for many thought-provoking discussions. Finally, Nate Saffold has been my lab partner, my editor, my sounding board, and my friend throughout graduate school. I am so grateful to have grown up in physics with one so curious and thoughtful as you.

To my collaborators on the Sagittarius B2 analysis, it has been a pleasure to develop this work with you. I began this project as a novice astrophysicist. Shuo Zhang and Maïca Clavel taught me the practical, technical, historical, and theoretical bases I needed to engage with the data. Kerstin Perez guided me in making the most of my particle physics background to reveal the interdisciplinary nature of the project. Afura Taylor performed the initial data reduction and analysis, framing what followed. Additionally, I gratefully acknowledge Chuck Hailey, Roman Krivonos, Ekaterina Kuznetsova, Kaya Mori, and Gabriele Ponti for the useful discussions and Brandon Roach for the hours he spent helping me with astrophysics software.

I have been humbled by the generosity and kindness of many who have supported my education. I would like to thank Joe Formaggio for his encouragement and friendly presence over the years and Anna Frebel for her frank and unapologetic advice in both official and unofficial capacities. I looked forward to every E&M class with John

Belcher. Gabriela Soto Laveaga and her students welcomed me into the exhilarating world of science, technology, and society studies, subtly and crucially re-framed my scientific practice, and made me believe I could contribute. Ben Hansberry of the Teaching and Learning Lab provided invaluable training through the Subject Design and Teaching Practice Certificate Programs, and continued to provide guidance and support in my classroom after their conclusion. As the leader of a subject I TA'd, Joe Checkelsky provided valuable feedback and took my concerns seriously. Kurt Broderick of the Microsystems Technology Lab trained me to use the resources of that space safely and effectively for research. Mark Belanger directed and helped me in the student machine shop, which was a refuge as well as the origin of many necessary lab parts. This work would not have been possible without Jack McGlashing, Joe Cucinotta, and Lee Williams, who kept the labs running and always had a friendly word to share. Nicole Laraia, Rosaleah Brown-Gresham, Cathy Modica, Sydney Miller, Sabrina Salvati, Karen Dow, Lauren Saragosa, Elsye Luc, Alisa Cabral, and Lily Xu answered my questions large and small and helped me navigate MIT.

Many thanks go to my MIT classmates and colleagues for their friendship and support, which have made all the difference. I'm grateful for the long lunches, the game nights, the kitchen projects, the shared adventures, and all the time spent talking things over. To my NuPaX cohort, I'm so glad to have shared this journey with our group, who lifted each other up as we helped each other through classes, quals, and daily grad school life. Special thanks to Jo Johnston and Lauren Yates for lending their sympathetic and validating ears, Alex Diaz for being my original co-conspirator in physicist socialization, and Efrain Segarra for making qual preparation almost fun. Airlia Schaffer and Alysa Rudelis shared cozy projects and artful excursions. Joe Smolsky made me think and laugh every day we shared an office – and still owes me cookies! Nick Kamp, thanks for all the earnest conversation, for taking on the student seminar, and for hiding my phone so I had no choice but to finish my analyses. Jon Ouellet was one of the first people I met at MIT, and he has always been there to talk through a dilemma or a new idea, and to celebrate others. To Julieta Gruszco, thank you for being there when only you could and for staying you after becoming

a professor. Kaliroë Pappas organized the most lovely social things and showed up for a hug exactly when I needed it. Chiara Salemi has always been there to find a cupcake or a coffee and help put things in perspective.

I am forever grateful to the formidable trio of Yale faculty without whom I would certainly not be here today. Sarah Demers showed up and was present when I needed her most, let me see myself in her while meeting me exactly where I was, and shared her unapologetic frankness and vulnerability while in a position of power. Meg Urry created a place for me when I was at a loss, determined that I wanted to build detectors before I knew what that meant, and sent me off to do so while still keeping me in her generous circle. Finally, Reina Maruyama believed in me, saw the best in me, cared a lot, and provided the time, space, and encouragement I needed to find my own confidence and joy in physics.

I am also grateful to Ben Brubaker for his inexplicable patience teaching me LaTeX and for teaching me to think of myself as someone who thinks like a physicist. Thank you to Antonia Hubbard for her unparalleled lab playlists and her excellent advice over the years. Finally, Walter Pettus almost singlehandedly taught me the foundations of experimental physics while bringing his care and good humor to Wright Lab every day so that I wanted to keep showing up, too.

To my most wise Council of Graduate Student Life (and beyond), Danielle Norcini and Nikita Dutta, thank you for all the sorting and for being mutually present through the trivial, the frustrating, and the beautiful. And to Greg Kahanamoku-Meyer, thank you for being my very first friend in physics and the reason I didn't stop when I'd barely begun.

My students, especially Protyasha, Afura, Devin, Arianna, Hillary, Radhika, Talla, Ivy, Jonathon, and Nathalie, warmed my heart, contributed to this work, and taught me how to be a better mentor, teacher, and physicist. Mentorship is a two-way street. It has been my privilege to learn with you and from you, and I am honored to have shared in your journey. Thank you for teaching me how to be more vulnerable on both faces of mentorship and for healing some of my own wounds.

One of the most surprising joys of the past few years has been in finding that there

seems to be space for me in astroparticle physics. I am profoundly grateful both to those I've explicitly named and those I've never met who have carved out this space. I can only rededicate myself to making it ever wider.

The majority of these chapters were written in the warm presence of Chiara Salemi. While a preliminary investigation indicated that it may have been possible to write this thesis without her, the results were not encouraging, and the study was (thankfully) discontinued. Thanks for the tea breaks and enthusiastic pursuit of rabbit holes. I began typing these words at the kitchen table on Harvard Street in Spring 2020, while munching cinnamon coffee cake with Tsering, Julia, Edward, and Sarah. Portions of this thesis were also written at my parents', Clare and Lucy's, Laura and Stu's, and Chiara and David's kitchen tables. I hope that the care and intentionality of those days and spaces has found its way into these pages.

Finally, I would like to express my gratitude to my friends and family for being a part of this journey and making it worthwhile. Thanks to those who have shared so many therapeutic phone calls and cups of tea, who have persevered through talk of antideuterons while cleaning out chicken coops, hiking up mountains, or baking pie, who have laughed with me until we couldn't breathe, and who have opened my mind, repeatedly. Thanks especially to those who have shared my time in Cambridge and helped make it into a city I call home. These past few months have been uniquely challenging, and I am grateful to those who generously shared their spaces and their levity. Thanks, lastly, to my sister, Lucy, who is my role model and my steadfast supporter, and to my parents, Betsy and Paul, who always welcome me home.

Contents

List of Figures

7.5 *Panel 1:* The contours of the 6.4 keV line emission from 2018 are shown in the same projection as Figure 7.3. The regions (dark blue) identified as Sgr B2 substructures G0.66-0.13, G0.56-0.11, G0.75-0.10, and G0.61+0.00 are shown. G0.74-0.10, identified by [209], is also shown for reference, though it is not detected in 2018 and not treated in this work. We have further identified several 40″-radius features (magenta, A, B, C...) that illustrate the changes in morphology within each substructure over time. All region positions are given in Table 7.2. The arrow (light blue) shows the direction to Sgr A*. *Panels 2-4:* The remaining panels show the Fe Kα light curves extracted from the Sgr B2 substructures G0.66-0.13 (Panel 2), G0.56-0.11 (Panel 3), and G0.61+0.00 (Panel 4) outlined in Panel 1. The overall light curve from each substructure is in black, while the light curves of the corresponding 40″-radius features are plotted on the same axes. Substructure G0.66-0.13 was observed to brighten in 2012, but became dim again in 2018. Light curves for the 40″-radius regions (A, B, and C) associated with G0.66-0.13 behave differently over time, with circle A (magenta, farthest from Sgr A* in the projected plane) brightening only in 2018 while B and C follow the pattern of the parent substructure. Substructure G0.56-0.11 has brightened continuously since 2004, but analysis of 40″ features illustrates that this pattern is not uniform throughout the substructure. Instead, the brightening in 2012 is driven by region marked B (blue) while in 2018 the flux is driven by region A (magenta). Finally, while the light curve for the newly identified structure G0.61+0.00 is consistent with a constant in time, the 40″-radius features again illustrate an evolving morphology within the substructure. 210

List of Tables

Chapter 1

Introduction

This story begins with the question of matter. The goal of particle physics is to describe the materials of which the Universe is composed at its most fundamental level. The stars, the Earth, and everything humans can see or touch is made of atoms or subatomic particles described by the state-of-the-art Standard Model of particle physics (Section 1.1). However, over the last half-century, it has been increasingly clear that most of the Universe, $\sim$85% of its total mass, is not made of atoms but instead is made of some mysterious, invisible, form of matter which we call "dark matter." Further, even though it is invisible to us, dark matter is incredibly important, as it is the material that holds our Milky Way Galaxy together. This dissertation describes a few of many efforts to reveal the nature of the dark matter. In the same way that Earth is made of atoms, and atoms are made of protons, neutrons, and electrons, what is the dark matter made of? The story of the dark matter is arguably the central enigma for modern particle and astrophysics; much of the ongoing research in these fields relates to dark matter in some way.

In order to provide context for the unknowns of dark matter, this chapter briefly presents the two foundational Standard Models for astroparticle physics. Section 1.1 introduces the Standard Model of Particle Physics, which describes the properties of known matter in the Universe, including all atoms. This dissertation is concerned with a yet-undiscovered form of matter beyond the Standard Model. However, comparison with known particles provides a framework for what this new dark matter is not, and

experimental efforts to characterize the dark matter rely on Standard Model particles.

Meanwhile, Section 1.2 introduces the Standard Model of Cosmology, which describes how the Universe evolved from a hot Big Bang 14 billion years ago to form structures such as galaxies and stars that are observed today. Stars and planets are made of Standard Model particles, which are ingredients in this cosmology. However, the primary ingredients of the cosmological Standard Model are dark energy, which describes the observed expansion of the Universe, and dark matter, which is responsible for the formation of structures.

1.1 The Standard Model of Particle Physics

Standard Model of Particle Physics (following e.g., [1, 2]) is the theory that describes the known fundamental particles and their interactions. As illustrated in Figure 1.1, it consists of six quarks (up, down, charm, strange, top, bottom), three species of charged leptons (electron, muon, and tau) and the three corresponding neutral leptons (the electron, muon, and tau neutrinos), four force-mediating gauge bosons (photon, gluon, W, and Z), and the Higgs boson, whose interactions are responsible for the masses of the others. For each charged particle, there is a corresponding antiparticle with opposite charge. In the present-day conditions of the Universe, quarks are bound in composite states called hadrons via their strong-force exchange of gluons. The fundamental properties, including the particle masses and the strengths of the interactions, of these particles are determined experimentally, and can be used to calculate the cross section (which describes the interaction rate) for various processes and the characteristic decay lifetimes for unstable particles.

Considering the many fundamental particles, just five of them describe the bulk of the matter relevant both in everyday life and in the particle detectors and cosmic rays of this dissertation. Atomic nuclei are composed of protons and neutrons, which are in turn built from up and down quarks bound by gluons. Most of the mass of the protons and neutrons originates in the energy of the strong bonds between these particles, rather than in the particles themselves. Atoms are electromagnetic

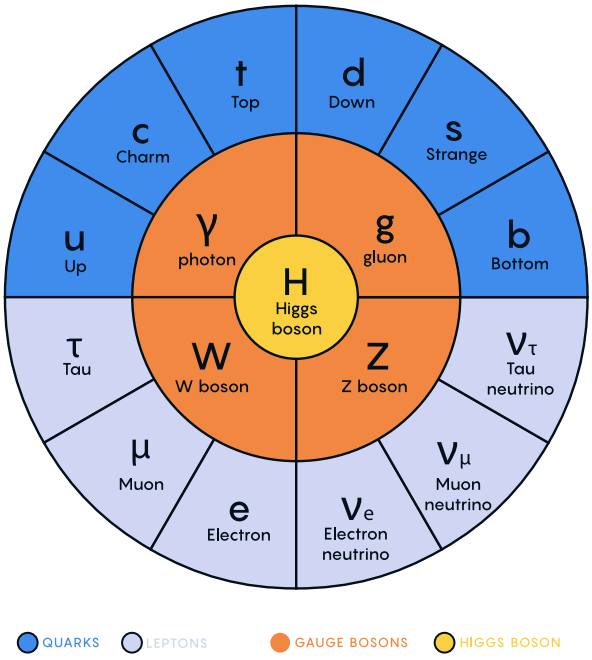

Figure 1.1: The Standard Model of Particle physics is composed of six flavors of quarks (blue), six flavors of leptons (lavender), four force-carrying gauge bosons (orange), and the Higgs boson (yellow). Image credit: Quanta Magazine.

(photon-mediated) bound states of electrons and nuclei. Photons also compose the electromagnetic radiation ubiquitous in our world, including visible light, X-rays, radio, and microwaves. The neutrinos are mostly invisible to humans and interact only rarely. The remainder are unstable, and in the present conditions of the Universe, they exist rarely and fleetingly before decaying to the particles named above.

Despite its successes, the Standard Model of Particle Physics is known to be an incomplete picture of the Universe. For one thing, it lacks a description of the gravitational force, and in conflict with experimental evidence, the Standard Model neutrinos are massless. A fine-tuning problem describes a situation in which a measured property of the Universe seems very unlikely to occur by random chance, suggesting the existence of a deeper explanation involving new physics. One example is the gauge hierarchy problem related to the mass of the Higgs boson, which has been measured at 125 GeV, despite the fact that if the Standard Model is part of a theory the is valid up to the energy scales relevant for gravity, quantum corrections predict a mass that is more than 20 orders of magnitude higher, requiring precise tuning of the model parameters to explain the observed mass [3, 4]. As another example, the "strong-CP problem," describes the apparent perfect symmetry of the strong force under a transformation called "charge-parity" (CP), despite no reason in the Standard Model for this to be so [5]. Precision measurements have also revealed anomalies (e.g., [6, 7]) that may indicate that the current picture is incomplete. Finally, as will be shown in Section 1.2, the Standard Model of Particle Physics also cannot explain the so-called dark matter and dark energy that compose the bulk of the energy budget of the Universe; in fact, Standard Model particles and interactions account for $<5\%$ of that energy budget. The identification of the dark matter is arguably the central problem of modern particle physics.

1.2 The Standard Model of Cosmology

The ΛCDM Cosmological Model [8] is the Standard Model of cosmology because it describes evolution of the Universe from hot and dense initial conditions to the struc-

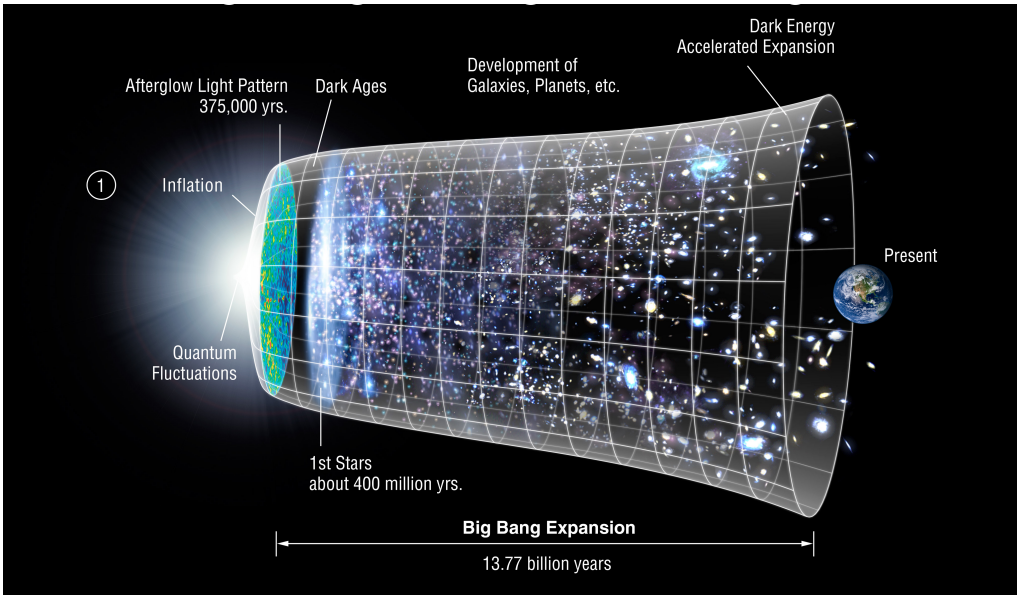

Figure 1.2: The Standard Model of Cosmology describes the evolution of the Universe with its dark energy and dark matter during its 13.8 billion year history. Image credit: NASA/ LAMBDA Archive / WMAP Science Team.

ture observed in the present day, in the presence of dark energy (Λ) and cold (non-relativistic) dark matter (CDM) as well as a relatively small abundance of Standard Model particles. Figure 1.2 schematically illustrates the history of the Universe. The Universe begins with a period of rapid expansion known as Inflation, during which quantum density fluctuations from the initially hot and dense Universe are translated into fluctuations on a cosmological scale. At first, all of the Standard Model particles, and possibly the dark matter, interact in equilibrium, but as the Universe cools, it undergoes phase transitions as the fundamental forces decouple from the equilibrium.

Once all but the electromagnetic force have decoupled, the Universe consists of a plasma of interacting protons, electrons, and photons, with the dark matter coupled to the protons via gravity. The original density fluctuations create pressure gradients that propagate through the plasma as sound waves. Then, $\sim$380,000 years after inflation when the Universe has sufficiently cooled, it undergoes another phase transition as protons and electrons recombine to form atoms, the photons begin to stream freely, and the density fluctuations are frozen in place. The free-streaming photons form the "afterglow light pattern" that is observed as the cosmic microwave background today

and used to precisely measure cosmological parameters as in Section 2.1.4. Meanwhile, the stars, galaxies, and planets develop from the continued gravitational collapse of the primordial density fluctuations as detailed in Section 2.1.3. Finally, in recent times, the Universe has begun a new period of accelerated expansion driven by the dark energy. While the microphysics of the dark energy and the dark matter may be unknown, we cannot describe our cosmology without them.

Chapter 2

Introduction to Dark Matter

"Dark matter" is a physicist's name for the invisible material that holds galaxies together. Though the dark matter comprises the majority of the mass in the Universe, and theories abound to explain its abundance, the fundamental particle nature of this mysterious substance eludes us. The interdisciplinary effort to reveal the nature and origin of the dark matter is thus a central and unifying motivation for modern particle physics, astrophysics, and cosmology.

Particle physics in the 20^{th} century was characterized by the rapid discovery of new particles leading to the development of the Standard Model of particle physics (Section 1.1). In the Standard Model, 17 fundamental particles and their interactions account for the existence and behavior of atoms and subatomic phenomena. However, persistent unexplained challenges, including the hierarchy problem and the strong CP problem, suggest that despite its successes, the Standard Model particles do not form a complete picture of matter in the Universe. Meanwhile, astrophysical observations have revealed, and the Standard Model of Cosmology (Section 1.2) requires, that only $\sim 15\%$ of all the matter in the Universe is composed of Standard Model particles including atoms, while the balance is what we call dark matter.

This chapter provides a brief treatment of the interdisciplinary field of dark matter physics. Section 2.1 introduces the evidence of a cosmological abundance of some unknown material. Section 2.2 summarizes the known characteristics of the material composing the dark matter and introduces some theoretical candidates, and Sec-

tion 2.3 discusses several experimental strategies to probe models of thermal relic dark matter in particular.

2.1 Gravitational Observation of Dark Matter

The standard ΛCDM model of cosmology (Section 1.2) describes the evolution of the Universe under the influence of dark energy (Λ), cold dark matter (CDM), and a relatively small amount of ordinary matter (composed of Standard Model particles, also known as "visible," "baryonic," or "ordinary" matter). The Universe as we know it today owes its structure, including its galaxies and, by extension, its stars, planets, and humans, to the gravitational effects of dark matter.

Specific proof of the existence of dark matter arises from evidence of its gravitational effects in individual astrophysical observations spanning timescales from the time of the first atoms to the present day and size scales from dwarf galaxies to the largest observed structures. This section introduces some of the most compelling astrophysical evidence of dark matter in the Universe, including velocity dispersion in galaxies and clusters in Section 2.1.1, evidence from gravitational lensing in Section 2.1.2, simulations of large scale structure formation in Section 2.1.3, and precision measurements of dark matter using the cosmic microwave background in Section 2.1.4. Each of these observations contributes to form a picture of dark matter that is cold (non-relativistic), collisionless (self-interactions apart from gravity occur rarely if at all), and dissipationless (cannot cool by radiating photons), that comprises 26.8% of the present total energy density of the Universe and >85% of the mass [9], that forms massive haloes around galaxies in the present day, and that has existed in its present form since at least 380,000 years after the Big Bang. Together, these interrelated observations contribute to a consistent cosmological model, in which dark matter is fundamental to our existence in the Universe.

2.1.1 Velocity Dispersions of Clusters and Galaxies

The earliest scientific evidence for the existence of nonluminous matter in galaxies came from astrophysical observations of the velocities of galaxies in galaxy clusters in the 1930s [10, 11] and, with greatly increased precision, accuracy, and significance, from measurements of the orbital velocities of stars and gas in galaxies in the 1970s [12, 13]. Common to the dark matter interpretation of both measurements is a comparison of two mass-estimation methods for galaxies. In the first method, mass is estimated by assuming a reasonable proportionality between visible light and mass, assuming galaxies are composed of visible stars and gases. In the second method, the kinetic energy of bound galaxies or stars is used to estimate the total mass of the gravitationally-bound system. Consistent deficits in the estimated luminous mass relative to the estimated gravitational mass (a high "mass to light ratio") was interpreted as evidence of a nonluminous form of matter.

The unexpectedly large velocities — up to 2000 km/s, and >1000 km/s on average — of galaxies in several galaxy clusters observed by Hubble and Humason [14] led Fritz Zwicky to his study of the Coma Cluster of galaxies. The virial theorem relates the total potential energy V of a bound system to the average kinetic energy T of its constituents as $T = \frac{1}{2}V$. Zwicky calculated the total mass of the Coma Cluster to be $>5 \times 10^{14}$ solar masses ($M_\odot$), considering a typical velocity of 1200 km/s for the ∼800 galaxies in the cluster and its $\sim 10^6$ light-year diameter. Assuming the (luminous) mass of a typical galaxy to be $\sim 10^9\,\mathrm{M}_\odot$ gives a total cluster mass $\sim 8 \times 10^{11}\,\mathrm{M}_\odot$. Zwicky interpreted the >100-fold deviation as evidence of a form of dark matter[1] excluded from the luminous galactic mass estimate [10, 11].

The rotation curve of a galaxy describes the velocity of stars in their orbits about the Galactic Center as a function of their orbital radii. In Newtonian gravity, the

[1] Zwicky's 1933 publication is often cited as the first use of the term "dark matter," but the astrophysics community had for several decades pondered dark forms of matter [15], including dark stars, as possible contributors to the mass of galaxies. For example, in his 1906 lectures [16], William Thompson Lord Kelvin noted that some fraction of stars could be sub-luminous or non-luminous and thus constitute a "dark matter."

acceleration a of a star of at radius r from the center of a galaxy is

$$a(r) = GM(r)/r^2 \tag{2.1}$$

where G is the gravitational constant and $M(r)$ is the total mass within r of the center of the galaxy. In most galaxies, the luminous mass (visible baryonic matter; primarily gas and dust) is observed to be clustered in a central bulge, so one would expect $M(r)$ to be approximately constant at large r. Considering the radial acceleration $a(r) = v^2/r$ of any body in a stable circular orbit, we obtain the expected form of the galactic rotation curves, $v^2/r = GM(r)/r^2$ or

$$v(r) \propto r^{-1/2} \tag{2.2}$$

outside the central bulge.

By observing the redshift of their hydrogen spectral emissions, Vera Rubin[2] and Kent Ford calculated the velocities of 67 stars in the Andromeda Galaxy (M31) at galactic radii in the range of $3 - 24\,\mathrm{kpc}$. In contrast to the expected $r^{-1/2}$ behavior, the measured stellar velocities were approximately constant out to the largest radii, as illustrated in Figure 2.1. A flat rotation curve at large r implies that a galaxy's mass is not concentrated in its center but is spatially distributed in a halo with $M(r) \propto r$ at least out to the radius of the farthest stars. Rubin and Ford calculated that the total enclosed mass $M(r)$ for M31 increased approximately linearly for $4\,\mathrm{kpc} < r < 14\,\mathrm{kpc}$ and then more slowly at larger r, for a total enclosed mass $M\,(24\mathrm{kpc}) = (1.85 \pm 0.01) \times 10^{11}\mathrm{M}_\odot$ [12]. Subsequent stellar velocity measurements for additional galaxies were all consistent with haloes of nonluminous matter extending beyond the galactic bulge [13]. These measurements were consistent with the previously-observed redshift for the 21 cm line of hydrogen gas [18].

Galactic rotation curves facilitate calculation of the total mass of a galaxy (out to the radius of the most distant velocity measurements) and its spatial distribution.

[2]For illuminating essays by Vera Rubin related to the dynamics surrounding her discovery of dark matter in galactic rotation curves, see reference [17].

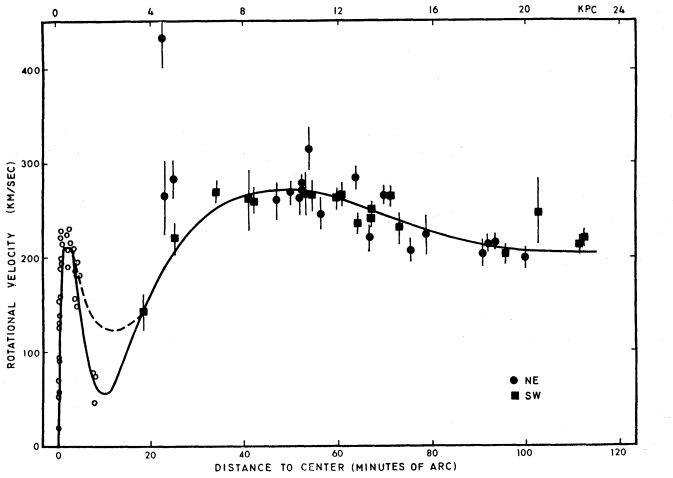

Figure 2.1: Rotational velocities are shown for the 67 stellar objects observed within M31 by Rubin and Ford. The data are fitted with two polynomial functions used to extract the required $M(r)$ [12].

Measured rotation curves consistently indicate both 1) a total gravitational mass several times the expectation based on observation of visible matter and 2) a spatial distribution that extends beyond the radius of the bulk of the visible matter. Luminous matter beyond the galactic bulge is distributed in a flat disk because it is able to interact with itself and lose angular momentum via radiation. The three-dimensional spatial distribution of a dark halo that has not collapsed into a disk indicates that its constituents behave differently from visible matter, specifically, that the constituents of the dark halo are dissipationless, and cannot radiate the energy required for collapse.

2.1.2 Gravitational Lensing and the Bullet Cluster

Weak gravitational lensing presents another method to directly measure the mass and mass distributions of galaxies and clusters. In weak lensing techniques, slight distortions in the images of distant galaxies reveal the gravitational potential in the foreground. In addition to providing additional evidence for mass in excess of the visible mass, weak lensing facilitates mapping of both the distribution of dark matter on large scales [19] and of dark matter distribution of galactic haloes, eg [20].

Figure 2.2 illustrates the colliding system E0657-55, better known as the Bullet

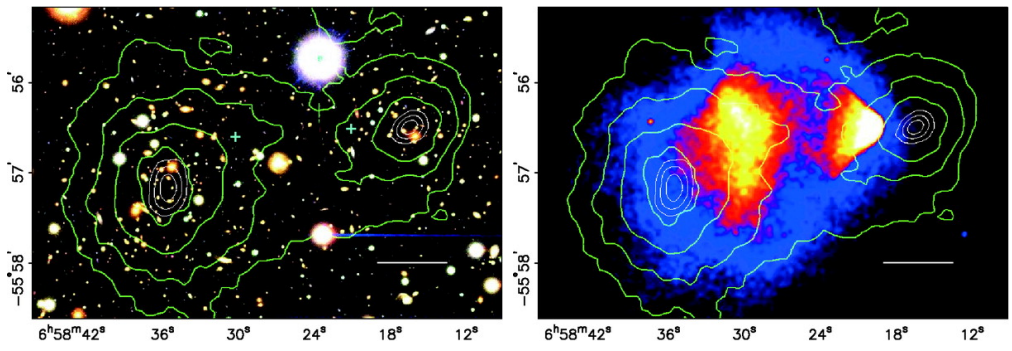

Figure 2.2: The centers of the gravitational potential as determined by weak lensing (green lines) are overlaid with images of the Bullet Cluster in visible light (*left*, mapping collisionless galaxies in the cluster) and in X-rays (*right*, mapping hot baryonic gas). The gravitational potential shows that the dark matter traces the trajectory of the collisionless galaxies and is displaced spatially from the hot gas. The scale bar indicates 200 kpc [21].

Cluster. In this system, the collisionless stars, observable in visible light, and the interacting hot baryonic gas, observable in X-rays, appear spatially separated due to their different levels of self-interaction during the collision. Clowe et al. (2006) [21] mapped the gravitational potential of the system using weak lensing and showed that the the potential, and thus the dark matter, was spatially separated from the X-ray component and instead followed the collisionless path of the stars.

The observation of the spatial offset between the bulk of the mass in the Bullet Cluster, as mapped by weak gravitational lensing, and the hot gas, as mapped by X-rays, proves that the dark matter must be a novel form of matter. Evidence for dark matter comes from observation of its gravitational effects. The velocity dispersions of the virialized systems in equilibrium in Section 2.1.1 could in principle be explained by models of modified Newton dynamics (MOND), in which the gravitational force is enhanced at large distance scales relative to the standard Newtonian $1/r^2$ formulation. However, models of modified gravity cannot explain a gravitational potential like the Bullet Cluster that is spatially offset from the true matter distribution. Observation of the Bullet Cluster also places some of the strongest limits on dark matter self-interactions, as self-interactions would cause the dark matter haloes to slow and interact during the collision. Numerical simulations of the Bullet Cluster place upper limits on dark matter self-interaction cross sections at $\sigma/M_{DM} \lesssim 2\text{cm}^2/\text{g}$ [22].

2.1.3 Structure Formation and Cosmological Simulations

Large-scale N-body simulations of the evolution of a cold dark matter Universe naturally predict the formation of galactic dark matter haloes such as those observed by Rubin and Ford as well as the large-scale structure of galaxy clusters, illustrated in Figure 2.3. In numerical simulations of cold dark matter, primordial density fluctuations seed small dark matter clumps under their self gravitation. Baryonic matter, which is not needed in simulations to reproduce the large-scale structure, falls into the gravitational potential of the dark matter clumps. These smaller clumps then accrete to form larger galaxies with distinct substructures, and the galaxies accrete into large clusters. The result is a complex large-scale structure known as the "cosmic web" made up of older substructures. This is in agreement with observations of large-scale structures of galaxy clusters [23] and of multiple substructures within the Milky Way halo, some of which are known to be older than the Milky Way itself [24, 25]. Simulations show that, by contrast, hot dark matter alone cannot form these ancient small-scale structures. The large velocities mix and erase the structure of small clumps. Instead, the cosmology of hot dark matter features ancient large-scale structures that fragments into younger small-scale structures, in conflict with observations. Based on these simulations, hot dark matter must be $<1\%$ of the total abundance [26].

The fine-grained phenomenology of the Universe depends on the physics of the dark matter, including its possible self interactions. When compared with observations including of dark matter structures from gravitational lensing, increasingly powerful simulations have the capability to reveal particle properties of the dark matter; critically, they can probe non-linear dynamics not accessible with analytical methods. At the smallest simulated scales, the results of N-body simulations diverge from observations of Galactic structure. For example, the N-body simulations predict 'cuspy' galactic density profiles that rise steeply near Galactic Centers [29], in contrast with the observed density profiles (less steeply rising 'cores') of many galaxies [30, 31]. Debate is ongoing in the field as to whether this means that the dark matter

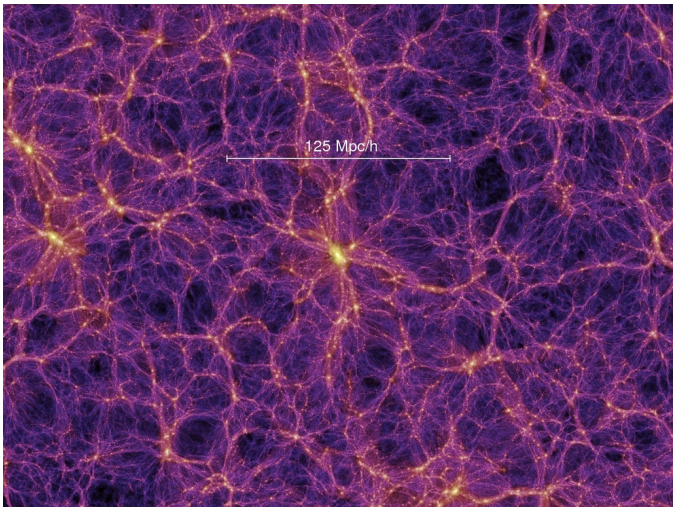

Figure 2.3: Visualization by the Millennium Simulation Project of the cosmic web structure of the Universe . Each bright spot is a galaxy cluster. Image Credit: V. Springel, Max-Planck Institut für Astrophysik [27, 28].

must not be perfectly cold and collisionless, or whether these features are due to the effects of baryonic matter not included in the simulations [32, 33, 34, 35].

2.1.4 Cosmic Microwave Background

The cosmic microwave background (CMB) is a population of 2.7 K photons that have been streaming through the Universe since the first hydrogen atoms formed in the "epoch of recombination" 380,000 years after the Big Bang (Section 1.2). The CMB photons are highly uniform and isotropic, corresponding to the high level of uniformity and isotropy in the early Universe and supporting the theory of inflation. Meanwhile, precise measurements of the $\mathcal{O}(10^{-5})$ fluctuations in the blackbody temperature (illustrated in Figure 2.4) reveal the structure of the Universe during this epoch. As shown in Figure 2.5, the degree of temperature fluctuations is quantified in a multipole power spectrum, which describes the correlations of the CMB photon temperature over different angular scales. Fluctuations on smaller angular scales correspond to higher multipoles l.

The CMB is a precise probe of the energy content of the Universe thanks to the phenomenon of baryon acoustic oscillations. Prior to the formation of the first hydro-

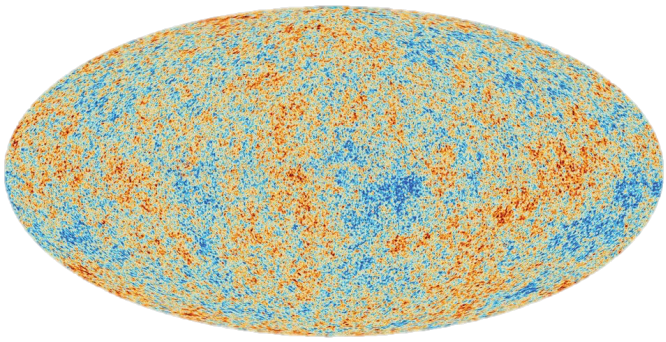

Figure 2.4: A map of the CMB temperature fluctuations observed by the Planck satellite. Image Credit: European Space Agency and Planck Collaboration.

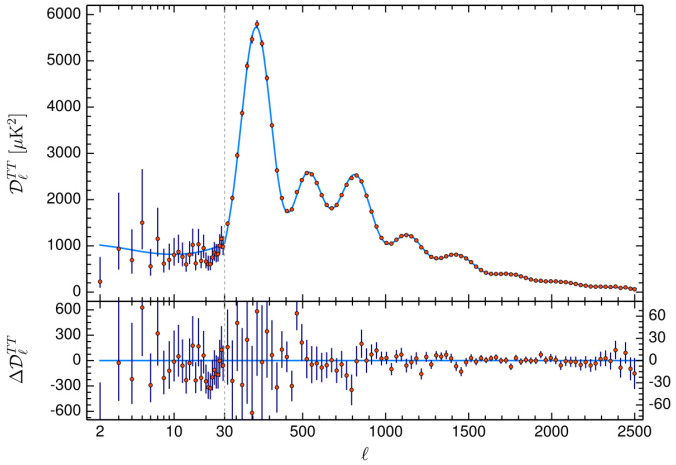

Figure 2.5: The power spectrum of the multipole moments of the CMB. The blue line is the theoretical ΛCDM spectrum with model parameters fitted to the data [9].

gen atoms, protons, electrons, and photons existed in an electromagentically-bound plasma that was coupled to clumps of dark matter through gravity. The balance between the gravitational force attracting the plasma to the dark matter clumps and the pressure of the dense plasma produced oscillations in the spatial distribution of the plasma. In contrast to the baryons, dark matter is pressureless to the extent that it has no self-interactions. The degree of the plasma oscillations reflected the relative importance of plasma pressure and gravity. The photons released from the plasma with the formation of neutral hydrogen and the corresponding depletion of charged particle have been streaming through space ever since. Their temperature reflects the the energy lost to the gravity of local density fluctuations at the time of their release.

The amplitude and angular size of the CMB temperature fluctuations today cor-

respond directly to the gravity (total matter) and pressure (baryonic matter) at the time of the CMB, providing the most precise measure of the energy content of the Universe [9]. Detailed analysis of the CMB parameters show that no more than 4% of the dark matter present at CMB times may have decayed away into dark radiation, and the constraints on decay to matter are much stronger [36].

2.2 Dark Matter Candidates

Together, the astrophysical and cosmological observations presented in Section 2.1 present a self-consistent picture, in which 26.8% of the total energy density of the Universe is composed of dark matter. The temperature, self-interactions, and electromagnetic interactions of the material(s) composing the dark matter are constrained based on the observations. Additionally, the dark matter originated before the time of the CMB, with <4% change in abundance in the intervening 13.8 billion years. Any theoretical model of the dark matter abundance must explain its origin in the early Universe and its stability over the history of the Universe.

No known particle can explain the dark matter abundance. Apart from the neutrinos, all of the massive Standard Model particles carry an electric charge. With the discovery of the non-zero neutrino mass [37], the Standard Model neutrinos, which are weakly interacting, stable over the timescale of the Universe, and produced in high numbers as thermal relics of the Big Bang, became an attractive candidate for the dark matter. However, the low Standard Model neutrino mass scale $m_\nu < 0.8\,\mathrm{eV}$ [38] means that neutrinos compose only ∼0.3% of the energy density of the Universe and thus do not explain the bulk of the dark matter. Additionally, the low mass means that the thermal relic neutrinos are relativistic (hot dark matter), and would have washed out the galactic substructures if they were more of the dark matter.

Theoretical models abound that explain some or all of the dark matter abundance. The dark matter candidates range over 90 orders of magnitude in mass. The lower limit, $M_{DM} > 10^{-21}\,\mathrm{eV}$ arises from observations of the Lyman-α forest [39] and the wavelength of low-mass dark matter compared to the halo mass distributions in galax-

ies [40] while the upper limit $M_{DM} \ll 10^7 M_\odot$ allows for many dark matter quanta for form a mass distribution in galactic haloes. Diverse models have been proposed to explain the origins of dark matter in the early Universe and its observed signatures for the present day. Beyond explaining the dark matter abundance, many of these models simultaneously resolve other outstanding inconsistencies with the Standard Model of particle physics. This section treats a few of the many broad classes of dark matter models that are most relevant for the experiments discussed in this thesis, including primordial black holes in Section 2.2.1 and dark matter particles produced through freeze out scenarios in Section 2.2.2.

2.2.1 Primordial Black Holes

Primordial black holes (PBH) are gravitationally-bound compact objects that could have formed through various early Universe phenomena including, most generically, the collapse of primordial density fluctuations [41]. The mass of a PBH roughly corresponds to the time at which it formed, with an approximate scaling [42, 43]

$$M_\star \sim \frac{c^3 t}{G} \sim 10^{15} \left(\frac{t}{10^{-23}\,\mathrm{s}} \right) \mathrm{g}. \tag{2.3}$$

In Eq. (2.3), t is the time of formation relative to the Big Bang, c is the speed of light, and G is the gravitational constant. Assuming $10^{-43}\,\mathrm{s} < t < 1\,\mathrm{s}$, PBH could have formed with mass $10^{-5}\,\mathrm{g} < M_\star < 10^{38}\,\mathrm{g}$ [41]. Note that, in contrast to PBH, the more familiar black holes formed in the explosions of massive stars were not present at the time of the CMB. While these objects behave as a form of dark matter today, they form an insignificant fraction of the total energy density of the Universe.

Any PBH formed with $M_\star < 10^{15}\,\mathrm{g}$ would have already evaporated via Hawking Radiation [44, 42, 45, 46, 47] and thus could not constitute a significant fraction of the cosmological dark matter abundance. PBH formed with $M_\star \sim 5 \times 10^{15}\,\mathrm{g}$ would be evaporating in the present-day; as such, they also cannot constitute a significant fraction of the dark matter, but their evaporation would produce observable signatures in the form of γ-rays or charged cosmic rays [48]. Any non-evaporating PBH would

constitute some fraction f_{PBH} of the dark matter, and, depending on their mass, would additionally be responsible for generation of large-scale structure, seeding the supermassive black holes that form galactic nuclei, or other cosmological effects [49].

These diverse cosmological effects can be interpreted as constraints on the PBH abundance relative to the dark matter abundance, as shown in Figure 2.6. Notably, Figure 2.6 illustrates a mass window (**A**) in which a population of asteroid-mass PBH formed with a monochromatic ($\Delta M_\star \sim M_\star$) mass distribution could constitute all of the dark matter. PBH in mass-range **D** would be heavier than a galactic halo and thus cannot constitute the dark matter. Outside of **A**, it is possible in some scenarios that PBH could form a significant fraction of the dark matter abundance if the mass distribution is extended. In particular, PBH with $M_\star \sim 10 M_\odot$ (**C** in Figure 2.6) could constitute a significant fraction of the dark matter and have received increased attention since the observation of gravitational waves from black hole mergers in this mass range [50, 51, 52, 53]. The range **B** is of interest due to possible detections in gravitational microlensing surveys [54].

2.2.2 Thermal Relic Dark Matter

Thermal relic models assume that some or all of the cosmological dark matter abundance is composed of a yet-undiscovered fundamental particle that interacts with the Standard Model particles through some interaction(s) beyond gravity alone. The dark matter particles were once in thermal equilibrium with some particle(s) of the Standard Model, but as the Universe cooled and expanded, the equilibrium interactions ended, leaving behind a relic abundance of dark matter particles. Such "freezeout" scenarios produce non-relativistic (ie, viable as cold dark matter) thermal relics if $M_{DM} \gtrsim 1\,\mathrm{MeV}$.

The canonical freezeout scenario [55] is illustrated in Figure 2.7. Following [56], the number density n of dark matter particles is determined by 1) dilution in an expanding Universe and 2) annihilation to and production from Standard Model

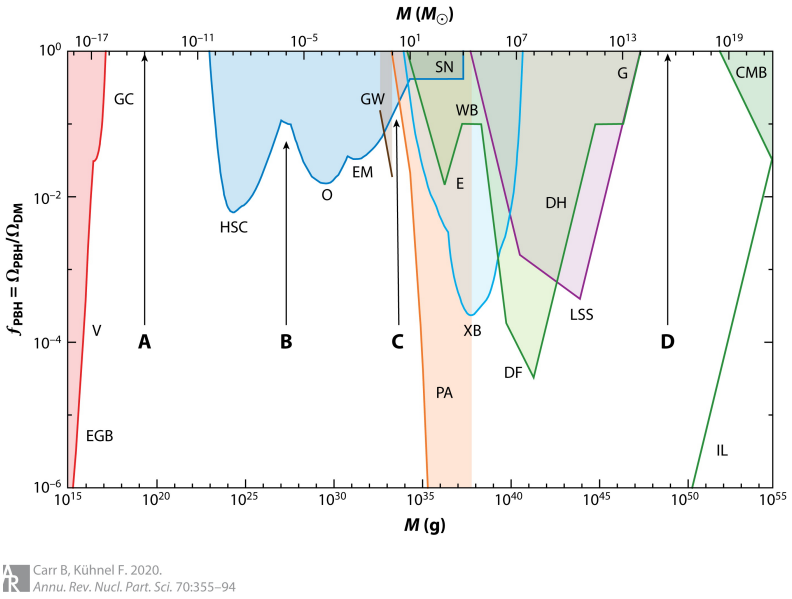

Figure 2.6: Constraints on the fraction f_{PBH} of the total dark matter density that could be composed on PBH is shown as a function of the PBH mass. The constraints come from evaporation (red), microlensing (dark blue) gravitational waves (GW; brown), dynamical effects (green), accretion (light blue), CMB distortions (orange) and dipole (dark green), and large-scale structure (purple). The incredulity limit (IL) refers to 1 PBH per galaxy, cluster, or Universe [41].

particles in a cooling Universe, as

$$\frac{dn}{dt} = -3nH - \langle\sigma v\rangle(n^2 - n_{eq}^2). \tag{2.4}$$

Note that the comoving number density (which appears in Figure 2.7) is the number density normalized to the expanding volume of the Universe, such that if the total number of particles is constant in time, the coming number density, in contrast to the number density, is also constant. In Eq. (2.4), H is the Hubble parameter that represents the expansion rate of space at time t, σ is the total cross section for dark matter annihilation to Standard Model particles, n_{eq} is the thermal equilibrium dark matter density at temperature T, and v is the relative velocity between any two annihilating dark matter particles. The reaction rate is parametrized by $\langle\sigma v\rangle$, which varies with T depending on the mean relative velocity of the dark matter particles. The scenario begins with $T \gg M_{DM}$. Under this condition, the dark

matter is relativistic, $\langle\sigma v\rangle$ is large, and both annihilation and production proceed rapidly, dominating dn/dt and maintaining a high dark matter abundance $n \sim n_{eq}$. As T decreases below M_{DM}, $\langle\sigma v\rangle$ decreases, the rate of dark matter production slows, and n_{eq} decreases exponentially with decreasing T per the non-relativistic Boltzmann velocity distribution. Freeze out occurs at temperature T_f when $n_{eq}\langle\sigma v\rangle \sim 3H$. After freeze out, dn/dt is dominated by the Hubble expansion rather than by equilibrium processes, such that the comoving number density remains constant, and $n \sim n_{eq}(T_f)$ diverges from $n_{eq}(T)$ as T falls.

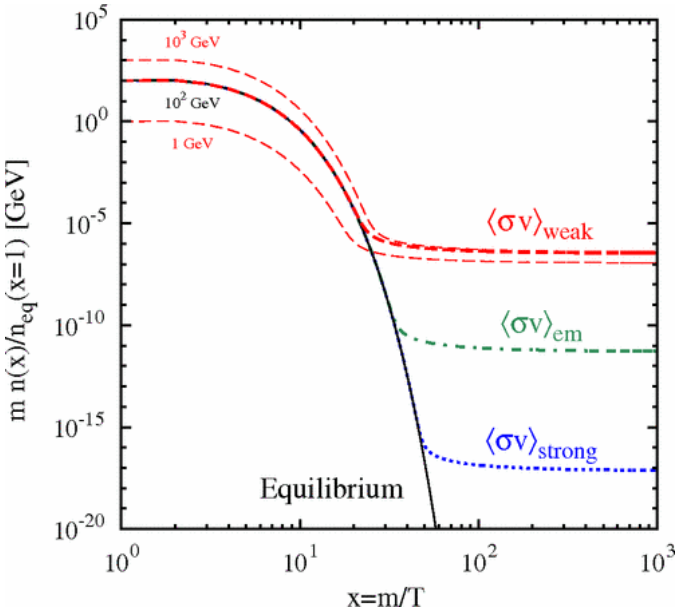

Figure 2.7: The comoving dark matter mass density, scaled relative to the equilibrium number density when $M_{DM} = T$, is shown as a function of $x = M_{DM}/T$, for the "freeze out" scenario of thermal-relic dark matter production. x increases monotonically with time. Relations are shown for typical $\langle\sigma v\rangle$ of weak (red dashed), electromagnetic (green dot-dashed), and strong (blue dotted) interactions. For the weak interaction case, the dependence on M_{DM} is also shown [55].

Thanks to the exponential decrease of n_{eq}, freezeout occurs quickly once $T < M_{DM}$, with $T_f \sim M_{DM}/20$ for typical M_{DM}. Comparing $n_{eq}(T_f)$ and H, a cross section $\langle\sigma v\rangle \sim 10^{-26}\,\mathrm{cm}^3\,\mathrm{s}^{-1}$, known as the "thermal relic cross section," can produce the observed dark matter relic density for dark matter with $1\,\mathrm{MeV} < M_{DM} < 100\,\mathrm{TeV}$, where the upper bound is due to unitarity [57]. Precise numerical calculation gives comparable results [55].

The term Weakly Interacting Massive Particle (WIMP) describes a thermal-relic dark matter particle that interacts at the scale of the weak nuclear force. In a typical weak-force interaction, $\langle \sigma v \rangle$ has the form α^2/M_{DM}^2 with coupling constant $\alpha \sim 10^{-2}$. Under this assumption, the thermal-relic cross section predicts a WIMP with $M_{DM} \sim 1\,\mathrm{TeV}$. The self-consistency of a dark matter candidate with a weak-scale coupling strength and mass M_{DM} on the scale of the weakly-interacting W, Z, and Higgs bosons of the Standard Model is known as the "WIMP Miracle."

Numerous theories of particle physics beyond the Standard Model (BSM) naturally introduce candidate dark matter particles that could be produced thermally through freeze out. For example, theories of supersymmetry (SUSY) [58] were developed to explain the gauge hierarchy problem related to the anomalous mass of the Higgs boson [3, 4]. In SUSY models, every Standard Model particle has a supersymmetric counterpart. The lightest supersymmetric particle (LSP) is absolutely stable thanks to a symmetry of the theory, and it can have a mass on the weak scale and couple directly to the weak force of the Standard Model. If the LSP is neutral, as in the case of a "neutralino" (neutrino superpartner) or "higgsino" (Higgs boson superpartner), it could be produced as a thermal relic and constitute the dark matter [59]. As another example, in theories of Universal Extra Dimensions (UED; also known as Kaluza-Klein theories), all Standard Model particles may propagate through one or more extra spacetime dimensions. Like SUSY, UED theories naturally resolve the gauge hierarchy problem and provide a counterpart for every Standard Model particle. In several versions of Kaluza-Klein theories, the lightest Kaluza-Klein particle (LZP) is a stable dark matter candidate [60].

2.3 Searches for Thermal Relic Dark Matter

Interactions with Standard Model particles are inherent to the production of thermal relic dark matter in the Universe. These interactions also correspond to multiple experimental handles through which to probe the existence of thermal-relic dark matter particles in the present day.

Figure 2.8 schematically illustrates the three primary detection strategies for thermal relic dark matter. Searches for dark matter particles produced from Standard Model particles at accelerators are discussed in Section 2.3.1. Section 2.3.2 treats searches for scattering of Galactic dark matter with Standard Model particles in terrestrial detectors. Finally, a general introduction indirect detection of the Galactic dark matter through observation of the Standard Model products of its annihilation or decay is in Section 2.3.3.

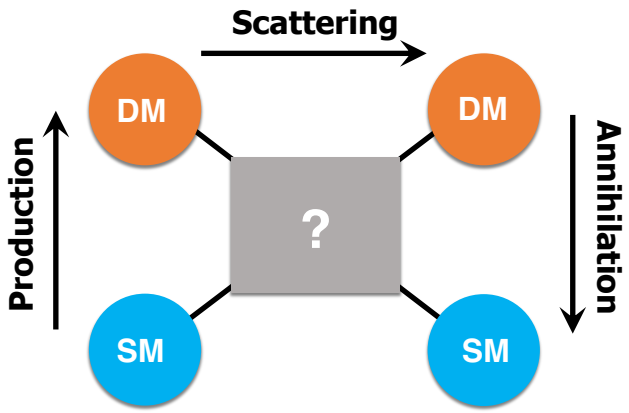

Figure 2.8: Searches for thermal relic dark matter are based on the presumption of some unspecified interaction (gray) between dark matter (DM; orange) and Standard Model particles (SM; blue). This interaction leads to possible experimental strategies including 1) production of dark matter particles from Standard Model particle collisions at accelerators, 2) direct detection of the Galactic dark matter via scattering processes with Standard Model particles, and 3) indirect detection of the Galactic dark matter via detection of its Standard Model annihilation products.

Each of these strategies features unique theoretical and experimental strengths and limitations. Common among them is that they probe some parameter space defined by a dark matter interaction strength and M_{DM}, though the particular interaction probed varies between the experiment types. To date, no experiment has provided a robust detection of particles (thermal relics or otherwise) that compose the cosmological dark matter abundance. On the other hand, multiple experimental searches for thermal relic dark matter have excluded dark matter parameter space based on non-observation of dark matter signatures. Comparison of limits between different detection strategies is highly model dependent, as the relative strengths of

the processes relevant for production, scattering, or annihilation depend strongly on the underlying particle physics. Each experimental strategy probes a subset of the possible thermal-relic dark matter candidates, and it is not possible to generically compare limits from one experiment-type to another.

2.3.1 Production at Colliders

Searches for production of dark matter at colliders assume that the dark matter couples to Standard Model particles either via a small direct coupling or via one or more BSM particles that act as mediators. Dark matter particles in a given model would then be produced with some calculable probability depending on the energy of the collision and the strength of the coupling. Because dark matter interacts so weakly, it is invisible to the detectors typical of collider experiments. Thus, the canonical model for these experiments is to search for interactions with both dark matter and Standard Model particles in the final state produced in the collision; the experimental signature of dark matter production is the missing energy and momentum carried away by the invisible dark matter particles but necessary to balance energy and momentum conservation in the collision [61]. Other strategies involve precision measurements of Standard Model couplings to test a specific BSM theory involving dark matter [62, 63].

Dark matter searches at colliders typically follow one of two main strategies. The first strategy begins with a more generic theory, such as the assumption that the dark matter particle is coupled to quarks by a new heavy mediator [64, 65, 66]. These models assume that, while additional BSM states may exist, they are not important at the energy scales accessible at current colliders. As illustrated in Figure 2.9 (*center*), some experimental signatures for such a generic model could be 1) anomalous resonances in Standard Model di-lepton or di-jet final states due to scattering by the mediator or 2) missing energy or momentum in final states with one or more Standard Model particle, where an invisible pair of dark matter particles produced via the heavy mediator carries away the missing energy. The results of this search strategy can be easily translated to many dark matter models, but there is no guarantee that

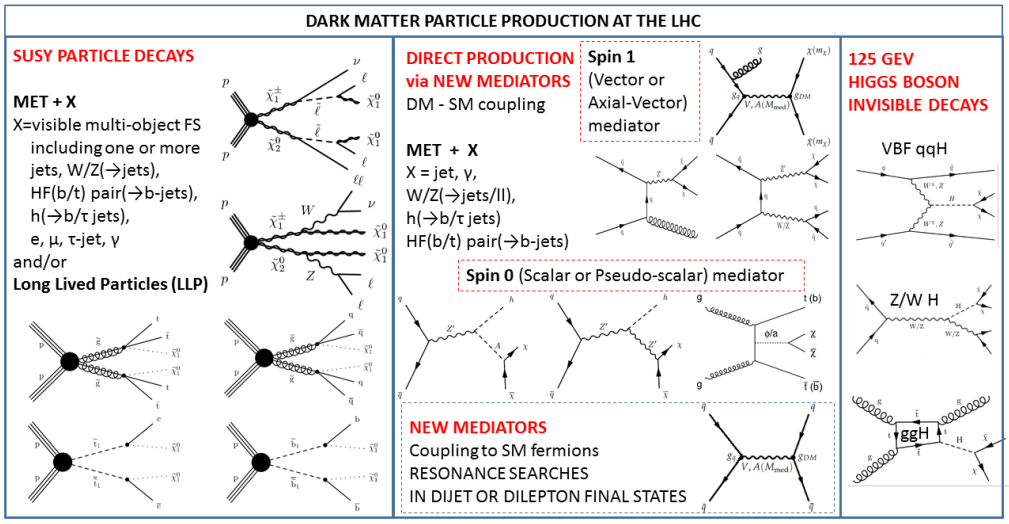

Figure 2.9: Examples of interactions producing detectible final states for SUSY (*left*), models of dark matter coupled to Standard Model quarks via a generic heavy mediator (*center*), and the specific case of searches for dark matter couplings to the Higgs boson (*right*) [62].

they can represent a real physical theory.

The second strategy begins with a complete particle physics theory that includes a dark matter particle, possible additional BSM particles, and their couplings to the Standard Model. Then, the search proceeds for specific self-consistent experimental signatures. For example, Figure 2.9 (*left*) illustrates several possible final states emerging from proton-proton collisions at the LHC in the case of a particular SUSY model. These include specific final states with Standard Model particles produced in the decay of heavier supersymmetric states and missing energy carried away by the invisible LSP. This strategy facilitates targeted searches for specific self-consistent particle physics theories that could explain the dark matter, but the constraints are highly dependent on the details of the particle physics model invoked and are difficult to translate between models.

2.3.2 Direct Detection

Experimental efforts toward the direct detection of dark matter search for scattering of Galactic dark matter in a terrestrial target. The experimental signature is the

recoil of the Standard Model target, typically an atomic electron or nucleus within a larger radiation detector. Some or all of the kinetic energy of the recoiling nucleus or electron is then converted to ionization, scintillation light, phonons, and/or other signatures and read out in the detector.

In practice, the kinematics of the system mean that the recoil energy transferred to a nucleus or electron is small,

$$E_R = \frac{2\mu^2 \mathbf{v}^2 \cos^2\theta}{M_T} \tag{2.5}$$

where M_T is the mass of the electron or nucleus target, $\mathbf{v}$ is the velocity of the dark matter particle relative to the detector, θ is the scattering angle of the recoiling target relative to $\mathbf{v}$, and $\mu \equiv \frac{M_T M_{DM}}{M_T + M_{DM}}$ is the reduced mass of the system. The distribution of $\mathbf{v}$ depends on the velocity dispersion of dark matter in the Milky Way, which is $\mathcal{O}(10^{-3})$ c [67], as well as, with decreasing significance, the orbital velocity of the Sun, the orbital velocity of the Earth, and the rotation of the Earth. For heavy dark matter ($M_{DM} > M_T$) in a typical nuclear target $M_T \sim 10 - 100\,\text{GeV}$, $0 < E_R \lesssim 10 - 100\,\text{keV}$ depending on the target mass. For $M_{DM} < M_T$, E_R is kinematically suppressed by a factor of $\left(\frac{M_{DM}}{M_T}\right)^2$. For this reason, searches for models with $M_{DM} \ll 1\,\text{GeV}$ typically proceed in electron-recoil channels so that $M_{DM} \gtrsim M_T$.

For the classic case of dark matter scattering with a nucleus, the expected interaction rate [68] is determined by a combination of 1) the particle physics of the dark matter scattering, 2) the nuclear physics of the target, and 3) the astrophysics determining the local dark matter distribution. In the typically-reported case of spin-independent dark matter-nucleus coupling, the total dark matter-nucleus scattering rate is assumed to be the sum of the dark matter scattering rates with the individual nucleons, and the total interaction rate is

$$\frac{dR}{dE_R} = \frac{\sigma_n}{M_{DM}\mu_{n,DM}^2} \cdot A^2 M_T N_T |F(E_R)|^2 \cdot \rho_{DM} \int_{v_{min}} \frac{dv}{v} f(v). \tag{2.6}$$

The first term of Eq. (2.6) describes the particle physics of dark matter-nucleon scat-

tering. $\mu_{n,DM}$ is the reduced mass of the dark matter-nucleon system and the effective dark matter-nucleon cross section $\sigma_n \equiv \frac{1}{16\pi}\frac{\mu_{n,DM}^2}{M_{DM}^2 M_T^2}\frac{|Zf_p+(A-Z)f_n|^2}{A^2}$, where Z is the number of protons, A is the number of nucleons, f_p is the dark matter-proton interaction rate, and f_n is the dark matter-neutron interaction rate. σ_n facilitates comparison between direct detection experiments using different nuclear targets, but folds the assumption of spin-independent scattering into the comparison. The second term contains the nuclear physics, where N_T is the number of target nuclei in the detector and the form factor $F(E_R)$ contains the physics of nucleons bound in the nucleus. Finally, the astrophysics is contained in the last term, where $\rho_{DM} \sim 0.4\,\mathrm{GeV/cm^3}$ [69] is the local dark matter number density and v_{min} is the minimum kinematically-allowed v for scattering. $f(v)$ describes the local dark matter velocity distribution; in the Standard Halo Model, $f(v) = \frac{4}{\sqrt{\pi}}\frac{v^2}{v_0^3}\exp\left(-\frac{v^2}{v_0^2}\right)$. The result is a spectral shape that decreases with increasing E_R, so that sensitivity at low energies (less than the maximum recoil energy) is critical for detection.

Eqs. (2.5) and (2.6) describe a rare process producing energy deposition $<10\,\mathrm{keV}$ in a typical dark matter-nucleus recoil. Sensitivity to dark matter-nucleus recoils thus requires a large-volume detector with low backgrounds and low noise to facilitate a low-energy threshold. Accordingly, typical direct detection experiments are situated in deep underground laboratories to protect from cosmic radiation. Care is taken to reduce radiogenic backgrounds by using low-radioactivity materials and by shielding the detector volume with passive materials. Precise characterization of the remaining backgrounds, particularly neutron-nucleus scattering, facilitates sensitivity to a rare signal. Some experimental strategies additionally rely on directional detection, or annual or daily modulation of the dark matter rate expected due to changes in the Earth's velocity in the Galaxy, to differentiate between a true dark matter signal and experimental backgrounds. These techniques will be particularly relevant for future experiments with sensitivity below the cross section known as the "neutrino floor," at which solar neutrinos create a background that cannot be mitigated by traditional underground or shielding techniques.

Figure 2.10 summarizes the results from several direct detection experiments. The

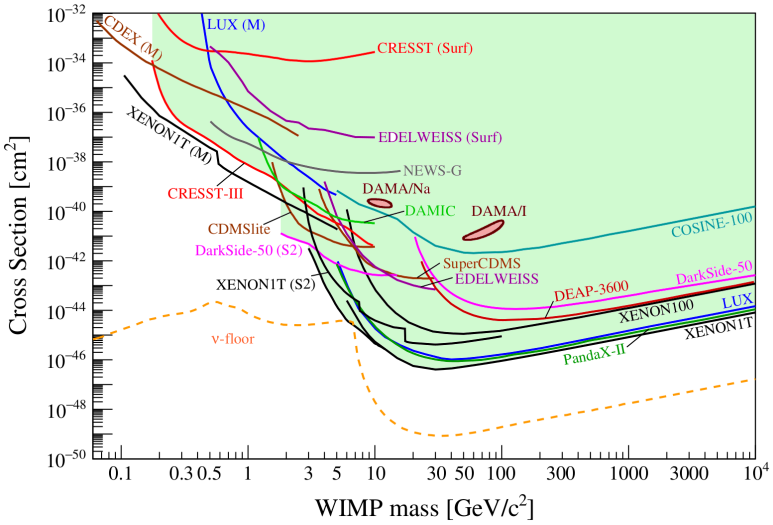

Figure 2.10: Spin-independent exclusion limits on σ_n in a range of M_{DM} for a range of direct detection experiments [70].

curves show regions of the $\sigma_n - M_{DM}$ parameter space that has been excluded based on non-detection of a dark matter signal; for a given experiment, the decreased sensitivity on the low-mass side of range is due to kinematic suppression of E_R for $M_{DM} < M_T$. The exclusion of the large breadth of parameter space reflects the high sensitivity of the instrumentation; recent results from ton-scale liquid Xenon experiments in particular have provided excluded spin-independent dark matter-nucleon scattering for $10 - 100\,\text{GeV}$-scale dark matter with $\sigma_n < 10^{-46}\,\text{cm}^2$ [71, 72, 73]. Several experiments with sensitivity to electron scattering of sub-GeV or even sub-MeV dark matter are currently in progress [74, 75, 76, 77].

The results of direct detection experiments must be interpreted with care thanks to the assumptions inherent in the reported limits. The limits reported in Figure 2.10 all assume a typical spin-independent dark matter-nucleus interaction. The results are also sensitive to systematic errors related to calculation of the local dark matter velocity distribution or density [69] on the astrophysics side, nuclear form factors on the nuclear physics side, and background characterization on the experimental side. The reported limits on σ_n also assume that the dark matter is composed entirely of one particle species. Further, many well-motivated models of thermal relic dark matter are inaccessible to even these sensitive experiments even with these assumptions. For

example, in a viable SUSY model with a higgsino as the dark matter, $\sigma_n < 10^{-48}\,\mathrm{cm}^2$ lies below the sensitivity of all current experiments [78]. This example illustrates the model-dependence of the direct detection results.

2.3.3 Indirect Detection

Indirect detection (see [56] for a useful discussion) describes searches for evidence of annihilation or decay products of the cosmological dark matter. This evidence can arise from measurements of the possible annihilation products themselves or from observation of their contributions to the thermal or ionization history of the Universe. The figure of merit for indirect searches is sensitivity to the annihilation cross section or decay lifetime of the dark matter to any or all final states, over a range of M_{DM}.

For the annihilation of thermal relic dark matter produced through freezeout, the thermal relic cross section (Section 2.2.2) provides a detection target sensitivity that is independent of the details of the particle physics model. This is in contrast to direct detection and production techniques, for which the required sensitivity depends inherently on the specific particle physics model. Thus, while any observation of dark matter in a production or direct detection experiment would provide invaluable information about its particle nature, indirect detection techniques often provide more robust model-independent signatures, and they are required to provide model-independent exclusion of dark matter produced through freezeout processes.

In the case of s-wave annihilation, dark matter produced by freezeout is excluded for $M_{DM} \lesssim 10\,\mathrm{GeV}$ based on the impacts of its annihilation products on the thermal history of the Universe. Note that these bounds can be evaded in the case of asymmetric dark matter models, dark matter annihilating entirely to neutrinos, or annihilation suppressed at low velocities (e.g., p-wave annihilation). Freezeout models with $M_{DM} \lesssim 1\,\mathrm{MeV}$ are excluded because the energy released in dark matter annihilation would interfere with the formation of light elements during Big Bang Nucleosynthesis, in conflict with observations [79]. Even stronger constraints are provided by analysis of the CMB power spectrum (Section 2.1.4). Too much ionization power from the products of dark matter annihilation or decay at the time of the CMB

would be in conflict with measurements of a Universe transparent to photons. Unless dark matter annihilates to a primarily-neutrino final state, the classic freezeout models with $M_{DM} \lesssim 10\,\mathrm{GeV}$ are excluded based on the low observed ionization rate at the time of the CMB [80, 9].

Indirect dark matter detection otherwise involves measurement of Standard Model particles. Regardless of the details of the annihilation or decay, the final products would be some mixture of stable particles including electrons, positrons, protons and heavier nuclei, antiprotons and heavier antinuclei, photons, or neutrinos. Self-consistent models typically produce some mixture of these. For example, dark matter annihilation to quarks would produce a final state with photons from the decay of neutral mesons; electrons, positrons, and neutrinos from the decay of charged mesons; as well as protons, antiprotons, and heavier (anti-)nuclei. The spectral shape of any of these final states varies depending on the kinematics of the particular processes involved, but the typical signal would be extended in energy thanks to the various decay chains leading to the final state.

The rate of dark matter annihilation (decay) typically scales as n^2 (n), where n is the dark matter number density. To maximize signal-to-background, indirect dark matter searches probing photon or neutrino channels target particles arriving from relatively nearby regions of high dark matter density. Typical choices involve the Galactic Center, which features the highest dark matter density in the Galaxy but suffers from high rates of astrophysical background, and dwarf galaxies, which feature a lower overall signal but higher signal-to-background. By contrast, charged particles lose their directional information due to diffusion in galactic magnetic fields; the result is a nearly isotropic particle flux with contributions from multiple astrophysical sources as well as, possibly, contributions from dark matter. To improve signal-to-background, indirect dark matter searches typically proceed in antimatter channels only, where astrophysical sources are somewhat less important.

The common challenge for indirect dark matter searches in nearly all channels pertains to the large and often uncertain astrophysical backgrounds. Possible dark matter signals have been reported in positrons above $\sim 10\,\mathrm{GeV}$ [81, 82, 83], in $\sim$

$10 - 20\,\mathrm{GeV}$ antiprotons [84], and in $\sim 1 - 4\,\mathrm{GeV}$ γ-rays from the Galactic Center [85, 86]. However, the dark matter interpretation has been vigorously debated for each of these possible signals. Both the γ-ray [87, 88, 89, 90, 91, 92, 93, 94, 95, 96, 97, 98, 99, 100] and positron [101, 102, 103, 104, 105, 106, 107] signals could arise from either dark matter or some previously-undiscovered astrophysical source, while the significance of the reported excess in the antiproton spectrum depends on the modeling of particle dynamics in the galaxy [108, 109, 110, 111, 112, 113, 114, 115, 116, 117]. The astrophysical backgrounds and the experimental strategies for detecting the cosmic-rays are detailed in Chapter 3.

The power of indirect detection techniques is evident considering the robust limits placed on various dark matter annihilation or decay scenarios. Observations of γ-rays from dwarf spheroidal galaxies provide the limits on individual decay channels from $10\,\mathrm{GeV} < M_{DM} < 100\,\mathrm{TeV}$, with sensitivity to the thermal relic cross section below $\sim 100\,\mathrm{GeV}$ for photon-heavy hadronic channels [118, 119, 120, 121, 122, 123]. Precision antiproton measurements [84] have excluded the thermal annihilation cross section for annihilation of WIMPs with $M_{DM} < 40\,\mathrm{GeV}$ and $150 < M_{DM} < 500\,\mathrm{GeV}$ into purely b quarks [108, 112], providing even more stringent limits even than dwarf spheroidal galaxies for $M_{DM} > 200\,\mathrm{GeV}$ [124]. Meanwhile, positron measurements provide the most stringent constrains for dark matter annihilation or decay to leptonic channels, where γ-ray signals are more faint [125, 83].

Combining the limits on individual annihilation channels and limits from the CMB facilitates a model-independent limit on the total annihilation cross section for WIMP dark matter; for $M_{DM} \lesssim 20\,\mathrm{GeV}$, this limit is below the thermal relic cross section and standard WIMPs cannot form all of the dark matter. This analysis also illustrates that despite robust limits on individual annihilation channels, the window of parameter space for thermal relic WIMPs that constitute 100% of the dark matter spans nearly 4 orders of magnitude in M_{DM}. If WIMPs compose only part of the dark matter, the allowed parameter space is further expanded [126].

In the case of hidden sector models, dark matter particles annihilate through a cascade of one or more unstable dark sector states that ends with decay to Standard

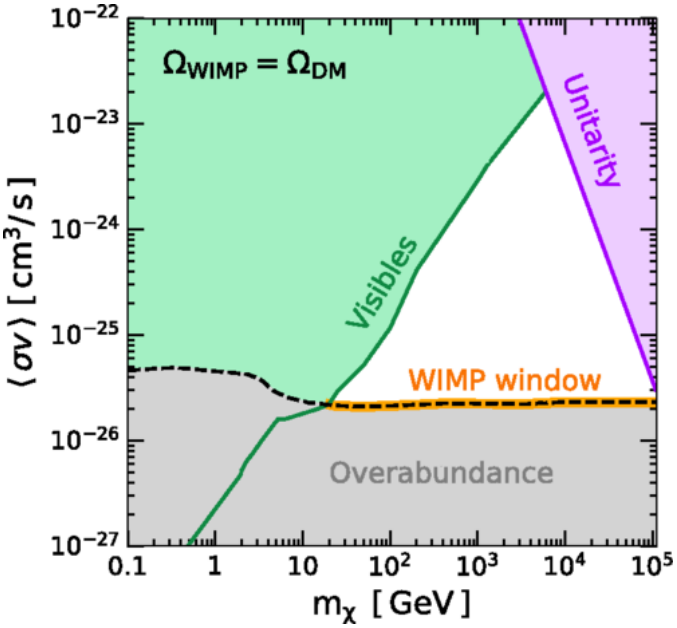

Figure 2.11: Limits on WIMP parameter space are shown based on indirect detection constraints (green; [126]) and unitarity bounds (purple; [57]). WIMP models with annihilation cross sections below the thermal relic cross section (black dashed; [55]) are excluded because they would over-produce dark matter (gray). WIMP models within the WIMP Window (orange) could compose all of the dark matter [126].

Model particles. Indirect detection is a particularly important technique for hidden sector models because the small couplings between hidden sector and Standard Model particles can suppress production or direct detection but do not impact the annihilation rate. Because of the wider range of decay channels and the possibility of multiple intermediate steps, limits on the annihilation cross section for hidden sector dark matter can differ by an order of magnitude from limits on WIMP annihilation to the same final state using the same data [127].

Chapter 3

Introduction to Galactic Cosmic Rays

Cosmic rays are non-thermal particles that permeate the Galaxy. With their energy density comparable to that of the interstellar magnetic fields, thermal gas, and starlight, the presence of cosmic-ray particles is fundamental for diverse Galactic processes. The interactions of cosmic rays are responsible for the elemental abundances of boron and beryllium. Low-energy cosmic rays in particular heat and ionize the interstellar medium (ISM) and the gases within molecular clouds, possibly determining the rate of star formation [128, 129]. Cosmic rays could also impact Galactic structure formation [130], generate turbulent magnetohydrodynamic waves [131], drive winds that remove material from Galaxies [132], and even change the climate of exoplanets [133]. The propagation and dynamics of cosmic rays in a range of energies spanning $<10^6$ eV to $>10^{20}$ eV produce diffuse emission in our Galaxy and beyond.

Observation of cosmic rays across a range of energies provides powerful probes of otherwise inaccessible physics including the most extreme events in the Universe [134], particle physics at energies inaccessible at terrestrial accelerators, Galactic and solar magnetic fields [135, 131], diffusive shock acceleration [131], and dark matter [136]. Remote observation of cosmic ray acceleration via electromagnetic signatures is a critical component of multimessenger astronomy [137]. These observations highlight the symbiosis between efforts to study cosmic rays to learn about their Galactic sources, and efforts to study the effects of cosmic rays as central to Galactic dynamics.

Despite both precise local measurements and indirect probes of cosmic ray popula-

tions across the Galaxy, the origins and propagation details of the cosmic rays remain ambiguous. In the current standard paradigm, cosmic rays originate primarily in supernova remnants (SNR) in the Galactic disk. They diffuse though an extended, magnetized Galactic halo, losing energy, and producing secondary isotopes through spallation reactions with the ISM. The tensions between the increasingly precise cosmic ray observations and the increasingly detailed models highlight puzzles in our current picture of Galactic dynamics, from the most extreme events to the ubiquitous magnetic fields.

This chapter opens with experimental measurements and centers them throughout. Since the first balloon-borne detection of cosmic radiation [138], developments in detector and space technologies have facilitated increasingly precise measurements of the cosmic-ray particles in and near the solar system, while the observation of cosmic ray showers in the atmosphere facilitates indirect detection of higher-energy particles, as detailed in Section 3.1. Section 3.2 discusses astrophysical probes of cosmic-ray populations in far regions of the Galaxy. Finally, Section 3.3 synthesizes these observations into a model of cosmic-ray particles in the Galaxy, including numerical methods to predict their spectra.

3.1 Local Measurements of Cosmic Particles

This section describes the range of missions to directly measure cosmic-ray particles using space-based, high-altitude, and terrestrial detectors. Detection of cosmic ray particles or their air showers provides the most precise and model-independent measurements of the cosmic particle fluxes, often with resolution power for isotopes. However, all particle detectors are limited to the local interstellar region, in the Galactic periphery, $\sim 8\,\mathrm{kpc}$[1] from the dynamic center.

Section 3.1.1 describes unique measurements made by cosmic-ray detectors aboard the Voyager spacecraft, which have direct access to the local interstellar spectra (LIS).

[1] One parsec (pc; $\sim$ 3.26 light years) is the distance to an astronomical object with a 1 arcsec parallax angle relative to the Earth's orbit.

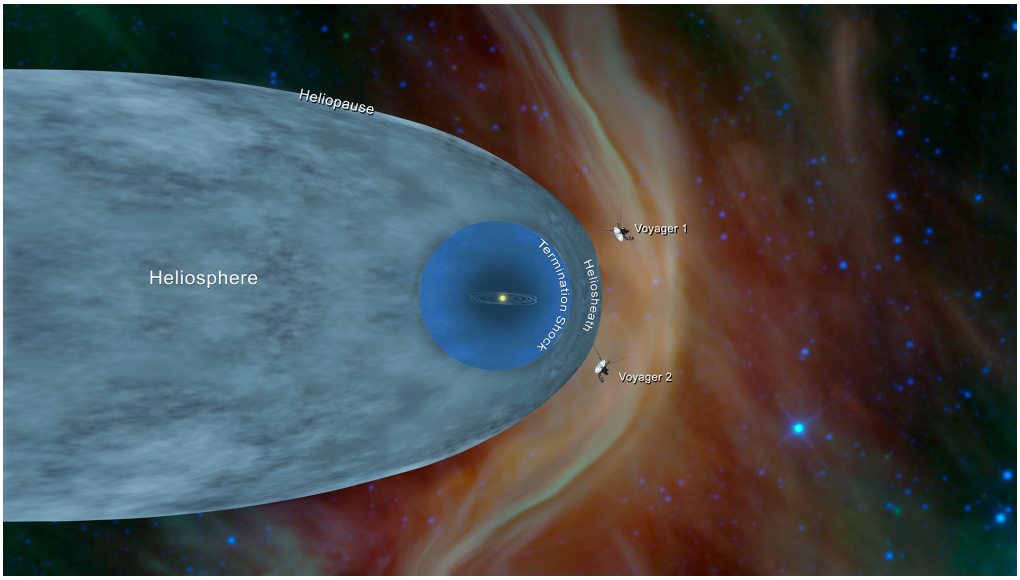

Figure 3.1: An artist's depiction of heliopause, the interface between the local interstellar environment and the magnetic solar-plasma environment of the heliosphere. The heliosphere is asymmetric due to the motion of the sun. Both Voyager spacecraft have traversed heliopause. Image credit: NASA/JPL-Caltech.

As illustrated in Figure 3.1, all other particle detectors measure fluxes that have been modulated in the solar magnetic field. Solar activity varies on a ∼11-year cycle and significantly attenuates the particle fluxes $\lesssim$10 GeV/n. Interpretation of cosmic-ray measurements by instruments aboard satellites (Section 3.1.2) requires modeling of both the solar modulation and of attenuation in the Earth's magnetic field. Cosmic-ray particles incident on the top of the atmosphere (TOA) can fragment via spallation reactions on the molecules of the atmosphere, forming particle showers; low-energy particles also lose energy through ionization and excitation of the atmosphere. Thus, measurements by high-altitude detectors must account for the resulting atmospheric[2] component. Meanwhile, ground-based detectors (Section 3.1.3) observe the showers produced by cosmic-ray interactions in the atmosphere, allowing indirect access to higher-energy events than can be observed directly in a detector.

[2]Particles produced by spallation of cosmic rays on the Earth's atmosphere are commonly referred to as "secondaries;" this work uses the term "atmospheric" to avoid confusion with the secondary particle fluxes produced during Galactic propagation. These atmospheric particles are the cosmic rays of interest to many terrestrial particle physics experiments, in which they present a significant background.

3.1.1 Local Interstellar Spectra with Voyager Spacecraft

The Voyager I spacecraft traversed heliopause in August, 2012 [139, 140], followed by Voyager II in November, 2018 [141, 142]. Using their cosmic-ray detector systems [143], the Voyager missions have observed the LIS of electrons and of nuclei from protons to nickel. A proton spectrum was measured in the energy range of $3\,\mathrm{MeV}/n$ to $>1\,\mathrm{GeV}/n$, while for heavier nuclei the energy range is restricted relative to hydrogen [144]. These direct LIS measurements, in an energy range where solar modulation effects can attenuate the particle flux at Earth by several orders of magnitude, are thus of crucial importance both for modeling the sources and propagation of galactic cosmic rays [145] and for developing a solar modulation model necessary for interpreting the the large number of Earth-based measurements [146, 147].

3.1.2 High-altitude Measurements

High-altitude and space-based measurements facilitate direct detection of cosmic rays in particle detectors located above most or all of the atmosphere. The current state-of-the-art for direct measurements of cosmic-ray particles from a few $100\,\mathrm{MeV}/n$ to $>\mathrm{TeV}/n$ is the Alpha Magnetic Spectrometer (AMS-02) aboard the International Space Station [148]. With its redundant velocity, energy, momentum, and charge measurements, this multi-purpose particle detector provides high-statistics spectral information for cosmic-ray nuclei, antiprotons, electrons, and positrons. The particular emphasis on matter-antimatter discrimination has allowed precision measurements of the positrons (Figure 3.2) and antiprotons, which are preferred channels for indirect dark matter detection as discussed in Chapter 2. Meanwhile, the high statistics across a wide energy range in both matter and antimatter channels has allowed precise tuning of cosmic-ray models, critical to enable significant detection of any anomalies.

As illustrated in Figure 3.3, a wide range of satellite and balloon missions have contributed to the TOA spectra, with measurements largely consistent between experiments. The different combinations of instrumentation strategies on each mission facilitate a combined picture of the TOA spectra for nuclei from hydrogen to iron in

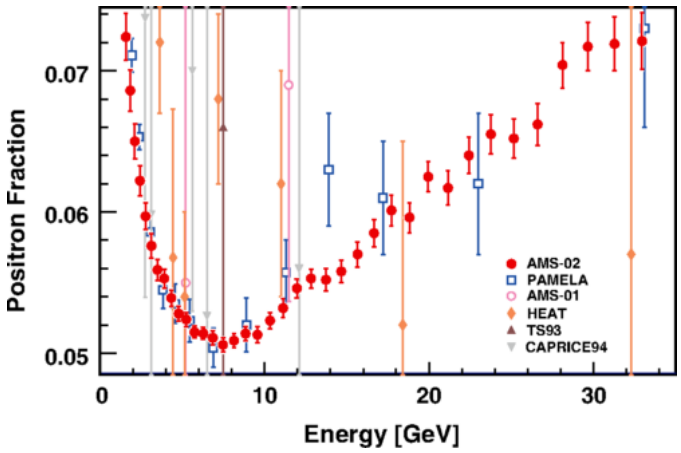

Figure 3.2: The positron fraction ($e^+/(e^- + e^+)$) exhibits an anomalous increase at energies $\gtrsim$10 GeV, as observed by PAMELA [149] and confirmed with high statistics by AMS-02 [125].

the range of 200 MeV/n to 600 TeV/n. Figure 3.3 specifically illustrates the "primary" cosmic rays, those species that are abundant in the ISM and are thus assumed to be the particles to which energy is transferred at Galactic accelerators. For energies $\gtrsim$ 10 GeV/n, the spectrum of each primary cosmic ray species follows a powerlaw, with the intensity $I \propto E^{-2.7}$ as illustrated by the black dash lines in the figure. The common spectral characteristics between these isotopes suggest a common astrophysical origin. Meanwhile, relatively high cosmic-ray abundances of are also observed for isotopes of Li, Be, and B, as well as antiprotons, which are not present in large quantities in the ISM. These "secondary" cosmic rays are produced in spallation of primaries on the ISM, and their relatively high abundance indicates a large number of collisions between primaries and the ISM [131].

Compared to particle detectors aboard satellites, balloon missions provide access to a high-altitude environment at a fraction of the cost, enabling rapid development of novel detector technologies, as well as forming a testbed for future space missions. Additionally, polar flight paths facilitated by balloon missions feature low rates of geomagnetic cutoff compared to typical satellite trajectories. This allows measurement of the low-energy portion of the cosmic-ray spectrum that is deflected at the lower latitudes, as demonstrated by the high-statistics low-energy proton spectrum recorded by the BESS-Polar missions [151].

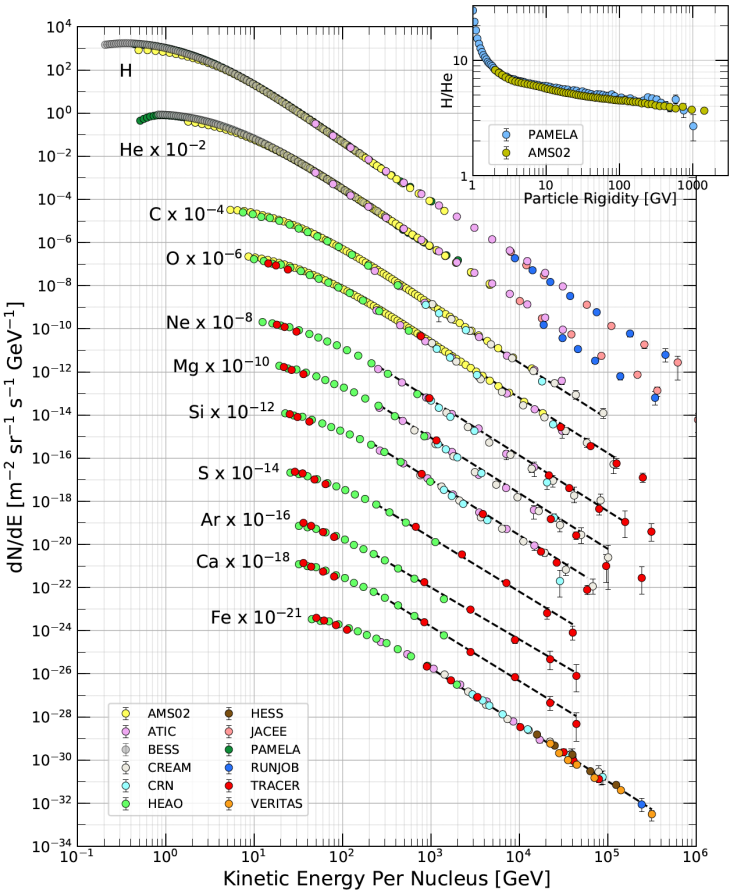

Figure 3.3: The spectra of primary cosmic-ray nuclei as measured directly by satellite and balloon experiments (as well as VERITAS) from ∼200 MeV to 600 TeV. Image credit: Particle Data Group [150].

3.1.3 Measurements of Atmospheric Showers

Observation of atmospheric showers provides access to charged cosmic rays at higher energies than can be detected directly in detectors. In this method of particle identification, the atmosphere is used as a calorimeter. Observables of atmospheric showers include the charged particles produced in the shower, fluorescence of atmospheric nitrogen molecules following ionization by charged particles, and Askaryan radio signals. The energy and angle of the incident cosmic ray are reconstructed based on the shape, spatial extent, and amount of ionizing radiation in the shower. Discrimination between the electromagnetic showers of γ-rays, electrons, and positrons and the hadronic showers of protons and nuclei is also based on the shower shape, as

hadronic showers have a wider lateral extent compared to electromagnetic showers of the same energy. Meanwhile, isotope discrimination is possible but challenging using air showers, and consequently air-shower experiments typically report a spectrum of the total particle flux in terms of the total particle energy.

Cosmic-ray detectors focused on atmospheric showers detect some or all of these signatures. Ground-based observatories typically employ some combination of fluorescence telescopes and muon detectors [152, 153, 154, 155]. Together, these observatories have provided information on the cosmic-ray spectrum in the range of 10 TeV to >100 EeV. Future space-based fluorescence detectors could provide higher statistics at the highest energies, thanks to their excellent effective area [156, 157]. Figure 3.4 illustrates the current state of cosmic-ray spectral information based on these experiments. The data overlap with data from space-based experiments (Figure 3.3) in the energy range of $\sim 100 - 600$ TeV. In contrast to the featureless spectrum observed at lower energies, the cosmic-ray energy spectrum above 1 PeV features several breaks in the powerlaw, including a softening (the "knee") around 2 PeV [158] and a second knee around 100 PeV [159], a hardening (the "ankle") around 5 EeV [160], and a steep cut-off beyond ∼40 EeV, as well as more subtle features. These spectral features are expected to correlate with the transition from a Galactic to an extragalactic cosmic-ray population, where the maximum energy attainable at Galactic accelerators is in the PeV range, but the details of this transition remain uncertain [161, 162, 163].

Ultra-high energy cosmic rays (UHECR; $E > 1$ EeV) retain directional information due to their high rigidities. The gyroradius of an $\mathcal{O}(1)$ EeV particle in a μG field is $\mathcal{O}(100)$ kpc, which is larger than the Galactic disk; despite poor constraints on the absolute magnitudes of the Galactic and intergalactic magnetic fields, it is clear that some directionality is retained. Small (∼10% effect at the highest energies) but significant (6.6σ) anisotropies pointing away from the Galactic disk suggest an extragalactic origin [164]. Thanks to the retention of their directionality, UHECRs, alongside gravitational waves, γ-rays, and neutrinos, can contribute to multimessenger astrophysics studies of the highest-energy events in the Universe [156].

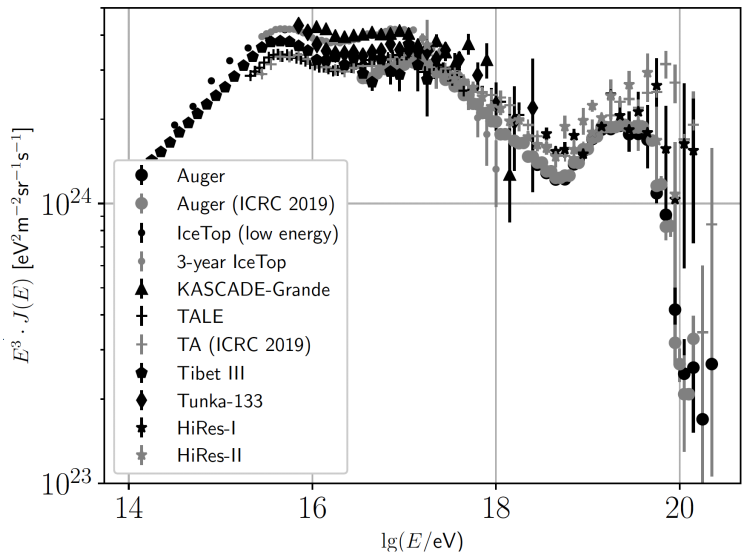

Figure 3.4: The cosmic ray spectrum from 100 TeV to 100 EeV is shown using measurements from several ground-based instruments. Image credit: Alex Kääpä [163].

3.2 Probes of Cosmic Rays in the Galaxy

Astrophysical observations can detect the electromagnetic signatures of cosmic-ray propagation in the Galaxy. These measurements crucially provide information related to the distribution of cosmic rays near Galactic accelerators, possible extragalactic accelerators, and other regions of space not accessible directly. However, the interpretation of signals and the treatment of astrophysical backgrounds are typically both model-dependent.

Figure 3.5 models the specific contribution of cosmic rays to the total electromagnetic radiation from the Galaxy. A breadth of physics processes leads to the characteristic emission signatures. Electrons and positrons radiate synchrotron emission, which falls in the radio band to X-ray band from the propagation of MeV to TeV-scale particles [166, 167]. Relativistic protons and heavier nuclei produce GeV-scale γ-rays from the decay of pions produced in collisions with the ISM [168], while MeV nuclear de-excitation lines (beyond the sensitivity of current instruments) follow nuclear excitation of atoms in the ISM by low-energy hadrons [169]. Additionally, particles across a broad energy range produce a continuum emission via inverse Compton scattering

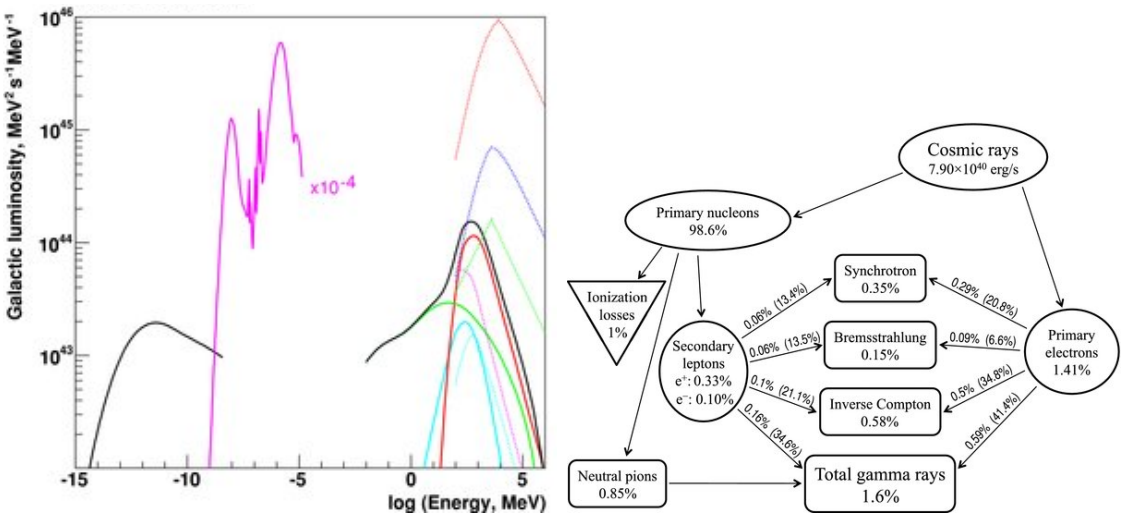

Figure 3.5: (*left*) The cosmic-ray induced synchrotron (black solid, left) and the inverse Compton (green solid), bremsstrahlung (cyan solid), neutral pion decay (red solid), and total γ-ray (black solid) emission is shown for a self-consistent model with a given optical and infrared interstellar radiation field (magenta solid) and cosmic-ray proton (red dashed), helium (blue dashed), primary electrons (green dashed) and secondary positrons (magenta dashed). (*right*) The schematic illustrates a self-consistent model of the energy budget for each population [165].

of starlight and CMB photons and Bremsstrahlung processes with the ISM, where the energy of the emitted photons scales with the energy of the cosmic-ray particles [170, 168]. Low-energy (sub-GeV) particles of all species produce fluorescence lines via ionization and excitation of the ISM atoms and molecules; this is detectable through observation of the ionization rates of ISM gas and, for fluorescence photons that are energetic enough to reach Earth without being absorbed, in the resulting X-rays [170, 131]. Some of these features are accessible by currently operating instruments, requiring a mutually-consistent cosmic-ray interpretation [171].

This section briefly discusses a few of these observables of interest in different regions of the Galaxy. First, Section 3.2.1 discusses the large-scale diffuse emission from the Galaxy, which probes propagation broadly. Section 3.2.2 introduces some observed Galactic accelerators of cosmic rays. Finally, Section 3.2.3 presents some phenomena of particular interest at the Galactic Center.

3.2.1 Galactic Diffuse Emission

Figure 3.6 illustrates the total γ-ray emission above 1 GeV as observed by the Fermi Large Area Telescope (LAT) [172]. Most of this emission is due to cosmic-ray propagation. The bulk is attributed to the decay of neutral pions produced in spallation of cosmic-ray protons and nuclei on the ISM. Cosmic-ray electrons and positrons also contribute via Inverse Compton scattering and Bremsstrahlung processes; while this process is expected to be subdominant, the exact contribution is poorly constrained [168, 171]. Still, in combination with independent measurements of the local gas densities, measurement of the γ-rays emitted from different regions of the Galaxy, including nearby spiral arms, provide a map of the energetic protons in the Galaxy. The observation that the γ-ray intensity correlates with the density of interstellar dust suggests a relatively uniform population of GeV $-$ TeV protons and nuclei throughout the Galaxy [131].

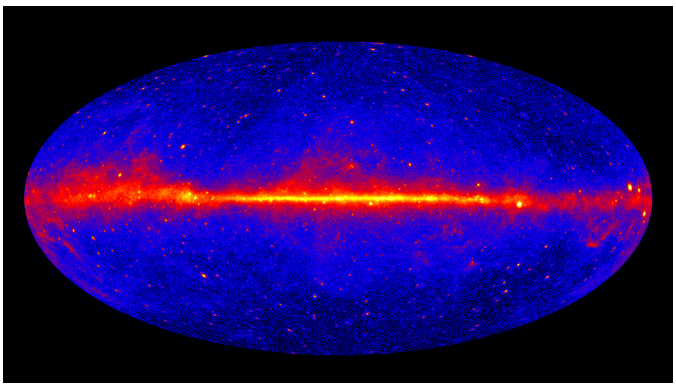

Figure 3.6: An all-sky map of $>$1 GeV γ-rays measured by the Fermi Large Area Telescope. The luminous band is the Galactic disk. Most of the emission is due to scattering of cosmic rays on the ISM. Image credit: NASA/DOE/Fermi LAT Collaboration.

Meanwhile, radio and microwave signatures trace synchrotron emission from relativistic electron and positron populations [166, 173]. In this case, the emission depends on both the typical strength of the Galactic magnetic field and on the spectra of the cosmic rays. This dependence introduces a partial degeneracy in the modeling, as synchrotron measurements provide one of the best probes of the Galactic magnetic field strength [166].

Tracing low-energy cosmic rays in the Galaxy is a topic of particular interest thanks to the unique role these particles play in ionizing and heating the ISM. The X-ray band signatures (fluorescence lines and bremsstrahlung and inverse Compton scattering continuum) from low-energy cosmic rays are too faint to be detected from the interstellar medium overall, but they may be visible in the most dense molecular clouds, as detailed in Chapter 7. Future telescopes with sensitivity for MeV γ-rays will additionally provide sensitivity to low-energy protons and nuclei across the Galaxy, by mapping the nuclear de-excitation lines they induce.

3.2.2 Accelerators in the Galactic Disk

Core-collapse SNR have long been the suspected accelerators of the Galactic cosmic rays because of their high energies and because the supersonic shock waves resulting from supernova explosions provide a plausible mechanism for particle acceleration. In Diffusive Shock Acceleration (DSA) [174, 175], particles repeatedly cross a shock, gaining a fractional momentum boost with every crossing. The result of DSA is a powerlaw spectrum of accelerated particles with index $\sim$2, i.e. intensity $I \propto E^{-2}$, with isotopic abundance matching that of the initial material near the shockwave. Some calculations predict that DSA in SNR can accelerate particles up to $10^{15} - 10^{18}$ eV [176]. However, other models suggest that SNR cannot accelerate protons beyond $\sim 10^{14}$ eV (100 TeV) [177], leading to searches for other astrophysical "PeVatrons" that could accelerate the highest-energy Galactic cosmic rays.

Observation of GeV [178] and TeV [179] γ-rays near several known SRN distributed through the Galactic disc supports the hypothesis of SRN as cosmic-ray accelerators. However, there is a degeneracy in the γ-ray signatures expected from relativistic protons and relativistic electrons. Acceleration of protons is necessary to explain the cosmic-ray fluxes observed at Earth. Detection by Fermi-LAT of a γ-ray spectrum characteristic of neutral pion decay near several SRN suggests that these objects do accelerate at least some of the Galactic cosmic rays [168]. However, a cut-off in the observed TeV spectra of many, though possibly not all, SRN provides evidence that these objects are not the primary Galactic PeVatrons [180, 179].

Other known or suspected cosmic-ray accelerators include pulsars, pulsar wind nebulae, and young stellar clustars. TeV γ-rays from the HAWC observatory suggest that young stellar clusters may be the Galactic PeVatrons and could be responsible for acceleration of many of the Galactic cosmic rays, in possible conflict with the longtime orthodoxy of SRN as the primary Galactic cosmic-ray accelerators [180, 181]. Additionally, pulsars and pulsar wind nebulae have been objects of increased observational interest as pertains to cosmic-ray acceleration due to their possible role as a local source of the positron excess (Section 3.1.2). These objects are typically observable via the synchrotron and inverse Compton emissions from the relativistic electrons and positrons they accelerate. However, debate is ongoing pertaining to the efficiency of particle escape from these objects [182, 183, 184, 185, 186, 187, 188].

Meanwhile, evidence of 12 PeVatrons in the Galactic disk has already been detected using PeV γ-rays from the newly-operational LHAASO observatory. This suggests that PeVatrons specifically are much more abundant in the Galaxy than previously thought. One of the PeV sources has been definitively associated with the Crab Nebula, providing evidence that pulsar wind nebulae can behave as PeVatrons. Though the remaining PeV sources have not yet been definitively associated with specific accelerators, pulsars, pulsar wind nebula, stellar clusters, and SNR all exist in spatial coincidence [189].

3.2.3 Cosmic Rays at the Galactic Center

Observational evidence points to elevated cosmic-ray populations in the Galactic Center relative to the peripheral regions. Cosmic rays in a broad energy range have been invoked to explain non-thermal emissions from the Galactic Center at a range of wavelengths. Note that many of these signatures emerge in observations of the Galactic Center molecular clouds, which can serve as calorimeters or target material for local cosmic-ray interactions; one such analysis is the subject of Chapter 7. TeV-scale γ-ray emission from the Galactic Center molecular clouds has been taken as evidence of protons up to a few PeV, indicating a PeVatron in the Galactic Center [190, 191], or possibly of inverse Compton scattering of submillimeter radiation by TeV-scale

electrons [192]. Meanwhile, nonthermal radio filaments have been interpreted as synchrotron radiation from a population of GeV-scale electrons [193, 194, 195]. Similarly, nonthermal X-ray filaments are evidence of TeV-scale electrons [167]. Evidence for elevated low-energy cosmic ray populations relative to the local Galactic environment comes principally from modeling observed hydrogen ionization rates at the Galactic Center, which are in excess of local rates by a factor of ~ 10 [196, 197, 198]. Heating by low-energy cosmic-ray electrons consistent with the ionization rates would also naturally explain anomalously warm gas temperatures observed in the central $\sim$100 pc [192].

Evidence of elevated comic ray populations at the Galactic Center motivates a discussion of and search for particle accelerators in the region. While there are several supernova remnants within the central 1°, it is unclear if they can be responsible for the cosmic rays observed today, particularly at the highest energies [199, 192, 200, 201]. Similar to the discussion in Section 3.2.2, possible Galactic Center accelerators include pulsars [202], stellar winds [203], and magnetic reconnection [204], though direct evidence of particle acceleration by these mechanisms in the Galactic Center region specifically is lacking.

At the dynamic center of the Galaxy is the supermassive black hole Sagittarius A* (Sgr A*; [205]). Though direct observation shows that Sgr A* is presently in a quiescent state [206], the X-ray observations of several molecular clouds (details in Chapter 7) reveal that Sgr A* has been brighter in the past few hundred years, with at least two short outbursts [207, 208, 209]. Possible indication of the brilliance of Sgr A* in the more distant past, over 10^6 years ago, comes from observation of the Fermi Bubbles [210, 211], a ~ 15 kpc bi-lobed γ-ray structure extending out of the Galactic Plane, as well as from the even more extended X-ray eROSITA bubbles [212], the ~ 100 pc X-ray Chimneys [213], and the ~ 450 pc radio lobes [195]. The origin of these structures is debated, but may be due to a past Active Galactic Nucleus (AGN) phase of Sgr A*, during which the AGN itself could have been a PeVatron at the Galactic Center (reviews in [214, 215, 216, 217]).

3.3 Modeling Galactic Particle Propagation

Particle propagation in the Galaxy is modeled as a diffusive process, with possible additional contributions from convection and reacceleration. Due to the critical effects of diffusion in magnetic fields, the kinematic variable for cosmic rays is typically the rigidity $R \equiv pc/Ze$, where p is the momentum, Ze is the charge, and particles of equal rigidity follow identical trajectories in a magnetic field. For a given particle species, the density $\psi(\vec{r}, R, t)$ at position $\vec{r}$ in the galaxy per unit rigidity R at time t can be formalized as [218]

$$\frac{\delta\psi(\vec{r}, R, t)}{\delta t} = q(\vec{r}, R, t) + \vec{\nabla} \cdot (D_{xx}\vec{\nabla}\psi - \vec{V}\psi) + \frac{\delta}{\delta p}R^2 D_{pp}\frac{\delta}{\delta R}\frac{\psi}{R^2} - \frac{\delta}{\delta R}\left[\dot{R}\psi - \frac{R}{3}(\vec{\nabla} \cdot \vec{V})\psi\right] - \left(\frac{1}{\tau_f} + \frac{1}{\tau_r}\right)\psi. \quad (3.1)$$

In Eq. (3.1), q includes both primary sources, such as astrophysical accelerators and possible dark matter annihilation or decay, and secondary contributions from spallation or decay of other particle species. D_{xx} is the coefficient of spatial diffusion, diffusive re-acceleration is described as diffusion in momentum space and parametrized by D_{pp}, and the effects of convection is described by its characteristic velocity $\vec{V}$. Finally, energy loss is parametrized by the $\dot{R}$ term, while τ_f and τ_r respectively describe the timescales for loss due to fragmentation through spallation on the ISM and radioactive decay.

The cosmic-ray spectra observed today are expected to follow a steady-state solution of Eq. 3.1 with $\delta\psi/\delta t \sim 0$. In addition to the model parameters, the equilibrium ψ depends on the boundary conditions describing the spatial extent of the galaxy and on the distribution of the gas, radiation, and magnetic fields. Typically, the galaxy is modeled as a cylinder of some radius and scale height in which propagation is characterized by Eq. 3.1; the typical lifetime of cosmic rays in the galaxy depends on the size of the diffusion zone.

The remainder of this section describes some of the ways in which experimental handles contribute to a model of cosmic-ray propagation in the Milky Way Galaxy.

Section 3.3.1 discusses the effects of spallation and secondary production in the cosmic-ray modeling. Experimental handles on spatial diffusion, including the diffusion coefficient and the size of the Galaxy through with particles diffuse are treated in Section 3.3.2. Section 3.3.3 introduces the effects of energy loss in the case of electrons and positrons, where it is particularly critical. Finally, Section 3.3.4 introduces some of the numerical methods used to describe cosmic-ray populations in the Galaxy under different physical scenarios.

3.3.1 Spallation and Production of Secondaries

Isotopes of Li, Be, and B are rarely formed during stellar nucleosynthesis, and their cosmological abundance is primarily attributed to the spallation of cosmic rays on the ISM as well as, to a secondary degree, neutrino-induced spallation in supernove [131]. Cosmic-ray antimatter is also produce primarily in the collisions of primary cosmic rays on the ISM. The typical fragmentation time $\tau_f(R)$ for a cosmic-ray species to produce secondaries depends on the distribution of the ISM gas density $n(\vec{r})$, the large-scale features of which can be measured in surveys of atomic and molecular gas, and the relevant nuclear cross sections, which are measured independently at terrestrial collider experiments, e.g. [219, 220]. The corresponding production rate $q(\vec{r}, R, t)$ for secondary particles depends on the spectra of the primary cosmic-ray species. Thanks to the precision cosmic-ray spectral measurements and advancements in modeling techniques, the uncertainty in the predicted spectra for antiprotons in particular is now dominated by the experimental uncertainties in the relevant nuclear cross sections [221].

3.3.2 Constraining Diffusion

For protons and heavier nuclei, spatial diffusion explains their highly isotropic distributions and their long lifetimes in the Galaxy compared to the size of the Galaxy. Considering Eq. 3.1 for the case of diffusion alone gives a typical timescale $\tau_{diff}(d) \sim d^2/D_{xx}$ for traveling distance d. Because spatial diffusion is due to the effects of mag-

netic fields, D_{xx} is an energy-dependent quantity. It is typically parameterized with an exponential dependence δ on the particle rigidity R, as

$$D_{xx}(R) = D_{xx,0} \left(\frac{R}{R_0} \right)^{\delta}. \tag{3.2}$$

Diffusion following Eq. (3.2) preferentially allows the escape of higher-energy particles with their larger D_{xx} and corresponding faster propagation over large distances. For the typical case of a power-law source spectrum $q(R) \propto R^{-\lambda}$, the result is a steady-state powerlaw spectrum that is softer than the source as $\psi(R) = q(R) \cdot R^{-\delta} \propto R^{-\lambda-\delta}$.

In practice, δ is constrained by comparing the spectra of secondary cosmic rays to those of primary cosmic rays. In typical spallation on the proton-dominated ISM, the average energy per nucleon is conserved. Secondary cosmic rays are produced with source $q(R) \propto R^{-\lambda-\delta}$ following the equilibrium distribution of the primary parent population. Through their own diffusion, their equilibrium spectra become softer still, with $\psi(F) = q(R) \cdot R^{-\delta} \propto R^{-\lambda-2\delta}$. Thus, in the case of diffusion-dominated propagation, comparison of the energy dependence of the primary and secondary cosmic-ray spectra reveals the energy dependence of the diffusion coefficient. This comparison is most cleanly performed using the Boron-to-Carbon spectral ratio, shown in Figure 3.7. In typical models, $\delta \sim 0.3 - 0.4$, though for various models accounting for additional transport processes, values of $0.3 \lesssim \delta \lesssim 0.8$ are consistent with the data [222, 223, 224]. The observed fluxes are consistent with $D_{xx}(1\,\mathrm{GV}) \sim (3-5) \times 10^{28}\,\mathrm{cm^2\,s^{-1}}$ [218].

The abundance of radioactive secondaries is sensitive to the typical time in the Galaxy and thus to the size of the Galaxy. Measurements $^{10}\mathrm{Be}/^{9}\mathrm{Be}$ provide the best constraints on the scale-heigh of the Galaxy due to the relatively long half-life ($\tau_{1/2} = 1.4 \times 10^6$ years) of ^{10}Be. Recent results using data from AMS-02 are consistent with a halo scale height $\gtrsim$5 kpc, though the result is subject to a systematic error related to measurements of the cross sections for production of the Be isotopes [225].

The purely diffusion-driven picture of cosmic-ray propagation can be modified if convection of Galactic winds or reacceleration on Alfvén waves is important. In

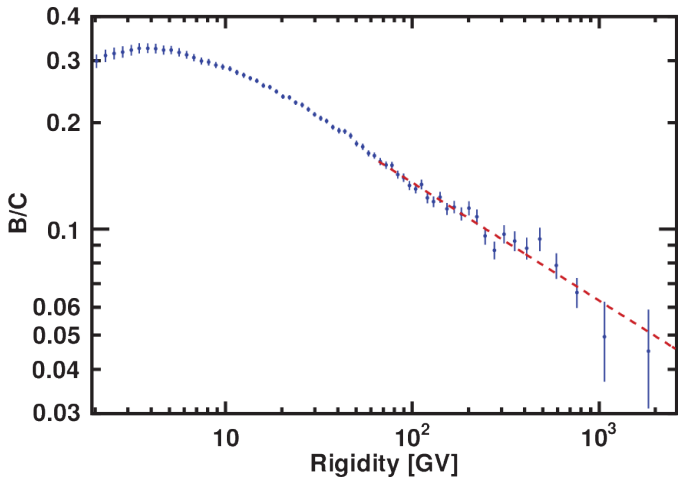

Figure 3.7: The Boron-to-Carbon flux ratio as measured by AMS-02. The dashed line is a powerlaw with index 1/3 [224].

combination with diffusion, convection of cosmic rays on Galactic winds in some or all of the Galaxy would introduce an energy-dependent mechanism to remove material from the Galaxy, and has been invoked to explain the observed deviation of the Boron-to-Carbon ratio from a powerlaw at high energies [226]. While Alfvén acceleration cannot be the primary cosmic-ray acceleration mechanism [218], reacceleration of cosmic rays on Alfvén waves could explain GeV-scale peaks observed in the secondary-to-primary ratio.

3.3.3 Radiative Energy Loss

Mechanisms for cosmic-ray energy loss, characterized by $\dot{R}$, include synchrotron radiation, Bremsstrahlung, and scattering on starlight and CMB photons. Compared to protons and nuclei, the much-lighter electrons and positrons rapidly lose energy through synchrotron radiation. In the case of synchrotron radiation, $\dot{R} \propto R^2$, leading to a characteristic lifetime $\tau_{loss} \propto R^{-1}$. For high-$R$ electrons and positrons, $\tau_{loss} \ll \tau_{diff}$ is small and propagation is dominated by synchrotron losses. Considering Eq. (3.1) in the case of radiation losses alone, a powerlaw source spectrum $q(R)$ corresponds to an equilibrium powerlaw spectrum that is softer than the source by a factor of R^{-1}, consistent with the observed break in the electron spectrum at ∼GeV energies.

The high rate of energy loss means that, depending on the overall propagation model and in contrast to heavier particles, electrons and positrons typically travel only $\sim$1 kpc before losing their energy to synchrotron radiation and inverse Compton scattering. This means that the electron and positron spectra observed directly originate locally in the Galaxy, either in local particle accelerators or as secondaries in the collisions of heavier cosmic rays.

3.3.4 Numerical Methods

While analytical methods are useful for understanding the physics of each process individually, the general case of Eq. (3.1) is best solved numerically. Given boundary conditions describing the size of the Galaxy; a model of the Galactic structure including distributions of the ISM gas, radiation, and magnetic fields; and the parameters of Eq. (3.1), `GALPROP`[3] [227, 218] software solves Eq. (3.1) numerically until a steady state is reached. It begins with the heaviest nucleus species and proceeds using the spallation products as part of the source distribution for lighter species. The result is a self-consistent result for ϕ of each species, which can be compared with the observed LIS. Meanwhile, `DRAGON`[4] [223, 228] is a commonly-used software based on the `GALPROP` framework that additionally allows for spatially-dependent and anisotropic diffusion.

[3] https://galprop.stanford.edu
[4] http://www.dragonproject.org

Chapter 4

The GAPS Antarctic Balloon Mission

The General AntiParticle Spectrometer (GAPS) [229, 230, 231] is the first instrument optimized for detection of low-energy cosmic antideuterons. This is a dark-matter signal channel in which any detection would indicate new physics due to kinematic suppression of the astrophysical antideuteron flux from collisions of cosmic rays [232, 233, 234]. GAPS will also deliver a precision cosmic antiproton spectrum in a previously-unexplored low-energy range, open new sensitivity for cosmic antihelium-3, and provide spectral information for low-energy proton and deuteron fluxes. GAPS will observe these cosmic particles from the vantage point of a NASA Antarctic long-duration balloon (LDB) mission, from an altitude of $\sim 37\,\mathrm{km}$. To deliver its unprecedented sensitivity for low-energy antinuclei, the GAPS team has developed a novel particle identification system based on the formation and decay of exotic atoms (Section 4.1). The instrument, detailed in Section 4.2, is unique among balloon payloads for its large sensitive area and its relatively complex design. The expected timeline of the GAPS project is detailed in Section 4.3. Since the first test of the exotic atom particle identification concept in 2004, the elements of the detector, electronics, mechanical, and thermal systems have been developed individually. The first operation of the integrated components was celebrated in 2021, and the first GAPS flight is anticipated in the Austral summer of 2023-24.

4.1 Particle Identification Using Exotic Atoms

The novel GAPS particle identification concept is based on the formation, de-excitation, and annihilation of exotic atoms [229, 230, 231]. In comparison to the more broadly applicable particle identification techniques based on magnetic spectrometers, the exotic atom technique is only suitable for detection of negatively-charged particles in the highly-ionizing regime. However, for this signal type, the exotic atom technique gives greater background rejection capability due to the unique antiparticle signature. The exotic atom technique does not require a magnet, facilitating a larger sensitive volume within the mass, size, and power constraints of an Antarctic balloon mission. Additionally, the method has orthogonal sources of systematic uncertainty compared to magnetic spectrometer techniques, particularly as pertains to the rejection of positively-charged particle backgrounds. Thus, the exotic atom-based detection technique is uniquely suited for the GAPS mission to detect rare low-energy antinuclei while rejecting abundant positive nuclei.

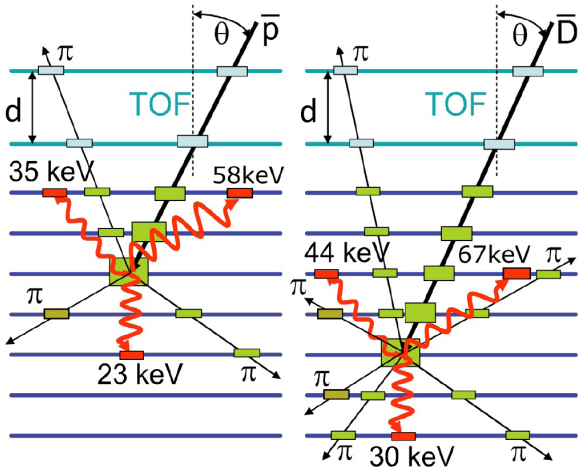

Figure 4.1: The novel GAPS particle identification is based on the formation and decay of exotic atoms. Antiparticle species (here antideuterons $\bar{\mathrm{D}}$, right, compared to antiprotons $\bar{\mathrm{p}}$, left) are identified on the basis of their $\mathrm{d}E/\mathrm{d}x$ loss patterns in the TOF (teal), their $\mathrm{d}E/\mathrm{d}x$ patterns and stopping depth in the tracker (purple) systems, the characteristic energies of the de-excitation X-rays (red) and the multiplicity of secondary tracks.

Fig. 4.1 illustrates the GAPS particle identification concept. The sensitive elements of the GAPS instrument (detailed in Section 4.2) include a time-of-flight

(TOF) system surrounding a 10-layer particle tracker and X-ray spectrometer system (the "tracker"). When a low-energy antinucleus traverses the GAPS instrument, it first crosses two TOF layers, which measure the kinematic variable $\beta = v/c$, where v is the particle velocity and c is the speed of light. It then slows down via ionization and excitation losses in the detector material, with energy depositions characteristic of its charge Z and velocity. Once the kinetic energy of the antinucleus is comparable to the binding energy of the nearby atoms, it is captured with near-unity probability by the nucleus of a target atom, forming an exotic atom in an excited state. Within $\mathcal{O}(1)$ ns of formation, the exotic atom de-excites via emission of Auger electrons, resulting in a hydrogen-like system, and characteristic X-rays. Following de-excitation, the captured antinucleus annihilates with the target nucleus, producing secondary hadrons which form tracks through the tracker and TOF. The characteristic "annihilation star" signature of exotic atom formation and decay consists of secondary tracks emerging from the annihilation vertex.

The products of exotic atom de-excitation and annihilation, together with ionization loss patterns on the primary track, are the basis for identifying rare antideuterons and antihelium-3 nuclei from a background of relatively abundant antiprotons. When normalized by the density of the target material, the rate of energy deposition from ionization and excitation losses per unit distance traveled in a material $\mathrm{d}E/\mathrm{d}x \propto Z^2/\beta^2$, where Z is the charge of the particle. This results in a unique energy-loss pattern for each antinucleus species. Given an initial β, antideuterons have twice the kinetic energy and slow down through a longer track in the instrument compared to antiprotons. Meanwhile with $|Z| = 2$, antihelium-3 deposits four times the energy per unit length for a given β. Figure 4.2 illustrates the X-ray and secondary particle characteristics of antiprotons and antideuterons. The characteristic de-excitation X-rays are uniquely determined by the reduced mass and charge of the antinucleus and target atom, and were experimentally verified for antiprotonic exotic atoms using the antiproton beam at the High Energy Accelerator Research Organization (KEK) facilty [235]. With at least 5 keV separating X-rays from the different species, a sensitive tracker element with 4 keV (FWHM) energy resolution

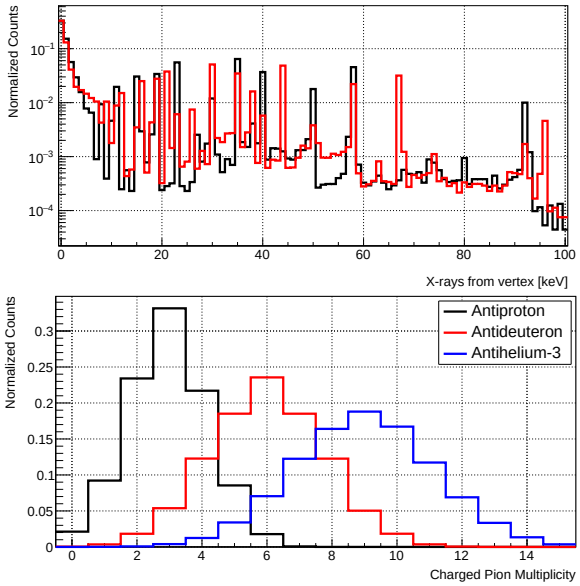

Figure 4.2: *Upper panel:* The simulated X-rays emerging from the annihilation vertices of antiprotonic (black) and antideuteronic (red) exotic atoms in silicon. Electromagnetic showers developed from the secondary particle propagation causes the continuum emission. *Lower panel:* The characteristic multiplicity of charged pions emerging from the annihilation of antiprotonic (black), antideuteronic (red), and antihelium-3-based (blue) exotic atoms. Each species features several hadronic annihilation modes, with different distributions of the annihilation energy between charged pions, neutral pions, and baryons.

can distinguish antiprotonic from antideuteronic X-rays. Meanwhile, the secondary particle multiplicity scales with the number of antinucleons in the exotic atom annihilation. Together, the energy loss patterns, de-excitation X-rays, and secondary particle characteristics provide a multiple variables for antinucleus identification.

Positively-charged nuclei outnumber antiprotons by a factor of $\sim 10^6$ in the GAPS energy range, such that measurements of the low-energy proton and deuteron fluxes is possible using the primary track information alone. Meanwhile, due to their high flux, rejection of these events is crucial for any antinucleus measurement. Positive nuclei that stop in the tracker do not form exotic atoms or the characteristic annihilation star signature and can be rejected. However, when they undergo hard interactions from inelastic collisions in the detector material, these nuclei can produce secondary particles which can mimic the annihilation star signature. Rejection of such events is possible based on the different kinematics of the secondary particles in this event

type. Further, interactions of positive nuclei do not produce de-excitation X-rays.

4.2 GAPS Instrument Design

Figure 4.3 illustrates the GAPS payload design, which is optimized to provide a large sensitive area for identification of rare cosmic particle species while operating within the constraints of an Antarctic long-duration balloon flight. The instrument consists of a ten-layer silicon tracker and particle spectrometer system (the "tracker", detailed in Section 4.2.1) enclosed by a two-layer plastic scintillator TOF system (detailed in Section 4.2.2). Temperature is regulated using an integrated oscillating heat pipe (OHP) system and passive heat shields (detailed Section 4.2.3). The electronics bay, which houses the flight computer, batteries, and associated electronics systems, is located below the science payload to minimize material between the detectors and incident particles. The entire payload is powered by solar panels mounted at the side of the payload.

The GAPS instrument has been engineered to meet the specific and interrelated requirements associated with operating 37 km above the continent of Antarctica suspended from a NASA long-duration balloon. The payload is limited to < 3638 kg, of which 1136 kg is reserved for balloon equipment including ballast, leaving 2492 kg for the science instrument. Power is limited to 1292 W, which can be delivered in light of the mass allotted for solar panels. The physical size of the payload is constrained by the launch apparatus. Meanwhile, the entire instrument must be able to withstand the forces of the balloon launch and operate at the ambient pressure at float altitude. The use of the integrated thermal system rather than a bulky and heavy cryostat, the ability to identify particles without the use of a magnet, and the robustness of the sensitive elements to the space environment without the use of a pressure vessel enable the large-area acceptance of GAPS and are thus crucial to the success of GAPS. The system-level power and mass allocations are detailed in Section 4.2.4.

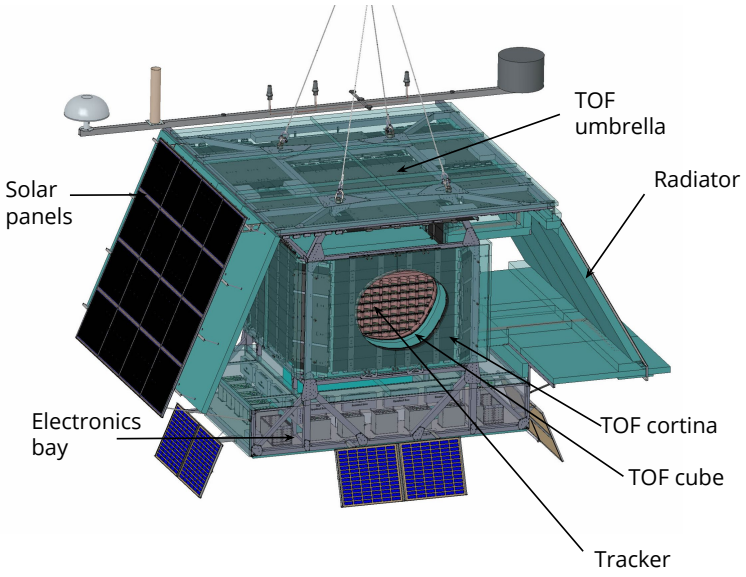

Figure 4.3: A mechanical drawing of the GAPS payload illustrates the outer TOF umbrella and cortina and the inner TOF cube. The cut-away panels reveal the layers of detectors in the Si(Li) tracker. The electronics bay is located beneath the sensitive material while the solar panels and the radiator for the oscillating heat pipe thermal system are to the side, minimizing the mass directly above the science payload.

4.2.1 The Silicon Tracker System

The GAPS tracker serves as target material, particle tracker, and X-ray spectrometer for particle identification. It is designed to accommodate 1440 10 cm-diameter, 0.25 mm-thick lithium-drifted silicon (Si(Li)) detectors arranged in ten layers to instrument a 1.6 m × 1.6 m × 1 m volume. The ten tracker layers are separated by polyethylene foam and supported by an aluminum frame. During the first flight, the tracker will be instrumented with approximately 1000 detectors, with the remaining spaces filled with blank silicon disks. Subsequent flights will operate with the full complement of 1440 detectors.

The Si(Li) detectors provide the large-area coverage, stopping depth, X-ray absorption efficiency and escape fraction, noise characteristics, and tracking capability necessary for the success of the exotic atom-based identification, and they can be produced en masse within the budget of a balloon mission. The detectors are segmented into 8 equal-area parallel strips to facilitate the required spatial and energy resolution.

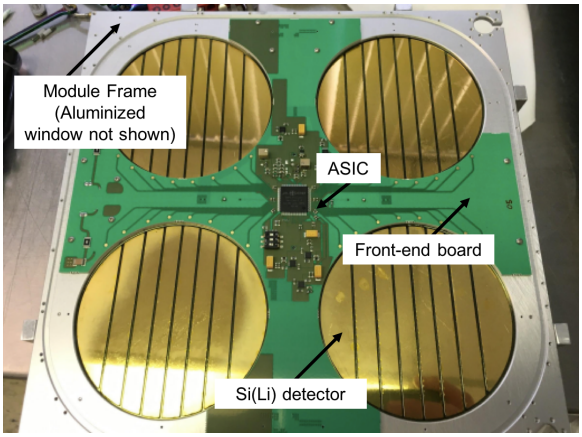

Figure 4.4: Each GAPS detector module houses four Si(Li) detectors in a protective aluminum frame. The detectors are read out by a 32-channel ASIC connected via wire bonds. The front end board housing the ASIC is designed to minimize passive material directly above the active silicon. The heat pipes of the OHP thermal system are integrated via the pass-through (top right). The aluminized window is not shown.

They are operable in the range of -50 to -30°C provided by the OHP, and at ambient pressure both on the ground and at float altitude. They are passivated for long-term stability and robustness to environmental conditions. The development, fabrication, characterization, and calibration of this crucial component of GAPS hardware, which is a substantial component of my graduate research, is detailed in Chapter 5.

The GAPS tracker module, pictured in Figure 4.4, forms the basic organizational unit of the GAPS tracker and consists of four Si(Li) detectors with their front-end electronics. Each tracker layer consists of a 6×6 array of modules, with orthogonal strip orientation in adjacent layers to maximize tracking capability. The aluminum module frames provide both mechanical support to protect the Si(Li) detectors and an interface with the OHP thermal system. An aluminized polypropylene window provides shielding from external sources of noise and any environmental contaminants. The module design is optimized to minimize passive material that could distort particle tracks or absorb X-rays.

Each module is read out by custom 32-channel ASIC connected to the detector strips via wire bonds and integrated into a front-end board mounted on the module frame. The ASIC is optimized for low power and makes use of a novel signal compression technique that enables $\lesssim 4\,\text{keV}$ energy resolution for X-rays in the $20 - 100\,\text{keV}$

range simultaneously with $< 10\%$ resolution up to $\sim 100\,\mathrm{MeV}$ [236, 237, 238]. The ASIC design requires less power and is more compact compared to a system of discrete preamplifiers and associated electronics with comparable performance.

The ASICs in each tracker layer are controlled by a backend DAQ module, which provides power to the ASICs and packages the ASIC data for delivery to the flight computer.

4.2.2 The Time of Flight System

The GAPS TOF [239, 240] measures the kinematic variable β and the initial $\mathrm{d}E/\mathrm{d}x$ energy losses of an incident particle, and it forms the basis of the trigger. The TOF system is composed of 160 $16\,\mathrm{cm} \times 0.6\,\mathrm{cm} \times 108 - 180\,\mathrm{cm}$ plastic scintillator paddles, arranged as an inner "cube" and a two-part outer TOF system (the "umbrella" and "cortina") as illustrated in Figure 4.3. With this design, most down-going incident particles interact first with one of the outer TOF structures and second with the cube to enable the TOF measurement. The cube, which covers $\sim 15\,\mathrm{m}^2$ using 60 paddles, is designed to nearly hermetically enclose the tracker volume and register at least one hit for each primary or secondary track. The umbrella consists of a plane of 48 paddles $\sim 90\,\mathrm{cm}$ above the cube, while the 52-paddle cortina surrounds the side of the cube at a distance of 30 cm. Structural support is provided by an aluminum frame.

Figure 4.5 illustrates a typical TOF paddle. Each paddle is read out by 6 silicon photomultipliers (SiPMs) at either end, coupled to the scintillator by optical silicone cookies. A custom preamplifier board delivers power at $\sim 58\,\mathrm{V}$ and provides high-speed signal amplification, producing both low-gain output for the trigger and high-gain output for the waveform digitizer. The paddles provide timing resolution of $< 300\,\mathrm{ps}$ and spatial resolution of $\sim 4\,\mathrm{cm}$ in the lateral direction. For particles that interact in the umbrella, this translates to a typical β resolution of $0.015 - 0.02$ (RMS) in the GAPS range of $0.25 \lesssim \beta \lesssim 0.7$ and an angular resolution of $< 3\%$. For particles that interact with the cortina, the β resolution is reduced due to the smaller separation distance.

The TOF electronics are managed locally by 20 readout boxes, each containing

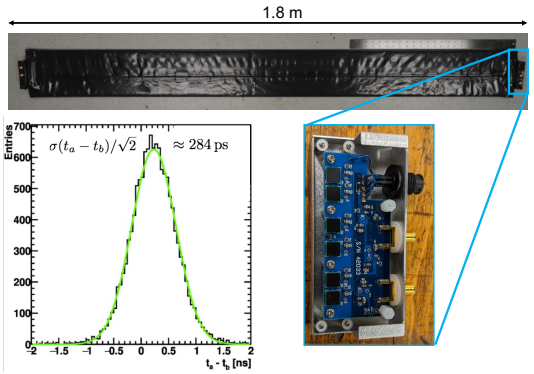

Figure 4.5: Each TOF paddle (top) is wrapped in aluminum foil and blackout material for optical light collection and to ensure a clean signal. Each paddle is read out by 3 SiPMs at either end, illustrated together with their preamp at lower right. Better than 300 ps timing resolution has been achieved for vertical muons (lower left) and further improvements in timing are expected for slower particles, which induce a larger signal in the paddle.

a power board, a local trigger board, and two readout boards. Information on the energy deposition (which carries information of particle charge and velocity) and number of hits is passed to a central trigger board. The Trigger Interface Unit (TIU) is responsible for distributing the TOF system trigger to all of the tracker DAQ boxes and for distributing a tracker BUSY signal to the TOF. Meanwhile, the TOF computer is responsible for sending the TOF data to the flight computer (Section 4.2.4) after trigger.

4.2.3 The Thermal System

Due to the low atmospheric pressure at 37 km float altitude, the thermal environment for the GAPS payload is dominated by radiative heat transfer. Both direct sunlight and albedo from the highly reflective Antarctic ice contribute to heating of the GAPS payload. The detectors and electronics generate additional heat. Given the optimal Si(Li) operating temperature around -40°C, a dedicated thermal system is necessary during flight.

The novel oscillating heat pipe (OHP) thermal system developed for use in the GAPS flight cools the sensitive detectors of the tracker to their operating temperatures of around -45 to -35°C via a low-power and relatively lightweight system [241, 242,

243]. The system consists of 1 mm-diameter capillary tubes filled with a two-phase fluid integrated in the tracker modules, and a $>8\,m^2$ radiator oriented away from the sun-facing side of the payload. The fluid in the warmer tracker expands into vapor, while the fluid in the colder radiator condenses into liquid, generating a self-oscillating flow which carries heat generated during detector operation from the tracker to the radiator. Compared to a cryostat, this integrated OHP system is less bulky and less massive, facilitating a larger sensitive area and reducing passive materials that could distort or attenuate cosmic particle tracks.

In complement to the active cooling provided by the active OHP system, passive thermal regulation is provided by foam insulation, thermal shields, and the white paint of the gondola. These mitigate heating from solar radiation in the high-altitude environment and complement the OHP to provide a stable thermal environment for detector operation.

4.2.4 Flight Systems

The GAPS flight computer is based on a Versalogic EBX-38 CPU board with a total of four 1.91 GHz cores and 8 GB of random access memory (RAM). The system features two 960 GB Swissbit industrial grade solid state drives (SSDs) rated for a wide temperature range and a power board with DC-to-DC converters, power monitoring, and general-purpose input/output (GPIO). It is enclosed in a custom box with a custom heatsink suitable for the high-altitude environment. For each event, the flight computer receives and processes the arrival times, charges, and peak voltages for all TOF channels with a pulse from the TOF computer as well as the associated tracker energy deposition information from the tracker backend.

Power is provided by 16 100-Watt solar panels from SunCat Solar, positioned in a 4×4 array at the side of the gondola to reduce mass directly above the payload. Together, these panels supply 1.3 kW after accounting for temperature derating (15%) and solar angle derating (5%). A system of four $LiFeMgPO_4$ batteries, which provide

Table 4.1. The power distribution of the GAPS payload components.

System	Estimate [W]	Allocation [W]
Tracker ASIC	127	134
Digital Interface Boards	10	12
Tracker Digital Backend	73	88
Tracker Power Systems	60	72
TOF	475	525
Thermal	220	265
Flight Operations*	220	265
Margin		126
Total	1029	1292

Note. — This table is compiled with thanks to Florian Gabhauer and is current as of January, 2022.

*Includes CPU, ethernet, GPS system, and miscellaneous flight operations.

Table 4.2. The mass distribution of the GAPS science payload components. The maximum science weight is 2494 kg, which leaves a margin of 7.3%. Additional suspended mass is allocated to ballast and balloon systems.

System	Estimate [kg]	Allocation [kg]
Tracker	504	537
TOF	678	730
Power System	159	173
Thermal	350	397
Gondola Systems*	34	37
Gondola	379	398
Crush Pad	38	38
Margin		183
Total	2142	2492

Note. — This table is compiled with thanks to Florian Gabhauer and is current as of January, 2022.

*Includes CPU, ethernet, GPS system, and miscellaneous flight operations.

69 A h 1.76 kW h, can power the entire payload for 5.4 hr. The battery system critically enables operation during launch. Table 4.1 summarizes the power requirements of the GAPS instrument systems, which have been optimized considering the power delivered by the panels within margin.

The entire instrument design is optimized for low mass, to enable as safe, long-duration, and high-altitude a flight as possible within the constraints of the Antarctic LDB program and thus to maximize the science potential of each flight. Table 4.2 summarizes the mass allocation between the tracker and TOF, the thermal systems (with significant contributions from the OHP and the passive cooling structures), the solar panels and batteries, and the payload structure.

4.3 GAPS Project Timeline

The GAPS exotic atom detection concept was first demonstrated using the antiproton beam at the KEK facility in 2004 and 2005 [235]. In 2012, a prototype GAPS flight from Hokkaido, Japan demonstrated operation of sample tracker and TOF detector components at high altitude [244, 245, 246]. The OHP was successfully operated as a piggyback payload on a balloon flight from Fort Sumner, NM in 2019. Meanwhile, the electronics backend is closely based on a similar system that flew on multiple missions with the Gamma-Ray Imager/Polarimeter for Solar flares (GRIPS) and COmpton Spectrometer and Imager (COSI) balloon payloads.

GAPS was selected as a NASA Astrophysics Research and Analysis (APRA) balloon mission in 2016. International collaborators include the Japan Space Exploration Agency (JAXA), the Italian Space Agency (ASI), and the Italian National Institute for Nuclear Physics (INFN). Several years of parallel development have prepared the TOF, tracker, thermal, software, and associated electronics systems for flight.

Integration of the hardware and software systems for the first GAPS flight began in fall 2021. The first phase of integration, assembled at MIT's Bates Research and Engineering Center and pictured in Figure 4.6, demonstrated the successful integration of the tracker modules and their associated power and readout electronics; the

Figure 4.6: The GAPS functional prototype demonstrated the successful operation of all flight systems using $\sim 10\%$ of the Si(Li) modules and TOF paddles of the full flight payload. Photo courtesy of Mengjiao Xiao.

TOF paddles with their SiPMs and associated power, readout, and trigger electronics; the OHP system using a chiller designed for ground operations; and the flight computer. This first phase of integration consists of a system of three tracker layers with 6×2 modules per layer and two TOF layers with 12 scintillator paddles per layer, approximately 10% of the detectors in the full payload.

Integration of the full payload is already underway, with the construction of the flight TOF at UCLA (pictured in Figure 4.7). The full tracker with an integrated OHP system modified for ground operations is currently in assembly at Bates. Beginning in summer 2022 at the University of California Berkeley's Space Sciences Laboratory, the flight TOF and tracker will be integrated in preparation for extensive ground testing, optimization, and operation. Following thermal and vacuum testing at the Space Environments Complex at NASA's Armstrong Test Facility (formerly known as Plum Brook Station), and compatibility tests at Columbia Scientific Ballooning Facility, the payload will be shipped to McMurdo Station in Antarctica. The first $\sim$ 35-day balloon flight is expected in December 2023, with at least two subsequent flights anticipated on a nominally biennial basis.

Figure 4.7: The frame for the TOF umbrella and cortina is shown at Bates in preparation for integration. Photo courtesy of M. Xiao.

Chapter 5

Development and Characterization of the GAPS Silicon Sensors

This chapter treats the development and characterization of the large-area, high-temperature lithium-drifted silicon (Si(Li)) sensors at the heart of the GAPS instrument. The Si(Li) detectors serve as the target material, particle tracker, and X-ray spectrometer for particle identification, and the combination of these roles drives the unique performance requirements. Particle tracking is enabled by a multi-layer system of segmented detectors. The detectors must be thick enough for the tracker system to provide stopping power for antideuterons with β up to 0.6. Conversely, the sensor geometry must be thin enough to allow a high escape fraction for X-rays in the $20-100\,\mathrm{keV}$ regime. To distinguish antideuteronic from antiproton exotic atoms, energy resolution of $<4\,\mathrm{keV}$ is required, at the relatively high temperatures achievable by the integrated OHP cooling system. Finally, the large-acceptance nature of the GAPS design mandates a low-cost, large-area, low-power sensor design, in order to instrument $\sim 10\,\mathrm{m}^2$ within the monetary and power budgets of a balloon mission.

The development and characterization of the GAPS Si(Li) detectors is an ongoing and highly collaborative effort involving an international team of scientists and engineers from private industry, academia, and government laboratories. While Si(Li) technology has been in use since the 1960s, the GAPS detectors represent a unique design developed by the collaboration to meet the specific requirements of exotic

atom-based particle identification from a balloon platform. During my tenure as a PhD student, I led the characterization of the Si(Li) detectors through the development of the fabrication and passivation protocols, working closely with collaborators to develop the final flight protocols during just a few years. I also led the characterization of the final flight detector model, which serves as the foundation for the effort to calibrate the 1000 detectors for the first GAPS flight. In tandem with these efforts, I led or supervised several projects to explore the details of the detector performance and develop an improved detector model for future flights.

Section 5.1 introduces the general operating principle of semiconductor radiation detectors and the history and utility of Si(Li) detectors specifically for large-volume applications. Section 5.2 discusses the development and validation of the GAPS Si(Li) fabrication protocol. The testing and performance of the flight-model detectors, including specific diagnostics used in Section 5.2, is treated in Section 5.3. Section 5.4 describes the procedure developed to stably maintain the detector performance over time.

5.1 Introduction to Semiconductor Radiation Detectors

Semiconductors make excellent radiation detectors thanks to the low average energy ($\sim 3.6\,\text{eV}$ for silicon at room temperature) required to produce an electron-hole pair as a quantum of signal. The result is excellent intrinsic energy resolution and better sensitivity at low energies compared to gaseous ionization detectors or scintillation detectors.

5.1.1 Semiconductor Basics

Semiconductors are solid-state materials with a small band gap ($E_g \sim 1\,\text{eV}$) between the valence band, composed of energy states occupied by electrons that are localized to a particular nucleus, and the conduction band, composed of energy states occupied

by electrons that move freely through the crystal [247]. Due to the close packing of atoms in the crystal structure, each energy band is composed of many states with similar energy levels, forming a quasi-continuum, while in a chemically-pure crystal, no energy states exist in the "forbidden band" defined by the band gap. In semiconductors, thermal energy is sufficient to excite small numbers of electrons from the valence band to the conduction band. If a bias (potential difference) is applied across a semiconductor crystal, a small current will flow. By comparison, insulators feature a larger band gap, not accessible by thermal excitations at standard operating temperatures, while in conductors, the valence and conduction bands overlap, so that electrons fill the conduction band even at 0 K.

When a valence electron in a semiconductor is excited to the conduction band, it leaves a "hole" in the valence electron structure, forming an "electron-hole pair." The electron in the conduction band is a mobile carrier of negative charge. The hole is also mobile, as it can be filled by a neighboring valence electron, producing a hole offset spatially from the original hole position. Because a hole is the absence of an electron next to a positive nucleus, it is effectively a mobile carrier of positive charge.

Electron-hole pairs can recombine via the opposite equilibrium process of electron-hole pair formation. Because recombination of free electrons and holes in pure silicon requires exact conservation of energy and momentum, this process most commonly occurs at sites of chemical impurities in the crystal called "recombination centers." These impurities disrupt the semiconductor band structure, adding energy states in the forbidden band. They can capture a free electron (or hole), holding it for a characteristic time before releasing it. If a complementary hole (or electron) is captured during the holding time, the electron-hole pair recombines. Chemical impurities can also lead to "trapping sites," which hold electrons or holes for a characteristic time before releasing them but do not facilitate recombination.

The equilibrium concentration n_i of free electrons or holes in chemically-pure ("intrinsic"; i) silicon depends on temperature T as

$$n_i = \sqrt{N_c(T)N_v(T)}\exp\left(\frac{-E_g}{2k_BT}\right) = AT^{3/2}\exp\left(\frac{-E_g}{2k_BT}\right). \tag{5.1}$$

In Eq. (5.1), E_g is the band gap at 0 K and k_B is the Boltzmann constant. $N_c(T)$ and $N_v(T)$ are the number of states in the conduction and valence band, respectively, both of which vary as $T^{3/2}$, resulting in the second representation where A is a temperature-independent constant. For chemically pure silicon at 300 K, $n_i \sim 1.5 \times 10^{10}\,\mathrm{cm}^3$, corresponding to one electron-hole pair for every $\sim 10^{-12}$ silicon atoms [247].

In the presence of an electric field $\mathbf{E}$, free electrons and holes drift with velocity

$$\begin{aligned} \mathbf{v}_e &= -\mu_e(T)\mathbf{E}, \\ \mathbf{v}_h &= \mu_h(T)\mathbf{E}. \end{aligned} \tag{5.2}$$

In Eq. (5.2), $\mu_e(T)$ ($\mu_h(T)$) is the mobility of electrons (holes) at temperature T. For $E < 10^3\,\mathrm{V/cm}$ at 300 K, $\mu_e \sim 1350\,\mathrm{cm}^2/\mathrm{Vs}$ and $\mu_h \sim 480\,\mathrm{cm}^2/\mathrm{Vs}$, while for $E > 10^3\,\mathrm{V/cm}$, μ_e and μ_h decrease with increasing E, resulting in velocity saturation by $E \sim 10^4\,\mathrm{V/cm}$. The result of the drift of electrons and holes in an $\mathbf{E}$ field is a current density

$$\mathbf{J} = qn_i(\mu_e + \mu_h)\mathbf{E}, \tag{5.3}$$

where q is the elementary charge. By comparing Eq. (5.3) to Ohm's Law ($\mathbf{J} = \sigma\mathbf{E}$), the conductivity σ and the resistivity $\rho \equiv \sigma^{-1}$ are defined as

$$\begin{aligned} \sigma &= qn_i(\mu_e + \mu_h), \\ \rho &= [qn_i(\mu_e + \mu_h)]^{-1}. \end{aligned} \tag{5.4}$$

Equations (5.3) and (5.4) illustrate that the "bulk leakage current", or the current arising within the material in the absence of ionizing radiation, depends on both $n_i(T)$ and the material-determined quantities $\mu_e(T)$ and $\mu_h(T)$. As will be shown in Section 5.1.4, the leakage current is a fundamental contributor to the noise properties of a semiconductor radiation detector.

Silicon (or germanium) has valency four, and in its intrinsic form, its crystals form a lattice with eight covalent bonds per silicon atom as illustrated in Figure 5.1 (*left*). In reality, no materially is chemically pure, and the electrical properties of semiconductors are dominated by their impurities, even if they occur in minute concentrations.

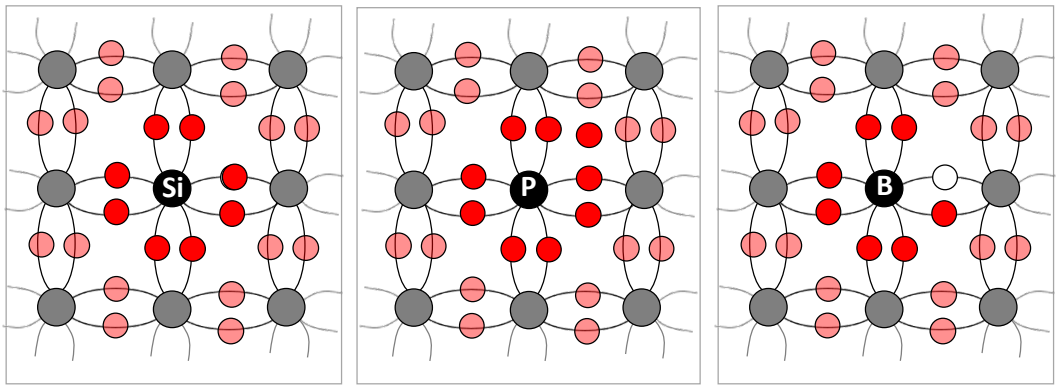

Figure 5.1: Diagrams illustrate the electron structure of intrinsic (*left*), n-type (*center*), and p-type (*right*) silicon at 0 K. Black circles indicate nuclei, red circles indicate electrons, and white circles indicate holes. Image credit: K. Perez.

Impurities called "dopants" are often intentionally incorporated into semiconductors. Compared to the silicon or germanium crystalline structure, valency-five elements such as phosphorus, arsenic, and antimony contribute free electrons that do not fit into the covalent bond structure as shown in Figure 5.1 (*center*). Inclusion of such "donor" dopants results in an "n-type" semiconductor with free negative charges and fixed positive ions. Meanwhile, elements with valency three, especially boron, gallium, and indium, have insufficient valence electrons to fill in the covalent bond structure of the semiconductor crystal, as illustrated in Figure 5.1 (*right*). The result of doping with these "acceptor" elements is a p-type semiconductor with free positive holes and fixed negative ions. Typical dopant concentrations in silicon are a few parts per billion. Dopant concentrations up to one part per hundred can be used to produce highly conductive materials, denoted p^+ or n^+, that are useful for specific applications.

In a doped "extrinsic" material, the concentration of electrons (n) differs from the concentration of holes (p), but the product still obeys the generalized form of Eq. (5.1):

$$np = n_i^2 = AT^3 \exp\left(\frac{-E_g}{2k_B T}\right) \tag{5.5}$$

where n_i is the intrinsic concentration. To conserve charge, it is required that

$$N_D + p = N_A + n \tag{5.6}$$

$$\rho = [q(n\mu_e + p\mu_h)]^{-1}. \tag{5.7}$$

Because $np = n_i^2$ implies $n + p > 2n_i$, it is clear that ρ is smaller for extrinsic semiconductors compared to the higher-resistivity intrinsic state.

By contrast to n- or p-type materials, "compensated" semiconductors, also denoted i, contain equal concentrations of donor and acceptor dopants. While these materials are not truly intrinsic, they retain many of the electrical properties of intrinsic materials, including the equal concentration n_i of electrons and holes from Eq. (5.1). With $N_A = N_D$, the total number of free charges is minimized, corresponding to the low relative conductivity of intrinsic and compensated silicon. Production of compensated silicon is non-trivial, however, and cannot be accomplished by typical doping methods, because even a small imbalance between N_D and N_A results in n or p-type behavior.

5.1.2 Physics of a *pn*-Junction

This section focuses on the principles of semiconductor radiation detectors based on the interface of n-type and p-type silicon, at "pn junctions." These devices are typically created by beginning with a uniformly doped silicon wafer and then diffusing or implanting the opposite dopant type into one side. The result is a diode, which allows high currents under forward bias but acts as a rectifier under reverse bias.

Though both the n and p material are electrically neutral in isolation, the n-type material has free negative electrons while the p-type material has free positive holes. At the junction, holes diffuse from p to n (from high hole concentration to low hole concentration), and electrons diffuse from n to p (from the region of high electron concentration to low electron concentration). The result is 1) recombination of electron-hole pairs to produce a charge-free "depleted" zone around the junction, which forms the active volume of a pn-detector and 2) an electric potential (the "contact" potential V_0) between the n side with its remaining fixed positive ions and the p side with its remaining fixed negative ions. Once the resulting electric field is sufficiently strong, it ends the diffusion, leaving $V_0 \sim 1\,\mathrm{V}$ for typical doping

concentrations N_A and N_D in silicon. This situation is summarized in Figure 5.2.

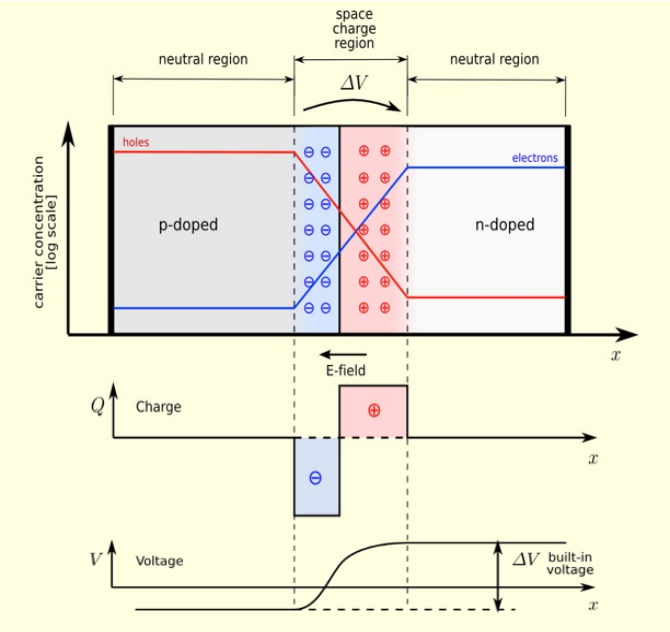

Figure 5.2: A cartoon view of the hole and electron concentration (*upper panel*), net charge (*center panel*), and voltage (*lower panel*) arising across a *pn*-junction. Image credit: Wikimedia Commons.

The depleted region extends into either side of the junction, with depth

$$x_n = \sqrt{\frac{2\epsilon V}{qN_D(1+N_D/N_A)}}$$
$$x_p = \sqrt{\frac{2\epsilon V}{qN_A(1+N_A/N_D)}} \tag{5.8}$$

in the n and p sides of the junction, respectively, where $\epsilon \sim 1.05 \times 10^{-13}\,\mathrm{F/m}$ is the dielectric constant and V is the voltage across the junction. As Eq. (5.8) indicates, if $N_D \neq N_A$, the depletion zone extends primarily into the side with lower dopant concentration, and a less-highly-doped material results in a thicker depletion zone. A *pn*-junction used as a typical radiation detector consists of a thin n^+ layer and a thick p layer, with the depleted zone extending through most of the p-type silicon.

With only the contact potential ($V = V_0$) and no applied bias, the depth $d \equiv x_n + x_p$ of the depletion zone is $<$100 µm in a typical *pn*-junction. Many applications require a larger sensitive depth for a detector. The application of a reverse bias V_B

across the junction, such that $V = V_0 + V_B \sim V_B$, increases the depleted depth. For high-resistivity silicon, a typical depleted depth $d \lesssim 5\,\text{mm}$ is possible; with the higher bias voltages required to produce a larger depth, avalanche breakdown occurs due to secondary ionization in the high electric fields.

Considering the low resistivity of the n and p material and the high resistivity of the depleted zone, the junction behaves as a capacitor. In a typical geometry, the junction is parallel to either end of a silicon wafer, forming a parallel-plate capacitor with capacitance

$$C = \epsilon \frac{A}{d}, \tag{5.9}$$

where A is the area of the depletion zone. As detailed in Section 5.1.4, capacitance fundamentally limits a *pn*-detector's noise performance given the choice of readout electronics. Segmentation of the active detector area and application of an external reverse bias to increase d decreases the capacitance, critical for high-performance large-area sensors.

Any new electron or hole generated in the depleted zone is swept out by the electric potential, creating a current. When ionizing radiation traverses the depleted zone and forms electron-hole pairs, it frees a total charge

$$Q = \frac{nE}{w}, \tag{5.10}$$

where E is the total deposited energy, $w \sim 3.6\,\text{eV}$ is the average energy per electron-hole pair, and n is the collection efficiency. Note that $w > E_g$, as a portion of the deposited energy is converted into phonons, and E_g is the minimum, not the average, energy between any individual valence state and conduction state. The readout time depends on the velocity of the charge carries in the detector bulk, as in Eq. (5.2). Application of a reverse bias not only increases the active volume of the detector while reducing detector capacitance; it also increases the velocity of the charge carriers, resulting in high charge-collection efficiency.

As a final note, electrodes are required on the p and n side of the junction in order to apply an external bias across and read out signals from a semiconductor

device. Direct deposition of metal electrodes on n or p-type semiconductors results in a "rectifying junction" with a (high-resistivity) depleted zone extending into the detector volume. This is the desired behavior on the p-side, where the Schottky behavior impedes charge injection from the p surface. The rectifying behavior of a Schottky contact is not desired on the n side, where it would oppose charge readout. The ideal case for the n-side is the formation of a low-resistivity "ohmic" contact. The use of a heavily-doped n^+ material interfacing with the contact results in a vanishing depleted zone and the desired ohmic behavior.

5.1.3 Operation of pn-Junction Detectors

Charge is induced on the electrodes via induction from the movement of the ionized charge (Eq. (5.10)) within the detector bulk. The characteristic time of the response is derived using Poisson's equation, $\delta^2 V/\delta x^2 = -\rho(x)/\epsilon$. In a typical detector with the depleted zone almost entirely in the p-side, $\rho(x) = -qN_A$ throughout the depleted zone. Defining a coordinate system with $x = 0$ at the p-edge of the depleted zone, integrating Poisson's equation gives the electric field

$$E \equiv \frac{\delta V}{\delta x} = -\frac{qN_A}{\epsilon}x = -\frac{x}{\mu_h \epsilon \rho}. \tag{5.11}$$

In Eq. (5.11), the last equivalency comes from substituting Eq. (5.7) with $p \sim N_A \gg n$ for the n-type material. When an electron-hole pair is created at depth x_0 in the depletion zone, the electron and hole drift with respective velocities

$$\begin{aligned} \mathbf{v}_e(x) &= \frac{\delta x}{\delta t}\hat{\mathbf{x}} = -\mu_e(T)\mathbf{E} = \frac{\mu_e x}{\mu_h \epsilon \rho}\hat{\mathbf{x}}, \\ \mathbf{v}_h(x) &= \frac{\delta x}{\delta t}\hat{\mathbf{x}} = \mu_h(T)\mathbf{E} = \frac{x}{\epsilon \rho}\hat{\mathbf{x}}. \end{aligned} \tag{5.12}$$

Eq. (5.12) is derived from Eq. (5.2) by substituting Eq. (5.11). Integration of Eq. (5.12) gives the position of the electron and hole at time t after creation of the pair,

$$\begin{aligned} x_e(t) &= x_0 \exp \frac{\mu_e t}{\mu_h \rho \epsilon}, \\ x_p(t) &= x_0 \exp -\frac{t}{\rho \epsilon}. \end{aligned} \tag{5.13}$$

Setting $x_e(t) = d$, the time for the electron or hole to reach its respective electrode is

$$t_e = \frac{\mu_h \rho \epsilon}{\mu_e} \ln \frac{d}{x_0}. \tag{5.14}$$

The total time for the hole to reach the electrode is infinite, but it is still parameterized by a characteristic time $\tau_h = \rho\epsilon$, where $\rho\epsilon \sim 1\,\text{ns}$ for $1000\,\Omega\,\text{cm}$ silicon. From Eq. (5.14), 99.7% of the charge from holes will be collected within $3\tau_h$.

Using $\delta Q/q = \delta x/d$, the cumulative induced charge from the electron and hole on the n and p contacts, respectively, is

$$\begin{aligned} Q_e(t_e) &= -\frac{q}{d} \int \frac{\delta x}{\delta t} dt = \frac{q x_0}{d} \left(1 - \exp \frac{\mu_e t_e}{\mu_h \rho \epsilon}\right) \\ Q_h(t) &= -\frac{q x_0}{d} \int \exp \frac{-t}{\rho \epsilon} \frac{dt}{\rho \epsilon} = -\frac{q x_0}{d} \left(1 - \exp \frac{-t}{\rho \epsilon}\right). \end{aligned} \tag{5.15}$$

Evaluating at long times, $Q_e(t_e) = \frac{q x_0}{d} - q$ and $Q_h(t \to \infty) = -\frac{q x_0}{d}$, so that the total charge induced for one electron-hole pair in the detector is the electron charge, $-q$. In reality, charge is integrated over a fixed window, and the benefits of increased charge collection at longer times are weighted with the noise consequences, as discussed in Section 5.1.4.

Readout of the the induced charge proceeds by processing individual pulses. In a typical setup, signal is read out from either the p or the n side of the semiconductor detector by a charge-sensitive preamplifier coupled to the device through an additional capacitor C_f. The output of the charge-sensitive preamplifier is thus

$$V_0 \sim -\frac{Q}{C_f} \tag{5.16}$$

where the approximate relation is due to incomplete collection of the induced charge Q related to the infinite collection time for holes. Eq. (5.16) illustrates that, due to the use of the coupling capacitor C_f, the preamplifier output voltage V_0 does not depend on the detector capacitance. The charge collected on the capacitor is typically discharged through a resistor in series R_s, resulting in an exponential decay of the preamp output over a characteristic timescale (typically μs to ms). Note that a voltage-sensitive preamplifier, which does not require the use of a coupling capacitor, is not suitable for readout of semiconductors, due to the slight dependence of the detector capacitance, and thus the output voltage, on the operating temperature.

The preamplifier output is processed using shaping electronics (a "spectrum amplifier"). The signal is integrated over a timescale characteristic of the chosen system (typically $\mathcal{O}(1)$ μs), with a time dependence characteristic of the integrating circuit (eg a R-C circuit). Depending on the characteristics of the shaper and the timescale of the integration, different components of the noise are emphasized. The pulse height from the spectrum amplifier is measured and digitized by a multi-channel analyzer (MCA). As an alternative to analog shaping electronics, digital shaping electronics can provide custom shaping characteristics, not possible with analog system, for optimized noise performance. Additionally, an application-specific integrated circuit (ASIC) containing a charge-sensitive amplifier and shaping elements can provide all of the necessary pulse processing capability, delivering a digital signal directly.

During operation, the reverse bias is applied to the opposite side of device via a parallel resistor. With this setup, the bias power supply is isolated from the signal readout.

5.1.4 Noise Model for *pn*-Junction Detectors

The energy resolution of a semiconductor detector read out via a charge-sensitive preamplifier is described by three terms. (1) A "parallel noise" (also known as "step noise" or "current noise") term includes noise from the detector leakage current and thermal noise in any parallel resistance. This term typically dominates the noise at longer pulse peaking times. (2) A "series noise" (also known as "delta noise" or "voltage

noise) term accounts for thermal noise from any series resistance and preamplifier FET noise. This term scales as the detector capacitance and contributes the most noise at short pulse peaking time. (3) A "$\frac{1}{f}$ noise" (also known as "flicker noise") term has equal intensity at all peaking times and scales directly with the detector capacitance.

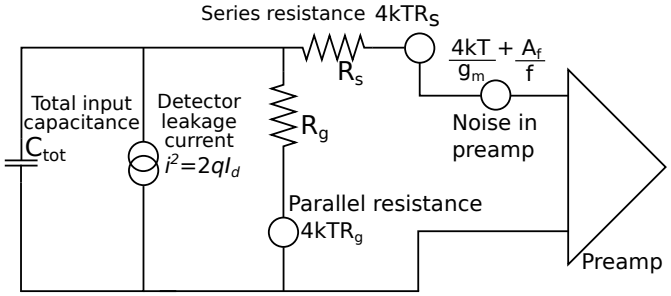

Figure 5.3: The equivalent noise charge for a silicon detector read out by a charge-sensitive preamplifier. Image credit: N. Saffold.

The equivalent noise charge (ENC) that is read out is illustrated in Figure 5.3 and calculated as [248, 249, 250]:

$$ENC^2 = \Big(2qI_{leak}(T) + \frac{4kT}{R_p}\Big)\tau F_i + 4kT\Big(R_s + \frac{\Gamma}{g_m}\Big)\frac{C_{tot}^2}{\tau}F_\nu + A_f(T)C_{tot}^2 F_{\nu f}\,, \tag{5.17a}$$

such that the FWHM energy resolution is given by:

$$FWHM = 2.35w\frac{ENC}{q}\,. \tag{5.17b}$$

In Eq. (5.17) as in the previous sections, q is the fundamental electron charge, k_B is Boltzmann's constant, w is the average ionization energy of silicon (3.6 eV per electron-hole pair), and T is the temperature. R_p is the parallel resistance of the preamplifier, while R_s is the sum of all series resistance with possible contributions from the preamplifier mounting method and the detector itself. The transconductance of the preamplifier input FET, g_m, can be measured, and the constant Γ relates to the behavior of the channel in the JFET. $A_f(T)$ is the coefficient of $\frac{1}{f}$ noise, a temperature-dependent quantity that may include contributions from preamplifier noise, detector

surface effects, or other electronic components. The total input capacitance, $C_{tot} = C_{det} + C_{FET} + C_{int} + C_{stray}$, is the sum of all the parallel capacitance, including the individual strip capacitance C_{det}, the capacitance of the preamplifier FET C_{FET}, any inter-strip capacitance C_{int}, and any stray capacitance C_{stray}. $I_{leak}(T)$ is the temperature-dependent leakage current of the strip. The dependence of each noise term on the particular pulse shaping system is parameterized by the form factors F_i, F_ν, and $F_{\nu f}$, such that different components of the noise model can be evaluated by varying the peaking time of the spectroscopy amplifier.

Eq. (5.17) clearly illustrates the benefit of semiconductor-based detectors, as w is directly proportional to the energy resolution. Compared to the average ionization energy in silicon, $\mathcal{O}(10)$ eV is required to produce a photon in a typical scintillator or to ionize an electron in a gas counter.

As noted in the previous sections, the leakage current and the strip capacitance are dominant detector characteristics contributing to the noise of a well-behaved detector. The capacitance, which is determined by the geometry of the depleted detector volume, fundamentally limits the energy resolution of the system regardless of peaking time because of its contribution to the $\frac{1}{f}$ noise term. In contrast to the capacitance, the leakage current is sensitive to the details of fabrication, including the microphysics of the bulk material, the surface states, and the detector geometry.

5.2 Development of the GAPS Si(Li) Detectors

This section treats the development and validation of the fabrication protocol for the large-area, low-cost, and relatively high-temperature GAPS Si(Li) detectors. Throughout the stages of development, the MIT group led the operation and evaluation of detector performance, and the results of these assessments are emphasized here.

A large-area Si(Li) model (the "Semikon detectors") meeting the noise and temperature requirements of the GAPS mission was previously developed by Semikon Detektor GmbH of Jülich, Germany [251]. Six of these detectors were successfully

operated on a prototype GAPS balloon flight in 2012 (see Section 4.3; [244, 245, 246]); however, the materials cost alone prohibited production in the quantity needed for GAPS, and the fabrication procedure was lost when the company went out of business.

A 5-cm diameter Si(Li) "test detector" model was developed in-house. Operation of the first test detectors fabricated by GAPS collaborations was achieved at Columbia University prior to my tenure as a graduate student. During my graduate studies, fabrication and operation of the test detectors was re-established and used to study variations in the materials, fabrication protocol, and detector handling. The Columbia University group led detector fabrication, while the MIT group led the operation and performance studies, operating in close feedback.

The 10 cm-diameter flight-model "Shimadzu detectors" were developed in a collaboration between the GAPS team, whose test detectors provided experience with large-area, high-temperature sensors, and researchers at Shimadzu Corporation, a Japanese private company with years of experience producing cm-scale low-temperature sensors for commercial applications. As with the test detectors, the MIT group led the operation and evaluation of the detectors to assess variations on the fabrication and handling.

Section 5.2.1 introduces the general fabrication concept for Si(Li) sensors. Fabrication, operation, and research and development with the test detectors is in Section 5.2.2 while the Shimadzu detectors are discussed in Section 5.2.3. Details of the testing setup and detector performance are deferred to Section 5.3.

5.2.1 Fabrication of Lithium-drifted Silicon Sensors

Lithium-drifting is a process, originally developed by Pell [252], that produces a thick region of compensated silicon. The result is a thick depletion zone in a detector operable at a much lower bias compared to that required for a device based on high-resistivity silicon alone. Lithium acts as an electron donor, with the unique property that the ions are mobile in silicon at high temperatures. Lithium-drifting results in a *pin*-junction. Compared to the pn-junctions of Section 5.1.3, the i material of

the *pin*-junction is a region with no space charge, resulting in a constant electric field through the compensated silicon during detector operation. The relatively large depletion depth enabled by this technique means that low-temperature operation is typically required to control leakage current from thermal electron-hole production through the large volume of the silicon bulk.

The basic Si(Li) fabrication process begins with a p-type silicon wafer, typically a boron-doped wafer with acceptor concentration N_A. High-quality Si substrate is critical to the success of Li drifting, as defects and contaminants can behave as Li traps, causing irregular drifts. Li is diffused onto one side of the wafer with concentration $N_0 \gg N_A$ at the surface, producing a n^+ layer and a *pn*-junction. After diffusion for time t_0 at a sufficiently high temperature that diffusion is the dominant process driving the motion of lithium ions, the lithium concentration as a function of the distance x from the surface [253] is

$$N_D(x) = N_0 \cdot \mathrm{erfc}\left(\frac{x}{2(D(T)t_0)^{1/2}}\right). \tag{5.18}$$

In Eq. (5.18), $D(T)$ is the diffusion constant at temperature T, parametrized as

$$D(T) \sim 0.0023\,\mathrm{cm}^2/\mathrm{s} \cdot \exp\left(\frac{-7700\,\mathrm{K}}{T}\right) \tag{5.19}$$

in $1000\,\Omega\,\mathrm{cm}$ silicon, though the scaling factors vary depending on the properties of the silicon. The junction is located at the depth x_j that satisfies $N_D(x_j) = N_A$.

Following the initial diffusion of lithium on the the silicon wafer, the lithium is drifted through the bulk of the wafer under a reverse bias. The reverse bias causes an electric field E in the depleted region of the *pn*-junction. The result is a force on the lithium ions in the junction toward the p-side of the wafer. The mobility of lithium ions in silicon is:

$$\mu_{Li}(T) = \frac{26.6\,\mathrm{K}}{T}\exp\left(\frac{-7500\,\mathrm{K}}{T}\right)\,\mathrm{cm}^2\,\mathrm{V}^{-1}\,\mathrm{s}^{-1}. \tag{5.20}$$

Thus, for sufficiently high temperature and high fields, the drift of lithium ions under

the reverse bias is the dominant process governing the motion of lithium ions in the wafer. For $x < c$, the lithium concentration remains $\gtrsim N_A$, as any concentration $< N_A$ would result distort the local electric field, applying a force back toward the n^+ side on the lithium ions. Similarly, for $x > c$, the lithium concentration remains $\lesssim N_A$. Thus, the lithium concentration N_D approaches N_A in the junction, producing a region of compensated, charge-free silicon and increasing the depth through which the E-field is distributed. The electric field continues to move lithium ions from the n^+ region into the p region, extending the compensated width through which $N_A \sim N_D$. After a drift time t, the width of the compensated region is approximately

$$W(t) = (2V\mu t)^{1/2}. \tag{5.21}$$

As shown by Eq. (5.21), the compensated width grows as the square root of the drift time t in seconds, given a constant applied voltage V and temperature-dependent lithium-ion mobility.

The electrical properties of the finished Si(Li) detector depend strongly on the parameters (time, temperature, bias, initial silicon characteristics) of the drift. Of particular interest is the method for determining the end of the drifting time. Some examples follow: 1) In a fabrication protocol for small ($\mathcal{O}\,\mathrm{cm}^2$) detectors [248, 254, 255], the leakage current is monitored during drifting, until it increases dramatically, indicating that the lithium is approaching the p-side of the detector. Any lithium excess on the p-side is then removed via physical lapping or chemical etching. 2) In a fabrication protocol used for larger detectors, boron contacts are implanted into the p-side before drifting, creating a p^+ layer, and the intrinsic region width is confirmed using measurements of α-particles [256, 257]. 3) The drift is ended after a time calculated using Eq. (5.21) to correspond to the depth of the wafer [258] or 4) to correspond to a fraction of the wafer, allowing the undrifted material to be subsequently removed [259]. 5) Capacitance is probed during the drift to measure the compensated depth in real-time [260].

Sometimes, the initial drift is followed by a "clean up" drift at a lower tempera-

ture. While the lower temperature reduces the lithium mobility μ_{Li}, it also reduces the number of thermally-generated electrons and holes, which can disturb the compensation. The clean up drift thus forces the lithium ions to more precisely align with the acceptor dopant ions and with any impurities, resulting in a more precisely compensated material. In reality, some space charge always persists after the drift, due to distortions of the local electric field by the thermal electrons and holes during drifting [261]. The clean up drift also mitigates any lithium over-density (a lithium "tail") that can form below the n^+ layer via diffusion due to the high temperatures and long time period involved in the drift [257, 251].

Of great importance is the control of surface leakage currents in Si(Li) detectors. Critically, geometric controls are necessary to ensure lithium drifting through the bulk of the detector but prevent drifting down the sides. Two geometries are typically used for this purpose. Following Llacer [262], in the "inverted-T" geometry, a circular groove is milled to below the *pn*-junction following lithium diffusion. Meanwhile, in the "top-hat" geometry, a ring of material several inches wide is removed from the top surface of the wafer. In either case, the lower edge of the detector the is electrically isolated from the center of the n^+ side, and the drift bias can be applied to the center of the detector without biasing the sides. For low-noise Si(Li) detectors, a "guard ring" [263] is additionally made by machining a ring into the active surface after drifting. The guard ring (outside the groove) can be grounded during operation, isolating surface currents originating in the sides of the detector from the active detector area inside the groove. The guard ring is only effective if the groove is deep enough to extend into the compensated region, which has a high resistivity when the detector is biased during operation.

5.2.2 In-house Production of 5-cm Prototype Sensors

This section, which follows the work reported by Perez et al. [264], treats the development and testing of large-area, high-temperature, low-noise Si(Li) test detectors. Figure 5.4 illustrates a typical test detector in the configuration for testing. These detectors were fabricated by GAPS collaborators at in-house facilities at the Columbia

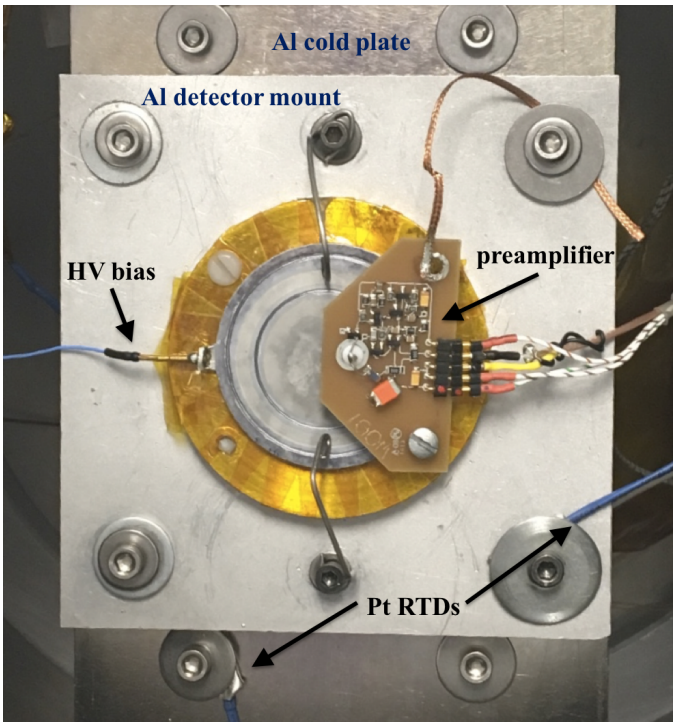

Figure 5.4: A test detector in the configuration for testing with a custom preamplifier.

Initial thickness	$1.25 - 1.7\,\mathrm{mm}$
Crystal Orientation	1-1-1 $\pm 1°$
Bulk ingot lifetime	$> 400\,\mu\mathrm{s}$
Resistivity	$800 - 2000\,\Omega\,\mathrm{cm}$
O impurity	$< 2 \times 10^{16}\,\mathrm{cm}^{-3}$
C impurity	$< 2 \times 10^{16}\,\mathrm{cm}^{-3}$

Table 5.1: Specifications for the Si substrate for the GAPS test detectors [264].

University Nano Initiative Cleanroom, the CCNY Grove School of Engineering Cleanroom, and Columbia University's campus and tested at MIT. The detector geometry, based on 2-inch wafers with a $1 - 2\,\mathrm{mm}$ deep compensated region and a single-strip 1.25-inch-diameter active readout area, was developed to match the per-strip capacitance of the larger-area multi-strip flight geometry detectors (assuming 4 strips; see Section 5.2.3). Each step in the following fabrication procedure was optimized for low cost and for noise performance above cryogenic temperatures, which, taken together, are mission-enabling features for GAPS.

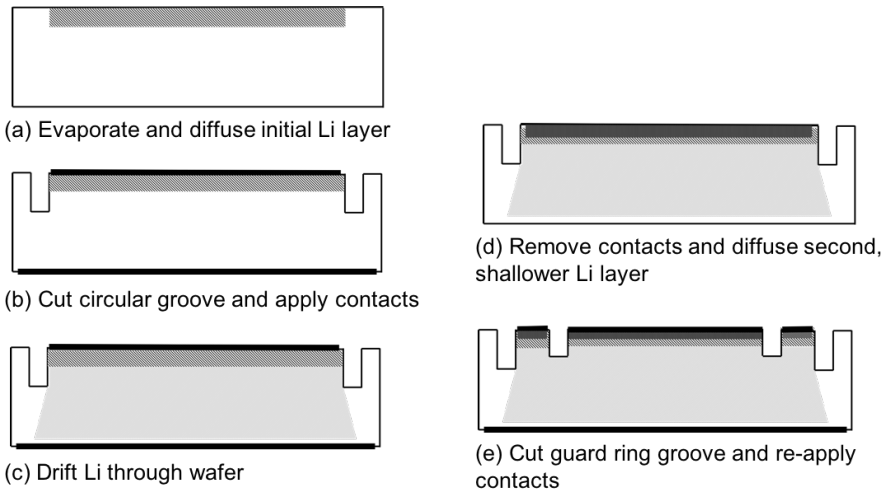

Figure 5.5: Overview of the prototype detector fabrication process [264].

The fabrication, illustrated in Figure 5.5, proceeds as follows:

1. **Cut wafers from Si boules:** Each test detector begins as a $1.25 - 1.7\,\mathrm{mm}$-thick wafer cut from a 2-inch diameter floating-zone boron-doped (p-type) Si boule. Previously, large-area Si(Li) detectors had only been successfully drifted using a Si substrate from Topsil Semiconductor Materials A/S.[1] Due to the high materials cost, this substrate was prohibitive for making a Si(Li) system on the size scale and budget of the GAPS tracker. Research and development with the GAPS test detectors demonstrated that high-performance Si(Li) detectors could be fabricated using a less costly substrate developed by SUMCO Corporation[2] meeting the requirements of Table 5.1. The floating-zone method of boule fabrication facilitates the low oxygen contamination necessary for a successful drift. A resistivity of $1000\,\Omega\,\mathrm{cm}$ corresponds to $N_A \sim 10^{13}\,\mathrm{cm}^{-3}$, which is an order of magnitude lower than typical values for Si(Li) fabrication, reducing the number of Li ions necessary for compensation and thus the necessary time and temperature of the drift.

2. **Etch clean the wafer:** A chemical etch is used throughout fabrication to clean and smooth the wafer surface, leaving a lightly n-type surface state. The

[1] http://www.topsil.com/
[2] https://www.sumcosi.com/english

etching solution is a 4:7:11 mixture of a 48% HF, glacial acetic acid, and reagent-grade nitric acid. The nitric acid forms an oxide layer on the Si surface, the HF removes the layer, and the acetic acid moderates the process. Periodic draining and agitation of the wafer during etching removes any bubbles that form, resulting in a smooth etch. In sum $\sim 30\,\mu\text{m}$ is removed at this stage, after which the wafer is quenched in a contained of deionized water, rinsed in running deionized water, and dried in flowing N_2.

3. **Evaporate Li onto one surface of the wafer:** Li evaporation is performed using a custom setup in vacuum bell jar at a few 10^{-5} Torr. The wafer is held in thermal contact with a heater plate at 300°C and is fitted with an Al mask to prevent Li evaporation on the wafer sides. A current, which is slowly increased to 40 A, is run through a tungsten boat situated $\sim 14\,\text{cm}$ below the wafer and containing $\sim 1\,\text{g}$ of Li until the Li has all evaporated. The wafer is held at 300°C for a total of 30 min from the start of the evaporation before being rapidly cooled using a flowing ice-water system.

   As shown in Eq. (5.18), the exact diffusion depth depends steeply on N_0, t_0, and T, so the lithium diffusion depth is also directly measured as $\sim 150 - 250\,\mu\text{m}$ using a copper staining technique (see Section 5.2.4).

4. **Cut a groove to form the top-hat geometry:** A circular 0.5 mm-wide, 0.5 mm-deep, 1.7 or 1.8 mm-diameter groove is milled into the n-side of the wafer using a Raytheon Model 2-334 ultrasonic impact grinder (UIG). Assuming it is deeper than the n^+-region, this groove defines the biased area during drifting, so that the detector edges do not experience an electric field during the drift and Li does not drift down the wafer sides.

5. **Etch the wafer and groove:** Etching is performed as in Step 2 but for a shorter time period. This etching cleans the wafer after exposure to the abrasives used in the UIG process, removes oxidation from the Li layer, smooths the surface produced by the UIG, and leaves a lightly n-type surface state. Agita-

tion during etching is particularly important during this step because bubbles can easily become trapped in the groove, creating irregularities.

6. **Apply drifting electrodes:** Metal contacts are applied to either surface of the wafer to facilitate the drift. The n-side contact has a 1.6-inch diameter and sits within the circular groove, while the p-side contact has a 1.9-inch diameter. Detectors were successfully fabricated using a $\sim 40\,\text{nm}$ layer of Al, Au, or Ni applied via thermal evaporation or electron-beam vapor deposition, however Al is preferred as it adheres well with the underlying SiO_2. For the drifting electrodes in particular, Al was also preferred because compared to other metals, it produced a more obvious current spike at the end of the drift in Step 7.

7. **Drift the Li from n^+ to p:** Drifting is performed in a custom station. The wafer sits on a large Au-coated Cu plate, which is thermally coupled to a heating element and which provides uniform temperature to within 1°C across the detector surface, facilitating a uniform drift. Figure 5.6 illustrates the progress of a successful drift in this setup. First, the bias voltage is raised to 250V. If the leakage current is $> 100\,\mu\text{A}$ at this stage, it is left for several hours to allow the Li to redistribute; if this the leakage current is still high, etching is repeated and a low-leakage current is ensured before proceeding. Then, the temperature is increased in $4-5$ stages up to 100°C, maintaining each temperature for at least 30 min, or until the leakage current stabilizes, before proceeding to the next stage. When the leakage current increases suddenly to a set point, the heater is turned off, and the bias is decreased after the wafer has cooled. Under these conditions, a 1 mm compensated region is achieved after ~ 42 hours. The increasing leakage current provided a more reliable indicator of the end of the drift compared to the calculated time from Eq. (5.21) due to the strong dependence of the diffusion rate on small variations in temperature.

8. **Evaporate a second Li layer:** After drifting, the electrodes from Step 6 are removed by lapping with 320 mesh slurry or 400 grit sand paper and deionized water, and the surfaces are polished. The wafers are ultrasonically cleaned in

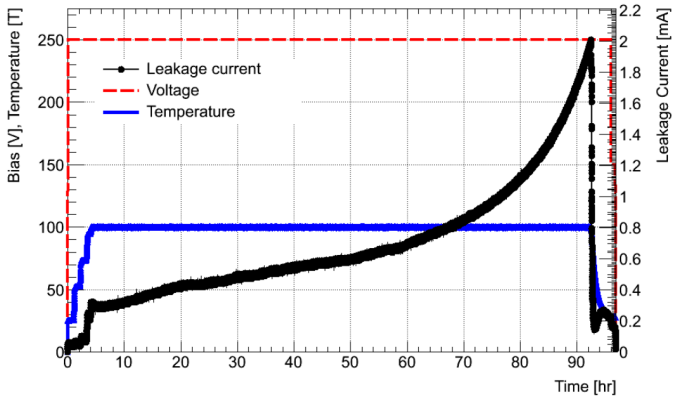

Figure 5.6: Bias voltage, temperature, and leakage current of TD0093 as a function of time during the drift [264].

acetone, methanol, and deionized water for 3 minutes each and then etched as in Step 2 for 1 minute. An Al mask is used to protect the groove and sides of the detector before a new Li layer is evaporated as in Step 3. This diffusion proceeds at a cooler temperature, 140°C, for 30 minutes to produce a $\sim 30\,\mu$m thick n^+-region. The lower temperature also mitigates diffusion of the previously evaporated and drifted Li.

9. **Cut the guard ring groove:** A second groove (350 µm deep, 500 µm wide, 1.25-inch diameter) is machined into the n^+ wafer surface via UIG, defining the circular active area (within this groove) and the guard ring structure (between this groove and that of Step 4) as illustrated in Figure 5.5 (e). A sharp, square profile of this groove is critical to forming the desired "pinch points" of high electric field and thus electrically separating the active area from the guard ring during operation. The groove profile was probed using an optical profilometer.

10. **Apply an Ohmic contact to the n-side:** A 40 nm Al layer is applied to the n^+ side using thermal evaporation or electron-beam thermal vapor deposition to form an Ohmic contact.

11. **Etch the exposed Si:** The exposed Si is then etched again as in Step 2 for $4-6$ minutes to set the final surface state of the grooves and sides to be lightly n-type. The Ohmic contact from Step 10 is protected during etching by painting

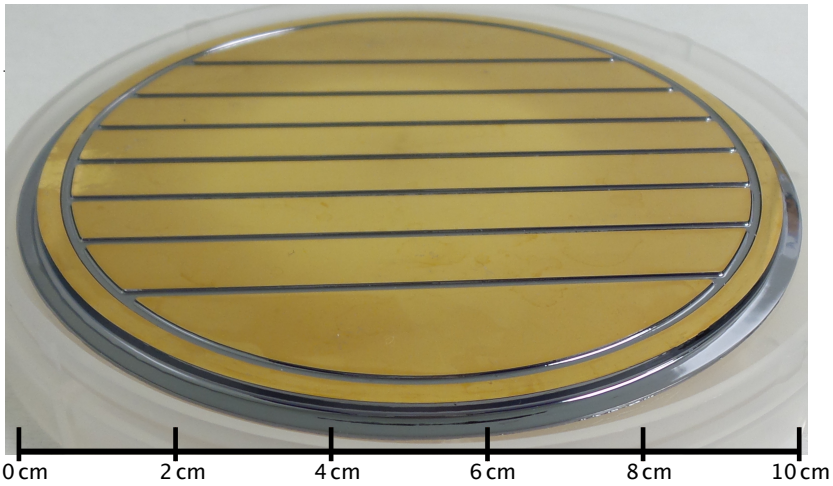

Figure 5.7: A photograph of an 8-strip Shimadzu detector.

on Apiezon brand wax dissolved in hexane or xylene. After etching, the wax is removed using hexane or xylene, and the wafer is then ultrasonically cleaned in hexane and acetone for three minutes each, repeated three times.

12. **Apply a Schottky contact to the *p*-side:** A $\sim$ 100 nm-thick, 1.9 inch-diameter Ni contact is finally applied to the *p*-side via either thermal or electron-beam deposition. Ni is relatively cheap and durable, which is important, as scratches in this layer can result in charge injection during operation, causing a high leakage current and ruining the noise performance of the detector.

5.2.3 Fabrication of the Custom GAPS Flight Detectors

This discussion of the development of the flight-geometry Shimadzu detectors, pictured in Figure 5.7, follows the work by Kozai et al. [265, 266]. The fabrication process is based on the in-house development in Section 5.2.2 and also builds from Shimadzu Corporation's 40+ years of experience with smaller Si(Li) detectors operated at liquid nitrogen temperatures. The Shimadzu detectors differ from the test detectors in their larger area and depth, their tophat rather than inverted-T geometry, their gold layer on the readout contacts for long-term durability, and the lack of a second lithiation.

Each Shimadzu detector begins as a 101 mm-diameter, 2.5 mm-thick Si wafer. Each wafer is cleaned with methanol, xylene, and acetone to remove any surface

contaminants and is then etched with a solution of HF, nitric acid, and acetic acid similar to Step 2 of Section 5.2.2. An additional step of immersing in an HF solution removes SiO_2 from the surface.

Lithium evaporation proceeds in a similar manner to Step 3 of Section 5.2.2, but at a higher pressure (10^{-4} Pa), slightly lower temperature (280°C), and a shorter time (one minute of evaporation plus one more minute at the pressure and temperature), followed by a slow cool (over ~ 150 min) to room temperature at atmospheric pressure. The result is a n^+ region with depth $\sim 100\,\mu$m.

Evaporation is followed by a second chemical etch to remove both the lithium oxide layer formed on the n^+-surface and any chemical contaminants. 18 nm of Ni, chosen for its good adhesion with Si, and 120 nm Au, chosen for its high resistance to oxidation, are evaporated onto the n^+ surface using a thermal evaporator. The outer circumference of the n^+ side is machined via UIG to remove a ring, forming the top-hat geometry and leaving a 97 mm-diameter n^+ surface. After machining, a 2 mm-wide, 1 mm-deep "top hat brim" remains. After machining, the exposed Si surface is etched to remove any damaged Si or contaminants leftover from the UIG; as in Step 11 of Section 5.2.2, the electrode is protected by an etchant-resistant wax, which is later removed.

Li drifting is performed over a typical timescale of ~ 110 hours as illustrated in Figure 5.8. The wafer is heated to 100°C. The voltage is increased in 100-V intervals every 30 minutes, up to a drift bias of 600 V. As the drift progresses, the leakage current increases, ending with a rapid increase as the depletion layer approaches the p-side of the detector. The detector temperature then exceeds 100°C due to Joule heating, which triggers the bias to turn off. The drift is ended and the wafer is cooled to room temperature. During drift under the high 600 V bias, the depletion layer always extends into the p-side of the i-p-junction. Thus, in this method, the depletion layer reaches the p-side before the Li ions, leaving a thin undrifted layer of p-type Si.

After lithium drifting, a circular 300 μm-deep, 90 mm-diameter, 1 mm-wide groove is cut into the n^+-side, producing a guard ring outside the groove surrounding a

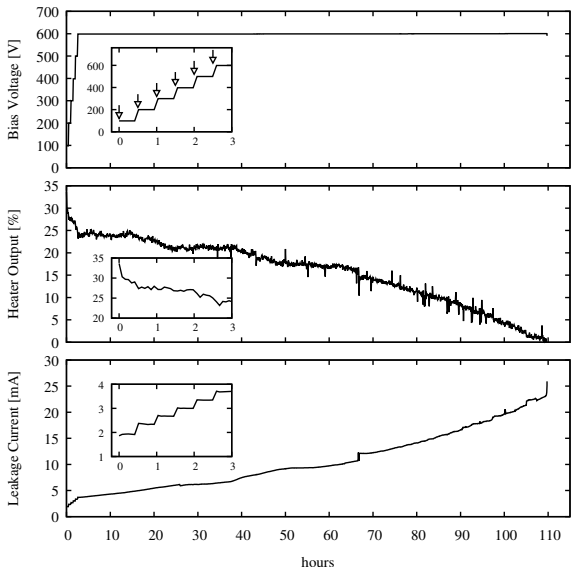

Figure 5.8: Bias voltage (top panel), heater output (middle panel), and leakage current (lower panel) of a Shimadzu detector during its 110 hour drift. As the leakage current increases, the Joule heating lowers the required output from the heater to maintain a detector temperature of 100°C [266].

circular active region within the groove. The groove is deep enough to cut through the n^+-layer, so that during operation, the guard ring, which catches surface leakage current from the exposed sides of the detector, is isolated from the active area. Parallel grooves are also cut to divide the active area into 8 strips of equal area. The groove size is optimized to facilitate a clean etching process that can be made with a physically robust UIG tool, while minimizing the exposed area of compensated Si. Note that the original GAPS tracker design was based on 4-strip rather than 8-strip detectors, so the earlier prototypes were produced with 4 strips. The 8-strip design was ultimately chosen because of the better energy resolution associated with a smaller capacitance (Section 5.1.4).

The detector surface is etched to prepare for the application of p-side contacts. The n-side contacts and grooves are protected from etching using wax, which is later removed before the Ni and Au contacts are evaporated as for the n^+-side. Following the application of the p-side contact, all contacts are masked with wax again, and the grooves and top-hat sides are etched a final time to remove all contaminants from

the exposed Si. After removal of the wax, the detector is cleaned with methanol, leaving a lightly n-type surface on the exposed i region. The n surface state prevents breakdown under reverse bias.

5.2.4 Lithium Mapping using Copper Staining Techniques

Throughout the development of the test detector and Shimadzu detector fabrication protocols in Sections 5.2.2 and 5.2.3, copper staining techniques were used to directly measure the distribution of Li in the wafer during the various stages of fabrication. Copper staining is a chemical plating procedure, in which Cu preferentially plates onto Si surfaces with the highest concentration of Li [267].

Copper staining was performed in the wet lab facilities of the MIT Microsystems Technology Laboratory. First, a saturated solution of $CuSO_4$ was prepared in 100 mL of deionized water (requiring $40 - 50$ g $CuSO_4$). 1 mL of 50% HF was then added to the solution. The wafer was prepared by slicing a cross-section using a diamond saw followed by sanding of the cross-section surface using 2000 and 2500 grit diamond sandpaper. A total of around 10 minutes of sanding is necessary to remove ridges leftover from the saw, but care is taken to avoid rounding the edges of the slice in the sanding process. The wafer section is briefly rinsed in deionized water before being submerged in the $CuSO_4$ solution for exactly 12 seconds, during which Cu plates onto the sanded Si surface. Immediately after exposure to the solution, a flashlight is shined on the surface of interest for 30 seconds to cure the surface before the wafer is again rinsed in deionized water and allowed to dry. The rate of Cu plating onto Si varies with the Li concentration. The precise timing is necessary to obtain the desired resolution between the detector regions of different Li concentration. By viewing the exposed Si edge using a dim flashlight at a shallow angle, it is possible to visually inspect the distribution of the Li in the wafer cross-section.

Figure 5.9 shows the Cu-stained cross sections of a lithiated test-detector wafer and a finished Shimadzu detector. In both cases, the thin, bright region at the top of the cross-section is the Li-diffused region. In the case of the finished detector, comparison with the groove profile illustrates that this n^+-layer is much shallower

than the groove, allowing successful operation of the detector.

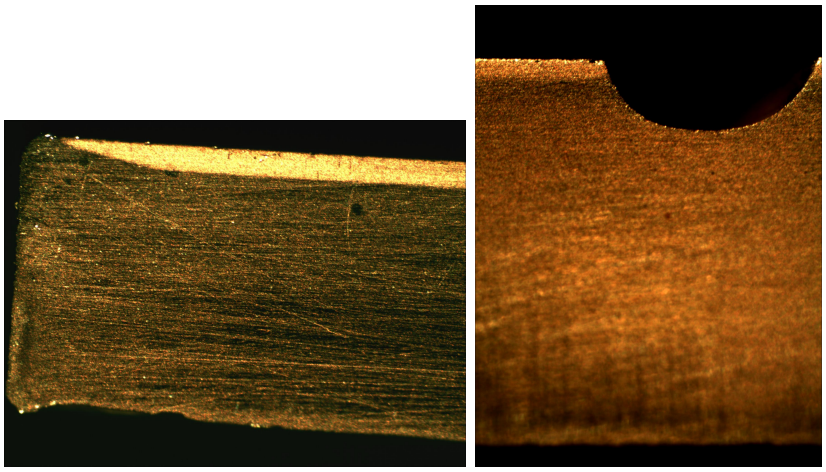

Figure 5.9: Microscope photos of the Cu-stained cross sections of a lithiated test-detector wafer (*left*) and a fully-fabricated Shimadzu detector (*right*).

5.3 Performance of the GAPS Si(Li) Detectors

This section, which is based closely on my 2019 *JINST* publication and subsequent conference presentations [268, 269], details the performance of the flight-model Shimadzu detectors developed in Section 5.2.3. Data are shown for both 4- and 8-strip detectors. The measurements in this section are the basis for the ongoing large-scale calibration of the GAPS flight detector modules.

5.3.1 Detector Handling and Storage

Care in the storage, handling, and preparation of the Si(Li) detectors is necessary to prevent Li diffusion in the n^+ and compensated regions of the detectors and to protect the delicate exposed Si surfaces. This section treats the protocols and consequences associated with detector handling and storage.

The Si(Li) detectors have a large area of exposed silicon in the grooves and top-hat brim (see Figure 5.7). Changes in the silicon surface state can occur due to exposure to humidity or organic contaminants. This can increase conductivity along the surface, increasing surface leakage currents and thus degrading the X-ray energy resolution, as

discussed in Section 5.1.4. In addition, dust or particulate contaminants on the bare silicon can change the electric field configuration along the groove, possibly increasing leakage current and affecting charge collection efficiency or cross talk.

To mitigate damage due to these effects, the detectors are stored in a desiccant box with relative humidity maintained $<10\%$, and the laboratory space is maintained at $<30\%$ relative humidity. The detectors are handled only using clean wafer tweezers or gloves, and electronic components are chosen to be low-outgassing. Prior to testing, the exposed silicon surfaces are prepared by swabbing with ACS-grade methanol in a flowing nitrogen environment to remove any particle or dust contamination and set a lightly n-type surface state. During testing and operation, the detectors are cooled under either vacuum or flowing nitrogen conditions to avoid condensation.

Exposure to light while a detector is biased results in the production of surface leakage currents when the exposed silicon acts as a photodiode. In one test, leakage current was measured while a test detector was exposed to varying levels of light from a light emitting diode (LED). During the testing, the leakage current increased by more than 10 times. After the LED was turned off, the leakage current remained elevated, slowly decreasing with a half-life of a few hours. This demonstrates photo-activation of the detectors. Care has therefore been taken to mitigate access exposure to stray photons during testing and in the design of the GAPS instrument payload. Additionally, the desiccant box is covered in blackout cloth to reduce the overall exposure to light during storage.

Movement of Li ions within the finished detectors threatens the detector performance through a few distinct mechanisms. First, growth of the n^+ layer thickness due to diffusion of ions decreases the active depth of the detector. If the n^+ layer expands deeper than the guard ring groove depth, then there is no high-resistivity material to electrically isolate the readout contact from the grounded guard ring, rendering detector operation impossible. Secondly, the Li ions in the compensated depth are positioned during the drift to exactly compensate impurities in the Si crystal. Diffusion of these Li ions without the guidance of the drift bias can cause the drifted region to become decompensated. During operation, the electric field defects related

to decompensation can lead to 1) incomplete or delayed charge collection or 2) an increased bias required to deplete the drifted region.

The mobility of Li ions in Si grows exponentially with temperature, as quantified in Eq. (5.20). Therefore, for long-term storage, detectors are stored in nitrogen-flushed modules in a commercial freezer at $-25°$C, where the diffusion constant for lithium is 150 times smaller than at room temperature. Additionally, at no point in the detector handling is the temperature raised above 280°C, as even brief exposure to these temperatures can destroy a detector.

5.3.2 Leakage Current Measurements

As shown in Section 5.1.4, the leakage current, with both bulk and surface contributions, is fundamental to the noise characteristics of a detector. Leakage current is highly sensitive by the details of detector fabrication and handling, and variation in performance of different detectors and detector strips is typically attributed to this parameter. Leakage current measurements therefore provide a relatively rapid method to determine the quality of a detector or to diagnose problems with the fabrication and handling.

Measurements of the variation in leakage current with applied reverse bias ("IV curves") were performed at room temperature in an Alessi REL-4500 probe station housed inside a dark box. Current was recorded and a reverse bias was applied using a Keithley 487 Picoammeter controlled using LabView program that stepped up the bias by 10- or 25 V increments, waited 1 s to allow the current to stabilize, and then recorded the current. As shown in Figure 5.10, the bias was applied through the p-side of the detector via a gold-plated chuck, while a signal probe was connected to a single strip of interest. Additional probes connected the guard ring and any inactive strips to a common ground between the signal and the bias.

Room-temperature IV curves provides a useful detector diagnostic in a measurement that is faster and requires fewer specialized pieces of equipment compared to noise measurements at typical operating temperatures. Room temperature leakage current of $\mathcal{O}(1)$ µA corresponds to $\mathcal{O}(1)$ nA at detector operating temperatures, suffi-

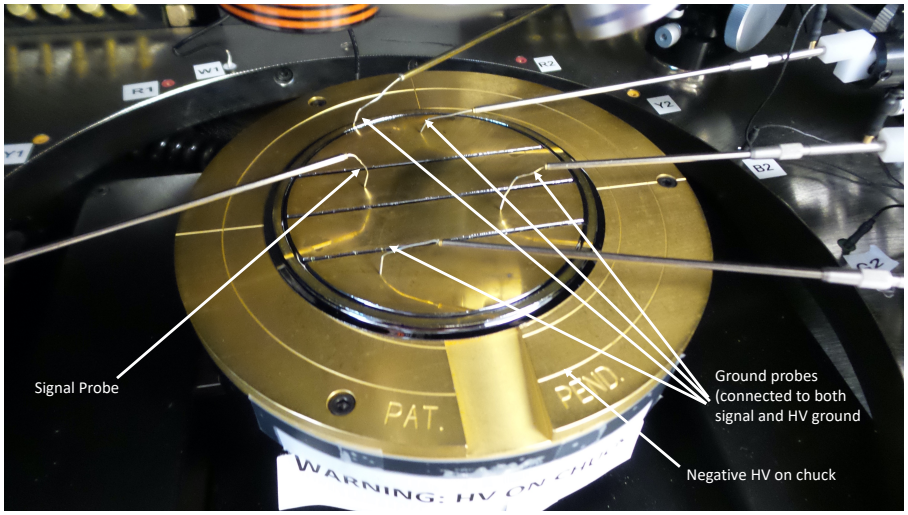

Figure 5.10: A four-strip detector is prepared for room-temperature leakage current measurements in the probe station.

cient for the noise requirements of GAPS. The shape of the IV curve can also diagnose problems with the detector fabrication or preparation.

Direct leakage current measurements at GAPS operating temperatures are performed in a custom aluminum vacuum chamber with pressure maintained below 2 Pa using an oil-free scroll pump. In an alternate setup, the detector-mount apparatus is cooled in a flowing nitrogen atmosphere in an EC13 environmental chamber from SUN Electronics, allowing for automatic, stable temperature control. Either a nitrogen environment or a vacuum environment protects the sensitive detector surfaces from condensation during cooling. Though these detectors must ultimately operate in a low-pressure environment at 37 km altitude, we have demonstrated identical performance in a nitrogen atmosphere and a low-pressure environment.

The grounding configuration and readout are the same as for the room temperature measurements. Mechanically, the detectors are held in aluminum mounts. When mounted, the 5 cm-diameter test detectors rest on an electrically isolated ring that delivers the reverse bias to the p-side of the detector, and they are are secured to their mount via aluminum fasteners that ground the guard ring to the mount. Meanwhile, the 10 cm-diameter Shimadzu detectors are secured to their mount via pressure from an aluminum ring on the p-side, which is electrically isolated from the p-side electrode

and the bias via an insulating ring of FR-4. A simple board, pressure-mounted to the detector strip(s), delivers the current signal to the chamber feed-through. Either detector-mount apparatus is bolted to a nickel-coated copper cold plate that is cooled by flowing cold gaseous nitrogen. Temperature is monitored using a calibrated diode positioned on the detector mount and powered by a custom low-noise power supply. Temperature is controlled by manually adjusting the flow rate of nitrogen through the system and, with constant attention, can be stably maintained within ± 1–2°C for time periods up to $\sim$30 minutes.

Figure 5.11 illustrates the leakage current for a test detector TD0049 measured as a function of bias voltage across a range of temperatures. At a given temperature, the leakage current rises steeply with increasing voltage until a bias of $\sim 10\,\mathrm{V}$ is applied across the detector, after which the current increases only gradually with increasing applied bias, exhibiting the diode behavior characteristic of *pin*-junctions. Following Equations (5.1) - (5.3), the bulk leakage current is expected to double every $\sim 8^{\circ}$C for bias voltages $\lesssim 1000\,\mathrm{V/cm}$, for which the mobility of charge carriers is constant. Deviations from this behavior indicate charge injection from a contact, surface contributions to the leakage current, or other non-bulk properties. The measurement is consistent (within temperature stability considerations) with bulk leakage current considering its exponential increase with temperature.

5.3.3 Capacitance and Setting the Operating Bias

As shown in Section 5.1.4, the per-strip capacitance is an important contributor to the detector's overall noise performance. Unlike the leakage current, the detector capacitance is primarily determined by the detector geometry, and large variations are not expected between strips with the same geometry. Thanks to the inverse relation (see Eq. (5.9)) between the detector capacitance and the depleted (highly resistive) depth, capacitance measurements can probe 1) the dependence of the depleted depth d in the compensated region on the external bias and 2) the total depth of the Li drift at sufficiently high external bias that the entire compensated region is depleted.

Measurement of the dependence of capacitance on the applied reverse bias ("CV

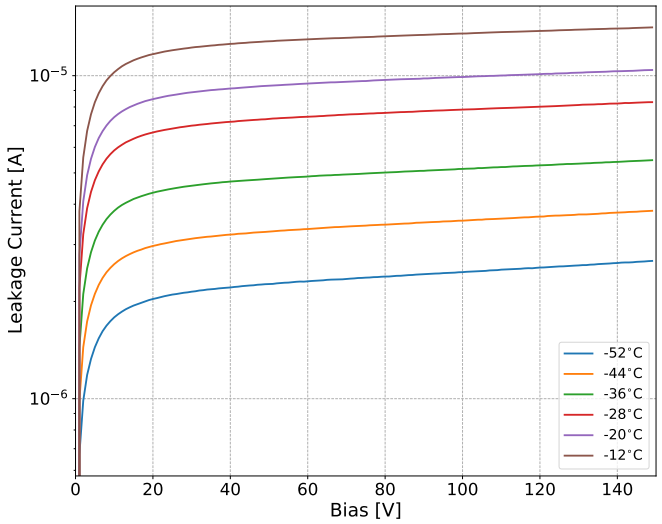

Figure 5.11: Leakage current for a sample test detector is shown as a function of bias voltage in temperature increments of 8°C.

curves") were performed at room temperature ($\sim$ 23°C), as capacitance at $\sim$1000 V/cm varies only 1–2% between room temperature and the typical operating temperature range. Capacitance was measured at MIT in the probe station apparatus from Section 5.3.2, with a similar setup used to ground the guard ring and any strips except the one being measured. A reverse bias was applied manually using the Keithley Keithley 487 Picoammeter as an external voltage source. The capacitance was read out by a Boonton 7200 capacitance meter; after waiting $\sim$ 5 s at each bias voltage to allow the apparatus to stabilize, the capacitance was recorded manually. CV curves for the Shimadzu detectors, including that in Figure 5.12, were made in Japan and were not repeated in-house at MIT. These measurements were made using a HP 4280A meter with bias supplied by an ORTEC 428 module. The grounding configuration was identical to the setup at MIT.

An appropriate operating bias will be high enough to fully deplete the bulk of the detector, while minimizing both power requirements for this balloon-borne experiment and noise from leakage current, which increases with bias. As bias increases, the depletion region grows, increasing the depleted depth until the entire compensated region is depleted and the capacitance approaches its asymptotic value. For an 8-strip

(4-strip[3]) Shimadzu detector with per-strip area $\sim 8\,\mathrm{cm}^2$ ($\sim 14.5\,\mathrm{cm}^2$) and maximum depleted depth of $\sim 2.3\,\mathrm{mm}$, the per-strip capacitance is $\sim 35\,\mathrm{pF}$ ($\sim 72\,\mathrm{pF}$).

Based on the capacitance measurements, the operating bias has been fixed at $-250\,\mathrm{V}$ for the flight-model Shimadzu detectors and $-100\,\mathrm{V}$ for typical test detectors. In both cases, this corresponds to $\sim 1000\,\mathrm{V/cm}$. To validate this choice, the energy resolution at $59.5\,\mathrm{keV}$ was recorded using a Shimadzu detector operating at a range of bias voltages from $-54\,\mathrm{V}$, the lowest operable bias, to $-400\,\mathrm{V}$. Figure 5.12 shows the energy resolution for a typical flight-model detector, along with the capacitance around the selected operating bias of $-250V$. Under these experimental conditions, the energy resolution is near minimum and the detector is fully depleted.

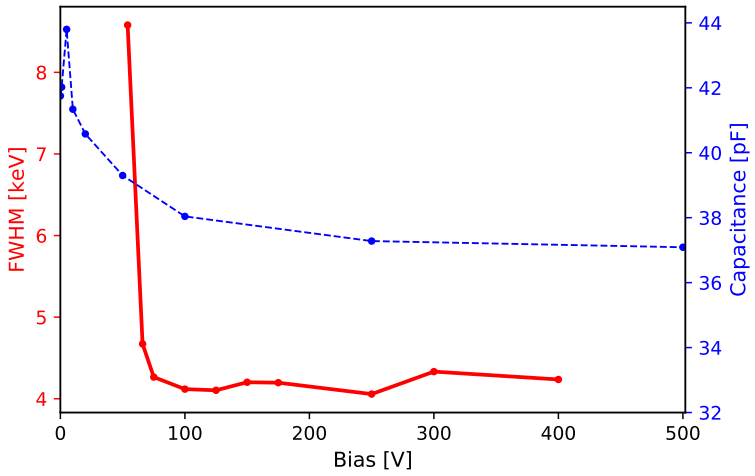

Figure 5.12: Energy resolution (red solid) at $59.5\,\mathrm{keV}$ as a function of applied bias, recorded using one strip of Sh0079 operated at $-35°\mathrm{C}$ and processed with $10.8\,\mu\mathrm{s}$ peaking time, near the minimum of the resolution vs. peaking time curve for this high-capacitance setup. The energy resolution is affected as discussed in section 5.1.4 by the capacitance (blue dashed) which decreases with increasing bias and the leakage current which increases with increasing bias. Based on the capacitance curve, the detector is fully depleted by $-250\,\mathrm{V}$ bias [268].

[3]The 4-strip detector model featured an overall smaller active area than the 8-strip model, so the difference in capacitance is not simply a factor of 2.

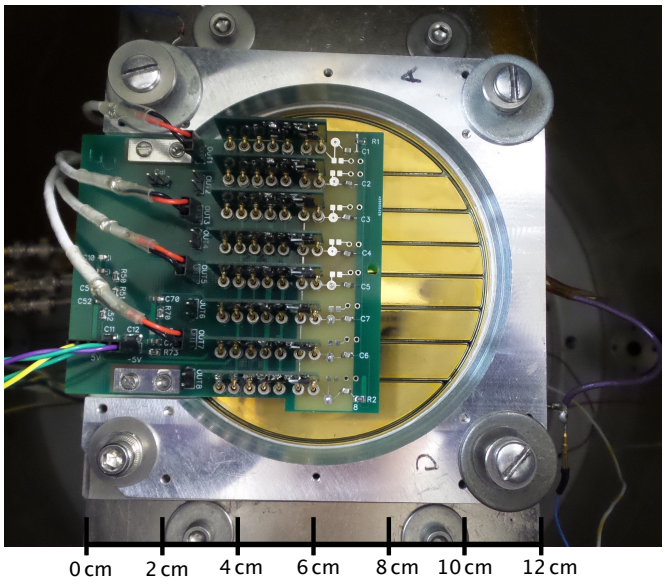

Figure 5.13: An 8-strip detector mounted in the setup for energy resolution measurements [268].

5.3.4 Detector Operation

Spectral measurements are performed in the custom vacuum chamber or the SUN chamber as in Section 5.3.2. As shown in Figure 5.13, the detectors are mounted as in Section 5.3.2, with a preamplifier board pressure-mounted to the detector strips via spring-loaded pins, the guard ring grounded to the detector mount, and bias applied to the p-side. A ~ 5 cm-tall aluminum cover placed over the preamplifier, detector, and mount acts as a Faraday cage, providing protection from electromagnetic interference pickup and any stray light. Two radioactive sources, a 100 µCi ^{241}Am source and a 1 mCi ^{109}Cd source in stainless steel housings, are used. The ^{241}Am source rests on top of the aluminum cover $\sim$5 cm from the surface of the detector. The ^{109}Cd source is positioned $\sim$20 cm from the detector on top of the vacuum chamber, such that the 88.0 keV line is visible but the X-rays around 22 keV are absorbed in the vacuum chamber material.

The power and signal processing scheme is illustrated in Figure 5.14. The detector is biased from the p-side at -250 V by a Tennelec 953 HV supply fitted with an RC circuit that provides a local low impedance signal path and limits the maximum DC current. The negative bias voltage is supplied to the p-side of the detector and

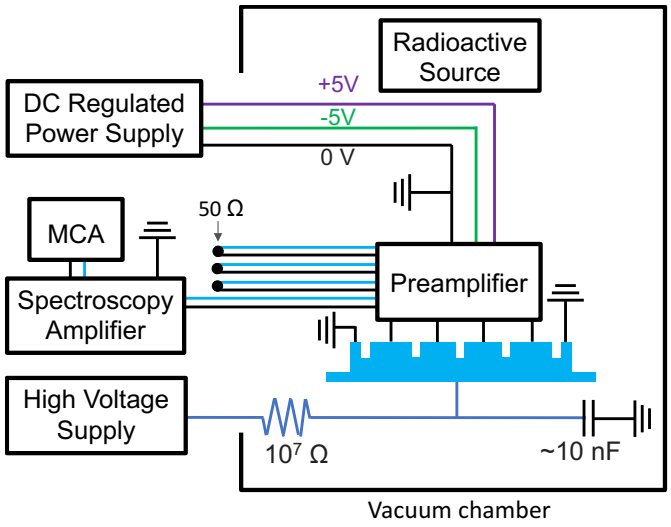

Figure 5.14: The power and readout scheme, shown for a 4-strip detector [268].

isolated from the ground via a partially gold-plated ring of FR4. The signal is read out from the n^+-side by a custom 4- or 8-channel discrete-component charge-sensitive preamplifier board, which is pressure mounted to the strips via spring-loaded pins. Though a custom ASIC will ultimately be used for detector readout in final calibration and on the GAPS flights, a discrete preamplifier based on the architecture described in [270] is used for detector testing while the ASIC is still under development. Each preamplifier channel consists of a 100 MΩ feedback resistor, 0.5 pF feedback capacitor, and a low-noise N-channel JFET with a capacitance of ∼10 pF. The preamplifier is powered by ±5 V from a DC regulated power supply. The operating bias of +5 V DC rail and the 100 MΩ feedback resistor limit the per-strip leakage current to a maximum of 50 nA before saturation. Signal from the preamplifier is processed by a Canberra 2020 Spectroscopy Amplifier with variable peaking time and digitized by an Ortec Ametek Easy MCA module. This system allows for readout of a single preamplifier channel; outputs for the remaining channels end in a 50 Ω termination to prevent noise injection from external sources. A common ground from the NIM crate holding the spectroscopy amplifier is provided via the power supply to the preamplifier, the detector guard ring, and the RC circuit on the high voltage.

For the cosmic-ray muon measurement (Section 5.3.5), a slightly modified setup is used, in the SUN Electronics environmental chamber. The detector is cooled in

a nitrogen atmosphere in an EC13 environmental chamber from SUN Electronics, allowing for automatic, stable temperature control. The spectroscopy amplifier and MCA are replaced by a CAEN N6725 digitizer, using 4 μs peaking time. The use of the digitizer allows multiple channels to be read out simultaneously and enables the use of coincident trigger conditions. All other power and readout components are the same as in Figure 5.14.

5.3.5 Response to Ionizing Particles

The GAPS particle identification scheme relies on the Si(Li) detectors for tracking both incoming cosmic particles and outgoing annihilation products. In the laboratory, the Si(Li) detectors' tracking capability for charged particles is demonstrated using cosmic-ray muons. A relativistic atmospheric muon vertically-incident on these 2.3 mm active-depth Si(Li) detectors has a most probable value (MPV) of ∼750–800 keV energy deposition from $\mathrm{d}E/\mathrm{d}x$ loss, while those arriving at greater angles deposit more energy.

The muon spectrum in Figure 5.15 is produced by operating one strip of the 4-strip detector Sh0035 for ∼40 min at a relatively high threshold of ∼200 keV. To eliminate non-muon background events and bias the sample toward vertical muons, a coincident signal is required with the corresponding strip of a second detector positioned ∼10 cm below Sh0035, illustrated in Figure 5.16. A Landau distribution, which describes fluctuations of energy deposition in the material, is fitted to the data, indicating a most probable value of 757 ± 5 keV and a standard deviation of 94 ± 4 keV. The calibration is performed based on the 59.5 keV peak of ^{241}Am and extrapolated to the higher-energy regime, introducing calibration uncertainty due to possible non-linear effects at higher energies. Still, the data in Figure 5.15 are consistent with the expected distribution for atmospheric muons at sea level and they are within the required 10% energy resolution for energy deposits of $1 - 200$ MeV.

Antiprotons, antideuterons, and antihelium in the GAPS energy range are slower than the cosmic muons and therefore will deposit more energy as they traverse the Si(Li) detectors. The different energy deposition signatures can be used for iden-

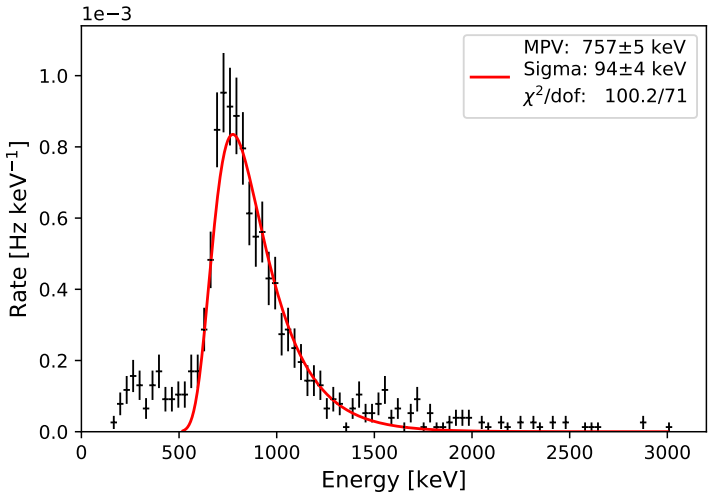

Figure 5.15: A spectrum of cosmic-ray muons overlaid with a Laudau distribution fitted to the data [268].

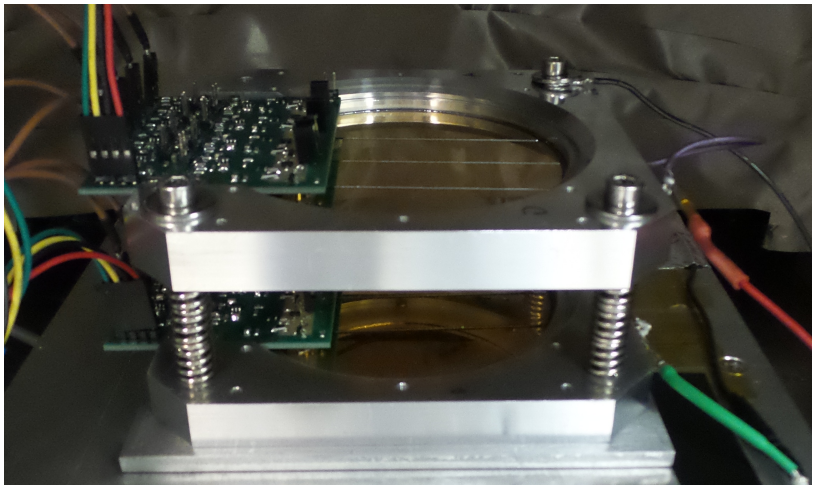

Figure 5.16: The geometry of the Si(Li) detector operation for the cosmic muon spectrum. Photo courtesy of Mengjiao Xiao.

tification of the incident particle. In the GAPS flight, sensitivity to higher energy depositions will be limited by the ASIC, which has been designed to deliver energy deposition information in the range of $1 - 100\,\mathrm{MeV}$ per strip with $\lesssim$10% energy resolution.

Cross talk due to electromagnetic coupling between the strips of a detector could reduce tracking or spectroscopy performance by splitting a signal from a charged particle between multiple strips or changing the amplitude of an observed signal. In a preliminary test using an anti-coincidence trigger between adjacent strips of an 8-strip detector irradiated by a ^{241}Am source, energy resolution, peak location, and count rate at 59.5 keV were consistent with and without the anti-coincidence requirement. However, detailed cross-talk studies of these detectors are ongoing, especially as pertains to the effect of cross-talk on charged particle reconstruction. Note that the per-strip count rate expected from the flux of cosmic ray particles and exotic atom annihilation products through the Si(Li) tracker is low relative to the μs-scale readout time of the Si(Li) detectors. Therefore, cross talk is not anticipated to inhibit track reconstruction for GAPS.

5.3.6 Spectral Measurements

The GAPS particle identification scheme relies on Si(Li) detectors with X-ray energy resolution of $\lesssim 4\,\mathrm{keV}$ (FWHM) in the 20-100 keV range to discriminate between the characteristic de-excitation X-rays of different antiparticle species. Figure 5.17 shows the response of one strip of the 4-strip detector Sh0025 to 59.5 keV γ-rays from ^{241}Am and 88.0 keV γ-rays from ^{109}Cd, demonstrating that the required energy resolution can be achieved at the relatively high temperature of -35°C.

The feature on the low-energy side of each photopeak is due to Compton scattering from the surrounding materials. For a 59.5 (88.0 keV) photon, the minimum scattered energy, corresponding to 180° backscatter, is 48.3 keV (65.5 keV). Each spectral peak is fitted with a function consisting of the sum of a Gaussian distribution and an error function. The error function is constrained to the same position and width as the Gaussian and roughly accounts for the nearly-flat higher-energy portion of

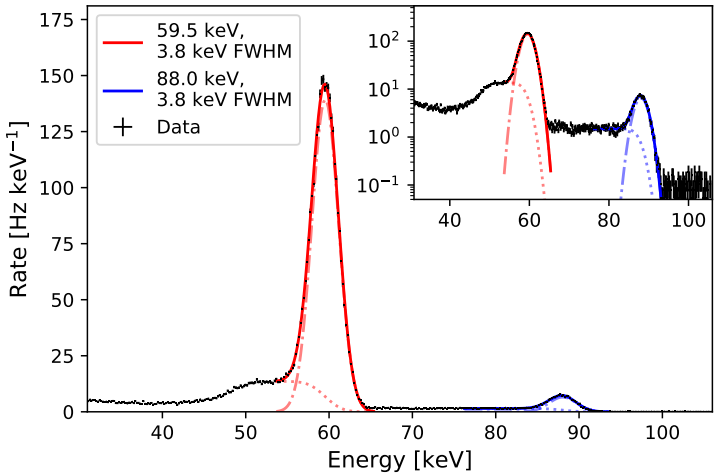

Figure 5.17: Example spectrum of ^{241}Am and ^{109}Cd, recorded with one strip of Sh0025 at -35°C and processed with a 4 µs peaking time. The data show each photopeak together with a low-energy tail of scattered γ-rays. The functional form is of a Gaussian (dash-dotted) plus an error function (dotted), as discussed in the text. The inset shows the same data in semi-log format, to display the 88.0 keV peak more clearly [268].

the Compton scattering feature. The range for each fit is from the midpoint of the Compton scattering region to 6 keV above the photopeak, or one FWHM above the photopeak if FWHM >6 keV. The goodness of the fit is assessed using the reduced χ^2 as a figure of merit. Using the fitted position of the 59.5 keV and the 88.0 keV peaks, we find an offset from the zero energy intercept of < 2 keV.

5.3.7 Noise Modeling

This section treats the comparison of the detector performance with the noise model of Eq. (5.17). Use of the noise model facilitates disentangling the noise due to intrinsic detector effects from that of the pulse shaping and readout electronics, allowing us to predict the performance of a particular detector under different conditions, such as temperature, or with different readout electronics. Indeed, these measurements were performed in 2019, prior to the production of the first functional ASIC, using a custom preamplifier and shaping electronics for readout. Thanks to the well-behaved noise performance that we characterized using the noise model, we were able to predict the performance of these detectors when read out by the final flight electronics.

The following general procedure was used to facilitate a comparison between the noise model and the detector performance. For each detector and for each temperature, spectra of ^{241}Am were recorded using pulse peaking time τ from 0.68 to 32 µs (corresponding to a shaping time of 0.25 to 12 µs indicated on the shaper). The spectral data were fitted to extract the FWHM energy resolution at 59.5 keV, following the procedure in Section 5.3.6. In Eq. (5.17), T was as measured for each data set, g_m was fixed at 18 mS according to a room-temperature measurement, and the constant Γ was set to 1. Any small temperature variations in these parameters were absorbed into the complementary R_s term for the purpose of fitting to our data. C_{det} was measured directly for each electrode, and C_{FET} was approximately 10 pF for each preamplifier. The form factors were calculated as $F_i = 0.367$, $F_\nu = 1.15$, and $F_{\nu f} = 3.287$ for our Sin^4 semi-Gaussian Canberra shaper, following [271]. Eq. (5.17) was then fitted to the measured energy resolution as a function of peaking time by minimizing the reduced χ^2 while varying the fitted leakage current $I_{leak}(T)$, $A_f(T)$, C_{tot}, and R_s.

The measured energy resolution as a function of peaking time is compared for all strips of four 4-strip detectors in Figure 5.18, for two operating temperatures of one 4-strip detector in Figure 5.19, and for two operating temperatures of one 8-strip detector in Figure 5.20. To produce the plots in Figures 5.18 – 5.20, we first fit Eq. (5.17) to the data for each strip at each temperature individually. Then, we combine the fitted values for each strip (Figure 5.18) or each temperature (Figures 5.19 and 5.20) to produce the curves shown. For each strip at a given temperature, we derive the parameters A_f, $C_{int} + C_{stray}$, and R_s from a fit to the measured energy resolution as a function of peaking time. Though I_{leak} can be measured directly, we also fit this variable as a cross-check on the consistency of the fit. Because the first three parameters are degenerate, they cannot be fitted simultaneously, so an iterative approach is used. First, since the $\frac{1}{f}$ component of the noise is constant in peaking time, it is fixed to a typical value of 0.6×10^{-13} V^2, while $C_{stray} + C_{int}$, R_s, and I_{leak} are varied. Second, the value of R_s is fixed at the best value from the first fit, and A_f is instead varied. Finally, C_{tot} is fixed at the best value from the second fit, and

A_f and R_s, along with I_{leak} are varied. In each case, the previous best-fit values are used as the seed values for the next iteration. The χ^2 per degree of freedom is used to assess goodness of fit. We confirm at the end of this fitting procedure that the best-fit leakage current is consistent with the directly measured value.

Figures 5.18 and 5.19 illustrate that the best-fit R_s and C_{tot} at a given temperature are consistent to within a few percent. This is consistent with the expectation of minimal capacitance variation between strips. The measured strip capacitance ($C_{det} \approx 73\,\mathrm{pF}$ for a 4-strip detector) dominates C_{tot} and is typically consistent to within $\sim$1 pF between the equal-area strips. Meanwhile, the preamplifiers and their 10 pF capacitors are built to be identical, leaving $\sim$3 pF stray and inter-electrode capacitance per strip.

The A_f parameter extracted from fits may contain contributions from multiple sources, including the discrete preamplifier and associated electronics, but is nonetheless consistently in the 0.5 to $1.5 \times 10^{-13}\,\mathrm{V}^2$ range. Measurements of the preamplifier alone indicate that a large component of the total observed noise may be due to the readout electronics, which have been optimized for low-power rather than low-noise operation; however, measurements with a lower-noise preamplifier design would be necessary to correctly identify all sources of $\frac{1}{f}$ noise.

Fixing R_s and A_f to the arithmetic mean of the best-fit values from the four strips, the energy resolution as a function of peaking time for each strip can be well described by eq. (5.17) by varying only the value of I_{leak} and C_{tot} for each strip, as shown for several 4-strip detectors in Figure 5.18. Thus, the parallel and series components of noise intrinsic to the detector can be clearly separated from those that depend on the readout, while the A_f component can be attributed to a combination of the detector and the preamplifier.

For those 4-strip detectors in Figure 5.18 with per-strip leakage current $<$10 nA in the appropriate temperature region, the required energy resolution of $\lesssim$4 keV FWHM was achieved. Two of the detectors (Sh0025 and Sh0037) have one strip with elevated leakage current. However, the remaining strips of those detectors reach the required energy resolution, apparently free of deleterious effects due to their high-leakage cur-

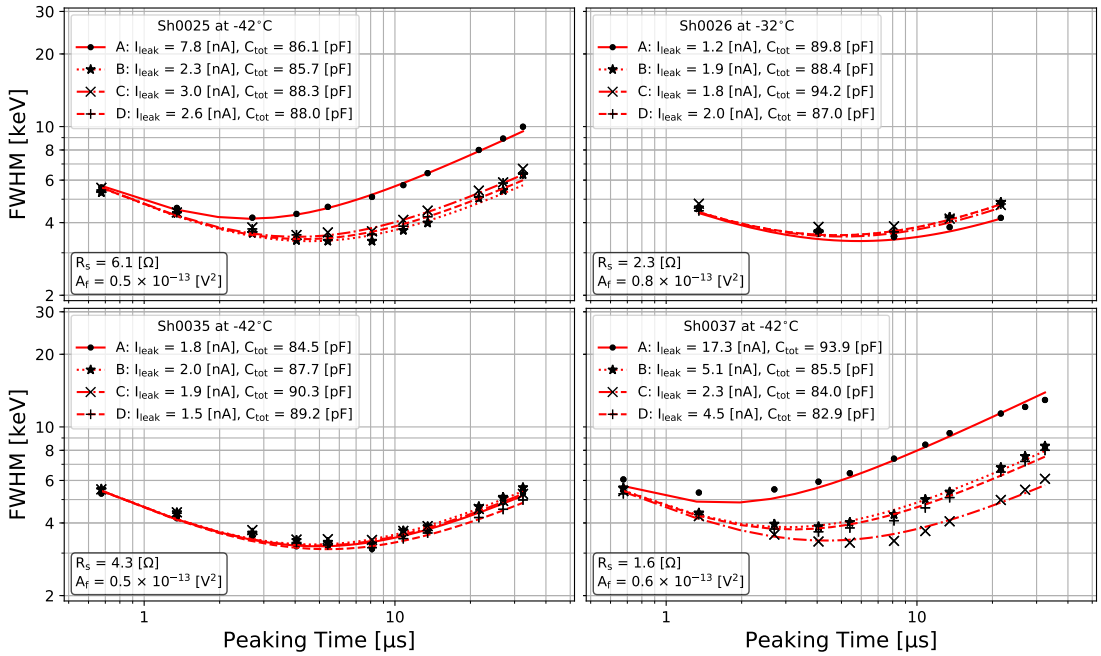

Figure 5.18: Each panel above shows data for a single 4-strip detector, measured within or above the nominal GAPS temperature range of −35 to −45°C. The measured energy resolution (FWHM) at 59.5 keV is plotted as a function of peaking time for each strip A–D (black markers). For each detector, the noise model (red lines, Eq. (5.17)) can describe the data for all four strips, varying only I_{leak} and C_{tot} from strip to strip. R_s and A_f are fixed at their mean values from the fits for individual strips of each detector. The remaining noise model components are constant: $R_{\rm p} = 100\,{\rm M}\Omega$, $g_{\rm m} = 18\,{\rm mS}$, $\Gamma = 1$, $F_{\rm i} = 0.367$, $F_\nu = 1.15$, and $F_{\nu{\rm f}} = 3.287$, as described in the text [268].

rent neighbors.

The energy resolution at different temperatures can be consistently described using this model by varying only the temperature-dependent parameters A_f and I_{leak}, as shown in Figures 5.19 and 5.20. For each strip, the total capacitance C_{tot} and the series resistance R_s, which show a weak dependence on the temperature, are fixed as the mean of the best-fit values at the two temperatures. A_f and I_{leak} are then fit, and T is fixed to the measured temperature. For the 4-strip detector Sh0035, Figure 5.19 demonstrates that the temperature variation of the energy resolution is well described by the noise model, varying only A_f and I_{leak}.

The energy resolution at two temperatures for a flight-geometry 8-strip detector is shown in Figure 5.20. The typical energy resolution for an 8-strip detector is improved

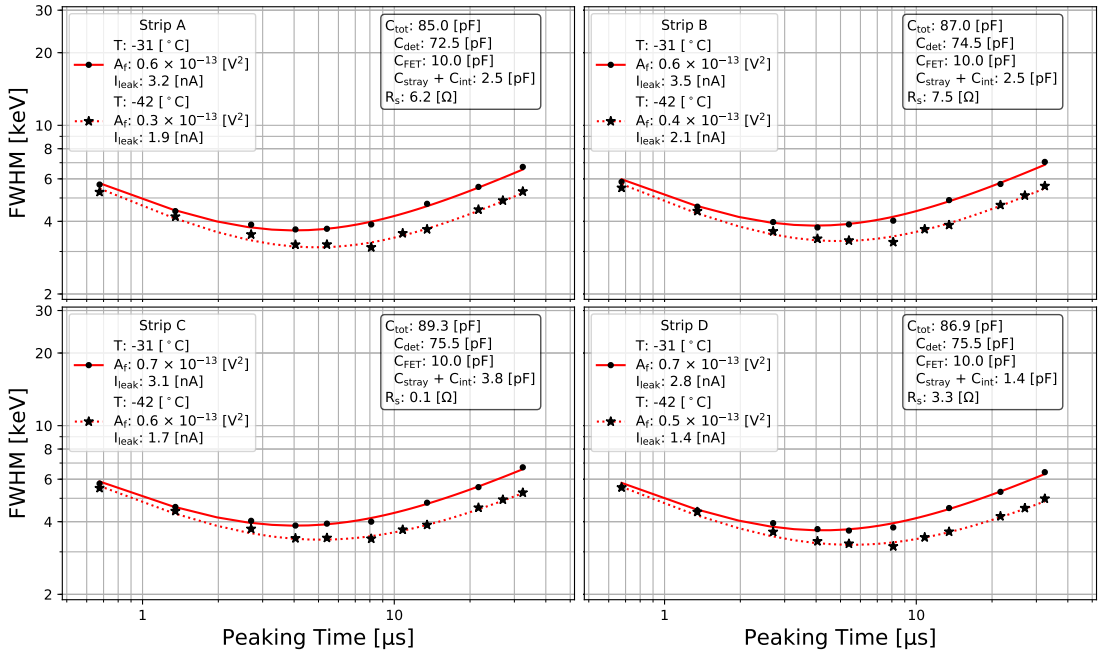

Figure 5.19: Each panel shows data for one strip of the 4-strip detector Sh0035. For each strip, the measured energy resolution (FWHM) is plotted as a function of peaking time at two temperatures (black markers). The noise model (red lines, Eq. (5.17)) can fit the data at both temperatures while changing only the parameters A_f and I_{leak}, which are expected to vary with temperature, in addition to T. The capacitance C_{tot} and series resistance R_s values are determined for each strip, and the remaining noise parameters are fixed as described in Figure 5.18 and the text [268].

relative to that of a 4-strip detector primarily due to the smaller strip capacitance and leakage current. The total capacitance of ∼60 pF per strip (∼36 pF C_{det}, ∼10 pF C_{FET}, and ∼14 pF $C_{stray}+C_{int}$), reflects the reduction in area as compared with 86 pF per strip for the 4-strip detectors (∼73 pF C_{det}, 10 pF C_{FET}, and ∼3 pF $C_{stray}+C_{int}$). The relatively high C_{stray} in the 8-strip detector noise is attributed to the geometry of the larger 8-channel preamplifier board positioned above the detector. While the strip capacitance is consistent between strips of the same size, the leakage current can vary between equal-area strips, though in general I_{leak} is expected to be lower for smaller strip area. All else being equal, the 8-strip design reduces the per-strip noise when compared to the 4-strip design, particularly at lower peaking times where capacitance drives the noise. Even with the noise contribution from the preamplifier or associated electronics, the energy resolution requirement $\lesssim$4 keV FWHM was met for $20 - 100$ keV X-rays.

5.4 Development of the Si(Li) Passivation Protocol

This section treats the development of a passivation protocol to preserve the performance described in Sections 5.2 and 5.3 over the years-long timescale of the GAPS program, following [272]. The large exposed silicon surfaces of the bare silicon detectors require handling in a humidity-controlled lab environment, with careful surface treatment prior to every use, as discussed in Section 5.3.1. The chemical state of a detector surface is sensitive to environmental conditions, and large surface leakage currents, which can render the detectors temporarily or permanently inoperable, arise following exposure to humidity or organic contaminants. Additionally, the detector surfaces are sensitive to particulate matter, including dust and metal flakes from the electrodes, which can be sources of charge injection.

Passivation is meant to maintain stable detector performance by protecting the detectors from particulates and from changes to the surface state during long-term storage between flights as well as during shorter periods of high activity during calibration, integration, shipping, and flight. The challenge is to develop a passivation

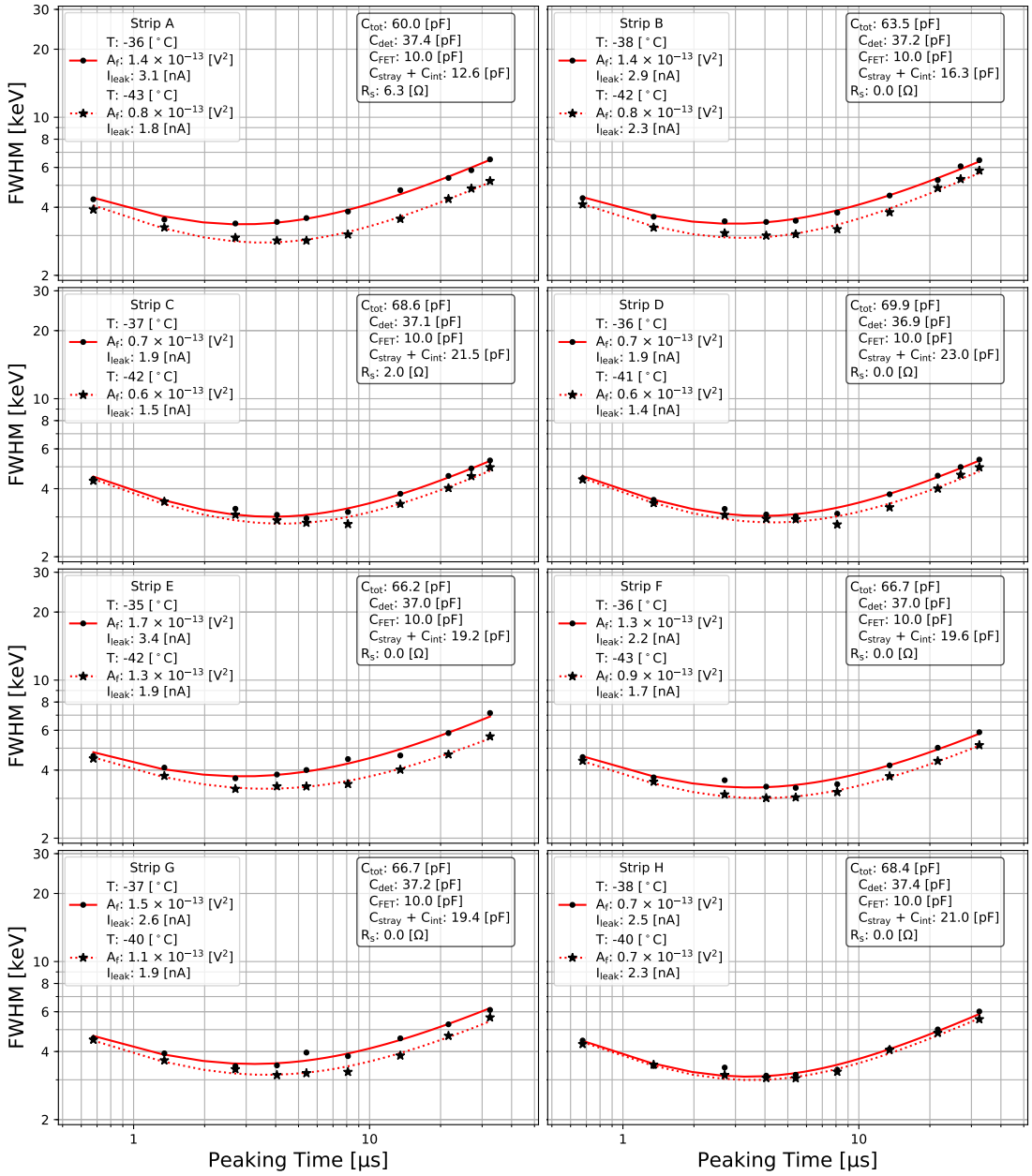

Figure 5.20: Each panel shows data for one strip of the 8-strip detector Sh0077. For each strip, the measured energy resolution (FWHM) at 59.5 keV is plotted as a function of peaking time at two temperatures (black markers). The noise model (red lines, (5.17)) can describe the data at both temperatures while keeping all parameters constant apart from T, A_f, and I_{leak}, which are expected to vary with temperature. The capacitance C_{tot} and series resistance R_s values are determined for each strip independently while the remaining noise parameters are fixed, as described in Figure 5.18 and the text. The as-predicted temperature scaling indicates that based on calibration at only a few temperatures, we will understand detector performance at different temperatures during flight [268].

method that 1) provides protection from humidity, chemical contaminants, and particulate matter over the years-long timescale, 2) is robust to thermal cycling and mechanical shocks such as are expected during calibration and flight (Section 5.4.2), and 3) does not itself degrade the detector performance through its own chemical effects on the silicon surface or through the movement of lithium due to heating during application. As I primarily contributed to the development of the passivation protocol by evaluating the performance of passivated detector samples, I emphasize that aspect of the passivation project here.

Two polymers (Section 5.4.1), polyimide (PI) and Parylene-C, were tested for passivation of the GAPS Si(Li) detectors. These polymers have previously been used for passivation of Si(Li) detectors operated at cryogenic temperatures [273, 274], but they have never been used at the GAPS operating temperatures, where leakage current plays a more important role in the overall noise performance. While thermally-grown SiO_2 is the most common method for passivating silicon detectors, it was not explored for the GAPS application due to the high (>1000°C) temperatures required for its growth. Other materials including SiN, TaN, TiN, SiO, and amorphous silicon (α-Si:H) were also not explored due to high temperatures required for the application, deprecated noise performance above cryogenic temperatures, and/or poor reproducibility of results in previous studies [275, 276, 277, 278, 279].

5.4.1 Passivation Methods

PI passivation is performed by applying a polyimide precursor onto a wafer surface and then curing in a furnace. A polyimide precursor is a mixture of a diamine and a dianhydride in N-Methyl-2-Pyrrolidine (NMP). During curing, the NMP is driven out of the precursor, and the diamine and dianhydride imidize to form a PI. The quality of the PI coating depends heavily on the curing temperature and time as well as on the heating and cooling rate. While curing at temperatures above 250°C is desired to fully drive out the NMP, this is not possible with Si(Li) detectors due to the high mobility of Li ions at high temperatures.

Two polyimide precursors were used: VTEC PI-1388 was selected for its relatively

low cure temperature, while Ube U-Varnish-S was selected because its coefficient of thermal expansion matches that of silicon. A variety of curing temperatures, times, and heating rates were tested. Polyimide was applied either diluted with additional NMP or neat. Additionally, the use of a silane precursor (APS), applied in a 0.1% aqueous solution and cured on a 85° hot plate, was tested to improve adhesion.

By contrast, Parylene-C was deposited in a 5 μm layer using a vapor deposition chamber. Two methods were tested to mask the readout strips and exclude Parylene-C from the electrodes. In shadow masking, a physical barrier was produced by wedging the wafer between two parallel aluminum plates with machined cut-outs around the detector electrodes, which were cut away after deposition. In surface priming, a soap-like solution (Micro-90) was painted onto the electrodes prior to deposition. After deposition, the Parylene-C was peeled off, and then the Micro-90 was removed using a methanol-soaked swab. The use of a silane precursor (A-174) was also tested to improve adhesion, using the same method as for the polyimide.

5.4.2 Mechanical Testing

Any suitable passivation material must reliably adhere to the silicon surfaces without cracking or delaminating, even after mechanical stresses including expansion during temperature cycling. Mechanical testing was performed to 1) test the strength of the passivation adhesion to a silicon surface and 2) examine the quality of the lamination after temperature cycling. Because these initial tests were mechanical only, they were performed on test-grade silicon wafers rather than detectors.

Adhesion test: To test the adhesion strength of the passivation material on a silicon surface, the wafers were first cleaned in a three-step process in ACS-grade acetone, methanol, and DI water. The samples were etched in an HNA (20 mL 49% HF, 35 mL 60% Nitric Acid, 55 mL Glacial Acetic Acid) solution for 10 minutes to produce a smooth, chemically polished surface characteristic of the GAPS Si(Li) detectors [266]. Then, a passivation material was applied to the wafer surface following one of the process variations outlined in Section 5.4.1. Adhesion testing was then performed using an ASTM D3359 cross hatch adhesion test [280]. In this process, an X-shaped

cut was pressed into the polymer, and tape was pressed into the surface on top of the cut. The tape was pulled off at 180° angle, and both the tape and the wafer surface were inspected for the amount of polymer removed. For polyimide, the use of the silane adhesion promotor resulted in successful adhesion, while samples without silane failed regardless of the other variables, so silane was used in all subsequent tests. For Parylene-C, all samples, with and without silane, passed the adhesion test, so silane was not used in subsequent preparations.

Thermal test: To test the robustness of each polymer's adhesion to the silicon surface following thermal cycling, an ultrasonic impact grinder was used to cut 1 mm grooves into the test wafers, to most closely resemble the Si(Li) detector geometry. The wafers were then prepared with the three-step cleaning process followed by etching as for the adhesion test, and the polymer was applied in the grooves following the protocol permutations outlined in Section 5.4.1. Samples were cycled between 23°C and −50°C at a rate of 5°C/min using a custom apparatus of dry ice and EPS foam to mimic the rate of cooling expected during testing and in flight. Each sample was cycled a total of 12 times, with visual inspection and inspection under a microscope following each thermal cycle. All Parylene-C samples passed the thermal cycling tests, showing no signs of de-lamination. PI samples cured at 120°C for 25 min delaminated and cracked through successive thermal cycles, so a 180°C cure temperature was used in subsequent tests. A slow (5°C/min) ramp up to the curing temperature also produced better results, by promoting better solvent removal and preventing thermal shock during curing [281]. Furthermore, PI applied neat tended to form beads during curing, leaving exposed silicon, so only PI diluted with NMP was used in subsequent tests. In the end, either VTEC or Ube polyimide applied diluted with NMP and cured for 10 min at 180°C following a slow temperature ramp up produced reliable results that passed the thermal test.

5.4.3 Noise Testing

This section describes tests used to evaluate any degradation in detector performance due to the application of a polymer for passivation. Test detectors were used for

initial testing, and Shimadzu detectors were used for subsequent verification of the results. To prepare detector passivation samples, a methanol soaked swab was used in a flowing nitrogen environment to gently clean the exposed silicon surfaces, and then the detectors were passivated using Ube PI, VTEC PI, or Parylene-C following the protocols developed based on the adhesion test in Section 5.4.2. The detectors' noise performance was evaluated before and after application of the polymer, using the direct leakage current measurements and the energy resolution measurements detailed in Section 5.3.

Parylene-C was eliminated based on the high room-temperature leakage current through the guard ring, as measured on a test detector after application of the polymer.

After PI was applied to a test detector using the 180°C cure process, the leakage current increased by an order of magnitude both at room temperature and at −36°C and −48°C. A second, 25 min cure at 180°C returned the leakage current to the original level at all temperatures, indicating that an insufficient cure cycle was responsible for the original degradation. Subsequent samples were cured at 210°C for 60 min. Meanwhile, to isolate the effects of the silane precursor on noise performance, a Shimadzu detector was treated with silane only, following the protocol of curing on an 85°C hot plate for 30 min. While the silane application did not impact the leakage current, noise modeling revealed degraded energy resolution due to increased $1/f$ noise. A subsequent heating for 20 min at 110°C returned the noise performance to pre-passivation levels, and which indicated that the 85°C cure was insufficient to dry the APS solution. . Based on these results, previous silane and polyimide curing protocols were found to be insufficient, resulting in degraded noise performance in the passivated detectors, likely due to the presence of residual solvents. The curing temperature was increased for both the silane (to 110°C) and the polyimide (to 210°C). The higher temperatures did not negatively impact the energy resolution at the nominal −250 V operating bias. However, the minimum bias required to operate the detector increased after passivation, to ~ -150 V from ~ -80 V, indicating that Li in the n^+ layer had diffused closer to base of the grooves.

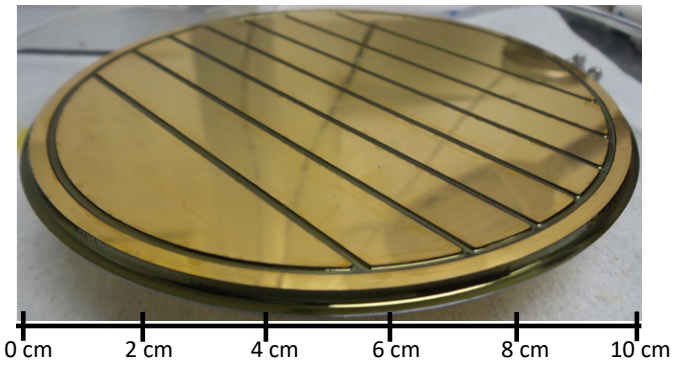

Figure 5.21: A Si(Li) detector passivated via the final passivation protocol [272].

Figure 5.21 illustrates the uniform coverage of polyimide in a detector passivated with the final passivation protocol. The protocol is summarized in the following steps:

- Mix 0.1% (v/v) silane solution in water for 1 hour
- Apply silane solution to detector grooves and top-hat using pipette
- Bake detector 20 minutes in open glass petri dish on a hot plate at 110°C
- While the detector cools, mix 1:1 dilution of PI precursor and NMP with a teflon applicator
- De-gas the PI precursor solution in a rough vacuum for 10 minutes to remove any bubbles
- Apply PI precursor solution to detector grooves and top hat using pipette
- Place detector in room-temperature oven and cure with 210°C set point and 5°C/min heating rate
- After 1 hour at 210°C set point, prop oven door to cool gradually
- When oven temperature reaches 70°C (∼40 minutes) remove detector from oven and place in a dry box

To test repeatability, the optimized passivation procedure was applied to 12 eight-strip Shimadzu detectors. After passivation, spectral measurements were performed

on at least four strips of each detector, and the noise model was used to evaluate the result. Each strip had $\lesssim 4\,\mathrm{keV}$ energy resolution at the best peaking time and was determined using the noise model to have A_f less than the $2.5 \times 10^{13}\,\mathrm{V}^2$ threshold for well-behaved detector performance.

5.4.4 Protection From Humidity and Contaminants

Having developed a passivation protocol that adhered to silicon surfaces even after thermal cycling and that did not degrade the energy resolution of the passivated detectors, the final step was to ensure that the PI coating would function to protect the silicon surfaces over the timescale of the GAPS program of multiple calibration and integration stages and three LDB flights. In accelerated lifetime testing, the detector was exposed to extreme conditions over a shorter time period to approximate the effects of exposure to more moderate conditions over an extended timescale. A longer-term monitoring project is also ongoing.

Accelerated Humidity Exposure: Accelerated humidity exposure was performed by exposing a detector to elevated temperature T and relative humidity (RH; h in Eq. (5.22)). The acceleration factor

$$a = \frac{hP_w^v(T)}{h_0 P_w^v(T_0)} \exp\left(-\frac{E_p}{R}\left[\frac{1}{T} - \frac{1}{T_0}\right]\right) \tag{5.22}$$

compares the relative rate of water molecules hitting the detector surface under the test conditions as compared to the expected temperature T_0 and RH h_0 in normal storage and operating conditions [282]. In Eq. (5.22), $P_w^v(T)$ is the water saturation vapor pressure, $E_p \approx 11\,\mathrm{kJ/mol}$ [283] is the activation energy for water diffusing into the polymer film, and R is the gas constant.

Accelerated humidity testing was performed on two passivated test detectors and one unpassivated control. Each detector sample was held in an airtight container with a dish of water and heated to 60°C for 3 hours, during which time the RH increased to 80%. Temperature and humidity were logged once per minute using a logging hygrometer. Using Eq. (5.22), this is equivalent to $\sim$ 2 days at 50% RH and 23°C

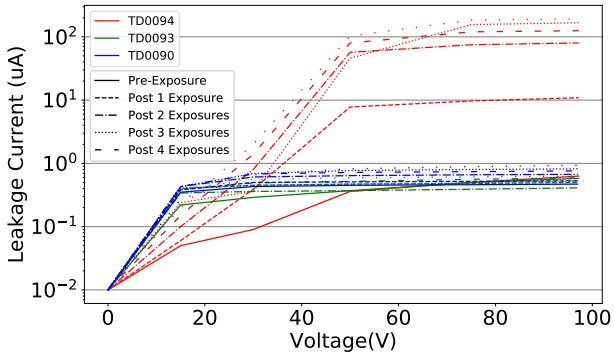

Figure 5.22: Room temperature IV curves were measured for two passivated test detectors (TD0090 and TD0093) and one unpassivated control (TD0094) before accelerated humidity exposure and after each of four 3-hour exposures [272].

or $\sim$ 4 days at typical lab conditions (30% RH and 23°C). This test was repeated until achieving a total exposure equivalent to 14 days at 50% RH. As illustrated in Figure 5.22, the room-temperature leakage current of the passivated test detectors remained low after consistent exposures, while that of the control increased by an order of magnitude after one exposure and by two orders of magnitude after several cycles of testing.

Accelerated Organics Exposure: Accelerated organics testing was performed to specifically test for protection against any adverse effects of outgassing from the materials present near the Si(Li) detectors when mounted in the detector modules (Section 4.2.1), including an FR4 circuit board, G10, fluorosilicone, and vacuum grease. While the modules are purged with N_2 to mitigate outgassing, the N_2 purge is not feasible 100% of the time. Assuming diffusion as the dominant source of outgassing, the acceleration factor is given by:

$$a = \exp\left(\frac{2E_a}{R}\left[\frac{1}{T_0} - \frac{1}{T}\right]\right). \tag{5.23}$$

In Eq. (5.23), R is the gas constant, and T and T_0 are the test temperature and the temperature of typical exposure, respectively, and E_a is the activation energy. E_a was assumed to be a typical value of 10 kJ/mol due to for each material, as direct measurements for each material were unavailable.

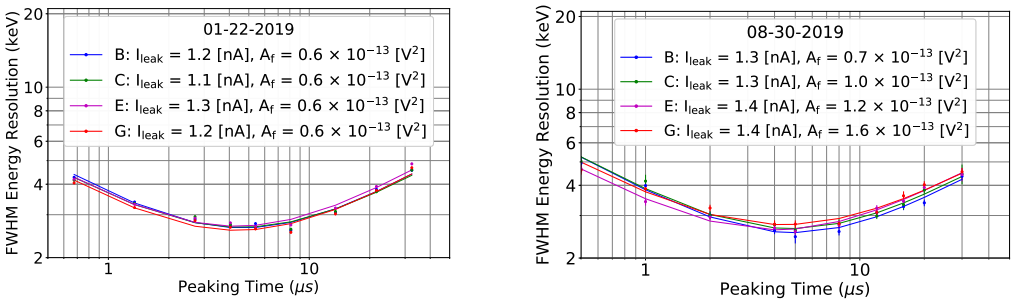

Figure 5.23: Energy resolution (FWHM) at −35°C is displayed as a function of peaking time for four strips (B, C, E, and G) of passivated Shimadzu detector Sh0079 immediately after passivation (left) and after the equivalent of >6 months exposure to organics. No significant degradation or change in the noise performance was observed [272].

Accelerated organics exposure was performed on two passivated 8-strip Shimadzu detectors. Each detector was placed in a chamber next to a hot plate on which an organics sample was heated to accelerate outgassing. In each of several exposures, the organic material was heated to 70°C for 6 hours, equivalent to ∼ 30 days of exposure at room temperature according to Eq. (5.23). The leakage current at room temperature was monitored after each exposure, and no change was detected. After an equivalent exposure of > 6 months, the energy resolution and noise performance were measured. No significant change was found relative to the noise performance immediately after passivation, as illustrated in Figure 5.23.

Long-term Monitoring: A long-term monitoring program to evaluate the performance of passivated detectors over time is ongoing. The energy resolution of several GAPS flight detectors was measured over the course of a year, and the detectors were stored in a freezer in a vacuum-sealed bag with desiccant when not undergoing testing. Figure 5.24 illustrates that the detector energy resolution performance was consistent within uncertainties over the course of the year.

5.4.5 Summary

In this section, a protocol to passivate the Si(Li) detectors using PI was developed that provides mechanical robustness even after repeated thermal cycling while main-

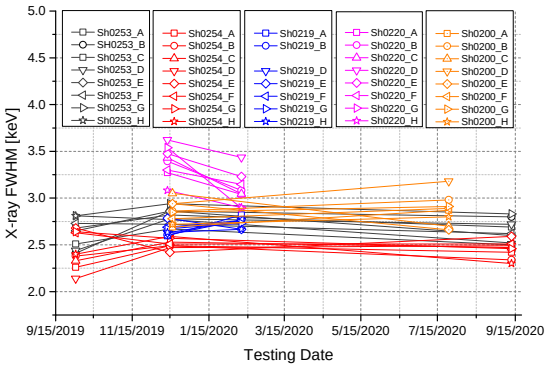

Figure 5.24: Energy resolution was measured for five 8-strip Shimadzu detectors at points during the year from September 2019 to September 2020. The graph shows the energy resolution at the optimal peaking time, as a function of measurement time, for each strip [272].

taining the unpassivated noise performance of the Si(Li) detectors. The PI passivation was also demonstrated to protect the detectors from degradation in their noise performance after exposure to the equivalent of the humidity and organics reasonably expected during the GAPS program. Long-term monitoring of the performance of the passivated detectors is also ongoing. Previous efforts to passivate Si(Li) detectors demonstrated successful passivation using polyimide and parylene-C for detectors operated at cryogenic temperatures, where the noise is more easily controlled. This is the first successful passivation protocol developed for high-performance Si(Li) detectors operated above cryogenic temperatures.

Chapter 6

Sensitivity of the GAPS Experiment to Cosmic-ray Antiprotons

Cosmic antinuclei present an excellent channel for detection of new physics due to their low astrophysical abundance. Antiprotons constitute $< 0.01\%$ of the cosmic particle flux at the top of Earth's atmosphere (TOA), such that precision spectral measurements are sensitive to new cosmic particle sources and to the details of Galactic propagation. Low-energy cosmic antiprotons in particular are sensitive to models of light dark matter (DM) and primordial black holes (PBHs), as well as Galactic propagation.

Since the first detections of cosmic antiprotons in the late 1970s [284, 285], various experiments have measured the antiproton spectrum at TOA. Recent measurements by AMS-02 [84, 286], BESS [287, 288], and PAMELA [289, 290] have provided information on the antiproton flux in the kinetic energy range of $0.17 - 450\,\mathrm{GeV}/n$. The potential of GAPS to provide unprecedented to antiprotons in a lower-energy range than any previous measurement has previously been established using preliminary simulation and analysis tools[291]. This work uses a detailed detector simulation with full event reconstruction to assess the sensitivity of the GAPS instrument to cosmic antiprotons in its first flight and through its full program of three or more LDB flights. The antiproton measurement will be the first GAPS antiparticle analysis, demonstrating for the first time the exotic atom method of antinucleus identification

in the GAPS instrument and validating its use for the rare event searches. The analysis presented here follows my work in [292, 293]. This is the first analysis to use a realistic detector simulation with event reconstruction to assess the sensitivity of the GAPS instrument to cosmic antiprotons.

Detection of antiprotons with GAPS differs from the GAPS rare-event searches in that discrimination between antinucleus species is not required. The backgrounds are positive nuclei, which do not form exotic atoms. In the GAPS energy range they typically stop in the tracker without producing secondary tracks, as distinct from antinuclei. However, with increasing β, the cross section for hard interactions with target nuclei increases relative to the cross section for ionization losses. For $\beta \gtrsim 0.4$, hard interactions of both primary positive nuclei and antinuclei are increasingly common. Because protons and heavier positive nuclei outnumber antiprotons by a factor of $>10^6$ in this energy range, even rare hard interactions of primary positive nuclei, whose interaction products can mimic the antinucleus event signature, present an important background to the antiproton measurement. Positive nuclei arriving with $\beta > 0.7$, outside of the GAPS energy range, also present a key background if they either 1) are wrongly reconstructed with β in the GAPS range before undergoing hard interactions or 2) interact in the TOF to produce a slow antiproton which is reconstructed.

Antinucleus identification amidst the cosmic-ray particle background, which forms the basis of the antiproton measurement, also critically paves the way for rare event searches amongst the antinucleus events. While X-rays are not treated in this study and are not required for nucleus-antinucleus discrimination, they will enhance signal identification power for the antideuteron and antihelium-3 nuclei searches. An antiproton analysis requiring identification of antiprotonic X-rays is deferred to a future publication; such an analysis will validate the X-ray signature for the rare event searches.

This chapter details the simulations and analysis technique used to demonstrate the GAPS sensitivity to low-energy cosmic antiprotons. The science probed by a precision low-energy cosmic antiproton measurement, including DM annihilation, pri-

mordial black holes (PBH) and Galactic propagation, is in Section 6.1. Section 6.2 details the models used to calculate the expected particle fluxes at float altitude (37 km; hereafter the top of the instrument, TOI) and the top of the atmosphere (TOA), including details of the atmospheric simulations. The particle fluxes define the necessary background rejection levels. Section 6.3 describes the simulation of the GAPS instrument, including the acceptance calculation and the event reconstruction. Section 6.4 treats the multiple stages of quality cuts and particle identification used to produce a clean sample of antiprotons, which is translated into a predicted cosmic antiproton spectrum in Section 7.4. Finally, Section 6.6 discusses the outlook for this measurement.

6.1 Low-energy Cosmic Antiproton Science

6.1.1 Indirect Dark Matter Detection

Precision antiproton measurements [84] have excluded the thermal annihilation cross section for annihilation of weakly interacting massive particles (WIMPs) with mass $M_{DM} < 40\,\mathrm{GeV}$ and $150 < M_{DM} < 500\,\mathrm{GeV}$ into purely $b\bar{b}$ final states [108, 112]. For $M_{DM} > 200\,\mathrm{GeV}$, antiprotons provide even more stringent limits than dwarf spheroidal galaxies [124]. As illustrated by the robust DM limits derived from the precision antiproton spectrum at higher energies, a precision low-energy ($<0.25\,\mathrm{GeV}/n$) cosmic antiproton spectrum would open sensitivity to possible new physics. In particular, several hidden sector DM models naturally predict large cosmic particle signals at low energies [294].

As was introduced in Section 2.3.3, discussion is also ongoing in the community related to a possible excess measured by AMS-02 around $10 - 20\,\mathrm{GeV}/n$, which has been interpreted as a signal of annihilating DM with M_{DM} in the range of $40-130\,\mathrm{GeV}$ [108, 109, 110, 111, 113, 112]. However, the significance of this detection depends on the treatment of systematic errors and on their correlations [110, 111, 113, 114, 115, 116, 117].

Beyond direct constraints on low-mass dark matter annihilation or decay in the Galaxy, tuning of Galactic propagation models to a low-energy antiproton spectrum (Section 6.1.3) can reduce the systematic uncertainty associated with the possible $10 - 20\,\mathrm{GeV}$ excess. Additionally, a precision measurement of the falling edge of this excess could improve the DM interpretation of this feature.

6.1.2 Primordial Black Holes

Hawking radiation [44, 42] from evaporation of PBHs that may have formed from density fluctuations in the early Universe would be a novel source of cosmic particles and antiparticles in equal abundance. As detailed in Chapter 2, the lifetime for PBHs formed with mass $M_\star \sim 5 \times 10^{14}\,\mathrm{g}$ is approximately the age of the Universe; any such PBHs would be evaporating in the present day. Evaporating PBH with $M < 10^{14}\,\mathrm{g}$ emit light quarks, which hadronize, and would contribute an antiproton flux broadly peaked at $\sim 0.5\,\mathrm{GeV}$ at TOA [46, 45]. If they exist, evaporation of a local population of such PBH could appear as an observable excess of antiprotons below $1\,\mathrm{GeV}$ [47] and thus in the range to be probed by a GAPS measurement. Because this source falls off less steeply at low energies than the expected secondary astrophysical flux of sub-GeV antiprotons, a PBH excess could appear below $0.25\,\mathrm{GeV}/n$ despite the lack of detection at higher energies by the BESS, PAMELA, and AMS-02 programs. PBH in this mass range do not contribute significantly to the DM abundance, since so much of their mass would have evaporated since recombination [295].

6.1.3 Galactic Propagation

As discussed in Chapter 3, interpretation of cosmic particle flux measurements relies on a precisely tuned model of particle transport in the Galaxy and in the heliosphere, with its attendant uncertainties due to both tuning of propagation parameters and knowledge of interaction cross sections. As a pertinent illustration, background flux predictions present a systematic uncertainty in interpretation of the reported AMS-02 antiproton excess [84], where the possible excess is only on the level of 10% of the

total flux. Low-energy antiprotons are sensitive to the Galactic and solar conditions affecting cosmic particle transport because 1) cosmic antiprotons arise principally from spallation of cosmic-ray nuclei on the interstellar medium and 2) low-energy particles are strongly deflected by magnetic fields [218]. A high-statistics low-energy antiproton spectrum will force a comparison with Galactic and solar propagation models that have been tuned to measurements at higher energies.

6.2 Simulation of Particle Fluxes

Particle fluxes at float altitude (top of instrument; TOI) are calculated by modulating the local interstellar spectra with solar, geomagnetic, and atmospheric effects. Fluxes for cosmic antiprotons, as well as isotopes of hydrogen, helium, and heavier positive nuclei in the local interstellar region are simulated using `Galprop` [227, 218], with propagation tuned to match *PAMELA* and *Voyager I* data as in [145]. These local interstellar spectra are modulated according to the solar activity anticipated for the Austral summer of $2022 - 23$, following the model in [146, 147] to produce the flux at TOA.

A model of particle energy loss and absorption in the atmosphere is required to predict fluxes for all particle species at TOI and to transform any GAPS measurement into a TOA measurement. Atmospheric effects are calculated assuming a 37 km float altitude using the `PLANETOCOSMICS`[1] [296, 297] simulation package updated to run with `Geant4`[2] v10.06 [298, 299, 300]. Assuming a realistic LDB flight trajectory uniformly distributed from $-78°$ to $-85°$ latitude, geomagnetic modulation allows $60 - 80\%$ survival in the GAPS energy range, where survival increases with particle rigidity. The simulations relating particle fluxes at TOI to those at TOA were provided by the GAPS simulation group.

The atmosphere introduces an angular dependence in the fluxes at float altitude, as the amount of atmosphere traversed varies with the zenith angle θ, defined such

[1] http://cosray.unibe.ch/~laurent/planetocosmics/
[2] https://geant4.web.cern.ch/

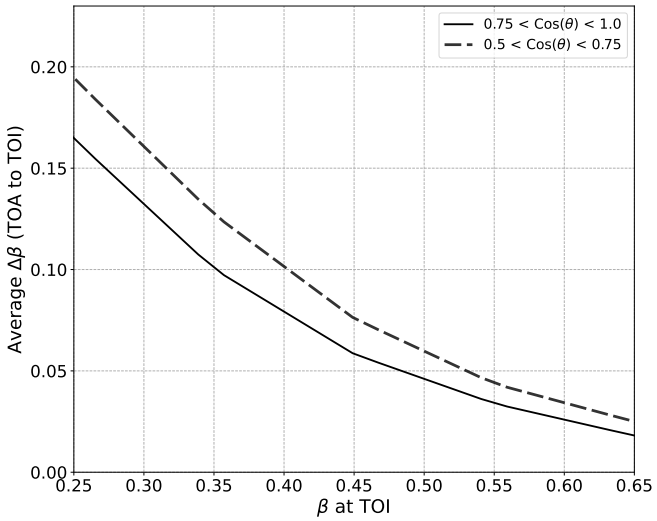

Figure 6.1: The average velocity loss for antiprotons from the top of the atmosphere (TOA) to the top of instrument (TOI) is shown as a function of β at TOI. The decrease depends on the zenith angle θ, defined such that $\cos\theta = 1$ indicates a vertical trajectory, and is presented here in two bins relevant for the cosmic antiproton analysis: $0.75 < \cos\theta < 1.0$ (solid) and $0.5 < \cos\theta < 0.75$ (dash). The sensitive range of $0.25 \lesssim \beta \lesssim 0.65$ at TOI corresponds to $0.41 \lesssim \beta \lesssim 0.68$ at TOA.

that $\cos\theta = 1$ indicates a vertically downward trajectory. As shown in Figure 6.1, the degree of velocity attenuation due to ionization and excitation losses in the atmosphere depends on β as well as θ. Likewise, Figure 6.2 demonstrates that cosmic particle fluxes also decrease due to absorption in the atmosphere and geomagnetic modulation, such that any particle at TOA has a β- and θ-dependent probability of surviving to TOI. Antiprotons with $\beta \lesssim 0.4$ at TOA are strongly absorbed and are unlikely to reach TOI.

Inelastic collisions of energetic particles in the atmosphere lead to the production of secondary "atmospheric" particle fluxes at TOI. Thus, the total (cosmic and atmospheric) particle fluxes observed by GAPS depend on the full cosmic-ray energy spectrum at TOA, and the atmospheric component varies with the depth of the atmosphere and thus with θ. For antiprotons in particular, most of the cosmic flux is produced in collisions of cosmic-ray protons and helium nuclei with the interstellar medium. Because the grammage traversed by particles from the top of the atmosphere to float altitude is comparable to the grammage traversed by a typical particle

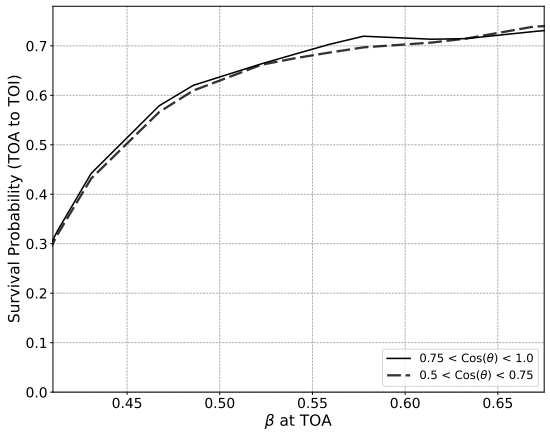

Figure 6.2: The survival probability for antiprotons at TOA to reach TOI without being absorbed is given as a function of β at TOA and presented in the same angular bins as Figure 6.1. Antiprotons with $\beta \lesssim 0.4$ at TOA are strongly absorbed and are unlikely to reach TOI.

in its journey through the Galaxy, the flux of atmospheric antiprotons is comparable to that of cosmic antiprotons at float altitude. Particles arriving at wider angles have traversed more atmosphere, with correspondingly increased velocity attenuation and opportunity for production of atmospheric antiprotons.

Cosmic antiprotons dominate the total flux for $\cos\theta > 0.5$, accounting for >70% of the total flux at the peak of the antiproton acceptance ($\beta \sim 0.4$). In contrast, for $\cos\theta < 0.5$, atmospheric antiprotons dominate the total flux, inherently limiting the possible precision of a cosmic antiproton spectrum. Thus, only antiprotons arriving with $\cos\theta > 0.5$ are treated in this analysis. Antiprotons with $\cos\theta < 0.5$ will be used to tune the atmospheric model, necessary to control systematic errors for all GAPS measurements.

Positive nuclei are the reducible backgrounds for the antiproton measurement, while atmospherically produced antiprotons form an irreducible background. Protons and ^{4}He nuclei are the most abundant background species, with the proton-to-antiproton flux ratio exceeding 10^6 in the lower-β portion of the GAPS energy range, as illustrated in Figure 6.3. The flux of background particles relative to antiprotons drives the background rejection power required in the analysis. Meanwhile, atmospheric antiprotons present an irreducible background for the cosmic antiproton

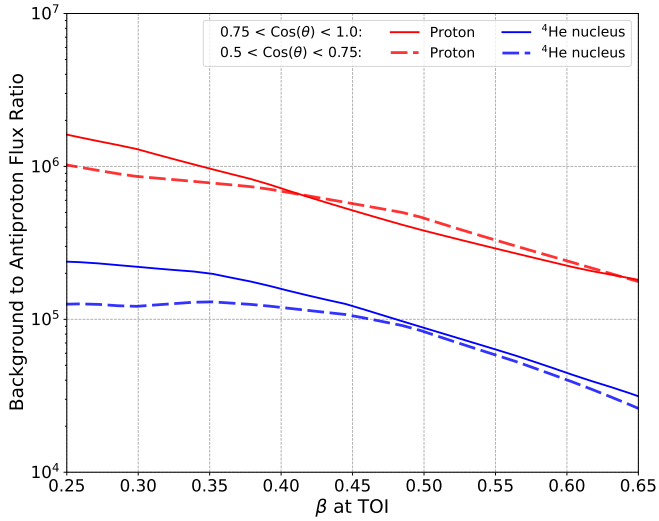

Figure 6.3: The ratios of the proton (red) and ^{4}He nucleus (blue) background fluxes to the total (cosmic and atmospheric) antiproton flux are shown as a function of β at TOI and presented in the same angular bins as Figure 6.1.

measurement. As shown in Figure 6.4, cosmic antiprotons dominate the total flux for $\cos\theta > 0.5$, accounting for >70% of the total flux at the peak of the antiproton acceptance ($\beta \sim 0.4$). In contrast, for $\cos\theta < 0.5$, atmospheric antiprotons dominate the total flux, inherently limiting the possible precision of a cosmic antiproton spectrum. Thus, only antiprotons arriving with $\cos\theta > 0.5$ are treated in this analysis. Antiprotons with $\cos\theta < 0.5$ will be used to tune the atmospheric model, necessary to control systematic errors for all GAPS measurements.

6.3 Simulation of the GAPS Instrument

This analysis makes use of a detector simulation based on the `Geant4` framework to model interactions of cosmic-ray particles with the GAPS instrument. The GAPS simulation includes a detailed implementation of the Si(Li) detectors and their associated passive readout and support material in the tracker, and of the scintillator paddles and associated passive material in the TOF. The simulation used in this analysis assumes 1000 Si(Li) detectors in the tracker, as in the first GAPS flight. It reflects the final flight geometry save for a slight modification of the corner paddles

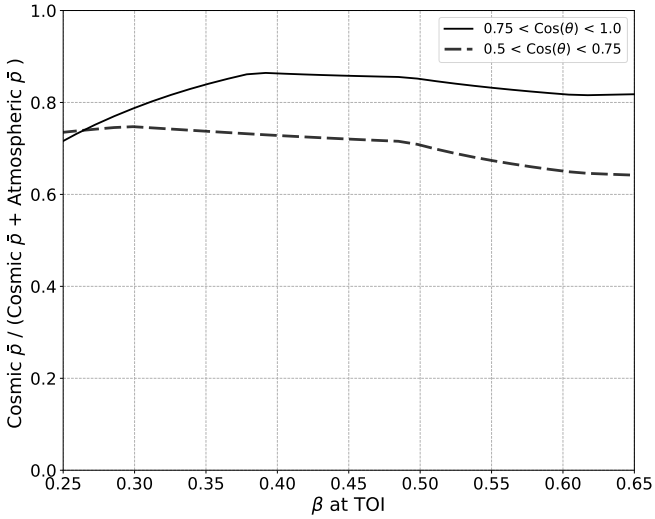

Figure 6.4: The ratio of the cosmic antiproton flux to the total antiproton flux at TOI is shown as a function of β in the same angular bins as Figure 6.1.

of the TOF cortina, whose mechanical implementation had not been finalized at the time of the simulation.

Figure 6.5 details my implementation of the Si(Li) detectors, which consist of 11 volumes each in `Geant4`. The detector strips are represented by eight active Si `Geant4` volumes ($00 - 07$ in the figure). The guard ring and side of the detector are represented by a ring of passive Si (08 in the figure). The top passive volume (09) accounts for the Si of the n^+-layer, as well as the Ni and Au of the top electrical contact and the polyimide (PI) of the grooves. The density of the simulated material was tuned to match the total mass of these detector components, while the use of a single simulated volume without grooves controlled the computational resources. Similarly, the bottom passive volume (10) accounts for the Si of the p-type layer as well as the Ni and Au of the bottom electrical contact. Altogether, the simulated detector deviated by $<2\%$ from the measured detector mass.

My implementation of the Si(Li) detector module is visualized in Figure 6.6 using `view3dscene`[3] software. Detailed simulation of the passive material of the detector modules is critical to enable realistic simulated event topologies because this passive material is in such physical proximity to the active Si and because the majority of the

[3]https://castle-engine.io/view3dscene.php

$\mathrm{d}E/\mathrm{d}x$ losses and particle annihilations actually occur in passive material, rather than active Si. On the other hand, an accurate implementation of 172 irregularly shaped pieces of each detector module would be computationally prohibitive. The module simulation is thus composed of 11 passive volumes (in addition to the four Si(Li) detectors), each representing the mass of multiple real-life components. These passive volumes were constructed to account for the total mass of each passive structure, while the mass was typically distributed within a few mm of its true position, comparable to the spatial precision of the vertex reconstruction. In total, the Si(Li) modules amount to $\sim 60\,\mathrm{kg}$ of active and passive Si and $\sim 140\,\mathrm{kg}$ of passive support structures in the GAPS instrument.

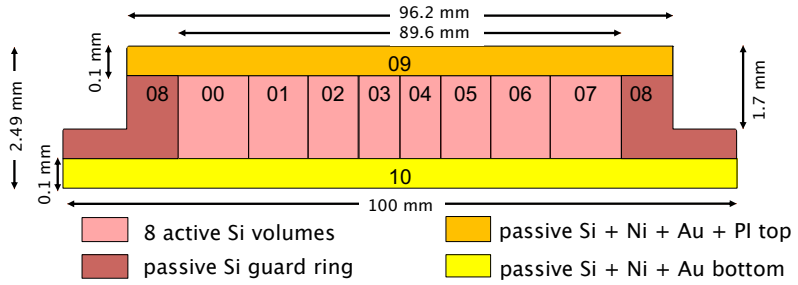

Figure 6.5: A diagram of the Si(Li) detectors as implemented in the GAPS instrument simulation (not to scale). Each simulated detector consists of 8 active and 3 passive `Geant4` volumes. The simulated material density and elemental composition have been tuned to account for the mass and spatial distribution of the Si detector bulk as well as the Ni and Au contacts and polyimide (PI) passivation, while controlling computational requirements by limiting the number of volumes.

6.4 GAPS Antiproton Analysis

The figure of merit for sensitivity to cosmic particles is the acceptance for signal and background species. The acceptance $\Gamma_a(E)$ [$\mathrm{m^2sr}$] describes the physical extent of the instrument modified by the β-dependent efficiency for particle species a to pass any selection criteria. Given $\Gamma_a(E)$, the expected number $\mathrm{d}N_a(E)/\mathrm{d}E$ of particles of species a per unit energy is calculated via:

$$\mathrm{d}N_a(E)/\mathrm{d}E = \Phi_a(E) \cdot \Gamma_a(E) \cdot T \tag{6.1}$$

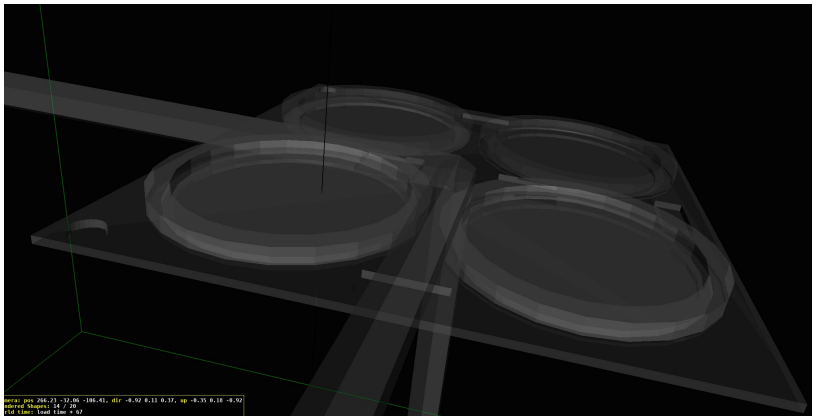

Figure 6.6: A visualization of the Si(Li) detector module implemented in the `Geant4` simulation. The spatial distribution of most module components is precise to within a few mm, smaller than the vertex resolution of the event reconstruction algorithm.

Equation (6.1) shows that $\mathrm{d}N_a(E)/\mathrm{d}E$ depends on the flux $\Phi_a(E)$ $[\mathrm{s}^{-1}\mathrm{m}^{-2}\mathrm{sr}^{-1}(\mathrm{GeV}/n)^{-1}]$ and instrument livetime T [s] as well as $\Gamma_a(E)$.

This section treats the calculation of the $\Gamma_a(E)$ factor, which depends on the instrument geometry and particle identification, in two angular regions. The multi-step analysis to identify antiproton events consists of event generation and trigger conditions in Section 6.4.1, event reconstruction and quality cuts in Section 6.4.2, and finally a likelihood analysis in Section 6.4.3.

6.4.1 Event Generation and Trigger Conditions

Particles are generated isotropically over the 2π solid angle of the downward momentum direction from the surface of a 4.4 m cube encapsulating the GAPS instrument. The generated β is uniform in the range of $0.1 \leq \beta < 0.7$ and uniform with higher statistics in the range of $0.7 \leq \beta < 1.0$. The physics list `FTFP_BERT_HP` is used in `Geant4` v10.07 to simulate interactions of these particles in the sensitive and passive detector materials. This analysis uses 1.2×10^9 simulated antiprotons, 2.8×10^{12} simulated protons, and 4.8×10^{11} simulated ^{4}He nuclei. Less abundant nuclei are not simulated for this analysis. As demonstrated in Ref. [301, 302], carbon and higher-Z nuclei are effectively rejected by the charge selection described in Section 6.4.2. Deuteron and ^{3}He nucleus fluxes are subdominant to those of protons and ^{4}He nu-

clei.

The analysis is based on trigger conditions designed to select antinuclei during the GAPS flight. The trigger requires at least eight hits in the TOF, distributed with at least three each in the outer and inner TOF. This requirement selects events that interact in the instrument to produce secondary tracks. The trigger also requires the two largest TOF energy depositions to be consistent with $|Z| = 1$ or $|Z| = 2$ particles with $0.2 < \beta < 0.6$. This rejects highly relativistic protons based on their low ionization losses as well as primaries with $|Z| \geq 6$ based on their high ionization losses. The trigger provides a rejection factor of approximately 700 (50) for protons (^{4}He nuclei) while retaining >60% of antinuclei in the GAPS β range [239].

For every generated event, each energy deposition (hit) in an active detector (TOF paddle or Si(Li) strip) is recorded and convolved with the timing, position, and energy resolution of the respective detector element. Of the simulated events, 3.5×10^7 antiprotons, 3.1×10^8 protons, and 3.6×10^8 ^{4}He nuclei pass the trigger conditions for use in the analysis.

6.4.2 Event Reconstruction and Quality Selection

Figure 6.7 illustrates a reconstructed antiproton event with the simulated active detector volumes in a 2-dimensional projection. Events passing antiparticle trigger conditions are passed through a full reconstruction sequence optimized for the GAPS annihilation star event topology [303, 304]. First, the primary track is reconstructed. The primary-track hits in the outer and inner TOF are identified based on their timestamps and energy depositions, while hits in the Si(Li) tracker are subsequently associated with the primary track based on the compatibility of their positions and energy depositions with the initial TOF hits. For >85% of events annihilating within the tracker volume, at most one hit is either wrongly associated with or wrongly missing from the reconstructed primary. The reconstructed primary trajectory is based on a least-squares fit to all of the hits on the primary track, and the primary β is calculated using the TOF timing information with this trajectory. A custom algorithm identifies secondary tracks based on the remaining TOF and Si(Li) hits not associ-

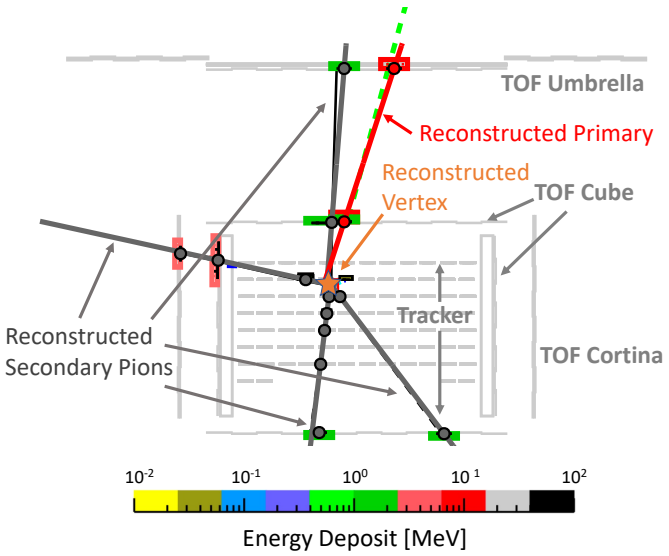

Figure 6.7: A reconstructed antiproton event (simulated with $\beta = 0.37$) shows the primary antiproton track (simulated green, reconstructed red), four secondary pion tracks (simulated black, reconstructed dark gray), and the annihilation vertex (reconstructed orange star). The boxes highlight sensitive detector volumes in which energy was deposited, where the color bar gives the total energy deposition in MeV. The largest energy depositions (red) are on the primary track. The remaining sensitive detector materials are represented in light gray.

ated with the primary track. For events with two or more hits on the primary track and with at least one secondary track with two or more hits, the annihilation vertex position is identified by minimizing the distance of closest approach to each secondary track. The efficiency for reconstructing an annihilation vertex is $\sim 90\%$, with a most probable distance of 9 mm from the true vertex and 68% of events reconstructed within 104 mm of the true vertex [303].

Following reconstruction, a correction is applied to the primary β to account for the typical energy loss by $|Z| = 1$ particles in the outer TOF paddle. More sophisticated correction techniques, which will result in improved resolution for the reconstructed β, are under development.

To ensure a sample of events with well-reconstructed topology, events are rejected if the reconstruction algorithm does not converge, which affects $<10\%$ of triggered

antiprotons with $0.25 < \beta < 0.65$ [303]. Events are also rejected if >1 sensitive detector intersecting the path of the reconstructed primary is without a hit or if the reconstructed vertex is outside the volume enclosed by the TOF cube.

Only events with ionization losses consistent with charge $|Z| = 1$ primaries with $0.25 < \beta < 0.65$ are used in the analysis. In the GAPS energy range, the typical energy loss per distance traveled ($\mathrm{d}E/\mathrm{d}x$) is proportional to Z^2/β^2 in a given material. The **primary truncated mean $\mathbf{d}\boldsymbol{E}/\mathbf{d}\boldsymbol{x}$** variable defined in Section 6.4.3 characterizes the initial $\mathrm{d}E/\mathrm{d}x$ of the primary track. Distributions of this variable are constructed using simulated antiprotons as a function of β, and events are required to fall within the central 90% of the distribution to be included in the analysis, where the high and low thresholds are functions of β. This selection criterion (cut) rejects particles with $|Z| \geq 3$. Over 99% of ^{4}He nuclei reconstructed within $\Delta\beta < 0.06$ of their true β are also rejected, though more higher-β ^{4}He nuclei persist.

Finally, events are selected that have primary β reconstructed in the range of $0.25 < \beta < 0.65$. Only events reconstructed with $\cos\theta > 0.5$, where cosmic antiprotons dominate the total flux, are selected. Additionally, this analysis only uses events in which the reconstructed primary traverses the TOF umbrella and cube, and thus where the β resolution $\Delta\beta \lesssim 0.02$, suitable for a precision spectrum.

6.4.3 Particle Identification

This section describes the particle identification tools developed to reject positive nucleus background events that pass trigger conditions due to production of secondary particles through hard interactions in the detector. Such events represent a small fraction of the total positive nucleus flux incident on GAPS. However, due to the signal-to-background flux ratios, positive nuclei still outnumber the antiprotons passing trigger and preselection conditions, requiring a robust analysis to produce a clean sample of antiprotons.

Particle identification is based on two likelihood classifiers. The "β-reconstruction likelihood" is constructed to target high-β background events that are incorrectly reconstructed in the GAPS β range. As discussed in the introduction to this section,

high-β background events can appear in the GAPS β region due to 1) β resolution effects or 2) hard interactions in an outer TOF paddle resulting in the production of an 'instrumental' antiproton that is subsequently reconstructed. In complement, the "identification likelihood" is targeted toward background events with good β reconstruction.

Particle identification is enabled by differences in the signal and backgrou nd event topologies. Hard interactions of background nuclei with target nuclei produce secondary particles that, due to baryon number conservation, are typically slower and less numerous compared to those arising from antiproton-nucleus annihilation. Additionally, these hard interactions always occur in flight while antiproton-nucleus annihilations can occur in flight or at rest following formation of an exotic atom. Compared to annihilation at rest, hard interactions lack the distinct β dependence of the ionization loss pattern on the primary track, and the interactions are boosted in the direction of the primary momentum. In addition, high-β background events with $Z = 1$ are rejected based on their overall lower ionization losses compared to antiprotons in the GAPS energy range. Instrumental antiprotons are rejected based on the anomalously large energy deposition in the outer TOF corresponding to the hard interaction site.

The two likelihood classifiers are constructed from the following event variables. The variables broadly characterize the energy deposition of the primary, the energy deposition of the secondaries, and the multiplicity and distribution of the secondaries. All of the variables used in either given classifier have mutual correlation coefficients <0.8. Distributions for those variables used in the identification likelihood classifier are shown in Figure 6.8.

Energy deposition on the primary track is the sum of the energy depositions in the TOF and tracker hits associated with the primary track, excluding the hit closest to the annihilation vertex. For a fully-stopped particle, this variable is approximately proportional to the kinetic energy.

Average energy deposition on primary track is the energy deposition on

the primary track, above, divided by the number of hits. For events reconstructed with $0.5 < \beta < 0.7$, fast $|Z| = 2$ particles exhibit a larger typical average energy deposition compared to correctly-reconstructed particles with $|Z| = 1$. Thus, high values of this variable are associated with fast ^{4}He nucleus events.

Max over mean energy deposition is the ratio of the highest primary-track energy deposition to the average of the remaining primary-track energy depositions, excluding the energy deposition closest to the vertex. This variable probes the high-energy deposition expected as a particle slows to a stop, which is not observed for high-β events.

Primary truncated mean dE/dx is the mean of the smaller half of the reconstructed dE/dx values for the TOF and tracker hits associated with the primary track. dE/dx for a given hit is the energy deposition normalized by the distance traveled in the detector. This variable identifies the typical dE/dx for the particle at its initial β. Removing hits with larger dE/dx reduces the spread due to Landau fluctuations and due to the decrease in β as the particle traverses the tracker. Fast primaries with $|Z| = 1$ have lower values of this variable compared to antiprotons with $0.25 < \beta < 0.65$.

Primary TOF dE/dx is the average dE/dx of the outer and inner TOF hits associated with the primary track. This variable gives the cleanest representation of the Z^2/β^2 energy deposition pattern prior to energy loss in the tracker.

TOF dE/dx over truncated mean dE/dx is the ratio of primary TOF dE/dx variable, above, to the truncated mean dE/dx variable, above. This variable rejects instrumental antiprotons based on the anomalously high energy deposition at the hard interaction point.

Vertex energy over truncated mean dE/dx is the ratio of the primary-track energy deposition closest to the vertex to the truncated mean energy

deposition. A large value is expected for slow particles that lose energy at a higher rate, and thus slow down faster, compared to fast particles.

Total energy deposition in the outer TOF is the sum of all energy depositions from primary and secondary tracks in the umbrella and cortina. Large values of this variable correspond to instrumental antiprotons.

Energy deposition within 45 cm of the vertex is the total energy deposited in detectors within a sphere of radius 45 cm from the reconstructed vertex. This variable scales with the number and particle type of the secondary tracks, where a larger number of tracks results in a larger value.

Average energy deposition per hit is the sum of all energy depositions in the TOF and tracker divided by the total number of hits. This variable picks out the higher energy depositions of the $Z = 2$ ^{4}He background relative to $Z = 1$ particles. Due to inclusion of the energy deposition associated with the vertex, it is not strongly correlated with the energy deposition on primary track variable.

Number of secondary tracks from the vertex is the total number of reconstructed secondary tracks emerging from the reconstructed vertex. The typical multiplicity of secondary tracks is higher for antiproton annihilations compared to hard proton interactions.

Tracker number of hits is the total number of energy depositions in the tracker. This variable scales with the number of secondary particles.

Isotropy of secondary hits in the TOF cube characterizes the degree to which the secondary tracks are boosted in the direction of the primary. Each reconstructed secondary track s emerges from the vertex with an angle ϕ_s relative to the primary, such that ϕ_s is defined by the primary momentum direction, the reconstructed vertex, and the hit in the TOF cube corresponding to track s. This variable is the mean $\cos\phi_s$ over all secondary hits in the cube. All

hard interactions of positive nuclei occur in flight, resulting in a boosted event topology, while antinucleus annihilations may occur in flight or at rest. This variable is most useful for events with large numbers of secondary tracks.

Isotropy of secondary hits in the tracker is constructed similarly to the previous isotropy variable, but using all hits in the tracker rather than the TOF cube. This variable folds the isotropy of the secondary tracks with the depth of the annihilation vertex in the tracker, as an annihilation vertex deeper in the tracker results in relatively more hits for backward-going tracks.

Average β of secondary tracks is calculated using the reconstructed time of the annihilation and the timestamps of the successive hits in the TOF cube. Antiproton annihilations typically result in faster secondaries compared to positive nucleus interactions. While antiprotons can annihilate entirely to pions, hard interactions of positive nuclei must produce heavier baryons to conserve baryon number. The distribution of this variable extends beyond $\beta = 1$ due to resolution effects.

In the likelihood analysis, probability distributions $P_i^a(q;\beta,\theta)$ of obtaining value q for each event variable i are first constructed for each event-type a of interest using simulations. Then, in the analysis phase, all individual reconstructed events, are evaluated against all of the $P_i^a(q;\beta,\theta)$ to determine their probability of being of event-type a. $P_i^a(q;\beta,\theta)$ were constructed bin-wise in true β and θ for each event-type a using simulated events and then smeared according to the β-dependent β resolution.

Table 6.1 indicates the event variables used in the construction of each likelihood classifier. Here, the event-types a are the antiproton ($\bar{p}$) signal or the proton (p) and ^{4}He nucleus (α) backgrounds. For the β-reconstruction likelihood, the $P_i^{\bar{p}}$ distributions were constructed using events reconstructed within 0.1 of the true β while the P_i^p and P_i^α distributions were constructed using simulated events reconstructed $>$0.3 below the true β or with true $\beta > 0.9$. Probability distributions for use in the identification likelihood were calculated using all simulated events.

For a particular reconstructed event in the analysis, the probability that this event

Variable	β	ID
Energy deposition on the primary track		✓
Average energy deposition on primary track	✓	
Max over mean energy deposition	✓	
Primary Truncated mean $\mathrm{d}E/\mathrm{d}x$	✓	
Primary TOF $\mathrm{d}E/\mathrm{d}x$		✓
TOF $\mathrm{d}E/\mathrm{d}x$ over truncated mean $\mathrm{d}E/\mathrm{d}x$	✓	
Vertex energy over truncated mean $\mathrm{d}E/\mathrm{d}x$	✓	
Total energy deposition in the outer TOF	✓	
Energy deposition within 45 cm of the vertex	✓	
Average energy deposition per hit		✓
Number of secondary tracks from the vertex	✓	✓
Tracker number of hits		✓
Isotropy of secondary hits in the TOF cube	✓	✓
Isotropy of secondary hits in the tracker		✓
Average β of secondary tracks		✓

Table 6.1: The event variables used in construction of the β-reconstruction (β) and identification (ID) likelihood classifiers characterize the energy deposition on the primary track (upper), the energy deposition of all of the particles (center), and the number and distribution of secondary tracks (lower).

is of type a is calculated using the values q_i of its event variables as:

$$\mathcal{P}^a = \sqrt[N]{\prod_i^N P_i^a(q_i;\beta,\theta)}. \tag{6.2}$$

The signal likelihood ratio L is then calculated as

$$L = \frac{\mathcal{P}^{\bar{p}}}{\mathcal{P}^{\bar{p}} + \mathcal{P}^{p} + \mathcal{P}^{\alpha}}. \tag{6.3}$$

For both the β-reconstruction and identification likelihood, analysis is based on the natural logarithm of the ratio calculated in Eq. (6.3). A low value of $-\ln(L)$ indicates high probability of a signal event.

Cuts are first applied based on the β-reconstruction likelihood classifier. The cut is constructed as a second-degree polynomial in the reconstructed β to reject high-β backgrounds while accepting at least 50% of signal events.

Following the cut on the β-reconstruction likelihood classifier, cuts are applied

based on the identification likelihood classifier. This analysis proceeds bin-wise in reconstructed β, and is conducted in two θ ranges: $0.5 < \theta < 0.75$ and $0.75 < \theta < 1.0$. For each bin, the target signal-to-background acceptance ratio is determined based on the TOI fluxes in Section 6.2 such that subtraction of the proton and ^{4}He nucleus contamination contributes a small statistical uncertainty compared to the irreducible atmospheric antiproton background. Figure 6.9 illustrates the signal and background distributions and the optimized identification likelihood classifier cut for the bin with $0.34 \leq \beta < 0.40$ and $\cos\theta > 0.75$. In this bin, the ^{4}He nucleus acceptance has been reduced below the required level by the earlier steps in the analysis, including the charge cut. The required antiproton-to-proton acceptance ratio is meanwhile achieved by imposing a cut on the identification likelihood classifier.

6.4.4 Calculating the Signal and Background Acceptance

The acceptance for each species is calculated based on the number of the simulated events passing all selection criteria, following [305]. Starting from the known geometric acceptance $\Gamma = 182\,\mathrm{m^2sr}$ of the surface from which simulated events are generated, the final acceptance is proportional to the fraction of simulated events passing all analysis cuts. Here, the acceptance is analyzed by binning the simulated events according to the generated or reconstructed β and $\cos\theta$.

Figure 6.10 presents the resulting acceptance for $\bar{p}$, p, and α binned in both the true β and the reconstructed β. Both background species have been rejected at the target levels for a precision antiproton spectrum. While the analysis is performed using reconstructed information, the final acceptance is presented in terms of the true β and $\cos\theta$ to facilitate comparison with the simulated fluxes. The reconstructed β is constrained to $0.25 < \beta < 0.65$. The non-zero acceptance for events with true β outside of this range is due to the intrinsic β resolution.

6.5 The Cosmic Antiproton Spectrum

Figure 6.11 illustrates the number of antiprotons (atmospheric + cosmic) expected in

this analysis in three 35-day flights. The reported number is scaled based on the flux expected for the December 2022 solar activity. The bin width $\Delta\beta = 0.06$ is much larger than the resolution $\Delta\beta_{RMS} \leq 0.02$ in the GAPS β range. The total number N_a of particles of each species a is calculated using Eq. (6.1), considering the distribution in true β for every reconstructed β bin due to resolution effects; Figure 6.12 gives an example of the true β distribution in one analysis bin. Assuming 90% livetime, ~ 1700 low-energy antiprotons are expected to be detected. Meanwhile, ~ 40 protons, ~ 15 ^{4}He nuclei, and even fewer other nuclei are expected to pass all selection criteria in the antiproton signal region.

Translating the TOI measurement to a cosmic antiproton spectrum at TOA requires statistical subtraction of both the positive nuclei and atmospheric antiprotons expected in the signal region and correction for atmospheric losses. For each data point at TOA, atmospheric β attenuation (Figure 6.1) is used to obtain the corresponding β range at TOI for each θ bin. Then, the expected number of signal and background events reconstructed in the corresponding β range at TOI is calculated.

Figure 7.2 shows the resulting anticipated cosmic spectrum at TOA for three LDB flights. This is a naive scaling using the flux modeled for the Dec. 2022 solar conditions. Detection of ~ 1500 cosmic antiprotons is expected after subtraction of the atmospheric antiproton background. The error bars illustrate the 1σ statistical uncertainty of $6 - 25\%$ per bin. Considering only data from the first LDB flight, the statistical errors will be larger by a factor of $\sqrt{3}$. This spectrum extends to lower energies than any previous cosmic antiproton measurement, with low statistical uncertainty. Expected sources of systematic error include the modeling of the atmospheric antiproton flux and of the atmospheric attenuation effects, the antiproton annihilation model, estimation of background nucleus contamination, and β resolution effects. The atmospheric model will be calibrated to GAPS measurements of atmospheric antiprotons and deuterons to ensure a self-consistent result. β-resolution effects will be constrained based on ground and in-flight measurements of atmospherically-produced minimum-ionizing particles (e.g., atmospherically-produced muons) using a dedicated trigger. Work is ongoing to improve the modeling of antiproton-nucleus annihilation

and its implementation in `Geant4`.

6.6 Outlook

This study uses a full instrument simulation with event reconstruction to demonstrate the power of the GAPS particle identification method for detecting cosmic antiprotons while rejecting cosmic-ray backgrounds. Antiprotons of both cosmic and atmospheric origin contribute to the flux at the anticipated 37 km float altitude. In its first flight, GAPS will detect ~ 600 antiprotons arriving with $0.25 < \beta < 0.65$ and $0.5 < \cos\theta < 1.0$ at TOI. Using a standard model of Galactic propagation, solar and geomagnetic modulation, and atmospheric effects, this study shows that significant detection of ~ 1500 cosmic antiprotons per flight is expected after subtraction of the atmospheric background. This corresponds to a high-statistics cosmic antiproton spectrum in the unprecedentedly low-energy range of $0.07 - 0.21\,\mathrm{GeV}/n$ at TOA. Analysis of events arriving with $\cos\theta < 0.5$ is deferred to a future study. The flux with $0 < \cos\theta < 0.5$ is dominated by atmospheric antiprotons, and while these events do not contribute to the cosmic antiproton spectrum, they will be critical to constrain systematic effects related to the atmospheric model.

With this unprecedented statistical power in a never-before probed low-energy regime, the GAPS antiproton measurement will search for new physics including DM annihilation and local PBH evaporation. It will provide the first spectral data for comparison with Galactic and solar propagation models in a sensitive low-energy regime. This measurement will also validate the GAPS particle identification in flight, paving the way for rare-event searches with heavier antinuclei.

Future developments in the analysis techniques to reject high-β backgrounds are expected to further increase the sensitivity of the GAPS cosmic antiproton measurement. The background-rejection power of a slow-down fit assessing the compatibility of the reconstructed β with the pattern of energy depositions on the primary track will be reported in a future publication.

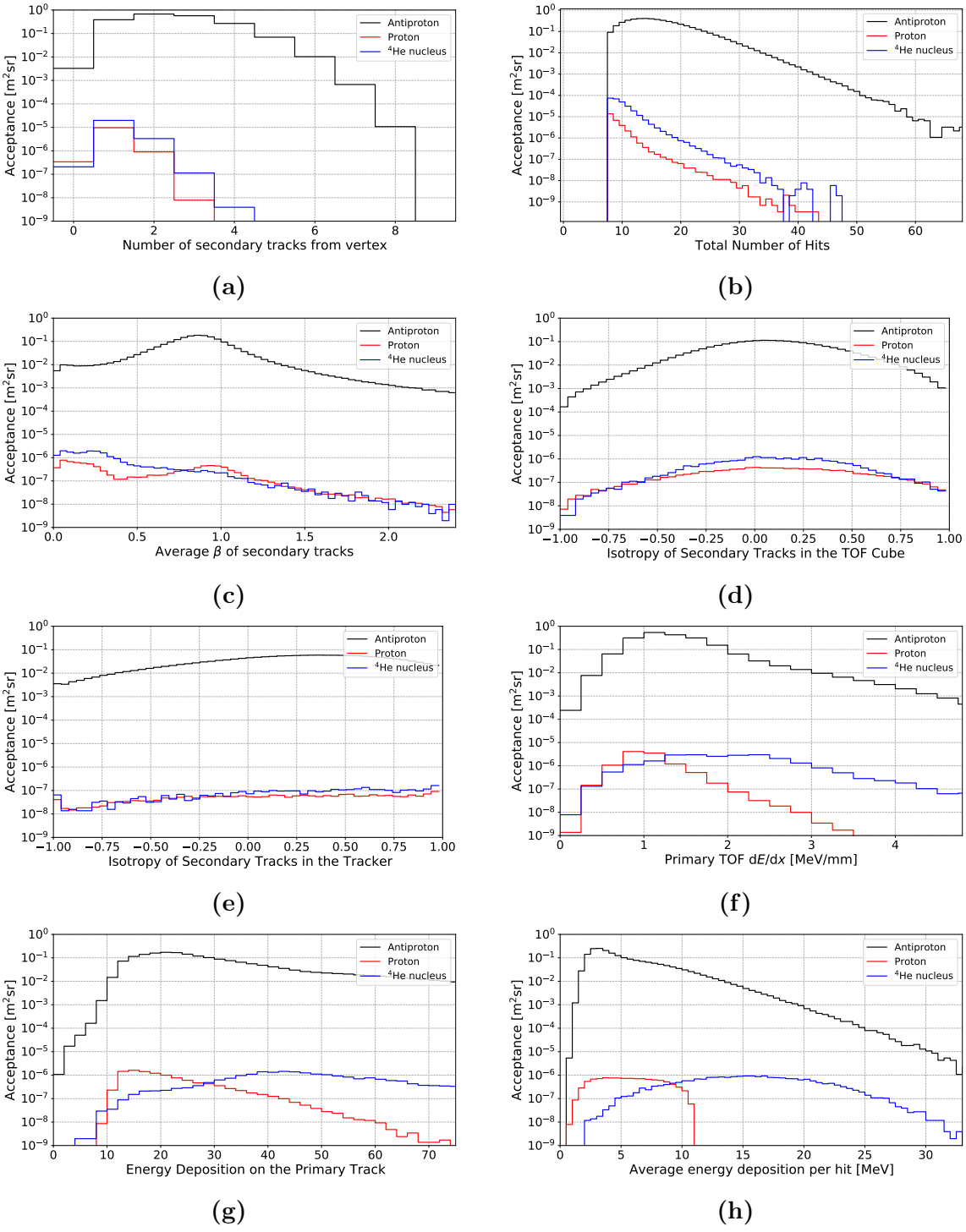

Figure 6.8: Acceptance distributions for the eight event variables used to construct the identification likelihood classifier are shown for antiprotons (black), protons (red), and ^{4}He nuclei (blue) passing trigger and quality cuts. Distributions are shown for triggered and reconstructed particles arriving with true velocity in the range of $0.3 < \beta < 0.4$.

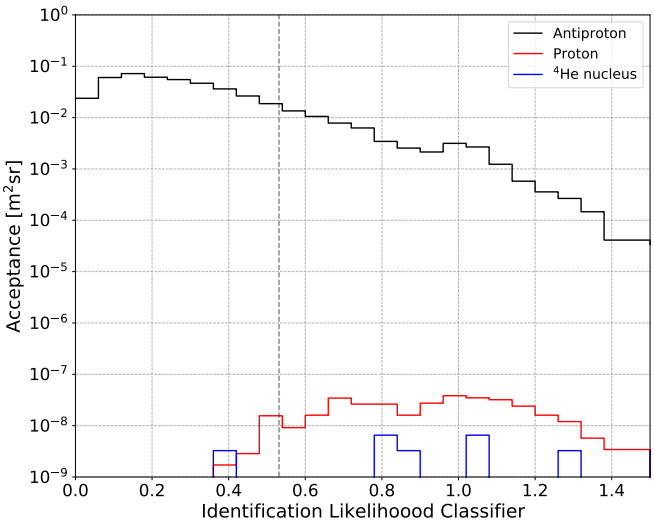

Figure 6.9: Distributions of the identification likelihood classifier are shown for antiprotons (black), protons (red), and ^{4}He nuclei (blue) reconstructed with $0.34 \leq \beta < 0.40$ and $\cos\theta > 0.75$. The distribution is shown for events that have passed trigger conditions, preselection, and the β-reconstruction likelihood classifier cut. Events in this analysis bin are selected if the identification likelihood classifier is less than 0.53 (gray dash).

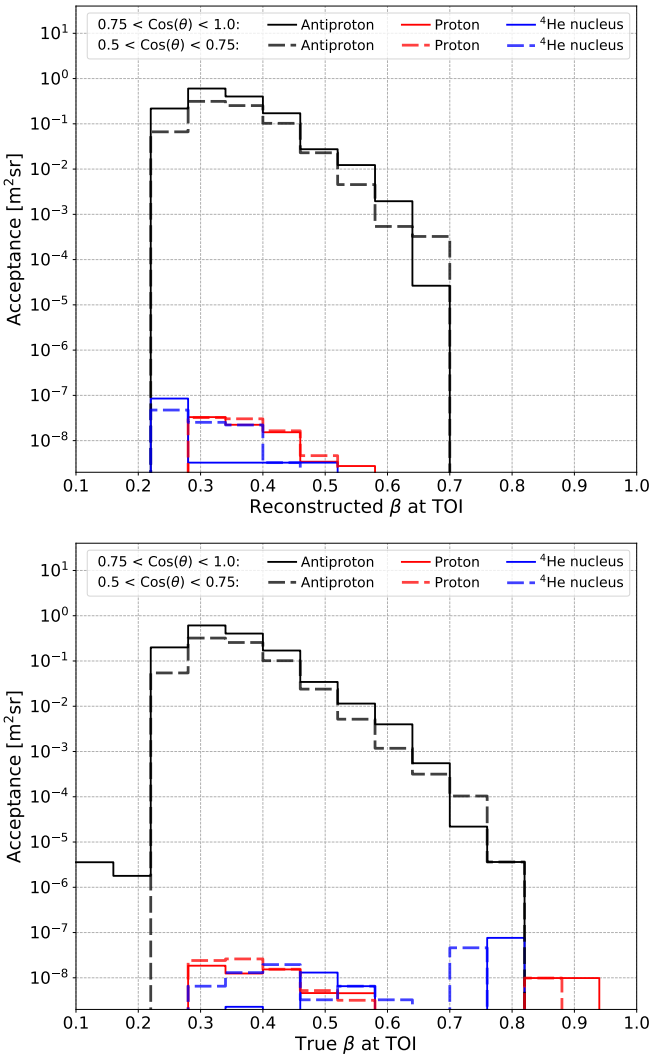

Figure 6.10: Acceptance of the GAPS instrument for antiprotons (black) as well as background species protons (red) and ^{4}He nuclei (blue) is shown after all analysis cuts binned in the corrected (upper panel) and true (lower panel) velocity β at TOI. The acceptance presented in two zenith angle ranges. All background species have been rejected at the target levels for a precision antiproton spectrum.

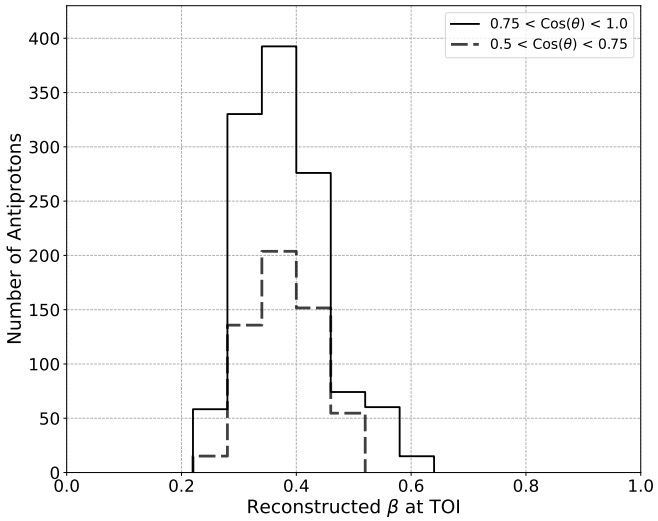

Figure 6.11: The total number of antiprotons (cosmic + atmospheric) expected in in three 35-day flights (90% livetime) is shown for two ranges in $\cos\theta$.

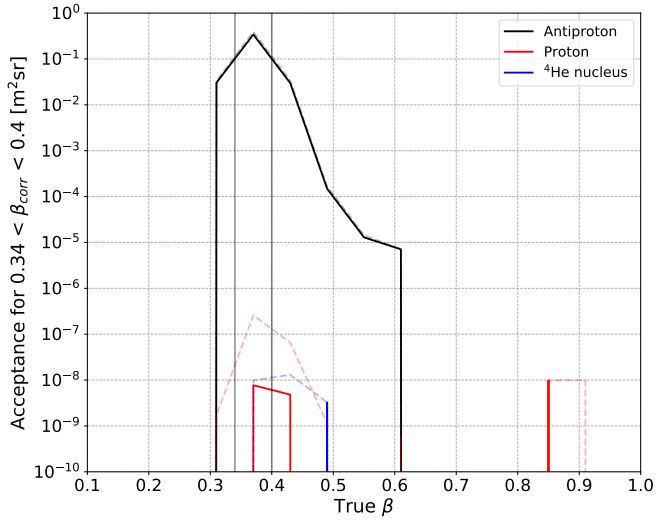

Figure 6.12: Acceptance for antiprotons (black), protons (red), and ^{4}He nuclei (blue) reconstructed with $0.34 < \beta < 0.4$ and $0.75 < \cos\theta < 1.0$ is shown projected in the true β, illustrating the spread due to the finite β resolution.

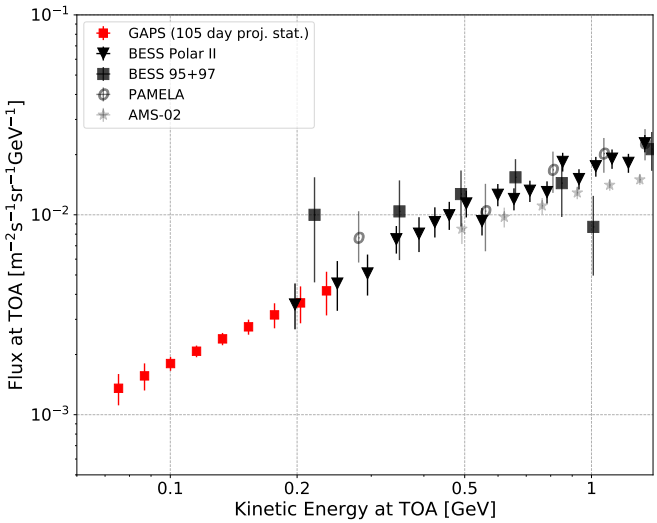

Figure 6.13: The projected GAPS precision cosmic antiproton spectrum (red) at the top of the atmosphere is shown with the statistics expected from three 35-day flights. Data from BESS (1995 and '97 solar minimum; [287]), BESS Polar II (2007−08 solar minimum; [288]), PAMELA (2006−09 with ~550 MV best-fit solar modulation potential; [290]), and AMS-02 (2011−18 with average solar modulation potential ~620 MV; [84, 286]) are also shown.

Chapter 7

X-ray Constraints on Low-energy Cosmic-rays in Sagittarius B2

Low-energy ($< 1\,\mathrm{GeV}$; i.e. highly ionizing) cosmic rays (LECR) ionize and heat the ISM gases as the traverse the Galaxy. Their dynamics within molecular clouds are of particular interest, where this ionization and heating could impact the rate of star formation. Additionally, due to their high energy loss rate compared with more energetic particles, LECR remain relatively near their sources, with the possibility of providing information on the source population.

As discussed in Chapter 3, evidence of LECR populations in the Universe comes primarily from observation of hydrogen ionization rates in the ISM, particularly in dense clouds [196, 197, 198]. Electromagnetic signatures of LECR propagation include nuclear de-excitation lines (MeV-scale), atomic fluorescence lines (keV-scale), and an X-ray continuum from scattering and Bremsstrahlung processes. In general, these signatures are beyond the sensitivity of current experiments, but they could be visible in a dense molecular cloud target.

The Galactic Center molecular cloud complex Sagittarius B2 (Sgr B2) is of particular interest for LECR detection because its large mass makes it an appealing target and because of the observed non-thermal X-rays emission from the cloud. Either a population of LECR or reprocessing of an incident hard X-ray front could produce the non-thermal X-ray spectral features observed from Sgr B2. Sgr B2 is a known

X-ray Reflection Nebula (XRN) whose total emissions have changed over time as it reprocesses one or more past X-ray outbursts from Sgr A*. Since the maximum emission level was last observed in 2001, the Fe fluorescence emission in particular has decrease with every subsequent observation raising the possibility of detecting LECR interactions as the dominant contributor to the emission either now or in the future [306].

This chapter presents recent deep observations of Sgr B2 obtained in 2018 by *XMM-Newton* and *NuSTAR* and describes the image and spectral analysis I performed using the data. Section 7.1 introduces the Sgr B2 complex and discusses prior observations. Section 7.2 details the observations and data preparation used in this analysis. In Section 7.3 the X-ray morphology of Sgr B2 is shown while Section 7.4 presents spectral analysis of the central region. Section 7.5 compares the 2018 flux with earlier data to discuss the continued decrease in X-ray reflection since 2001, while Section 7.6 contains main results on upper limits on Fe Kα emission from ambient LECR proton and electron populations in different regions of Sgr B2. Finally, Section 7.7 discusses these results in the GC context.

7.1 Introduction

Centered $\sim 100\,\mathrm{pc}$ projected distance from the supermassive black hole Sgr A* and $\sim 8\,\mathrm{kpc}$ from Earth, Sgr B2 is the densest and most massive molecular cloud in the Central Molecular Zone (CMZ), a region that extends several 100 pc from Sgr A* and contains $\sim 10\%$ of the Galaxy's total molecular material [307]. X-ray observations of Sgr B2 have revealed strong Fe Kα line emission at 6.4 keV [308, 309, 310, 311, 312, 313, 209] as well as a hard continuum up to $\sim 100\,\mathrm{keV}$ [311, 314, 306]. These features, which imply energetic, non-thermal interactions capable of ionizing the K-shell electrons of neutral Fe, have made Sgr B2 an object of interest for decades. The X-ray picture is further complicated by the time-varying nature of this emission. Since the peak flux was last observed in 2001, the Fe Kα emission has decreased with every subsequent observation, down to $\sim 20\%$ of the peak by 2013 [306, 209]. The

continuum emission from the complex has correspondingly decreased, by $\sim 50\%$ from 2003 to 2019 [315].

In a simplified gas model [316, 317], Sgr B2 consists of a dense ($(3-9)\times 10^6\,\mathrm{H_2\,cm^{-3}}$) star-forming core with radius $\sim 2-4''$, or $\sim 0.15-0.3\,\mathrm{pc}$ given $\sim 8\,\mathrm{kpc}$ distance to Sgr B2 [318]. The core is surrounded by an envelope of intermediate density ($10^4-10^5\,\mathrm{H_2\,cm^{-3}}$) with radius $2.2'$, or $\sim 5\,\mathrm{pc}$, and an extended diffuse ($\sim 10^3\,\mathrm{H_2\,cm^{-3}}$) region with radius $\sim 9.9'$ or $\sim 22.5\,\mathrm{pc}$. The model reproduces the observed column density $N_H \sim 10^{24}\,\mathrm{cm^{-2}}$ through the core and the total mass $\sim 6\times 10^6 M_{\odot}$ of Sgr B2. In reality, Sgr B2 has a more complicated structure including several subdominant cores [319, 320, 321] and an asymmetric overall gas distribution as revealed by images of cold dust [322].

In the X-ray reflection nebula (XRN) model, the Fe Kα X-rays originate in the reprocessing of external X-rays via K-shell photoionization and subsequent fluorescence of neutral Fe gas while the continuum emission arises from Rayleigh and Compton scattering [323, 308, 324]. Reprocessing of X-rays originating in past flaring activity of Sgr A* is the widely accepted explanation of the time-variable nonthermal emissions, where the time-variability emerges as the flares pass in and out of the MC [323]. Meanwhile, emission due to multiple scattering is expected from the densest cloud regions even after the flare has exited the cloud [324, 325, 326].

A short ($\lesssim$10-year) and bright event taking $\sim 10-20$ years to traverse the cloud could explain the peak luminosity from the Sgr B2 core as well as the subsequent dimming [209]. Though direct observation shows that Sgr A* is presently in a quiescent state [206, 327, 328], the XRN picture of Sgr B2 and other MCs in the CMZ reveals that Sgr A* has been brighter in the past few hundred years, with at least two short outbursts [329, 207, 330, 331, 208, 209].

A portion of the X-ray emission from Sgr B2 could arise from LECR electrons or protons, where the Fe Kα line arises from K-shell ionization of neutral Fe and the continuum arises from Bremsstrahlung processes [332, 333, 192, 170]. The observed rates of hydrogen ionization in the Galactic Center (Galactic Center) region, which are in excess of local rates by a factor of ~ 10, require models with elevated Galactic

Center LECR populations relative to the local galactic environment [196, 197, 198]. Neither LECR electrons nor protons can explain the full time-varying flux. The cooling time for $\sim$ 100 MeV protons is longer than the observed timescale of the decrease [311], and the proton population corresponding to the hydrogen ionization cannot explain the Fe Kα emission in the bright state [334]. Meanwhile, cooling of LECR electrons could explain the time variability [193], but the peak X-ray flux cannot be easily explained by LECR electrons alone [314], requiring a highly-tuned model, e.g. higher metallicity in Sgr B2 than surrounding clouds [193]. However, any steady-state population of LECRs in the cloud contributes a constant X-ray flux, in addition to the time-varying XRN flux.

Measuring X-ray flux levels enables setting upper limits on ionizing power from LECRs within a given region of Sgr B2 [332, 335, 333, 334, 311, 170, 306]. The flux levels alone can only produce upper limits due to uncertainties in both the time-varying contribution from primary XRN flares and the contribution from multiple scattering, which can vary with longer timescale. Limits on X-ray emission from LECR propagation in molecular clouds can probe ambient LECR populations in the CMZ, providing valuable input for CR models, though the ability of LECRs to traverse dense clouds is highly model dependent. The interactions of LECRs within clouds is of particular interest due to the impact of the local ionization environment inside clouds on star formation [336].

7.2 Observation and Data Reduction

Table 7.1 lists the observations discussed in this work. This analysis presents new observations of Sgr B2, taken jointly by the *XMM-Newton* and *NuSTAR* X-ray observatories in 2018. Select archival *XMM-Newton* observations of Sgr B2 are also included for comparison with the 2018 data.

Table 7.1. *NuSTAR* and *XMM-Newton* observations of Sgr B2.

Instrument	Observation ID	Start Time (UTC)	Exposure (ks)
XMM-Newton	0112971501	2001-04-01T00:25:11	9.2
XMM-Newton	0203930101	2004-09-04T02:53:45	48.5
XMM-Newton	0694640601	2012-09-06T10:56:15	66.6
XMM-Newton	0802410101	2018-04-02T00:59:38	103.0
NuSTAR	40401001002	2018-04-10T12:01:09	149.2

Note. — The exposure time reported for *XMM-Newton* observations is the *pn*-equivalent exposure.

7.2.1 XMM-Newton Observations

XMM-Newton consists of three European Photon Imaging Camera (EPIC) instruments: two Metal Oxide Semiconductor (MOS) arrays and a pn array. These cameras detect X-rays from $0.15 - 15\,\mathrm{keV}$ with typical energy resolution of $\sim 2 - 5\%$ and angular resolution of $6''$ FWHM [338, 339].

Analysis was performed using the *XMM-Newton* Extended Source Analysis Software (ESAS; [340]) distributed with v.12.0.1 of the *XMM-Newton* Science Analysis Software. We reduced the data using the standard procedure and filtered the event files to exclude intervals affected by soft proton contamination.

Spectra were extracted with the ESAS *mos-spectra* and *pn-spectra* scripts. The MOS1 and MOS2 spectra were combined and all were rebinned with 3σ significance after background subtraction. We analyzed MOS and pn data within the $2 - 10$ and $2 - 7.8\,\mathrm{keV}$ bands, respectively, where the pn spectra were truncated due to internal lines around $8\,\mathrm{keV}$.

7.2.2 NuSTAR Observations

NuSTAR operates in the $3 - 79\,\mathrm{keV}$ band using two focal plane modules (*FPMA* and

FPMB) with angular resolution of 18″ (FWHM) and typical energy resolution of 400 eV (FWHM) at 10 keV [341].

The data were reduced and analyzed using the NuSTAR Data Analysis Software (NuSTARDAS) v.1.3.1 and HEASOFT v.6.24 [342]. They were filtered for periods of high instrumental background due to South Atlantic Anomaly passages and according to a database of bad detector pixels. The data quality was impacted by stray light (unfocused photons arriving directly onto the detector at large off-axis angles) from both bright isolated sources and diffuse X-ray backgrounds. We removed the pixels contaminated by stray light from bright isolated sources using a geometrical model of the telescopes following Reference [343]. The *FMPB* observation has been disregarded because the removed pixels covered the Sgr B2 region. In *FPMA*, pixels were removed as close as ∼50″ from the center of Sgr B2. In contrast to the bright isolated sources, stray light from diffuse backgrounds fills the entire detector area with a non-uniform pattern, the brightness of which limits the signal-to-noise. We therefore used *NuSTAR* spectra in the range of $10 - 20\,\mathrm{keV}$, where the signal-to-noise ratio is highest.

7.3 Morphology of X-ray Emission

Figure 7.1 presents the 2018 observations in the $24' \times 24'$ region centered on Sgr B2. The upper panel shows the *XMM-Newton pn* images in the continuum-subtracted $6.4\,\mathrm{keV}$ line and in the $2 - 5\,\mathrm{keV}$ and $5 - 10\,\mathrm{keV}$ bands. The lower panel shows the *NuSTAR FPMA* images in the continuum-subtracted $6.4\,\mathrm{keV}$ line and in the $10 - 20\,\mathrm{keV}$ and $20 - 79\,\mathrm{keV}$ bands. The $6.4\,\mathrm{keV}$ line images were created by subtracting a continuum band, $5.8 - 6.2\,\mathrm{keV}$, from a $6.2 - 6.6\,\mathrm{keV}$ signal band. The 90″ (*XMM-Newton*) and 50″ (*NuSTAR*) source regions used for the primary spectral analysis of the core and envelope are shown in dark blue, where the smaller *NuSTAR* spectral extraction region is due to stray light contamination (see Section 7.2.2). The background regions used for spectral analysis with each instrument are in green. The *XMM-Newton* background region is located outside the Sgr B2 complex. In contrast,

the *NuSTAR* background region is located within the diffuse region of Sgr B2, due to the limited field of view (see Section 7.2.2). All regions shown in Figure 7.1 are listed in Table 7.2.

The *XMM-Newton* 6.4 keV line map shows that the core of Sgr B2 is detected at 13σ significance within the envelope region. The core is also detected at $> 5\sigma$ significance in the full energy band of *XMM-Newton* and by *NuSTAR* from $10-20$ keV. In the $20-79$ keV band, the *NuSTAR* observation is dominated by background, and the core is not significantly detected ($< 3\sigma$).

In addition to the central core and envelope, Fe Kα emission is detected at $> 5\sigma$ significance from four substructures within the diffuse region of the Sgr B2 in the projected plane. Two of these substructures coincide spatially with the cloud features previously identified by [209] as G0.66-0.13 and G0.56-0.11; Zhang et al (2015) [306] also detected G0.66-0.13 in hard X-rays in 2013. Here we additionally report two substructures, labeled G0.61+0.00 and G0.75-0.01, which were not detected in previous observations. Of these four substructures, only G0.66-0.13 and G0.61+0.00 lie within the *NuSTAR* field of view. These substructures, which are fainter than the core, are detected by *NuSTAR* at 6.4 keV but not resolved above background in the higher energy bands.

7.4 Spectral Analysis of the Sgr B2 Core

Figure 7.2 shows the background-subtracted spectrum of the central region of Sgr B2 as observed in 2018, overlaid with the best fits to three spectral models. All spectral fitting was performed using `XSPEC` software [344]. In this section, we detail the spectral fitting to models including a phenomenological model in Section 7.4.1, three XRN models in Section 7.4.2, and models of LECR-induced X-rays in Section 7.4.3.

We extracted spectra from *XMM-Newton* in a $90''$ source region, which includes the cloud's core and part of the envelope, consistent with [306]. We used a local background region, which includes any diffuse 6.4 keV emission from the larger GC

Table 7.2. Sky regions used for spectral extraction in Section 7.5 (upper), in Section 7.6 (middle), and for local background subtraction throughout this work (lower).

Region Name	R.A.	Dec.	Radius	Minor axis	Major axis	Angle
G0.74-0.10	$17^{h}47^{m}44.878^{s}$	$-28°21'22.60''$	...	$60''$	$150''$	$91.2°$
G0.75-0.01	$17^{h}47^{m}22.412^{s}$	$-28°18'38.91''$	$40''$	...	...	...
G0.66-0.13	$17^{h}47^{m}41.950^{s}$	$-28°26'23.15''$	...	$72''$	$144''$	$121.2°$
G0.66-0.13 A	$17^{h}47^{m}39.737^{s}$	$-28°24'58.48''$	$40''$	...	...	...
G0.66-0.13 B	$17^{h}47^{m}43.860^{s}$	$-28°27'08.63''$	$40''$	...	...	...
G0.66-0.13 C	$17^{h}47^{m}38.365^{s}$	$-28°25'45.64''$	$40''$	...	...	...
G0.56-0.11	$17^{h}47^{m}24.879^{s}$	$-28°30'50.91''$	$90''$	...	...	...
G0.56-0.11 A	$17^{h}47^{m}27.374^{s}$	$-28°29'30.58''$	$40''$	...	...	...
G0.56-0.11 B	$17^{h}47^{m}24.053^{s}$	$-28°30'52.82''$	$40''$	...	...	...
G0.56-0.11 C	$17^{h}47^{m}15.249^{s}$	$-28°31'2712''$	$40''$	...	...	...
G0.56-0.11 D	$17^{h}47^{m}18.848^{s}$	$-28°32'57.32''$	$40''$	...	...	...
G0.61+0.00	$17^{h}47^{m}03.925^{s}$	$-28°24'54.11''$	...	$72''$	$144''$	$16.2°$
G0.61+0.00 A	$17^{h}47^{m}04.276^{s}$	$-28°24'40.44''$	$40''$	...	...	...
G0.61+0.00 B	$17^{h}47^{m}06.275^{s}$	$-28°26'44.07''$	$40''$	...	...	...
$6'$ Region	$17^{h}47^{m}29.280^{s}$	$-28°21'57.60''$	$360''$	...	...	...
Diffuse Ellipse	$17^{h}47^{m}37.123^{s}$	$-28°17'26.16''$	...	$104''$	$236''$	$121.4°$
Envelope Ellipse	$17^{h}47^{m}18.070^{s}$	$-28°21'24.22''$	...	$36''$	$102''$	$255°$
NuSTAR Bkg	$17^{h}47^{m}17.695^{s}$	$-28°27'09.13''$	...	$65''$	$125''$	$93°$
XMM Bkg A*	$17^{h}46^{m}45.638^{s}$	$-28°13'29.32''$	...	$115''$	$150''$	$85°$
XMM Bkg B*	$17^{h}48^{m}23.336^{s}$	$-28°32'27.73''$	...	$115''$	$150''$	$30°$
XMM Bkg C*	$17^{h}46^{m}19.036^{s}$	$-28°27'40.30''$	...	$115''$	$150''$	$20°$

Note. — All coordinates are in terms of right ascension (R.A.) and declination (Dec.) using the J2000 system. Circular and annular regions centered on the Sgr B2 core are not listed in the table but assume the Sgr B2 complex is centered on RA=$17^{h}47^{m}19.992^{s}$, Dec=$-28°23'07.08''$.

*No single suitable region located outside of the spatial extent of Sgr B2 and unaffected by hard point sources was also compatible with the field of view of all four *XMM-Newton* observations. Thus, multiple background regions were used. *XMM-Newton Background A* was used for all analyses with the 2018 data (0802410101). The alternate *XMM-Newton Background B* was used for the 2012 and 2004 observations (0694640601 and 0203930101) while *XMM-Newton Background C* was used for the 2001 observation (0112971501).

Table 7.3. Best-fit spectral parameters for a joint fit of the 2018 *XMM-Newton* and *NuSTAR* observations, using the central 90″ of Sgr B2 for *XMM-Newton* and central 50″ of Sgr B2 for *NuSTAR*. We report flux parameters for the 90″ region.

Parameter	Pheno.[a]	LECRe[b]	LECRp[b]	LECRp (Z = 1)[b]
$N_H(f)$ $[10^{23}\,\mathrm{cm}^{-2}]$	$0.9^{+0.2}_{-0.1}$	0.9 ± 0.1	0.9 ± 0.1	1.0 ± 0.1
$N_H(i)$ $[10^{23}\,\mathrm{cm}^{-2}]$	$4.6^{+0.7}_{-0.6}$	$5.2^{+1.2}_{-1.1}$	$5.0^{+0.4}_{-1.0}$	3.7 ± 0.7
$Z/Z_\odot$ (apec)	2*	2*	2*	2*
$Z/Z_\odot$ (cloud)	...	$1.9^{+0.8}_{-0.4}$	$0.5^{+0.3}_{-...}$	1*
kT [keV]	$4.3^{+1.0}_{-0.7}$	$4.3^{+1.1}_{-0.7}$	$4.3^{+1.1}_{-0.7}$	$4.8^{+0.8}_{-0.9}$
$F_{apec,\ 2-10\,\mathrm{keV}}$ $[10^{-13}\,\mathrm{erg\,cm^{-2}\,s^{-1}}]$	5.6 ± 0.3	5.6 ± 0.3	5.6 ± 0.3	6.4 ± 0.03
$F_{6.4\,\mathrm{keV}}$ $[10^{-6}\,\mathrm{ph\,cm^{-2}\,s^{-1}}]$	6.7 ± 0.8	...	...	...
Γ_{pl}	2.0*	...	...	...
Λ $[10^{24}\,\mathrm{H\text{-}atoms\,cm^{-2}}]$	...	5.0*	5.0*	5.0*
s	...	$3.2^{+0.8}_{-0.7}$	$2.9^{+1.6}_{-1.2}$	1.5*
E_{min} [keV]	...	$3.2^{+27.7}_{-2.2}$	5600^{+54000}_{-5600}	$18000 \pm ...$
N_{LECR} $[10^{-6}\,\mathrm{erg\,cm^{-2}\,s^{-1}}]$	...	$0.9^{+2.0}_{-0.8}$	$0.6^{+75.8}_{-0.5}$	$0.17^{+0.04}_{-0.02}$
multiplicative factor	$0.11^{+0.04}_{-0.03}$	$0.12^{+0.06}_{-0.04}$	$0.12^{+0.06}_{-0.04}$	0.10 ± 0.03
χ^2_ν (d.o.f)	1.07 (257)	1.08 (255)	1.08 (255)	1.11 (257)

Note. — The goodness of fit is estimated by χ^2_ν with the number of degrees of freedom in parentheses. The errors represent 90% confidence. The multiplicative factor relates the flux from the 50″ source region to the 90″ region.

[a]The phenomenological model is given by `wabs*(apec+wabs*po+ga+ga)` in `XSPEC`. It is characterized by foreground absorption `wabs`, parametrized by the interstellar hydrogen column density $N_H(f)$, and by internal cloud absorption parametrized by column density $N_H(i)$. The thermal `apec` component is characterized from metallicity $Z/Z_\odot$ which could not be constrained and was thus fixed at 2, the plasma temperature kT, and total flux contribution of F_{apec}. The lines, `ga`, were fixed at 6.4 keV (neutral Fe Kα) and 7.06 keV (neutral Fe Kβ), with the Fe Kβ flux fixed at 0.15 of Fe Kα. The continuum was modeled by a pure powerlaw `po` characterized by the photon index Γ_{pl}.

[b]The LECR models are given by `wabs*(apec+wabs*LECR)` in `XSPEC`, where `LECR` is the electron (`LECRe`) or proton (`LECRp`) `XSPEC` model [170]. The `LECR` models are characterized by the maximum path length Λ of particles in the cloud, as well as the minimum energy E_{min} of particles able to traverse the cloud, and the metallicity $Z/Z_\odot$ of the cloud. In addition to these cloud parameters, the power law index s of the incident particle population is obtained in the fit. The fit with the LECRp model is reported under two conditions: first with the model parameters allowed to vary, and, second (labelled $Z = 1$) with parameters constrained to physical values. As described in the text, these `LECR` spectral fitting results do not clearly correspond to a physical ambient LECR scenario.

*Starred parameters were not allowed to vary in the fit.

region [345]. Constrained by stray light contamination (Section 7.2.2), we extracted *NuSTAR* spectra from the inner 50″ and from *FMPA* only. Due to the smaller *NuSTAR* field of view, background subtraction was performed using an ellipse located within the diffuse region of Sgr B2. The spectral extraction regions are illustrated in Figure 7.1 and listed in Table 7.2.

Background subtraction is expected to account for the instrument background as well as diffuse emission from the GC region. Any faint point sources within the selected background region are also subtracted. Due to the different sky regions, flux from the diffuse region of Sgr B2 is subtracted from the *NuSTAR* but not *XMM-Newton* spectra, leading to an underestimation of the emission from the core, which is corrected in the next paragraph. No hard point sources were detected in either background region, so above 10 keV, the contribution from both point sources and the diffuse GC emission is expected to be small.

The *XMM-Newton* and *NuSTAR* spectra differ in source and background regions used for spectral extraction, in energy band, and in instrument characteristics. Here, the *XMM-Newton* data are used from 2 to 10 keV to constrain most spectral characteristics. The *NuSTAR* spectrum is used from 10 to 20 keV to constrain the spectral index of the continuum, which is observed to be consistent with previous measurements. To facilitate a simultaneous spectral fit, we introduce a multiplicative factor relating the overall normalization of the *NuSTAR* spectrum to that of the *XMM-Newton* spectrum as a free parameter in the fit. We estimate a multiplicative factor of $\sim$0.16. Of this, a factor of 0.49 ± 0.05 in the relative normalization is attributed to the smaller *NuSTAR* source region, where the factor, which depends on the distribution of emission in the source area, was calculated based on image analysis of the 6.4 keV band of *XMM-Newton*. Based on similar image analysis, the location of the *NuSTAR* background region within the diffuse region of Sgr B2 contributes a factor of 0.66 ± 0.11. Finally, decrease of up to $\sim$50% is anticipated due to the larger *NuSTAR* point spread function.

In all models discussed below, we use `apec` to model thermal emissions remaining after background subtraction, following [306]. Other works used two `apec` compo-

nents [346, 347], where a cooler component at $1-2\,\mathrm{keV}$ accounts for diffuse GC X-ray emission while a warmer component at $6-8\,\mathrm{keV}$ accounts for unresolved point sources. Here, we use a single `apec`, for direct comparison with Reference [306]. There were no significant differences in nonthermal model parameters between our reported results using the single `apec` model and fits using two `apec` components with fixed temperatures.

In Sections 7.4.2−7.4.3 we also consider fitted metallicity Z of the cloud relative to solar abundance $Z_\odot$ as a metric for the physicality of a fit. In the CMZ, we expect $Z/Z_\odot$ in the range of $1-2$, based on previous measurements [314, 313, 348]. We nominally assume $Z/Z_\odot = 2$ in the fitting but consider $1 \leq Z/Z_\odot \leq 2$ as reasonable.

7.4.1 Phenomenological Model

Throughout this paper, we use a phenomenological model to directly evaluate the 6.4 keV line flux. This model is detailed by Zhang et al (2015) [306] and given by `wabs*(apec+wabs*po+ga+ga)`. The powerlaw continuum (`po`) and the neutral Fe Kα (6.4 keV) and Kβ (7.06 keV) lines (`ga`) expected in both the X-ray reflection and LECR scenarios are included explicitly. The model also accounts for thermal plasma (`apec`) emission that persists after background subtraction, as well as both intrinsic and foreground absorption (`wabs`). We use the `wabs` model, rather than updated models such as `tbabs`, to facilitate direct comparison with previous works.

We fix the line energies at 6.40 keV and 7.06 keV, noting that best-fit centroid energy of the Fe Kα line is at $(6.40 \pm 0.01)\,\mathrm{keV}$ when it is allowed to vary. We also fix the line widths at 10 eV, i.e. much less than the energy resolution of the instruments, and constrain the Fe Kβ normalization at Kβ/K$\alpha = 0.15$ [309]. We fit the `apec` plasma temperature but fix the `apec` metallicity $Z/Z_\odot = 2$ because it is not constrained by the data. The choice of $Z/Z_\odot$ impacts the relative flux of the fitted `apec` and `po` parameters. The intrinsic and foreground hydrogen column densities, $N_H(i)$ and $N_H(f)$, in `wabs`, are also fitted. After obtaining spectral index $\Gamma \sim 2$ from the *NuSTAR* data only, consistent with previous measurements [311, 306], we fix $\Gamma = 2$ in the combined fit. Following [306, 349], fixing Γ according to *NuSTAR*

data prevents the higher statistics of the *XMM-Newton* data from skewing Γ based on an energy region where the power law is both degenerate with the thermal emission and more strongly absorbed.

Figure 7.2 (left) shows the spectral fit for the inner 90″, and the best fit model parameters are in Table 7.3. We obtained a satisfactory fit with $\chi^2_\nu = 1.07$ for 257 d.o.f. The best fit foreground column density, $N_H(f) = 0.9^{+0.2}_{-0.1} \times 10^{23}\,\mathrm{cm}^{-2}$, was higher than the expected value of $0.7 \times 10^{23}\,\mathrm{cm}^{-2}$ to the GC, and the fitted intrinsic column density $N_H(i) = 4.6^{+0.7}_{-0.6} \times 10^{23}\,\mathrm{cm}^{-2}$ was comparable to the best fit of $5.0 \pm 1.3 \times 10^{23}\,\mathrm{cm}^{-2}$ found with *NuSTAR* for the same source region [306]. We do not expect a physical value for $N_H(i)$ in this case because it only represents an average over the region, rather than the complex scattering dynamics in the cloud. We note that all nonthermal parameters are consistent between the values reported here and those obtained in a fit with a two-`apec` plasma. The flux of Fe Kα photons, reported as $F_{6.4\,\mathrm{keV}} = 6.7 \pm 0.8 \times 10^{-6}\,\mathrm{ph\,cm^{-2}\,s^{-1}}$, depends only weakly on the other model parameters.

7.4.2 X-ray Reflection Nebula Models

We use three self-consistent `XSPEC` models of X-ray emission in the XRN scenario, including the `MyTorus` model [350, 351], the model developed by [347], and the uniform Cloud REFLection of 2016 (`CREFL16`) model [352], to assess the compatibility of the 2018 emissions with an XRN origin. All three models produce acceptable fits, but most model parameters are poorly constrained. Therefore, we conclude only that the emission spectrum observed in 2018 is not inconsistent with a primarily XRN origin. Because Sgr B2 is no longer in its brightest state, these models cannot produce new information about flaring behavior of the external X-ray source [347]. Details of the fitting with the three spectral models are in Reference [353].

7.4.3 Low-energy Cosmic Ray Models

We use the `LECRe` and `LECRp` `XSPEC` models [170] to understand if the spectral characteristics of the Sgr B2 core in 2018 are consistent with a LECR origin. However, we note that the physics of LECR diffusion into dense clouds is highly model dependent (see Section 7.7.2). The `LECR` (`LECRe` and `LECRp`) models were developed for the Arches cluster, which is smaller and less dense than Sgr B2 and features a stellar cluster which could be accelerate CRs. Further, the $90''$ region is not physically motivated as the X-ray production region corresponding to an ambient LECR population. Therefore, the results of the model fitting in this section do not correspond to the most physical ambient LECR scenario. More robust limits on ambient LECR populations are related to the Fe Kα line fluxes from different cloud regions, reported in Section 7.6.

The `XSPEC` model is given by `wabs*(apec+wabs*LECR)`, where the `wabs` and `apec` components account for foreground and internal absorption and any plasma emissions, as in Section 7.4.1. The `LECR` models assume a MC is bombarded by CRs from an external source whose spectrum follows a powerlaw with index s. The remaining parameters, including the path length Λ of CRs in the X-ray production (nonthermal) region, the minimum energy E_{min} for a LECR to enter the X-ray production region, and the metallicity Z, are properties of the MC. The normalization N_{LECR} describes the injected power $\mathrm{d}W/\mathrm{d}t = 4\pi D^2 N_{LECR}$ by LECRs from E_{min} to 1 GeV, given distance D to the MC.

The fitted parameters for the `LECRe` and `LECRp` models are in Table 7.3 and fitted spectra are in Figure 7.2. Λ could not be constrained by the data and is frozen at 5×10^{24} H-atoms per cm^2 in accordance with the column density through the core following [170, 306]. The metallicity in the `LECR` model is that of the molecular gas, distinct from that of the `apec` component.

In the electron (`LECRe`) case, the fit is satisfactory with $\chi^2_\nu = 1.08$ for 255 d.o.f. The best-fit foreground $N_H(f) = (0.9 \pm 0.1) \times 10^{23}\,\mathrm{cm}^{-2}$ and intrinsic $N_H(i) = 5.2^{+1.2}_{-1.1} \times 10^{23}\,\mathrm{cm}^{-2}$ column densities are consistent with previous observations. The best-fit

plasma temperature is $kT = 4.3^{+1.1}_{-0.7}\,\mathrm{keV}$, and the cloud metallicity is $Z = 1.9^{+0.8}_{-0.4}\,Z_\odot$, consistent with the expected range of $1 - 2\,Z_\odot$. The fit favors no lower cutoff on LECR energies in the cloud, with $E_{min} = 3.2^{+27.7}_{-2.2}\,\mathrm{keV}$, and an electron spectral index of $s = 3.2^{+0.8}_{-0.7}$. The fit normalization $N_{LECR} = 0.9^{+2.0}_{-0.8} \times 10^{-6}\,\mathrm{erg\,cm^{-2}\,s^{-1}}$. For $D = 8\,\mathrm{kpc}$ to Sgr B2, this corresponds to a limit (90% confidence) on the power of LECR electrons, $\mathrm{d}W/\mathrm{d}t < 2.2 \times 10^{40}\,\mathrm{erg\,s^{-1}}$ from the central 90″. However, the limit is of limited utility given the assumptions in the `LECR` model and considering that any ambient LECRs are not expected to reach the core region of Sgr B2.

In the proton (`LECRp`) case, the fit statistic for the central 90″ is also satisfactory, with $\chi^2_\nu = 1.08$ for 255 d.o.f. The best-fit foreground $N_H(f) = (0.9 \pm 0.1) \times 10^{23}\,\mathrm{cm^{-2}}$ and intrinsic $N_H(i) = 5.0^{+0.4}_{-1.0} \times 10^{23}\,\mathrm{cm^{-2}}$ column densities are consistent with previous observations. The plasma temperature is $kT = 4.3^{+1.1}_{-0.7}\,\mathrm{keV}$. E_{min} is completely unconstrained, while the fit favors a similar LECR proton spectrum as in the `LECRe` case, $s = 2.9^{+1.6}_{-1.2}$, consistent with the $1.5 < s < 2$ expected from diffusive shock acceleration [170]. The cloud metallicity is fitted as $Z < 0.8\,Z_\odot$ (90% confidence), which is inconsistent with the expected value of $1 - 2\,Z_\odot$, so this fit does not represent a physical scenario. However by fixing the metallicity at $Z/Z_\odot = 1$ and the proton power law index at $s = 1.5$, we obtain a similar quality fit with $\chi^2_\nu = 1.11$ for 257 d.o.f. and physical model parameters (see Table 7.3). In this case, $N_{LECR} = 1.7^{+0.4}_{-0.2} \times 10^{-7}\,\mathrm{erg\,cm^{-2}\,s^{-1}}$. The corresponding upper limit on the LECR proton power $\mathrm{d}W/\mathrm{d}t < 1.6 \times 10^{39}\,\mathrm{erg\,s^{-1}}$ is subject to the same caveats as in the electron case above.

7.5 Time Variability of X-ray Reflection

Figure 7.3 shows the morphology of 6.4 keV emission in four *XMM-Newton* observations of Sgr B2 from 2001 to 2018. The contour lines of the 2018 6.4 keV emission are overlaid, for comparison with Figure 7.1 despite the change in color scale. In these exposure-corrected and continuum-subtracted images, the surface brightness of the core and envelope decreases over time. In contrast to this continued dimming, substructures within the diffuse region, including those identified in Section 7.3, brighten

and dim from one observation to the next.

Here, we discuss this changing Fe Kα brightness and morphology from the cloud overall (Section 7.5.1) and from the substructures (Section 7.5.2). The sky regions are in Table 7.2 and details of the spectral fitting are in Reference [353] (Appendix B). All spectra were extracted using a local background region, such that the reported Fe Kα flux is in excess of the diffuse emission reported by e.g. [345].

7.5.1 Time Variability of the Central Region

Figure 7.4 presents light curves of the Fe Kα emission from Sgr B2, illustrating the behavior of the diffuse, envelope, and core regions. We use a $6'$ region (not concentric with the core; defined in Table 7.2 and illustrated in Figure 7.3) to illustrate the behavior of the cloud over all. We also analyze the $90''$ region detailed in Section 7.4 to probe the behavior of the envelope, and a $10''$ region to probe the core.

The $6'$ region includes the Sgr B2 envelope and core and the bulk of the emission from the diffuse portion of the cloud. Unlike the full $9.9'$ indicated by the simplified model, it is compatible with all four *XMM-Newton* observations. The resulting light curve illustrates that the total flux from Sgr B2 has continued to decrease with time, by a factor of $\sim$3.5 since 2001. Relative to the 2012 level, the 2018 emission represents a $(29 \pm 8)\%$ decrease, indicating that the primary XRN component was contributing to the total nonthermal emission from this region at least as late as 2012. The $6'$ region directly corresponds to the sky region detected with the *INTEGRAL* observatory (which has a $6'$ resolution), facilitating comparison with the light curve of hard continuum emission reported by Kuznetsova et al (2021) [315].

The light curve from the central $90''$ consists of the Fe Kα line flux measurement from Section 7.4.1, alongside measurements $(2001-2013)$ by Zhang et al (2015) [306], demonstrating the compatibility of this work with previous measurements. Consistent with the images in Figure 7.3, spectral analysis shows that the Fe Kα line flux from the central $90''$ (core and bulk of the envelope) decreased over time, with an overall decrease by a factor of 6 ± 1 since 2001. The 2018 flux is $(80 \pm 20)\%$ of the 2012 flux, and the decrease since 2012 is not significant considering the statistical uncertainty,

and we cannot determine based on the light curve if the flux from the central region has reached a constant level or if it will continue to decrease.

Finally, we show the light curve for the central $10''$, which corresponds to the $\sim 15''$ half-power diameter of *XMM-Newton* together with the width of the core. Though the fitting is less significant due to the small source size, we observe a similar pattern of decreasing emission for the core as for the cloud overall. Based on the small relative flux contribution from the core, we conclude that behavior of the $90''$ region is driven by interactions in the envelope.

The true shape of the XRN light curve depends on the shape of the original flare and the details of the density profile of the cloud [323]. Here, we fit the intensity I of the emission from the central $90''$ as a function of the time t since January 1, 2001 as an exponential decrease with a constant offset:

$$I(t) = a * \exp(-t/\tau) + b. \tag{7.1}$$

The best fit to Eq. (7.1) yields normalization $a = (3.9 \pm 0.5) \times 10^{-5}\,\mathrm{ph\,cm^{-2}\,s^{-1}}$, decay constant $\tau = (5.2 \pm 1.5)$ years, and constant flux $b = (0.5 \pm 0.2) \times 10^{-5}\,\mathrm{ph\,cm^{-2}\,s^{-1}}$. The best-fit τ is consistent with the expected superluminal light-crossing time for the $90''$ region, indicating that the illuminating flare itself must have been short. The constant flux b is inconsistent with 0, requiring an emission component that is stationary over the considered timescale.

In context of the light curves, Figure 7.3 illustrates how the geometry of the emission from the core and envelope has evolved over time. While the 2001 map is brightest on the Sgr A* side of the envelope, the emission is more balanced by 2004, and by 2012 and 2018, the envelope emission is more extended on the opposite side of Sgr A*, as illustrated by the contour lines. This provides further indication that the initial flare from Sgr A* has already passed through some or all of the envelope.

7.5.2 Time Variability of Diffuse Substructures

Figure 7.5 (panel 1) shows the ellipsoid regions defined to correspond to the substructures identified in Section 7.3. The remaining panels in Figure 7.5 show light curves of 6.4 keV line emission from three of the substructures (G0.66-0.13, G0.56-0.11, and G0.61+0.00) that were significantly detected in 2018. The substructures behave differently over time, as G0.66-0.13 (black, second panel) brightens in 2012 and then dims again, while G0.56-0.11 (black, third panel) continues to brighten after 2004.

Within each substructure, we defined several 40″-radius circular regions (∼10-year light-crossing time) to illustrate the patterns of light that appear to be moving through the larger substructure. In each substructure, the circles are ordered from least negative declination (A, magenta, i.e. farthest from Sgr A* in the projected plane) to most negative, and the circle A brightens last. For G0.66-0.13, the light curves for circles B and C follow the same pattern as the parent structure, while circle A brightens in 2018, consistent with a flare originating at Sgr A* propagating through the cloud. We note that while these X-ray substructures were identified within the projected area of diffuse region of Sgr B2, we cannot exclude that they may correspond to other structures along the line of sight but outside of the Sgr B2 complex. Efforts to clarify the location of the substructures using line-of-sight velocity maps from the MOPRA 3 mm survey [354] were inconclusive.

7.6 Low-energy Cosmic Ray Limits

Theoretical efforts to model the propagation of LECRs into Sgr B2 rely on simplified models of the gas distribution and cloud dynamics. Models are necessitated by the complex gas structure, illustrated in Figure 7.6. In this section, we have selected several sky regions (illustrated in Figure 7.6 and detailed in Table 7.2) that are compatible with the diffuse, envelope, and core components of Sgr B2 in both the simplified model and the observed hydrogen column density while also avoiding the bright substructures identified in Section 7.5.2.

Table 7.4. The Fe Kα flux and brightness from distinct regions of Sgr B2 can probe models of LECR transport into or production within Sgr B2.

Cloud Region	Fe Kα flux $10^{-6}\,\mathrm{ph\,cm^{-2}\,s^{-1}}$	Fe Kα surface brightness $10^{-7}\,\mathrm{ph\,cm^{-2}\,s^{-1}\,arcmin^{-2}}$	χ^2_ν (dof)
Diffuse*	6.1 ± 1.9	2.9 ± 0.9	1.41 (23)
Env. (ellipse)†	1.8 ± 0.5	5.7 ± 1.4	1.47 (41)
Env. $(0.5' - 2.2')$†	10.8 ± 1.2	7.5 ± 0.8	1.48 (317)
Central $30''$	1.3 ± 0.3	16 ± 4	1.25 (86)

Note. — Data are reported based on the 2018 *XMM-Newton* observation of Sgr B2. The region boundaries are in Table 7.2. Regions are circular or annular, with given angular size in radius, unless otherwise specified. Errors and upper limits indicate 90% confidence.

*The region selected from the diffuse portion of the cloud is an ellipse, chosen to fall within the diffuse region in both the simplified model and the n_H observations and to avoid hard point sources. The reported flux is thus the flux from this region, rather than the total flux from the diffuse region. Due to the more limited field of view of MOS1, we calculated flux using MOS2 and pn only for this region.

†Because the actual gas distribution in Sgr B2 is more complicated than the simplified model, two distinct sky regions were used to evaluate the envelope flux from Sgr B2, as shown in Figure 7.6. The annular region, Env. $(0.5' - 2.2')$, represents the bulk of the envelope in the simplified Sgr B2 model. While the total flux measurement from this region may be useful, Sgr B2 has subdominant cores located within this annulus, and portions of this annular region have a column density more similar to the diffuse region, so the surface brightness should be interpreted with caution. On the other hand, the elliptical envelope region, Env. (ellipse), is a region with typical column density for the Sgr B2 envelope. While the flux for this region does not represent the total flux from the Sgr B2 envelope, the surface brightness is typical of the portions of the cloud with the intermediate column density associated with the envelope.

Table 7.4 presents the Fe Kα flux and surface brightness based on spectral fitting of these sky regions. Details of the data and fitting are in Reference [353] (Appendix B). The Fe Kα surface brightness from the representative diffuse, envelope, and core regions of the cloud are 2.9 ± 0.9, 5.7 ± 1.4, and $16 \pm 4 \times 10^{-7}\,\mathrm{ph\,cm^{-2}\,s^{-1}\,arcmin^{-1}}$, respectively. Since the 2018 data are the dimmest deep observations of Sgr B2 in this band to-date, these are the current best upper limits on Fe fluorescence due to ionization by LECRs.

7.7 Discussion

7.7.1 Implications for the X-ray Reprocessing Scenario

The core and envelope region, previously the brightest part of the cloud, with multiple cores detected [306], is now very faint in Fe Kα fluorescence, as illustrated in Figures 7.3 and 7.4. The brightest emission is restricted to the densest core. The pattern of flux decrease from 2013 to 2018 from the core, envelope, and cloud overall indicates that most or all of the major X-ray flare previously driving the overall luminosity has passed through the cloud by 2018. The 2018 emission from the central $90''$ is most likely driven by a stationary component, as is expected from both multiple scattering and LECRs. Reprocessing of subdominant external flares may also contribute.

The total decrease in the Fe Kα emission from the $6'$ region from 2004 to 2018 is consistent with the total decrease in the $30 - 80\,\mathrm{keV}$ continuum observed by *INTEGRAL* over the same sky region. The best-fit *INTEGRAL* light curve is a linear decay before 2011 and a constant level thereafter [315]. In comparison, Fe Kα light curve reported here was decreasing at least as late as 2012, but due to limitations in the number and significance of the data points, the difference between the two light curves is not significant. A Fe Kα light curve that is consistent with that of the hard continuum indicates that the emission mechanisms for the two energy scales are related. This is expected, since the higher absorption at 6.4 keV is partially compensated by multiple scatterings of the Fe Kα line itself and because fluorescence

events are induced by continuum photons above 7.1 keV. If the emission is dominated by multiple scattering, the actual degree of correlation depends on geometry, optical depth and metallicity of the cloud [324, 325].

Kuznetsova et al (2021) [315] suggest multiple scattering of X-rays from the primary external flare as a probable origin of the $30-80$ keV emission after 2011. Multiple spectral handles can clarify the role of multiple scattering. First, this signal is expected to be more pronounced in the morphology of the hard X-ray continuum than the fluorescent lines, as the absorption cross section is larger than the scattering cross section $\lesssim$10 keV [325, 352]. Against a backdrop of fading emission, the 2013 *NuSTAR* detection of multiple cores above 10 keV [306] suggests that multiple scattering already played an increasingly important role. Continued decrease of the Fe Kα emission once the $30-80$ keV emission has reached a stationary level, as hinted by the data, would support the multiple scattering origin of the $30-80$ keV emission. A future *NuSTAR* observation less contaminated by stray light would constrain the hard-continuum light curves from the core and envelope, allowing the cleanest probe of the multiple scattering scenario. While the 2018 observation was optimized to minimize stray light contamination, cleaner *NuSTAR* data could be obtained using a contiguous deep observation of a nearby off-source region to measure the stray light background, as in the 2013 observation [306].

In the Fe Kα line, a Compton shoulder feature due to multiple scattering of fluorescence photons is expected on the low-energy side of the line complex [325]. While the Compton shoulder is not resolvable with the energy resolution of *XMM-Newton*, the centroid of the 6.4 keV line is expected to shift toward lower energies as the Compton shoulder becomes a more important contributor to the overall line flux [355]. The line centroid in 2018 was 6.40 ± 0.01 keV, compared with $\sim$6.44 keV in 2013 [306], pointing to an increasing multiple-scattered component of the Fe Kα line over time. Future high-resolution X-ray spectrometers including *XRISM/Resolve* [356] and *Athena/X-IFU* [357] could resolve the Compton shoulder, precisely measuring the relative contribution of multiple scattering [325].

The morphological and brightness variation from several X-ray substructures (re-

ported in Section 7.5.2) external to the Sgr B2 envelope also reveal implications for the timescale and number of the external X-ray flaring events. The small bright regions, with their relatively short light crossing times, have a faster timescale of emission decrease from X-ray reprocessing and thus better reflect the timescale of the external source than the Sgr B2 envelope [209]. In particular, G0.56-0.11, which was reported as brighting up in 2012 [209], is even brighter in 2018, with a significant morphologic change. While the 2012 emission is centered on clump B (see Figure 7.5), the 2018 emission is centered $\sim$ 13 light years (projected distance) away, in clump A. The light curve of clump B gives an upper limit of $\sim$14 years for the timescale of the flare illuminating this region. Future observation by *XMM-Newton* could further constrain the timescales of these flares based on the future behavior of the "A" clumps from each substructure.

Similar light curves to G0.56-0.11 clump B are observed in G0.66-0.13 clumps B and C, suggesting that these two substructures may be illuminated by the same flaring event, if they are a similar distance from Sgr A*. Unfortunately, without knowledge of the line-of-sight positions and detailed n_H distributions of these structures, we cannot clearly make this claim. References [207, 208, 209] provided evidence for a minimum of two illuminating events propagating through the CMZ. In the case that these substructures are illuminated by the same event as the core, if we assume Sgr B2 to be at least 50 pc in front of Sgr A* (following [347, 358], and references therein), the substructures could be $\gtrsim$60 pc behind Sgr B2, farther than the spatial extent of cloud. Therefore, if these substructures are linked to Sgr B2, they are illuminated by a secondary event.

7.7.2 Implications for Low-energy Cosmic Rays

This section discusses the upper limits on the Fe Kα emission from different cloud regions presented in Section 7.6 Table 7.4 in the context of physical models of LECR interactions in Sgr B2.

CR transport is modeled as a diffusive process modified by the effects of elastic and inelastic collisions, energy loss via ionization and excitation, and energy loss

via bremsstrahlung and synchrotron radiation in the surrounding medium. While transport into and within MCs is model dependent [359, 170, 360, 361, 336, 362], the low relative rates of hydrogen ionization observed within dense MCs indicate that LECRs do not freely traverse these structures [363, 364, 198, 361].

Using a simplified model of Sgr B2, [361] calculate that LECR propagation in the envelope[1] is best described by diffusion on turbulent magnetic fluctuations [365, 366]. Meanwhile, diffusion is negligible in the diffuse region, where fluctuations are small. Considering ionization and excitation losses, protons (electrons) with kinetic energy $E \gtrsim 20\,\mathrm{MeV}$ ($1\,\mathrm{MeV}$) traverse the diffuse region to reach the envelope, where they are absorbed within $0.1 - 0.3\,\mathrm{pc}$ [335]. The ambient LECR proton spectra derived by [361] would deposit the bulk of their energy in the the Sgr B2 envelope.

In the LECR proton case, [361] use the hydrogen ionization rates in Sgr B2 and the surrounding environment to estimate the intensity $I_{6.4} \approx (3-5)\frac{Z}{Z_\odot} \times 10^{-6}\,\mathrm{ph\,cm^{-2}\,s^{-1}}$ of the LECR-induced Fe Kα emission from the Sgr B2 complex. The range of $3-5$ depends on the details of the ambient LECR spectrum and the gas distribution of the cloud.

The measured Fe Kα flux of $(10.8 \pm 1.2) \times 10^{-6}\,\mathrm{ph\,cm^{-2}\,s^{-1}}$ from the envelope ($0.5' - 2.2'$) region in 2018 (Table 7.4) is comparable to the calculation by [361] if $Z/Z_\odot = 2$. Unless $Z/Z_\odot > 2$, ambient LECR protons in this model cannot explain all of the Fe Kα emission. However, propagation of ambient LECR protons could contribute >50% of the 2018 Fe Kα emission.

Kuznetsova et al (2021) [315] disfavor LECR proton propagation as the sole source of the $30 - 80\,\mathrm{keV}$ emission from 2011 to 2019 on the basis of the high overall flux compared to the observed hydrogen ionization rate. As detailed in Section 7.7.1, the $30 - 80\,\mathrm{keV}$ band could have more substantial contributions from multiple scattering compared to the Fe Kα line, and a portion of the flux in the $6'$ region of *INTEGRAL* is due to X-ray reflection from substructures. With improved characterization of the flux contribution expected from multiple scattering, enabled by future high-resolution

[1] [361] use the term 'envelope' for our 'diffuse region', and their 'core' approximately corresponds to our 'envelope'. They do not treat the dense star forming cores. For clarity, we have translated their terminology to match this work.

observations of the 6.4 keV line and the hard X-ray flux as discussed in Section 7.7.1, the LECR contribution could be more tightly constrained even as it coexists with the emission from multiple scattering.

Previous work has demonstrated that an ambient population of LECR electrons cannot explain the full hydrogen ionization rate in Sgr B2. The X-ray continuum from propagation of ambient LECR electrons is expected to have $\Gamma \sim 1$, harder than the $\Gamma \sim 2$ expected from LECR protons or X-ray reflection and observed from Sgr B2. Given the population of ambient LECR electrons that could explain the observed hydrogen ionization, the hard continuum should have been observable as early as 2009 [361, 306, 315]. While ambient LECR electrons are excluded as the sole origin of hydrogen ionization in Sgr B2, they may still contribute to the nonthermal X-ray emission observed in 2018 or in the future. The sensitivity of the 2018 observations to LECR electrons is restricted by the limitations of the *NuSTAR* observation. With spatial resolution for X-rays up to 79 keV, a future *NuSTAR* observation less severely contaminated by stray light could resolve this ambiguity.

We additionally considered the annihilation or decay of dark matter as a source of the LECRs responsible for the hydrogen ionization and the nonthermal X-ray emission, concluding that any contribution from dark matter would be small compared to the LECR electron population needed to explain the X-ray emission (details in Reference [353] Appendix C).

7.8 Summary and Outlook

The X-ray features of Sgr B2 provide a window into past energetic activity of Sgr A*, via X-ray reprocessing in the cloud, and to the GC LECR populations, via ionization and Bremsstrahlung processes.

This work presents the 103 ks and 149.2 ks observations of Sgr B2 taken jointly in 2018 by the *XMM-Newton* and *NuSTAR* X-ray telescopes, respectively. These data show that the the 2018 Fe Kα emission from the central region is 0.8 ± 0.2 of the 2012 level, consistent with significant contribution from a stationary component.

Meanwhile, they also reveal new brightening substructures, which, assuming they correspond to clumps within the Sgr B2 complex, are illuminated by one or more secondary external flares. Based on both the Fe Kα light curve and the spectral analysis, the 2018 emissions from the central region are consistent with arising primarily from X-ray reprocessing, with possible contributions from the tail of the original flare, multiple scattering albedo, and secondary flares, or with arising primarily from LECR interactions. Thus, the flux levels presented in Table 7.4 represent best upper limits on fluorescence from LECR interactions within different cloud regions. The Fe Kα emission observed from the Sgr B2 envelope is comparable with expectation from the low-energy cosmic proton population that would simultaneously explain the observed hydrogen ionization rates in the model of [361].

Future observations of Sgr B2 by *XMM-Newton* will further constrain the Fe Kα light curves from the envelope, core, and the diffuse substructures, clarifying the origins of the 2018 emission and the duration of the external flare(s) illuminating the bright substructures. Meanwhile, further observations resolving the dense cores can clarify the contribution of multiple scattering and facilitate correspondingly more precise limits on the contributions of LECRs. Two regimes are of particular interest. For hard X-rays above 10 keV, scattering is the dominant photon process, and a *NuSTAR* observation less contaminated by stray light could detect deviations in the light curve of the densest cores relative to the envelope and diffuse cloud regions. For the Fe Kα line, future high-resolution spectrometers could directly resolve the line features, including the Compton shoulder, expected in multiple scattering. If further decrease of the Fe Kα emission from the envelope is observed, or if a significant portion of the 2018 Fe Kα emission level is definitively attributed to multiple scattering, the LECR proton model of hydrogen ionization [361] would begin to be constrained.

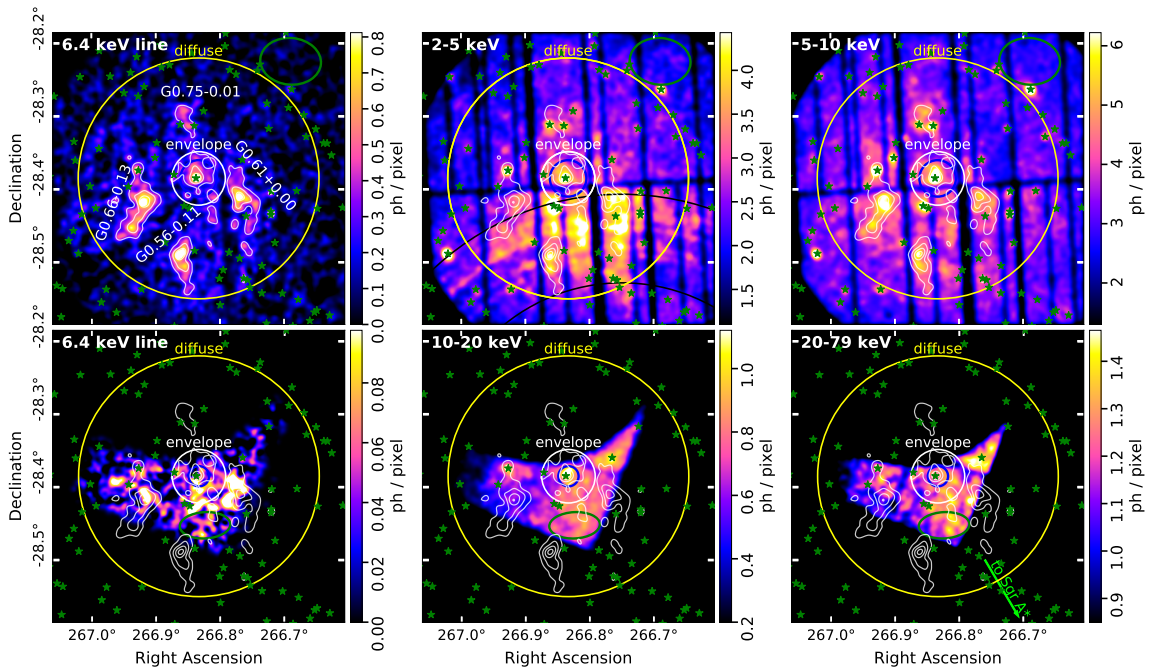

Figure 7.1: The 2018 X-ray morphology of the $24' \times 24'$ region surrounding Sgr B2 is shown as observed by *XMM-Newton pn* (top) in the 6.4 keV line (left), $2-5$ keV (center), and $5-10$ keV (right) bands; and by *NuSTAR FPMA* (bottom) in the 6.4 keV line (left), $10-20$ keV (center), and $20-79$ keV (right) bands. The 6.4 keV line images are continuum subtracted as in Section 7.3. Contours (white) of the *XMM-Newton* 6.4 keV map are overlaid on all images and illuminate the core and envelope of Sgr B2 as well as several substructures, labelled by their Galactic coordinates. The annular stray light pattern observed in all *EPIC* instruments is most evident in the $2-5$ keV band (top center, black), while the stray light in *FPMA* is evident the radial region removed from the top-left of the *NuSTAR* images. Circles indicating the diffuse (yellow, $9.9'$ radius) and envelope (white, $2.2'$ radius) regions of the simplified model are overlaid, while the core ($2-4''$ radius) is smaller than the angular resolution of both telescopes. The brightest ($> 10^{-6}$ ph cm^{-2} s^{-1} in $2-7$ keV) hard X-ray sources from the Chandra Source Catalog 2.0 [337] are shown (green stars), as well as the $90''$ (*XMM-Newton*) and $50''$ (*NuSTAR*) source regions (blue) and the respective elliptical regions used for background subtraction (green). The arrow (lime) indicates the direction to Sgr A*. Color bars indicate intensity in photons per pixel. The images have been smoothed using a 2D Gaussian kernel with standard deviation 3 pixels (*XMM-Newton pn*; pixel-size $4.3''$) or 5 pixels (*NuSTAR FPMA*; pixel-size $2.5''$).

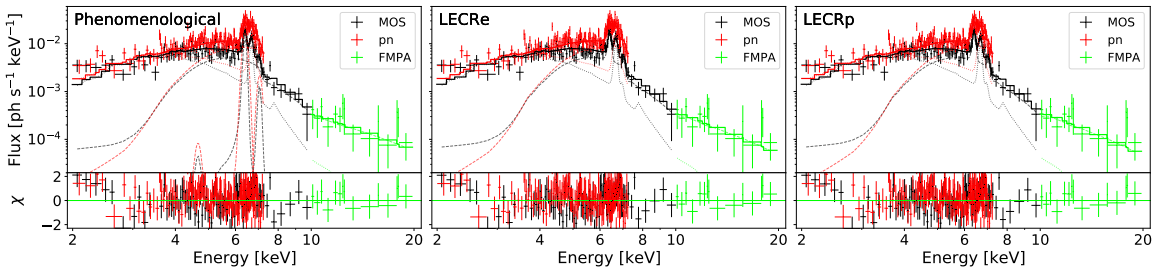

Figure 7.2: The background-subtracted 2018 spectra of the inner 90″ of Sgr B2 as observed by *XMM-Newton MOS* (black, $2-10$ keV) and *pn* (red, $2-7.8$ keV) and the inner 50″ as observed by *NuSTAR FPMA* (green, $10-20$ keV) are fitted with the phenomenological model (left), the `LECRe` model (center), and the `LECRp` model (right). The *XMM-Newton* data are binned with 3σ significance while the *NuSTAR* data are binned with 1.5σ significance. The best fit is shown in the solid lines. The contributions of the `apec` (dotted) and the nonthermal spectral components (dashed; `ga`, `po`, `LECRe`, and `LECRp` for the respective models) are also shown. All three models show satisfactory agreement with the data overall, though the fits are significantly lower than data below ∼2.3 keV.

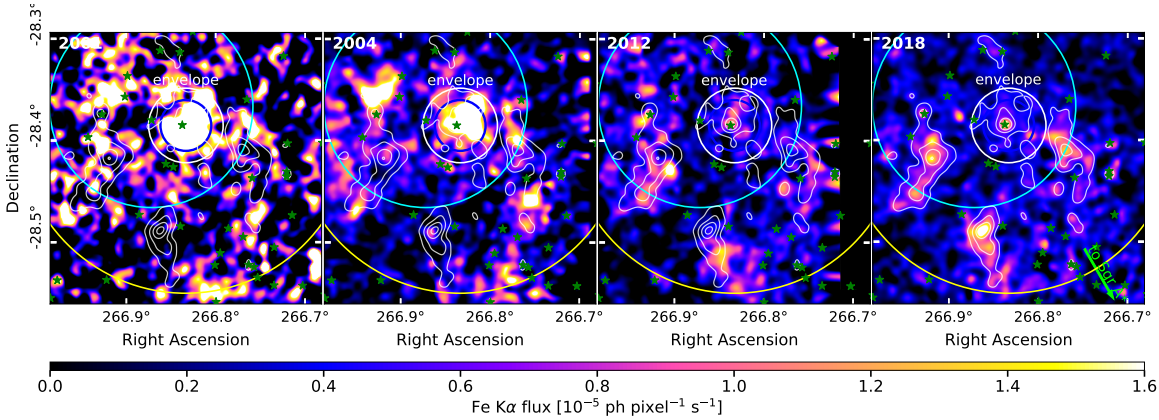

Figure 7.3: The morphology of Fe Kα emission from Sgr B2 is shown as observed in 2001 (left), 2004 (center left), 2012 (center right), and 2018 (right) by *XMM-Newton pn*. The images are exposure corrected, with continuum subtraction performed as in Figure 7.1. The contours (white) from Figure 7.1 illustrate the non-exposure-corrected Fe Kα morphology observed in 2018. The 6′ (cyan) and 90″ (dark blue) regions corresponding to Section 7.5.1 and Figure 7.4 are shown. The diffuse (yellow, 9.9′) and envelope (white, 2.2′) regions of the simplified Sgr B2 gas model, as well as the brightest hard X-ray sources (green stars) from the Chandra Source Catalog 2.0 [337], are also shown for reference. The arrow (lime) points toward Sgr A*.

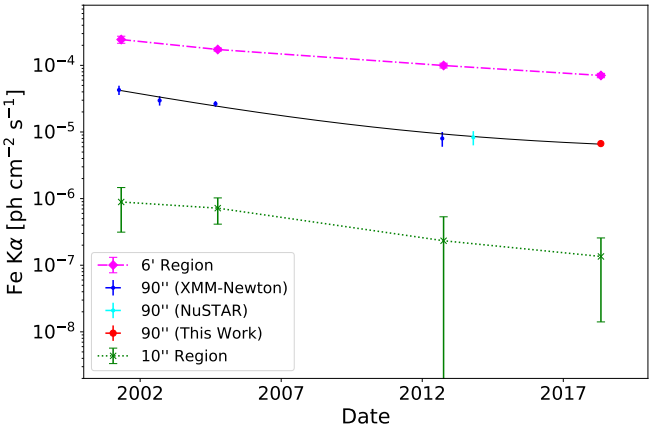

Figure 7.4: Time variability of the neutral Fe Kα line flux is shown for a 6′-radius region representing the cloud overall (magenta), the central 90″ (red, blue, and cyan) and the core (red). The light curve of the 6′ region, which includes most of the diffuse emission, shows that the Fe Kα flux from the cloud overall has decreased to $23 \pm 4\%$ of the 2001 over this time period. The light curve for the central 90″ contains the data point calculated in Section 7.4 (red) alongside earlier measurements by [306] with *XMM-Newton* (blue), and *NuSTAR* (cyan). The black curve is an exponential fitted to the data. We note that the emissions from the central 90″ fall off more steeply compared to the 6′ region, likely due to the effects of the irregularly brightening substructures in the diffuse region. The 2018 Fe Kα flux from the inner 90″ of Sgr B2 is $9 \pm 3\%$ of the value measured in 2001 and $54 \pm 18\%$ of its value in 2012. The green curve shows the light curve for the central 10″-radius region, which corresponds to the $\sim 15''$ half-power diameter of *XMM-Newton* together with the width of the core.

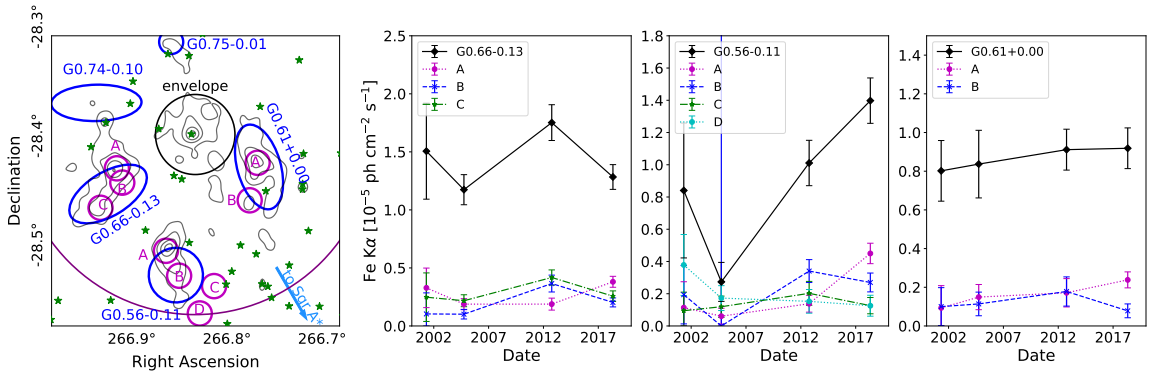

Figure 7.5: *Panel 1:* The contours of the 6.4 keV line emission from 2018 are shown in the same projection as Figure 7.3. The regions (dark blue) identified as Sgr B2 substructures G0.66-0.13, G0.56-0.11, G0.75-0.10, and G0.61+0.00 are shown. G0.74-0.10, identified by [209], is also shown for reference, though it is not detected in 2018 and not treated in this work. We have further identified several 40″-radius features (magenta, A, B, C...) that illustrate the changes in morphology within each substructure over time. All region positions are given in Table 7.2. The arrow (light blue) shows the direction to Sgr A*. *Panels 2-4:* The remaining panels show the Fe Kα light curves extracted from the Sgr B2 substructures G0.66-0.13 (Panel 2), G0.56-0.11 (Panel 3), and G0.61+0.00 (Panel 4) outlined in Panel 1. The overall light curve from each substructure is in black, while the light curves of the corresponding 40″-radius features are plotted on the same axes. Substructure G0.66-0.13 was observed to brighten in 2012, but became dim again in 2018. Light curves for the 40″-radius regions (A, B, and C) associated with G0.66-0.13 behave differently over time, with circle A (magenta, farthest from Sgr A* in the projected plane) brightening only in 2018 while B and C follow the pattern of the parent substructure. Substructure G0.56-0.11 has brightened continuously since 2004, but analysis of 40″ features illustrates that this pattern is not uniform throughout the substructure. Instead, the brightening in 2012 is driven by region marked B (blue) while in 2018 the flux is driven by region A (magenta). Finally, while the light curve for the newly identified structure G0.61+0.00 is consistent with a constant in time, the 40″-radius features again illustrate an evolving morphology within the substructure.

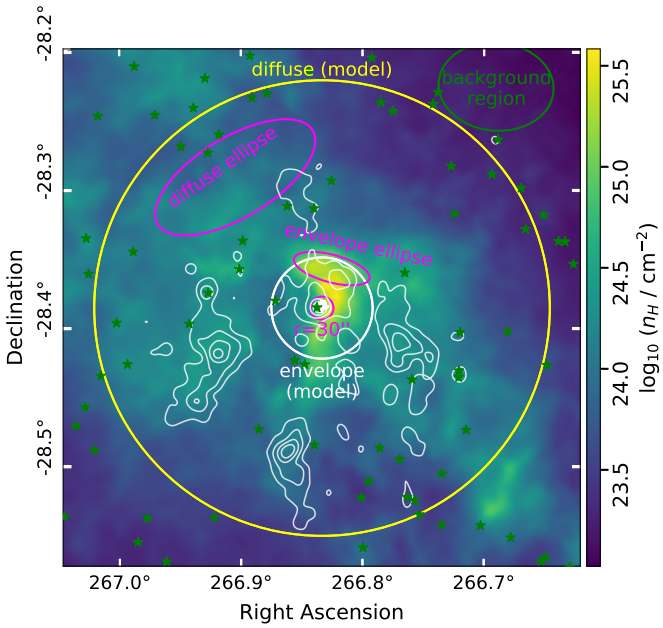

Figure 7.6: The hydrogen column density as measured by Herschel [322] is shown in log scale and illustrates the complexity of the Sgr B2 structure compared to the simple model (yellow, 9.9′ diffuse, and white, 2.2′ envelope). The regions used in Table 7.4 are shown in magenta as the ellipses representing the clean diffuse and envelope regions, and with the 30″ circle. The background region is also shown (green ellipse), alongside the brightest hard point sources from the Chandra Source Catalog (green stars).

Chapter 8

Conclusion

On Earth, we are situated near the edge of our Galaxy's disk of stars and gas, ∼26000 light years from the center. Gravitational observations have demonstrated that this disk is just a small part of the Galaxy's structure, which is dominated by a much larger halo of an invisible dark matter of unknown origin and composition. In the modern picture, this dark matter, which is >5 times more abundant than atoms, is responsible for the evolution of all galaxies and large-scale structure in the Universe. Despite the ubiquity of the dark matter, and despite years of searches, the microscopic physics of the dark matter remains a mystery. Detection of the particle nature of the dark matter is thus a central and unifying problem in modern particle and astrophysics.

Indirect dark matter detection experiments search for excesses in the fluxes of cosmic-ray particles as signatures of the annihilation or decay of the Galactic dark matter. In this framework, the entire Galaxy can be the laboratory. While cosmic rays from astrophysical sources form a challenging and persistent background for indirect dark matter searches, they also provide a unique window into the Galactic environment. In the context of this simultaneous challenge and opportunity, this dissertation describes two distinct experimental approaches. First, the GAPS Antarctic balloon mission is specifically designed to target low-energy antinuclei, which feature relatively low (antiprotons) to undetectably small (antideuterons and antihelium-3) expected fluxes from standard astrophysical sources but could be produced in the annihilation or decay of dark matter. GAPS is an international and collaborative ef-

fort whose origins far predate my tenure as a PhD student and whose first Antarctic flight is still upcoming. Therefore, this dissertation details my contributions to 1) the development and characterization of the unique silicon detectors that are central to GAPS' antinucleus particle identification strategy and 2) analysis tools demonstrating GAPS' sensitivity to detect antiprotons. As a second approach, this dissertation describes the analysis of X-ray astrophysics observations of Sagittarius B2, a dense molecular gas cloud near the galactic center. By analyzing these observations, we are able to probe the low-energy cosmic ray populations 26000 light years away, near the Galactic Center.

Both dark matter and cosmic rays are, each in their own way, agents of Galactic evolution. As fields of study, both require a fundamentally interdisciplinary approach, involving particle physics, astrophysics, and, in the case of dark matter, cosmology. In their dynamics and structures, both dark matter and cosmic rays require complex pictures and seem to resist the simplest models. What we can measure often depends on our situation in the Galaxy and on our Galaxy's specific history – a single nearby pulsar or a local clump of dark matter could fundamentally change our view.

Bibliography

[1] Thomson, M. *Modern Particle Physics*. Cambridge University Press (2013).

[2] Baak, M., et al. The electroweak fit of the standard model after the discovery of a new boson at the LHC. *European Physical Journal C* **72**:2205, 1209.2716.

[3] Weinberg, S. Implications of dynamical symmetry breaking. *Physical Review D* **13** (4) 1976 974.

[4] Susskind, L. Dynamics of spontaneous symmetry breaking in the Weinberg-Salam theory. *Physical Review D* **20** (10) 1979 2619.

[5] Peccei, R. and Quinn, H. Cp conservation in the presence of pseudoparticles. *Physical Review Letters - PHYS REV LETT* **38** 1977 1440.

[6] null null, et al. High-precision measurement of the w boson mass with the cdf ii detector. *Science* **376** (6589) 2022 170, https://www.science.org/doi/pdf/10.1126/science.abk1781, URL https://www.science.org/doi/abs/10.1126/science.abk1781.

[7] Abi, B., et al. (Muon $g-2$ Collaboration). Measurement of the positive muon anomalous magnetic moment to 0.46 ppm. *Phys. Rev. Lett.* **126** 2021 141801, URL https://link.aps.org/doi/10.1103/PhysRevLett.126.141801.

[8] Planck Collaboration, et al. Planck 2018 results. VI. Cosmological parameters. *A&A* **641**:A6, 1807.06209.

[9] Planck Collaboration, et al. Planck 2018 results. VI. Cosmological parameters. *Astronomy and Astrophysics* **641**:A6, 1807.06209.

[10] Zwicky, F. Die Rotverschiebung von extragalaktischen Nebeln. *Helvetica Physica Acta* **6** 1933 110.

[11] Zwicky, F. On the Masses of Nebulae and of Clusters of Nebulae. *The Astrophysical Journal* **86** 1937 217, URL https://ned.ipac.caltech.edu/level5/Sept01/Zwicky/paper.pdf.

[12] Rubin, V.C. and Ford, W. Kent, J. Rotation of the Andromeda Nebula from a Spectroscopic Survey of Emission Regions. *The Astrophysical Journal* **159** 1970 379.

[13] Rubin, V.C., Ford, W. K., J., and Thonnard, N. Extended rotation curves of high-luminosity spiral galaxies. IV. Systematic dynamical properties, Sa -> Sc. *The Astrophysical Journal Letters* **225** 1978 L107.

[14] Hubble, E. and Humason, M.L. The Velocity-Distance Relation among Extra-Galactic Nebulae. *The Astrophysical Journal* **74** 1931 43.

[15] Bertone, G. and Hooper, D. History of dark matter. *Reviews of Modern Physics* **90** (4):045002, 1605.04909.

[16] Kelvin, B. *Baltimore lectures on molecular dynamics and the wave theory of light*. Cambridge University Press (1904), URL https://archive.org/details/baltimorelecture00kelviala/page/n8/mode/2up.

[17] Rubin, V. *Bright Galaxies Dark Matters*. Masters of Modern Physics. Copernicus Books (1996).

[18] Roberts, M.S. A High-Resolution 21-CM Hydrogen-Line Survey of the Andromeda Nebula. *The Astrophysical Journal* **144** 1966 639.

[19] Massey, R., et al. Dark matter maps reveal cosmic scaffolding. *Nature* **445** (7125) 2007 286, URL https://doi.org/10.1038/nature05497.

[20] Parker, L.C., Hoekstra, H., Hudson, M.J., van Waerbeke, L., and Mellier, Y. The masses and shapes of dark matter halos from galaxy-galaxy lensing in the CFHT legacy survey. *The Astrophysical Journal* **669** (1) 2007 21, URL https://doi.org/10.1086/521541.

[21] Clowe, D., et al. A Direct Empirical Proof of the Existence of Dark Matter. *The Astrophysical Journal Letters* **648** (2) 2006 L109, astro-ph/0608407.

[22] Robertson, A., Massey, R., and Eke, V. What does the Bullet Cluster tell us about self-interacting dark matter? *Monthly Notices of the Royal Astronomical Society* **465** (1) 2017 569, 1605.04307.

[23] Bacon, R., et al. The MUSE Extremely Deep Field: The cosmic web in emission at high redshift. *Astronomy and Astrophysics* **647**:A107, 2102.05516.

[24] Necib, L., et al. Chasing Accreted Structures within Gaia DR2 Using Deep Learning. *The Astrophysical Journal* **903** (1):25, 1907.07681.

[25] Andrews, J.J., et al. A Young, Low-Density Stellar Stream in the Milky Way Disk: Theia 456. *arXiv e-prints* arXiv:2110.06278, 2110.06278.

[26] Archidiacono, M., Hannestad, S., Mirizzi, A., Raffelt, G., and Wong, Y.Y.Y. Axion hot dark matter bounds after Planck. *Journal of Cosmology and Astroparticle Physics* **2013** (10):020, 1307.0615.

[27] Springel, V., et al. Simulations of the formation, evolution and clustering of galaxies and quasars. *Nature* **435** (7042) 2005 629, astro-ph/0504097.

[28] Gao, L., Springel, V., and White, S.D.M. The age dependence of halo clustering. *Monthly Notices of the Royal Astronomical Society* **363** (1) 2005 L66, astro-ph/0506510.

[29] Navarro, J.F., Frenk, C.S., and White, S.D.M. The Structure of Cold Dark Matter Halos. *The Astrophysical Journal* **462** 1996 563, astro-ph/9508025.

[30] Walter, F., et al. THINGS: The H I Nearby Galaxy Survey. *The Astronomical Journal* **136** (6) 2008 2563, 0810.2125.

[31] Hunter, D.A., et al. Little Things. *The Astronomical Journal* **144** (5):134, 1208.5834.

[32] Spergel, D.N. and Steinhardt, P.J. Observational Evidence for Self-Interacting Cold Dark Matter. *Physical Review Letters* **84** (17) 2000 3760, astro-ph/9909386.

[33] El-Zant, A., Shlosman, I., and Hoffman, Y. Dark Halos: The Flattening of the Density Cusp by Dynamical Friction. *The Astrophysical Journal* **560** (2) 2001 636, astro-ph/0103386.

[34] Pontzen, A. and Governato, F. How supernova feedback turns dark matter cusps into cores. *Monthly Notices of the Royal Astronomical Society* **421** (4) 2012 3464, 1106.0499.

[35] Bullock, J.S. and Boylan-Kolchin, M. Small-Scale Challenges to the ΛCDM Paradigm. *Annual Review of Astronomy and Astrophysics* **55** (1) 2017 343, 1707.04256.

[36] Poulin, V., Serpico, P.D., and Lesgourgues, J. A fresh look at linear cosmological constraints on a decaying Dark Matter component. *Journal of Cosmology and Astroparticle Physics* **2016** (8):036, 1606.02073.

[37] Fukuda, Y., et al. Evidence for Oscillation of Atmospheric Neutrinos. *Physical Review Letters* **81** (8) 1998 1562, hep-ex/9807003.

[38] Aker, M., et al. Direct neutrino-mass measurement with sub-electronvolt sensitivity. *Nature Physics* **18** (2) 2022 160, URL https://doi.org/10.1038/s41567-021-01463-1.

[39] Iršič, V., Viel, M., Haehnelt, M.G., Bolton, J.S., and Becker, G.D. First Constraints on Fuzzy Dark Matter from Lyman-α Forest Data and Hydrodynamical Simulations. *Physical Review Letters* **119** (3):031302, 1703.04683.

[40] Schutz, K. Subhalo mass function and ultralight bosonic dark matter. *Physical Review D* **101** (12):123026, 2001.05503.

[41] Carr, B. and Kühnel, F. Primordial Black Holes as Dark Matter: Recent Developments. *Annual Review of Nuclear and Particle Science* **70** 2020 355, 2006.02838.

[42] Hawking, S. Gravitationally collapsed objects of very low mass. *Monthly Notices of the Royal Astronomical Society* **152** 1971 75.

[43] Carr, B.J. and Hawking, S.W. Black Holes in the Early Universe. *Monthly Notices of the Royal Astronomical Society* **168** (2) 1974 399. ISSN 0035-8711, https://academic.oup.com/mnras/article-pdf/168/2/399/8079885/mnras168-0399.pdf, URL https://doi.org/10.1093/mnras/168.2.399.

[44] Hawking, S.W. Particle creation by black holes. *Communications in Mathematical Physics* **43** (3) 1975 199.

[45] Carr, B., Kohri, K., Sendouda, Y., and Yokoyama, J. Constraints on Primordial Black Holes. *Reports on Progress in Physics* **84** (11):arXiv:2002.12778, 2002.12778.

[46] Barrau, A., et al. Antiprotons from primordial black holes. *Astronomy and Astrophysics* **388** 2002 676, astro-ph/0112486.

[47] Herms, J., Ibarra, A., Vittino, A., and Wild, S. Antideuterons in cosmic rays: sources and discovery potential. *Journal of Cosmology and Astroparticle Physics* **2017** (2):018, 1610.00699.

[48] Carr, B.J., Kohri, K., Sendouda, Y., and Yokoyama, J. New cosmological constraints on primordial black holes. *Phys. Rev. D* **81** 2010 104019, URL https://link.aps.org/doi/10.1103/PhysRevD.81.104019.

[49] Green, A.M. and Kavanagh, B.J. Primordial black holes as a dark matter candidate. *Journal of Physics G Nuclear Physics* **48** (4):043001, 2007.10722.

[50] Abbott, B.P., et al. (LIGO Scientific Collaboration and Virgo Collaboration). Observation of gravitational waves from a binary black hole merger. *Phys. Rev. Lett.* **116** 2016 061102, URL https://link.aps.org/doi/10.1103/PhysRevLett.116.061102.

[51] Abbott, B.P., et al. (LIGO Scientific Collaboration and Virgo Collaboration). Gw151226: Observation of gravitational waves from a 22-solar-mass binary black hole coalescence. *Phys. Rev. Lett.* **116** 2016 241103, URL https://link.aps.org/doi/10.1103/PhysRevLett.116.241103.

[52] Abbott, B.P., et al. The Rate of Binary Black Hole Mergers Inferred from Advanced LIGO Observations Surrounding GW150914. *The Astrophysical Journal Letters* **833** (1):L1, 1602.03842.

[53] Abbott, B.P., et al. (LIGO Scientific Collaboration and Virgo Collaboration). Gwtc-1: A gravitational-wave transient catalog of compact binary mergers observed by ligo and virgo during the first and second observing runs. *Phys. Rev. X* **9** 2019 031040, URL https://link.aps.org/doi/10.1103/PhysRevX.9.031040.

[54] Niikura, H., et al. Microlensing constraints on primordial black holes with subaru/hsc andromeda observations. *Nature Astronomy* **3** (6) 2019 524, URL https://doi.org/10.1038/s41550-019-0723-1.

[55] Steigman, G., Dasgupta, B., and Beacom, J.F. Precise relic WIMP abundance and its impact on searches for dark matter annihilation. *Physical Review D* **86** (2):023506, 1204.3622.

[56] Slatyer, T.R. TASI Lectures on Indirect Detection of Dark Matter. *arXiv e-prints* arXiv:1710.05137, 1710.05137.

[57] Griest, K. and Kamionkowski, M. Unitarity limits on the mass and radius of dark-matter particles. *Phys. Rev. Lett.* **64** 1990 615, URL https://link.aps.org/doi/10.1103/PhysRevLett.64.615.

[58] Feng, J.L. Naturalness and the status of supersymmetry. *Annual Review of Nuclear and Particle Science* **63** (1) 2013 351, https://doi.org/10.1146/annurev-nucl-102010-130447, URL https://doi.org/10.1146/annurev-nucl-102010-130447.

[59] Ellis, J. and Olive, K.A. Supersymmetric dark matter candidates. In G. Bertone, ed., *Particle Dark Matter : Observations, Models and Searches*, 142. Cambridge University Press (2010).

[60] Hooper, D. and Profumo, S. Dark matter and collider phenomenology of universal extra dimensions. *Physics Reports* **453** (2-4) 2007 29, hep-ph/0701197.

[61] Boveia, A. and Doglioni, C. Dark matter searches at colliders. *Annual Review of Nuclear and Particle Science* **68** (1) 2018 429, https://doi.org/10.1146/annurev-nucl-101917-021008, URL https://doi.org/10.1146/annurev-nucl-101917-021008.

[62] Felcini, M. Searches for Dark Matter Particles at the LHC. In *Proceedings of the 53rd Rencontres de Moriond on Cosmology* (2018), 1809.06341.

[63] ATLAS Collaboration. Search for invisible Higgs-boson decays in events with vector-boson fusion signatures using 139 fb^{-1} of proton-proton data recorded by the ATLAS experiment. *arXiv e-prints* arXiv:2202.07953, 2202.07953.

[64] Abdallah, J., et al. Simplified models for dark matter searches at the LHC. *Physics of the Dark Universe* **9** 2015 8, 1506.03116.

[65] Boveia, A., et al. Recommendations on presenting LHC searches for missing transverse energy signals using simplified s-channel models of dark matter. *arXiv e-prints* arXiv:1603.04156, 1603.04156.

[66] Albert, A., et al. Recommendations of the LHC Dark Matter Working Group: Comparing LHC searches for heavy mediators of dark matter production in visible and invisible decay channels. *arXiv e-prints* arXiv:1703.05703, 1703.05703.

[67] Bhattacharjee, P., Chaudhury, S., Kundu, S., and Majumdar, S. Deriving the velocity distribution of Galactic dark matter particles from the rotation curve data. *Physical Review D* **87** (8):083525, 1210.2328.

[68] Baudis, L. Direct dark matter detection: The next decade. *Physics of the Dark Universe* **1** (1) 2012 94. ISSN 2212-6864, URL https://www.sciencedirect.com/science/article/pii/S2212686412000106.

[69] Read, J.I. The local dark matter density. *Journal of Physics G Nuclear Physics* **41** (6):063101, 1404.1938.

[70] Billard, J., et al. Direct Detection of Dark Matter – APPEC Committee Report. *arXiv e-prints* arXiv:2104.07634, 2104.07634.

[71] Akerib, D.S., et al. Results from a Search for Dark Matter in the Complete LUX Exposure. *Physical Review Letters* **118** (2):021303, 1608.07648.

[72] Cui, X., et al. (PandaX-II Collaboration). Dark matter results from 54-ton-day exposure of pandax-ii experiment. *Phys. Rev. Lett.* **119** 2017 181302, URL https://link.aps.org/doi/10.1103/PhysRevLett.119.181302.

[73] Aprile, E., et al. (XENON Collaboration 7). Dark matter search results from a one ton-year exposure of xenon1t. *Phys. Rev. Lett.* **121** 2018 111302, URL https://link.aps.org/doi/10.1103/PhysRevLett.121.111302.

[74] Knapen, S., Lin, T., Pyle, M., and Zurek, K.M. Detection of light dark matter with optical phonons in polar materials. *Physics Letters B* **785** 2018 386, 1712.06598.

[75] Barak, L., et al. SENSEI: Direct-Detection Results on sub-GeV Dark Matter from a New Skipper CCD. *Physical Review Letters* **125** (17):171802, 2004.11378.

[76] Lee, S.J., Kilminster, B., and Macchiolo, A. Dark Matter in CCDs at Modane (DAMIC-M): a silicon detector apparatus searching for low-energy physics processes. *Journal of Instrumentation* **15** (2) 2020 C02050, 2001.01209.

[77] SPICE/HeRALD Collaboration, et al. Scintillation yield from electronic and nuclear recoils in superfluid ^{4}He. *arXiv e-prints* arXiv:2108.02176, 2108.02176.

[78] Hill, R.J. and Solon, M.P. WIMP-nucleon scattering with heavy WIMP effective theory. *Physical Review Letters* **112**:arXiv:1309.4092, 1309.4092.

[79] Steigman, G. Equivalent neutrinos, light WIMPs, and the chimera of dark radiation. *Physical Review D* **87** (10):103517, 1303.0049.

[80] Slatyer, T.R. Indirect dark matter signatures in the cosmic dark ages. I. Generalizing the bound on s -wave dark matter annihilation from Planck results. *Physical Review D* **93** (2):023527, 1506.03811.

[81] Adriani, O., et al. An anomalous positron abundance in cosmic rays with energies 1.5-100GeV. *Nature* **458** (7238) 2009 607, 0810.4995.

[82] Ackermann, M., et al. (Fermi LAT Collaboration). Measurement of separate cosmic-ray electron and positron spectra with the fermi large area telescope. *Phys. Rev. Lett.* **108** 2012 011103, URL https://link.aps.org/doi/10.1103/PhysRevLett.108.011103.

[83] Aguilar, M., et al. (AMS Collaboration). Towards understanding the origin of cosmic-ray positrons. *Phys. Rev. Lett.* **122** 2019 041102, URL https://link.aps.org/doi/10.1103/PhysRevLett.122.041102.

[84] Aguilar, M., et al. Antiproton Flux, Antiproton-to-Proton Flux Ratio, and Properties of Elementary Particle Fluxes in Primary Cosmic Rays Measured with the Alpha Magnetic Spectrometer on the International Space Station. *Physics Review Letters* **117** (9):091103.

[85] Goodenough, L. and Hooper, D. Possible Evidence For Dark Matter Annihilation In The Inner Milky Way From The Fermi Gamma Ray Space Telescope. *arXiv e-prints* arXiv:0910.2998, 0910.2998.

[86] Hooper, D. and Goodenough, L. Dark matter annihilation in the galactic center as seen by the fermi gamma ray space telescope. *Physics Letters B* **697** (5) 2011 412. ISSN 0370-2693, URL https://www.sciencedirect.com/science/article/pii/S0370269311001742.

[87] Petrović, J., Serpico, P.D., and Zaharijaš, G. Galactic Center gamma-ray "excess" from an active past of the Galactic Centre? *Journal of Cosmology and Astroparticle Physics* **2014** (10):052, 1405.7928.

[88] Carlson, E. and Profumo, S. Cosmic ray protons in the inner Galaxy and the Galactic Center gamma-ray excess. *Physical Review D* **90** (2):023015, 1405.7685.

[89] Cholis, I., et al. The Galactic Center GeV excess from a series of leptonic cosmic-ray outbursts. *Journal of Cosmology and Astroparticle Physics* **2015** (12):005, 1506.05119.

[90] Brandt, T.D. and Kocsis, B. DISRUPTED GLOBULAR CLUSTERS CAN EXPLAIN THE GALACTIC CENTER GAMMA-RAY EXCESS. *The Astrophysical Journal* **812** (1) 2015 15, URL https://doi.org/10.1088/0004-637x/812/1/15.

[91] Gaggero, D., Taoso, M., Urbano, A., Valli, M., and Ullio, P. Towards a realistic astrophysical interpretation of the gamma-ray Galactic center excess. *Journal of Cosmology and Astroparticle Physics* **2015** (12):056, 1507.06129.

[92] Lee, S.K., Lisanti, M., Safdi, B.R., Slatyer, T.R., and Xue, W. Evidence for Unresolved γ -Ray Point Sources in the Inner Galaxy. *Physical Review Letters* **116** (5):051103, 1506.05124.

[93] Bartels, R., Krishnamurthy, S., and Weniger, C. Strong Support for the Millisecond Pulsar Origin of the Galactic Center GeV Excess. *Physical Review Letters* **116** (5):051102, 1506.05104.

[94] Leane, R.K. and Slatyer, T.R. Revival of the dark matter hypothesis for the galactic center gamma-ray excess. *Phys. Rev. Lett.* **123** 2019 241101, URL https://link.aps.org/doi/10.1103/PhysRevLett.123.241101.

[95] Buschmann, Malte and Rodd, Nicholas L. and Safdi, Benjamin R. and Chang, Laura J. and Mishra-Sharma, Siddharth and Lisanti, Mariangela and Macias, Oscar. Foreground mismodeling and the point source explanation of the Fermi Galactic Center excess. *Physical Review D* **102** (2):023023, 2002.12373.

[96] Murgia, S. The fermi–lat galactic center excess: Evidence of annihilating dark matter? *Ann. Rev. Nucl. Part. Sci.* **70** (1) 2020 455, https://doi.org/10.1146/annurev-nucl-101916-123029, URL https://doi.org/10.1146/annurev-nucl-101916-123029.

[97] Chernyshov, D.O., Egorov, A.E., Dogiel, V.A., and Ivlev, A.V. On a Possible Origin of the Gamma-ray Excess around the Galactic Center. *Symmetry* **13** (8) 2021 1432, 2108.04104.

[98] Cholis, I., Zhong, Y.M., McDermott, S.D., and Surdutovich, J.P. The Return of the Templates: Revisiting the Galactic Center Excess with Multi-Messenger Observations. *arXiv e-prints* arXiv:2112.09706, 2112.09706.

[99] Dinsmore, J.T. and Slatyer, T.R. Luminosity functions consistent with a pulsar-dominated Galactic Center Excess. *arXiv e-prints* arXiv:2112.09699, 2112.09699.

[100] Ploeg, H. The Galactic Millisecond Pulsar Population: Implications for the Galactic Center Excess. *arXiv e-prints* arXiv:2109.08439, 2109.08439.

[101] Arkani-Hamed, N., Finkbeiner, D.P., Slatyer, T.R., and Weiner, N. A theory of dark matter. *Physical Review D* **79** (1):015014, 0810.0713.

[102] Blasi, P. Origin of the Positron Excess in Cosmic Rays. *Physical Review Letters* **103** (5):051104, 0903.2794.

[103] Grasso, D., et al. On possible interpretations of the high energy electron-positron spectrum measured by the Fermi Large Area Telescope. *Astroparticle Physics* **32** (2) 2009 140, 0905.0636.

[104] Gupta, N. and Torres, D.F. pγ interactions in Galactic jets as a plausible origin of the positron excess. *Monthly Notices of the Royal Astronomical Society* **441** (4) 2014 3122. ISSN 0035-8711, https://academic.oup.com/mnras/article-pdf/441/4/3122/4048961/stu770.pdf, URL https://doi.org/10.1093/mnras/stu770.

[105] Fang, K., Bi, X.J., and Yin, P.F. Reanalysis of the Pulsar Scenario to Explain the Cosmic Positron Excess Considering the Recent Developments. *The Astrophysical Journal* **884** (2):124, 1906.08542.

[106] Diesing, R. and Caprioli, D. Nonsecondary origin of cosmic ray positrons. *Physical Review D* **101** (10):103030, 2001.02240.

[107] De Sarkar, A., Biswas, S., and Gupta, N. Positron excess from cosmic ray interactions in galactic molecular clouds. *Journal of High Energy Astrophysics* **29** 2021 1, 1911.12977.

[108] Cuoco, A., Krämer, M., and Korsmeier, M. Novel Dark Matter Constraints from Antiprotons in Light of AMS-02. *Physics Review Letters* **118** (19):191102, 1610.03071.

[109] Cui, M.Y., Yuan, Q., Tsai, Y.L.S., and Fan, Y.Z. Possible Dark Matter Annihilation Signal in the AMS-02 Antiproton Data. *Physics Review Letters* **118** (19):191101, 1610.03840.

[110] Cui, M.Y., Pan, X., Yuan, Q., Fan, Y.Z., and Zong, H.S. Revisit of cosmic ray antiprotons from dark matter annihilation with updated constraints on the background model from AMS-02 and collider data. *Journal of Cosmology and Astroparticle Physics* **2018** (6):024, 1803.02163.

[111] Reinert, A. and Winkler, M.W. A precision search for WIMPs with charged cosmic rays. *Journal of Cosmology and Astroparticle Physics* **2018** (1):055, 1712.00002.

[112] Cholis, I., Linden, T., and Hooper, D. A robust excess in the cosmic-ray antiproton spectrum: Implications for annihilating dark matter. *Physics Review D* **99** (10):103026, 1903.02549.

[113] Cuoco, A., Heisig, J., Klamt, L., Korsmeier, M., and Krämer, M. Scrutinizing the evidence for dark matter in cosmic-ray antiprotons. *Physics Review D* **99** (10):103014, 1903.01472.

[114] Boudaud, M., et al. AMS-02 Antiprotons are Consistent with a Secondary Astrophysical Origin. In *36th International Cosmic Ray Conference (ICRC2019)*, vol. 36 of *International Cosmic Ray Conference*, 38 (2019).

[115] Boudaud, M., et al. Ams-02 antiprotons' consistency with a secondary astrophysical origin. *Phys. Rev. Research* **2** 2020 023022, URL https://link.aps.org/doi/10.1103/PhysRevResearch.2.023022.

[116] Heisig, J., Korsmeier, M., and Winkler, M.W. Dark matter or correlated errors: Systematics of the AMS-02 antiproton excess. *Physical Review Research* **2** (4):043017, 2005.04237.

[117] Calore, F., et al. AMS-02 antiprotons and dark matter: Trimmed hints and robust bounds. *arXiv e-prints* arXiv:2202.03076, 2202.03076.

[118] Abramowski, A., et al. Search for dark matter annihilation signatures in H.E.S.S. observations of dwarf spheroidal galaxies. *Physical Review D* **90** (11):112012, 1410.2589.

[119] Ackermann, M., et al. Dark matter constraints from observations of 25 MilkyÂ Way satellite galaxies with the Fermi Large Area Telescope. *Physical Review D* **89** (4):042001, 1310.0828.

[120] Ackermann, M., et al. Searching for Dark Matter Annihilation from Milky Way Dwarf Spheroidal Galaxies with Six Years of Fermi Large Area Telescope Data. *Physical Review Letters* **115** (23):231301, 1503.02641.

[121] Archambault, S., et al. Dark matter constraints from a joint analysis of dwarf Spheroidal galaxy observations with VERITAS. *Physical Review D* **95** (8):082001, 1703.04937.

[122] Albert, A., et al. Searching for Dark Matter Annihilation in Recently Discovered Milky Way Satellites with Fermi-Lat. *The Astrophysical Journal* **834** (2):110, 1611.03184.

[123] Albert, A., et al. Dark matter limits from dwarf spheroidal galaxies with the HAWC gamma-ray observatory. *The Astrophysical Journal* **853** (2) 2018 154, URL https://doi.org/10.3847/1538-4357/aaa6d8.

[124] Cuoco, A., Heisig, J., Korsmeier, M., and Krämer, M. Constraining heavy dark matter with cosmic-ray antiprotons. *Journal of Cosmology and Astroparticle Physics* **2018** (4):004, 1711.05274.

[125] Accardo, L., et al. (AMS Collaboration). High statistics measurement of the positron fraction in primary cosmic rays of 0.5–500 gev with the alpha magnetic spectrometer on the international space station. *Phys. Rev. Lett.* **113** 2014 121101, URL https://link.aps.org/doi/10.1103/PhysRevLett.113.121101.

[126] Leane, R.K., Slatyer, T.R., Beacom, J.F., and Ng, K.C.Y. GeV-scale thermal WIMPs: Not even slightly ruled out. *Phys. Rev. D* **98** (2):023016, 1805.10305.

[127] Elor, G., Rodd, N.L., Slatyer, T.R., and Xue, W. Model-independent indirect detection constraints on hidden sector dark matter. *Journal of Cosmology and Astroparticle Physics* **2016** (6):024, 1511.08787.

[128] Schlickeiser, R., Caglar, M., and Lazarian, A. Cosmic Rays and MHD Turbulence Generation in Interstellar Giant Molecular Clouds. *ApJ* **824** (2):89.

[129] Padovani, M., Ivlev, A.V., Galli, D., and Caselli, P. Cosmic-ray ionisation in circumstellar discs. *A&A* **614**:A111, 1803.09348.

[130] Enßlin, T.A., Pfrommer, C., Springel, V., and Jubelgas, M. Cosmic ray physics in calculations of cosmological structure formation. *A&A* **473** (1) 2007 41, astro-ph/0603484.

[131] Grenier, I.A., Black, J.H., and Strong, A.W. The Nine Lives of Cosmic Rays in Galaxies. *Ann. Rev. Astron. Astrophys.* **53** 2015 199.

[132] Ipavich, F.M. Galactic winds driven by cosmic rays. *ApJ* **196** 1975 107.

[133] Grießmeier, J.M., Tabataba-Vakili, F., Stadelmann, A., Grenfell, J.L., and Atri, D. Galactic cosmic rays on extrasolar Earth-like planets. I. Cosmic ray flux. *A&A* **581**:A44, 1509.00735.

[134] Ruszkowski, M., et al. Supermassive Black Hole Feedback. *BAAS* **51** (3):326, 1903.09686.

[135] Orlando, E. and Strong, A. Galactic synchrotron emission with cosmic ray propagation models. *MNRAS* **436** (3) 2013 2127, 1309.2947.

[136] Pérez de los Heros, C. Status, Challenges and Directions in Indirect Dark Matter Searches. *Symmetry* **12** (10) 2020 1648, 2008.11561.

[137] Mészáros, P., Fox, D.B., Hanna, C., and Murase, K. Multi-messenger astrophysics. *Nature Reviews Physics* **1** (10) 2019 585, 1906.10212.

[138] Hess, V.F. über neuerungen und erfahrungen an den radiummessungen nach der gamma-strahlenmethode. *Physikalische Zeitschrift* **14** 1913 1135.

[139] Webber, W.R. and McDonald, F.B. Recent voyager 1 data indicate that on 25 august 2012 at a distance of 121.7 au from the sun, sudden and unprecedented intensity changes were observed in anomalous and galactic cosmic rays. *Geophysical Research Letters* **40** (9) 2013 1665, https://agupubs.onlinelibrary.wiley.com/doi/pdf/10.1002/grl.50383, URL https://agupubs.onlinelibrary.wiley.com/doi/abs/10.1002/grl.50383.

[140] Gurnett, D.A., Kurth, W.S., Burlaga, L.F., and Ness, N.F. In situ observations of interstellar plasma with voyager 1. *Science* **341** (6153) 2013 1489, https://www.science.org/doi/pdf/10.1126/science.1241681, URL https://www.science.org/doi/abs/10.1126/science.1241681.

[141] Richardson, J.D., Belcher, J.W., Garcia-Galindo, P., and Burlaga, L.F. Voyager 2 plasma observations of the heliopause and interstellar medium. *Nature Astronomy* **3** (11) 2019 1019, URL https://doi.org/10.1038/s41550-019-0929-2.

[142] Stone, E.C., Cummings, A.C., Heikkila, B.C., and Lal, N. Cosmic ray measurements from voyager 2 as it crossed into interstellar space. *Nature Astronomy* **3** (11) 2019 1013, URL https://doi.org/10.1038/s41550-019-0928-3.

[143] Stone, E.C., et al. Cosmic ray investigation for the voyager missions; energetic particle studies in the outer heliosphere—and beyond. *Space Science Reviews* **21** (3) 1977 355, URL https://doi.org/10.1007/BF00211546.

[144] Cummings, A.C., et al. Galactic Cosmic Rays in the Local Interstellar Medium: Voyager 1 Observations and Model Results. *The Astrophysical Journal* **831** (1):18.

[145] Bisschoff, D., Potgieter, M.S., and Aslam, O.P.M. New Very Local Interstellar Spectra for Electrons, Positrons, Protons, and Light Cosmic Ray Nuclei. *Astrophysical Journal* **878** (1):59, 1902.10438.

[146] Aslam, O.P.M., Bisschoff, D., Potgieter, M.S., Boezio, M., and Munini, R. Modeling of Heliospheric Modulation of Cosmic-Ray Positrons in a Very Quiet Heliosphere. *Astrophysics Journal* **873** (1):70, 1811.10710.

[147] Munini, R., et al. (PAMELA). Isotope solar modulation with the PAMELA experiment. *PoS* **ICRC2019** 2020 1130.

[148] Battiston, R. The antimatter spectrometer (ams-02): A particle physics detector in space. *Nuclear Instruments and Methods in Physics Research Section A: Accelerators, Spectrometers, Detectors and Associated Equipment* **588** (1) 2008 227. ISSN 0168-9002, URL https://www.sciencedirect.com/science/article/pii/S0168900208000727.

[149] Adriani, O., et al. Cosmic-Ray Positron Energy Spectrum Measured by PAMELA. *Physical Review Letters* **111** (8):081102, 1308.0133.

[150] Zyla, P.A. et al. (Particle Data Group). Review of Particle Physics. *PTEP* **2020** (8) 2020 083C01.

[151] Abe, K., et al. Measurements of Cosmic-Ray Proton and Helium Spectra from the BESS-Polar Long-duration Balloon Flights over Antarctica. *The Astrophysical Journal* **822** (2):65, 1506.01267.

[152] Tokuno, H., et al. New air fluorescence detectors employed in the Telescope Array experiment. *Nuclear Instruments and Methods in Physics Research A* **676** 2012 54, 1201.0002.

[153] Abu-Zayyad, T., et al. Search for Anisotropy of Ultrahigh Energy Cosmic Rays with the Telescope Array Experiment. *The Astrophysical Journal* **757** (1):26, 1205.5984.

[154] Abbasi, R., et al. Icetop: The surface component of icecube. *Nuclear Instruments and Methods in Physics Research Section A: Accelerators, Spectrometers, Detectors and Associated Equipment* **700** 2013 188. ISSN 0168-9002, URL https://www.sciencedirect.com/science/article/pii/S016890021201217X.

[155] The Pierre Auger Collaboration. The pierre auger cosmic ray observatory. *Nuclear Instruments and Methods in Physics Research Section A: Accelerators, Spectrometers, Detectors and Associated Equipment* **798** 2015 172. ISSN 0168-9002, URL https://www.sciencedirect.com/science/article/pii/S0168900215008086.

[156] Olinto, A.V., et al. POEMMA: Probe Of Extreme Multi-Messenger Astrophysics. In *35th International Cosmic Ray Conference (ICRC2017)*, vol. 301 of *International Cosmic Ray Conference*, 542 (2017), 1708.07599.

[157] Wiencke, L. and Olinto, A. (JEM-EUSO). EUSO-SPB1 Mission and Science. *PoS* **ICRC2017** 2018 1097.

[158] Becker Tjus, J. and Merten, L. Closing in on the origin of Galactic cosmic rays using multimessenger information. *Physics Reports* **872** 2020 1, 2002.00964.

[159] Apel, W.D., et al. Kneelike Structure in the Spectrum of the Heavy Component of Cosmic Rays Observed with KASCADE-Grande. *Physical Review Letters* **107** (17):171104, 1107.5885.

[160] Apel, W.D., et al. (KASCADE-Grande Collaboration). Ankle-like feature in the energy spectrum of light elements of cosmic rays observed with kascade-grande. *Phys. Rev. D* **87** 2013 081101, URL https://link.aps.org/doi/10.1103/PhysRevD.87.081101.

[161] Thoudam, S., et al. Cosmic-ray energy spectrum and composition up to the ankle: the case for a second Galactic component. *Astronomy and Astrophysics* **595**:A33, 1605.03111.

[162] Alves Batista, R., et al. Open questions in cosmic-ray research at ultrahigh energies. *Frontiers in Astronomy and Space Sciences* **6**. ISSN 2296-987X, URL https://www.frontiersin.org/article/10.3389/fspas.2019.00023.

[163] Kääpä, A., Kampert, K.H., and Mayotte, E. Cherenkov Telescope Array: the World's largest VHE gamma-ray observatory. In *Proceedings of 37th International Cosmic Ray Conference — PoS(ICRC2021)*, vol. 395, 004 (2021).

[164] de Almeida, R., et al. Large-scale and multipolar anisotropies of cosmic rays detected at the Pierre Auger Observatory with energies above 4 EeV. In *Proceedings of 37th International Cosmic Ray Conference — PoS(ICRC2021)*, vol. 395, 335 (2021).

[165] Strong, A.W., et al. Global Cosmic-ray-related Luminosity and Energy Budget of the Milky Way. *The Astrophysical Journal Letters* **722** (1) 2010 L58, 1008.4330.

[166] Strong, A.W., Orlando, E., and Jaffe, T.R. The interstellar cosmic-ray electron spectrum from synchrotron radiation and direct measurements. *Astronomy and Astrophysics* **534**:A54, 1108.4822.

[167] Zhang, S., et al. NuSTAR and Chandra Observations of the Galactic Center Nonthermal X-Ray Filament G0.13-0.11: A Pulsar-wind-nebula-driven Magnetic Filament. *The Astrophysical Journal* **893** (1):3.

[168] Ackermann, M., et al. Detection of the Characteristic Pion-Decay Signature in Supernova Remnants. *Science* **339** (6121) 2013 807, 1302.3307.

[169] Orlando, E., et al. Cosmic Rays and interstellar medium with Gamma-Ray Observations at MeV Energies. *BAAS* **51** (3):151, 1903.05660.

[170] Tatischeff, V., Decourchelle, A., and Maurin, G. Nonthermal X-rays from low-energy cosmic rays: application to the 6.4 keV line emission from the Arches cluster region. *Astronomy and Astrophysics* **546**:A88, 1210.2108.

[171] Orlando, E. Imprints of cosmic rays in multifrequency observations of the interstellar emission. *Monthly Notices of the Royal Astronomical Society* **475** (2) 2017 2724. ISSN 0035-8711, https://academic.oup.com/mnras/article-pdf/475/2/2724/23763677/stx3280.pdf, URL https://doi.org/10.1093/mnras/stx3280.

[172] Ackermann, M., et al. The Fermi Large Area Telescope on Orbit: Event Classification, Instrument Response Functions, and Calibration. *ApJS* **203** (1):4, 1206.1896.

[173] Jaffe, T.R., Banday, A.J., Leahy, J.P., Leach, S., and Strong, A.W. Connecting synchrotron, cosmic rays and magnetic fields in the plane of the Galaxy. *Monthly Notices of the Royal Astronomical Society* **416** (2) 2011 1152, 1105.5885.

[174] Drury, L.O. An introduction to the theory of diffusive shock acceleration of energetic particles in tenuous plasmas. *Reports on Progress in Physics* **46** (8) 1983 973, URL https://doi.org/10.1088/0034-4885/46/8/002.

[175] Malkov, M.A. and Drury, L.O. Nonlinear theory of diffusive acceleration of particles by shock waves. *Reports on Progress in Physics* **64** (4) 2001 429.

[176] Ptuskin, V., Zirakashvili, V., and Seo, E.S. SPECTRUM OF GALACTIC COSMIC RAYS ACCELERATED IN SUPERNOVA REMNANTS. *The Astrophysical Journal* **718** (1) 2010 31, URL https://doi.org/10.1088/0004-637x/718/1/31.

[177] Hillas, A.M. TOPICAL REVIEW: Can diffusive shock acceleration in supernova remnants account for high-energy galactic cosmic rays? *Journal of Physics G Nuclear Physics* **31** (5) 2005 R95.

[178] Abdo, A.A., et al. Gamma-ray emission from the shell of supernova remnant w44 revealed by the fermi lat. *Science* **327** (5969) 2010 1103, https://www.science.org/doi/pdf/10.1126/science.1182787, URL https://www.science.org/doi/abs/10.1126/science.1182787.

[179] Albert, A., et al. HAWC J2227+610 and Its Association with G106.3+2.7, a New Potential Galactic PeVatron. *The Astrophysical Journal Letters* **896** (2):L29, 2005.13699.

[180] Aharonian, F., Yang, R., and de Oña Wilhelmi, E. Massive stars as major factories of Galactic cosmic rays. *Nature Astronomy* **3** 2019 561, 1804.02331.

[181] Albert, A., et al. Evidence of 200 TeV Photons from HAWC J1825-134. *The Astrophysical Journal Letters* **907** (2):L30, 2012.15275.

[182] Hooper, D., Blasi, P., and Serpico, P.D. Pulsars as the sources of high energy cosmic ray positrons. *Journal of Cosmology and Astroparticle Physics* **2009** (01) 2009 025, URL https://doi.org/10.1088/1475-7516/2009/01/025.

[183] Hooper, D., Cholis, I., Linden, T., and Fang, K. Hawc observations strongly favor pulsar interpretations of the cosmic-ray positron excess. *Phys. Rev. D* **96** 2017 103013, URL https://link.aps.org/doi/10.1103/PhysRevD.96.103013.

[184] Abeysekara, A.U., et al. Extended gamma-ray sources around pulsars constrain the origin of the positron flux at earth. *Science* **358** (6365) 2017 911, https://www.science.org/doi/pdf/10.1126/science.aan4880, URL https://www.science.org/doi/abs/10.1126/science.aan4880.

[185] Di Mauro, M., Manconi, S., and Donato, F. Detection of a γ-ray halo around geminga with the fermi-lat data and implications for the positron flux. *Phys. Rev. D* **100** 2019 123015, URL https://link.aps.org/doi/10.1103/PhysRevD.100.123015.

[186] Giacinti, G., et al. Halo fraction in tev-bright pulsar wind nebulae. *A&A* **636** 2020 A113, URL https://doi.org/10.1051/0004-6361/201936505.

[187] Wang, S.H., Fang, K., Bi, X.J., and Yin, P.F. Test of the superdiffusion model in the interstellar medium around the geminga pulsar. *Phys. Rev. D* **103** 2021 063035, URL https://link.aps.org/doi/10.1103/PhysRevD.103.063035.

[188] López-Coto, R., de Oña Wilhelmi, E., Aharonian, F., Amato, E., and Hinton, J. Gamma-ray haloes around pulsars as the key to understanding cosmic-ray transport in the Galaxy. *Nature Astronomy* **6** 2022 199, 2202.06899.

[189] Cao, Z., et al. Ultrahigh-energy photons up to 1.4 petaelectronvolts from 12 γ-ray galactic sources. *Nature* **594** (7861) 2021 33, URL `https://doi.org/10.1038/s41586-021-03498-z`.

[190] Aharonian, F., et al. Discovery of very-high-energy γ-rays from the Galactic Centre ridge. *Nature* **439** (7077) 2006 695, `astro-ph/0603021`.

[191] HESS Collaboration, et al. Acceleration of petaelectronvolt protons in the Galactic Centre. *Nature* **531** (7595) 2016 476, `1603.07730`.

[192] Yusef-Zadeh, F., Muno, M., Wardle, M., and Lis, D.C. The Origin of Diffuse X-Ray and γ-Ray Emission from the Galactic Center Region: Cosmic-Ray Particles. *The Astrophysical Journal* **656** (2) 2007 847, `astro-ph/0608710`.

[193] Yusef-Zadeh, F., et al. Interacting Cosmic Rays with Molecular Clouds: A Bremsstrahlung Origin of Diffuse High-energy Emission from the Inner $2^\circ \times 1^\circ$ of the Galactic Center. *The Astrophysical Journal* **762** (1):33, `1206.6882`.

[194] Zhang, S., et al. High-energy X-Ray Detection of G359.89-0.08 (Sgr A-E): Magnetic Flux Tube Emission Powered by Cosmic Rays? *The Astrophysical Journal* **784** (1):6, `1401.7706`.

[195] Heywood, I., et al. Inflation of 430-parsec bipolar radio bubbles in the Galactic Centre by an energetic event. *Nature* **573** (7773) 2019 235, `1909.05534`.

[196] Le Petit, F., et al. Physical conditions in the central molecular zone inferred by H_3^+. *Astronomy and Astrophysics* **585**:A105, `1510.02221`.

[197] Oka, T., et al. The Central 300 pc of the Galaxy Probed by Infrared Spectra of H_3^+ and CO. I. Predominance of Warm and Diffuse Gas and High H_2 Ionization Rate. *The Astrophysical Journal* **883** (1):54, `1910.04762`.

[198] Indriolo, N. and McCall, B.J. Investigating the Cosmic-Ray Ionization Rate in the Galactic Diffuse Interstellar Medium through Observations of $H^+{}_3$. *The Astrophysical Journal* **745** (1):91, `1111.6936`.

[199] LaRosa, T.N., Kassim, N.E., Lazio, T.J.W., and Hyman, S.D. A Wide-Field 90 Centimeter VLA Image of the Galactic Center Region. *The Astronomical Journal* **119** (1) 2000 207.

[200] Jouvin, L., Lemière, A., and Terrier, R. Time-dependent escape of cosmic rays from supernova remnants potentially at the origin of the very-high-energy cosmic-ray gradient of the Galactic center. *Astronomy and Astrophysics* **644**:A113, `2011.00214`.

[201] Ponti, G., et al. The XMM-Newton view of the central degrees of the Milky Way. *Monthly Notices of the Royal Astronomical Society* **453** (1) 2015 172, `1508.04445`.

[202] Guépin, C., et al. Pevatron at the Galactic Center: multi-wavelength signatures from millisecond pulsars. *Journal of Cosmology and Astroparticle Physics* **2018** (7):042, 1806.03307.

[203] Cesarsky, C.J. and Montmerle, T. Gamma-Rays from Active Regions in the Galaxy - the Possible Contribution of Stellar Winds. *Space Science Reviews* **36** (2) 1983 173.

[204] Medina-Torrejón, T.E., et al. Particle Acceleration by Relativistic Magnetic Reconnection Driven by Kink Instability Turbulence in Poynting Flux-Dominated Jets. *The Astrophysical Journal* **908** (2):193, 2009.08516.

[205] Ghez, A.M., et al. Measuring Distance and Properties of the Milky Way's Central Supermassive Black Hole with Stellar Orbits. *The Astrophysical Journal* **689** (2) 2008 1044, 0808.2870.

[206] Baganoff, F.K., et al. Chandra X-Ray Spectroscopic Imaging of Sagittarius A* and the Central Parsec of the Galaxy. *The Astrophysical Journal* **591** (2) 2003 891, astro-ph/0102151.

[207] Clavel, M., et al. Echoes of multiple outbursts of Sagittarius A* revealed by Chandra. *Astronomy and Astrophysics* **558**:A32, 1307.3954.

[208] Chuard, D., et al. Glimpses of the past activity of Sgr A* inferred from X-ray echoes in Sgr C. *Astronomy and Astrophysics* **610**:A34, 1712.02678.

[209] Terrier, R., et al. An X-ray survey of the central molecular zone: Variability of the Fe Kα emission line. *Astronomy and Astrophysics* **612**:A102, 1712.04232.

[210] Su, M., Slatyer, T.R., and Finkbeiner, D.P. Giant Gamma-ray Bubbles from Fermi-LAT: Active Galactic Nucleus Activity or Bipolar Galactic Wind? *The Astrophysical Journal* **724** (2) 2010 1044, 1005.5480.

[211] Dobler, G., Finkbeiner, D.P., Cholis, I., Slatyer, T., and Weiner, N. The Fermi Haze: A Gamma-ray Counterpart to the Microwave Haze. *The Astrophysical Journal* **717** (2) 2010 825, 0910.4583.

[212] Predehl, P., et al. Detection of large-scale X-ray bubbles in the Milky Way halo. *Nature* **588** (7837) 2020 227, 2012.05840.

[213] Ponti, G., et al. An X-ray chimney extending hundreds of parsecs above and below the Galactic Centre. *Nature* **567** (7748) 2019 347, 1904.05969.

[214] Yang, H.Y., Ruszkowski, M., and Zweibel, E. Unveiling the Origin of the Fermi Bubbles. *Galaxies* **6** (1) 2018 29, 1802.03890.

[215] Kataoka, J., et al. X-Ray and Gamma-Ray Observations of the Fermi Bubbles and NPS/Loop I Structures. *Galaxies* **6** (1) 2018 27, 1802.07463.

[216] Zhang, R. and Guo, F. Simulating the Fermi Bubbles as Forward Shocks Driven by AGN Jets. *The Astrophysical Journal* **894** (2):117, 2003.03625.

[217] Sofue, Y. and Kataoka, J. Interaction of the galactic-centre super bubbles with the gaseous disc. *Monthly Notices of the Royal Astronomical Society* **506** (2) 2021 2170, 2106.14955.

[218] Strong, A.W., Moskalenko, I.V., and Ptuskin, V.S. Cosmic-Ray Propagation and Interactions in the Galaxy. *Annual Review of Nuclear and Particle Science* **57** (1) 2007 285, astro-ph/0701517.

[219] Amin, N. Results from a Pilot Study on the Measurement of Nuclear Fragmentation with NA61/SHINE at the CERN SPS: ^{11}C Production in C+p Interactions at 13.5 A GeV/c. In *Proceedings of 37th International Cosmic Ray Conference — PoS(ICRC2021)*, vol. 395, 102 (2021).

[220] Naskręt, M. Light (anti)nuclei production cross section studies in p+C collisions at the NA61/SHINE experiment. In *Proceedings of 37th International Cosmic Ray Conference — PoS(ICRC2021)*, vol. 395, 535 (2021).

[221] Génolini, Y., et al. New minimal, median, and maximal propagation models for dark matter searches with Galactic cosmic rays. *Physical Review D* **104** (8):083005, 2103.04108.

[222] Adriani, O., et al. MEASUREMENT OF BORON AND CARBON FLUXES IN COSMIC RAYS WITH THE PAMELA EXPERIMENT. *The Astrophysical Journal* **791** (2) 2014 93, URL https://doi.org/10.1088/0004-637x/791/2/93.

[223] Gaggero, D., Maccione, L., Grasso, D., Di Bernardo, G., and Evoli, C. Pamela and ams-02 e^+ and e^- spectra are reproduced by three-dimensional cosmic-ray modeling. *Phys. Rev. D* **89** 2014 083007, URL https://link.aps.org/doi/10.1103/PhysRevD.89.083007.

[224] Aguilar, M., et al. (AMS Collaboration). Precision measurement of the boron to carbon flux ratio in cosmic rays from 1.9 gv to 2.6 tv with the alpha magnetic spectrometer on the international space station. *Phys. Rev. Lett.* **117** 2016 231102, URL https://link.aps.org/doi/10.1103/PhysRevLett.117.231102.

[225] Evoli, C., Morlino, G., Blasi, P., and Aloisio, R. AMS-02 beryllium data and its implication for cosmic ray transport. *Physical Review D* **101** (2):023013, 1910.04113.

[226] Ptuskin, V.S., Voelk, H.J., Zirakashvili, V.N., and Breitschwerdt, D. Transport of relativistic nucleons in a galactic wind driven by cosmic rays. *Astronomy and Astrophysics* **321** 1997 434.

[227] Strong, A.W. and Moskalenko, I.V. Propagation of Cosmic-Ray Nucleons in the Galaxy. *Astrophysical Journal* **509** (1) 1998 212, astro-ph/9807150.

[228] Evoli, C., et al. Cosmic-ray propagation with DRAGON2: I. numerical solver and astrophysical ingredients. *JCAP* **2017** (2):015, 1607.07886.

[229] Mori, K., et al. A novel antimatter detector based on X-ray deexcitation of exotic atoms. *The Astrophysical Journal* **566** 2002 604, astro-ph/0109463.

[230] Hailey, C.J., et al. Antideuteron based dark matter search with GAPS: Current progress and future prospects. *Advances in Space Research* **51** 2013 290.

[231] Hailey, C.J. An indirect search for dark matter using antideuterons: the GAPS experiment. *New Journal of Physics* **11** (10):105022.

[232] Donato, F., Fornengo, N., and Salati, P. Antideuterons as a signature of supersymmetric dark matter. *Physical Review D* **62** (4):043003, hep-ph/9904481.

[233] Aramaki, T., et al. Review of the theoretical and experimental status of dark matter identification with cosmic-ray antideuterons. *Physics Reports* **618** 2016 1, 1505.07785.

[234] Šerkšnytė, L., et al. Reevaluation of the cosmic antideuteron flux from cosmic-ray interactions and from exotic sources. *arXiv e-prints* arXiv:2201.00925, 2201.00925.

[235] Aramaki, T., et al. A measurement of atomic X-ray yields in exotic atoms and implications for an antideuteron-based dark matter search. *Astroparticle Physics* **49** 2013 52, 1303.3871.

[236] Manghisoni, M., et al. Novel active signal compression in low-noise analog readout at future X-ray FEL facilities. *Journal of Instrumentation* **10** (4):C04003.

[237] Scotti, V., et al. Front-end Electronics for the GAPS Tracker. In *36th International Cosmic Ray Conference (ICRC2019)*, vol. 36 of *International Cosmic Ray Conference*, 136 (2019), 1909.01682.

[238] Manghisoni, M., et al. Low-noise analog channel for the readout of the si(li) detector of the gaps experiment. *IEEE Transactions on Nuclear Science* 1–1.

[239] Quinn, S. Recent Progress on the GAPS Time of Flight System. In *36th International Cosmic Ray Conference (ICRC2019)*, vol. 36 of *International Cosmic Ray Conference*, 128 (2019), 1912.01675.

[240] Quinn, S. The GAPS Instrument: A Large Area Time of Flight and High Resolution Exotic Atom Spectrometer for Cosmic Antinuclei. In *Proceedings of 37th International Cosmic Ray Conference — PoS(ICRC2021)*, vol. 395, 079 (2021).

[241] Fuke, H., et al. Development of a cooling system for GAPS using oscillating heat pipe. *Transactions JSASS Aerospace Technology, Japan* **14** 2016 17.

[242] Okazaki, S., Fuke, H., Miyazaki, Y., and Takahashi, N. Meter-scale multi-loop capillary heat pipe. *Applied Thermal Engineering* **141** 2018 20.

[243] Fuke, H., Okazaki, S., Kondo, M., Kawachi, A., and Ogawa, H. Low-power, large-scale distributed hybrid thermal system to cool silicon detectors in the gaps instrument. In *2019 IEEE Nuclear Science Symposium and Medical Imaging Conference (NSS/MIC)*, 1–3 (2019).

[244] Fuke, H., et al. The pGAPS experiment: An engineering balloon flight of prototype GAPS. *Advances in Space Research* **53** 2014 1432, 1303.0380.

[245] Mognet, S.A.I., et al. The prototype GAPS (pGAPS) experiment. *Nuclear Instruments and Methods in Physics Research A* **735** 2014 24, 1303.1615.

[246] von Doetinchem, P., et al. The flight of the GAPS prototype experiment. *Astroparticle Physics* **54** 2014 93, 1307.3538.

[247] Leo, W.R. *Techniques for Nuclear and Particle Physics Experiments*. Springer, Berlin, Heidelberg (1994).

[248] Goulding, F.S. Semiconductor detectors for nuclear spectrometry, I. *Nuclear Instruments and Methods* **43** 1966 1.

[249] Spieler, H. *Semiconductor detector systems*. Oxford University Press (2005).

[250] Radeka, V. Signal, noise and resolution in position-sensitive detectors. *IEEE Transactions on Nuclear Science* **21** (1) 1974 51.

[251] Aramaki, T., et al. Development of large format Si(Li) detectors for the GAPS dark matter experiment. *Nuclear Instruments and Methods in Physics Research A* **682** 2012 90.

[252] Pell, E.M. Ion Drift in an n-p Junction. *Journal of Applied Physics* **31** 1960 291.

[253] Carslaw, H.S. and Jaeger, J.C. *Conduction of Heat in Solids*. Oxford University Press (1960).

[254] Ristinen, R., Lind, D., and Homan, J. The manufacture of thick lithium-drifted silicon detectors. *Nuclear Instruments and Methods* **56** (1) 1967 55. ISSN 0029-554X, URL https://www.sciencedirect.com/science/article/pii/0029554X67902583.

[255] Walton, J.T., Derhacobian, N., Wong, Y.K., and Haller, E.E. Lithium-ion mobility improvement in floating-zone silicon by external gettering. *Applied Physics Letters* **63** (3) 1993 343, https://doi.org/10.1063/1.110037, URL https://doi.org/10.1063/1.110037.

[256] Walton, J.T., Hubbard, G.S., Haller, E.E., and Sommer, H.A. A two-dimensional position sensitive si(li) detector. *IEEE Transactions on Nuclear Science* **26** (1) 1979 334.

[257] Protic, D., Hull, E., Krings, T., and Vetter, K. Large-volume si(li) orthogonal-strip detectors for compton-effect-based instruments. *IEEE Transactions on Nuclear Science* **52** (6) 2005 3181.

[258] Landis, D., Wong, Y., Walton, J., and Goulding, F. Computer controlled drifting of si(li) detectors. *IEEE Transactions on Nuclear Science* **36** (1) 1989 185.

[259] Baron, N. and Kaminski, G. Manufacture of lithium-drifted silicon surface barrier semiconductor counters. *Tech. rep.*, NASA Technical Note, https://ntrs.nasa.gov/citations/19660025035 (1966).

[260] Keffous, A., et al. Study of lithium behaviour in si(li) detectors. *Vacuum* **80** (8) 2006 908. ISSN 0042-207X, URL `https://www.sciencedirect.com/science/article/pii/S0042207X05004173`.

[261] Lauber, A. The theory of compensation in lithium drifted semiconductor detectors. *Nuclear Instruments and Methods* **75** 1969 297.

[262] Llacer, J. Geometric Control of Surface Leakage Current and Noise in Lithium Drifted Silicon Radiation Detectors. *IEEE Transactions on Nuclear Science* **13** 1966 93.

[263] Goulding, F.S. and Hansen, W.L. Leakage current in semiconductor junction radiation detectors and its influence on energy-resolution characteristics. *Nuclear Instruments and Methods* **12** 1961 249. ISSN 0029-554X, URL `https://www.sciencedirect.com/science/article/pii/0029554X61901409`.

[264] Perez, K., et al. Fabrication of low-cost, large-area prototype Si(Li) detectors for the GAPS experiment. *Nuclear Instruments and Methods in Physics Research A* **905** 2018 12, `1807.07912`.

[265] Kozai, M., et al. Development of Large-area Lithium-drifted Silicon Detectors for the GAPS Experiment. *2018 IEEE Nuclear Science Symposium and Medical Imaging Conference (2018 NSS/MIC)*, `1812.07255`.

[266] Kozai, M., et al. Developing a mass-production model of large-area Si(Li) detectors with high operating temperatures. *Nuclear Instruments and Methods in Physics Research A* **947**:162695, `1906.05577`.

[267] Iles, P.A. and Coppen, P.J. Location of p-n and l-h junctions in semiconductors. *British Journal of Applied Physics* **11** (5) 1960 177, URL `https://doi.org/10.1088/0508-3443/11/5/302`.

[268] Rogers, F., et al. Large-area Si(Li) detectors for X-ray spectrometry and particle tracking in the GAPS experiment. *Journal of Instrumentation* **14** (10) 2019 P10009, 1906.00054.

[269] Rogers, F., et al. Large-area si(li) detectors for x-ray spectrometry and particle tracking for the gaps experiment. In *2019 IEEE Nuclear Science Symposium and Medical Imaging Conference (NSS/MIC)*, 1–3 (2019), 1912.06571.

[270] Fabris, L., Madden, N.W., and Yaver, H. A fast, compact solution for low noise charge preamplifiers. *Nuclear Instruments and Methods in Physics Research A* **424** 1999 545.

[271] Goulding, F. and Landis, D.A. Signal processing for semiconductor detectors. *IEEE Transactions on Nuclear Science* **29** 1982 1125.

[272] Saffold, N., et al. Passivation of Si(Li) detectors operated above cryogenic temperatures for space-based applications. *Nuclear Instruments and Methods in Physics Research A* **997**:165015, 2102.06168.

[273] Rossington, C., Fine, P., and Madden, N. Large area, low capacitance si(li) detectors for high rate x-ray applications. *IEEE Transactions on Nuclear Science* **40** (4) 1993 354.

[274] Jantunen, M. and Audet, S.A. Surface passivated si(li) detectors for an x-ray detector array. *Nuclear Instruments and Methods in Physics Research A* **353** (1-3).

[275] Hansen, W.L., Haller, E.E., and Hubbard, G.S. Protective surface coatings on semiconductor nuclear radiation detectors. *IEEE Transactions on Nuclear Science* **27** (1) 1980 247.

[276] Walton, J.T., Pehl, R.H., Wong, Y.K., and Cork, C.P. Si(li) x-ray detectors with amorphous silicon passivation. *IEEE Transactions on Nuclear Science* **31** (1) 1984 331.

[277] Kim, O.H. *Atomic layer deposition of gallium nitride and tantalum nitride*. Ph.D. thesis, University of Florida (2009).

[278] Meng, X., et al. Atomic layer deposition of silicon nitride thin films: A review of recent progress, challenges, and outlooks. *Materials* **9** (12). ISSN 1996-1944, URL https://www.mdpi.com/1996-1944/9/12/1007.

[279] Kaloyeros, A.E., Jové, F.A., Goff, J., and Arkles, B. Review—silicon nitride and silicon nitride-rich thin film technologies: Trends in deposition techniques and related applications. *ECS Journal of Solid State Science and Technology* **6** (10) 2017 P691, URL https://doi.org/10.1149/2.0011710jss.

[280] Astm d3359-17 standard test methods for rating adhesion by tape test, standard. doi:https://doi.org/10.1520/D3359-17.

[281] Hsu, T.C.J. and Liu, Z.L. Solvent effect on the curing of polyimide resins. *Journal of Applied Polymer Science* **46** (10) 1992 1821, https://onlinelibrary.wiley.com/doi/pdf/10.1002/app.1992.070461014, URL https://onlinelibrary.wiley.com/doi/abs/10.1002/app.1992.070461014.

[282] Nelson, W.B. *Accelerated Testing: Statistical Models, Test Plans, and Data Analysis*. Wiley Series in probability and mathematical statistics: Applied probability and statistics. John Wiley & Sons (1990).

[283] Ogawa, T., Nagata, T., and Hamada, Y. Determination of diffusion coefficient of water in polymer films by tga. *Journal of Applied Polymer Science* **50** (6) 1993 981, https://onlinelibrary.wiley.com/doi/pdf/10.1002/app.1993.070500607, URL https://onlinelibrary.wiley.com/doi/abs/10.1002/app.1993.070500607.

[284] Golden, R.L., et al. Evidence for the existence of cosmic-ray antiprotons. *Phys. Rev. Lett.* **43** 1979 1196, URL https://link.aps.org/doi/10.1103/PhysRevLett.43.1196.

[285] Bogomolov, E.A., et al. Galactic Antiprotons of 0. 2-2 GEV Energy. In *19th International Cosmic Ray Conference (ICRC19), Volume 2*, vol. 2 of *International Cosmic Ray Conference*, 362 (1985).

[286] Aguilar, M., et al. The alpha magnetic spectrometer (ams) on the international space station: Part ii — results from the first seven years. *Physics Reports* **894** 2021 1. ISSN 0370-1573, URL https://www.sciencedirect.com/science/article/pii/S0370157320303434.

[287] Orito, S., et al. Precision Measurement of Cosmic-Ray Antiproton Spectrum. *Physical Review Letters* **84** (6) 2000 1078, astro-ph/9906426.

[288] Abe, K., et al. Measurement of the Cosmic-Ray Antiproton Spectrum at Solar Minimum with a Long-Duration Balloon Flight over Antarctica. *Physics Review Letters* **108** (5):051102, 1107.6000.

[289] Adriani, O., et al. PAMELA Results on the Cosmic-Ray Antiproton Flux from 60 MeV to 180 GeV in Kinetic Energy. *Physics Review Letters* **105** (12):121101, 1007.0821.

[290] Adriani, O., et al. Measurement of the flux of primary cosmic ray antiprotons with energies of 60 MeV to 350 GeV in the PAMELA experiment. *Soviet Journal of Experimental and Theoretical Physics Letters* **96** (10) 2013 621.

[291] Aramaki, T., et al. Potential for precision measurement of low-energy antiprotons with GAPS for dark matter and primordial black hole physics. *Astroparticle Physics* **59** 2014 12, 1401.8245.

[292] Rogers, F., et al. Cosmic Antiproton Sensitivity for the GAPS Experiment. In *Proceedings of 37th International Cosmic Ray Conference — PoS(ICRC2021)*, vol. 395, 136 (2021).

[293] Rogers, F. and GAPS Collaboration. Sensitivity of the gaps experiment to low-energy cosmic-ray antiprotons. *in preparation for Astroparticle Physics*.

[294] Hooper, D., Leane, R.K., Tsai, Y.D., Wegsman, S., and Witte, S.J. A Systematic Study of Hidden Sector Dark Matter: Application to the Gamma-Ray and Antiproton Excesses. *JHEP* **163**, 1912.08821.

[295] Villanueva-Domingo, P., Mena, O., and Palomares-Ruiz, S. A brief review on primordial black holes as dark matter. *Frontiers in Astronomy and Space Sciences* **8**. ISSN 2296-987X, URL https://www.frontiersin.org/article/10.3389/fspas.2021.681084.

[296] Desorgher, L. http://cosray.unibe.ch/ laurent/planetocosmics/ (2005).

[297] von Doetinchem, P. *Search for Cosmic-Ray Antiparticles with Balloon-borne and Space-borne Experiments*. PhD dissertation, RWTH Aachen University, Department of Physics (2009).

[298] Agostinelli, S., et al. G EANT4—a simulation toolkit. *Nuclear Instruments and Methods in Physics Research A* **506** (3) 2003 250.

[299] Allison, J., et al. Geant4 developments and applications. *IEEE Transactions on Nuclear Science* **53** (1) 2006 270.

[300] Allison, J., et al. Recent developments in geant4. *Nuclear Instruments and Methods in Physics Research Section A: Accelerators, Spectrometers, Detectors and Associated Equipment* **835** 2016 186. ISSN 0168-9002, URL https://www.sciencedirect.com/science/article/pii/S0168900216306957.

[301] Saffold, N., et al. Cosmic antihelium-3 nuclei sensitivity of the GAPS experiment. *Astroparticle Physics* **130**:102580, 2012.05834.

[302] Stoessl, A. Searching for cosmic antihelium nuclei with the GAPS experiment. In *Proceedings of 37th International Cosmic Ray Conference — PoS(ICRC2021)*, vol. 395, 499 (2021).

[303] Munini, R., et al. The antinucleus annihilation reconstruction algorithm of the gaps experiment. *Astroparticle Physics* **133** 2021 102640. ISSN 0927-6505, URL https://www.sciencedirect.com/science/article/pii/S0927650521000773.

[304] Munini, R., et al. Event reconstruction performance with the GAPS experiment. *PoS* **ICRC2019** 2020 535.

[305] Sullivan, J.D. Geometrical factor and directional response of single and multi-element particle telescopes. *Nuclear Instruments and Methods* **95** 1971 5.

[306] Zhang, S., et al. Hard X-Ray Morphological and Spectral Studies of the Galactic Center Molecular Cloud Sgr B2: Constraining Past Sgr A* Flaring Activity. *The Astrophysical Journal* **815** (2):132, 1507.08740.

[307] Morris, M. and Serabyn, E. The Galactic Center Environment. *Annual Review of Astronomy and Astrophysics* **34** 1996 645.

[308] Koyama, K., et al. ASCA View of Our Galactic Center: Remains of Past Activities in X-Rays? *Publications of the ASJ* **48** 1996 249.

[309] Murakami, H., Koyama, K., and Maeda, Y. Chandra Observations of Diffuse X-Rays from the Sagittarius B2 Cloud. *ApJ* **558** (2) 2001 687, astro-ph/0105273.

[310] Koyama, K., et al. Discoveries of Diffuse Iron Line Sources from the Sgr B Region. *Publications of the ASJ* **59** 2007 221, astro-ph/0609310.

[311] Terrier, R., et al. Fading Hard X-ray Emission from the Galactic Center Molecular Cloud Sgr B2. *The Astrophysical Journal* **719** (1) 2010 143, 1005.4807.

[312] Inui, T., Koyama, K., Matsumoto, H., and Tsuru, T.G. Time Variability of the Neutral Iron Lines from the Sagittarius B2 Region and Its Implication of a Past Outburst of Sagittarius A. *Publications of the ASJ* **61** 2009 S241.

[313] Nobukawa, M., Ryu, S.G., Tsuru, T.G., and Koyama, K. New Evidence for High Activity of the Supermassive Black Hole in our Galaxy. *The Astrophysical Journal Letters* **739** (2):L52, 1109.1950.

[314] Revnivtsev, M.G., et al. Hard X-ray view of the past activity of Sgr A* in a natural Compton mirror. *Astronomy and Astrophysics* **425** 2004 L49, astro-ph/0408190.

[315] Kuznetsova, E., Krivonos, R., Lutovinov, A., and Clavel, M. INTEGRAL Observations of Sgr B2. *submitted to MNRAS*.

[316] Lis, D.C. and Goldsmith, P.F. Modeling of the Continuum and Molecular Line Emission from the Sagittarius B2 Molecular Cloud. *The Astrophysical Journal* **356** 1990 195.

[317] de Vicente, P., Martin-Pintado, J., and Wilson, T.L. A hot ring in the Sagittarius B2 molecular cloud. *Astronomy and Astrophysics* **320** 1997 957.

[318] Reid, M.J., et al. Trigonometric Parallaxes of Massive Star-Forming Regions. VI. Galactic Structure, Fundamental Parameters, and Noncircular Motions. *The Astrophysical Journal* **700** (1) 2009 137, 0902.3913.

[319] Benson, J.M. and Johnston, K.J. Arc second resolution maps of the compact sources in Sagittarius B2 and G 34.3+0.2. *The Astrophysical Journal* **277** 1984 181.

[320] Sato, F., Hasegawa, T., Whiteoak, J.B., and Miyawaki, R. Cloud Collision-induced Star Formation in Sagittarius B2. I. Large-Scale Kinematics. *The Astrophysical Journal* **535** (2) 2000 857.

[321] Etxaluze, M., et al. Herschel observations of the Sagittarius B2 cores: Hydrides, warm CO, and cold dust. *Astronomy and Astrophysics* **556**:A137, 1307.0335.

[322] Molinari, S., et al. A 100 pc Elliptical and Twisted Ring of Cold and Dense Molecular Clouds Revealed by Herschel Around the Galactic Center. *The Astrophysical Journal Letters* **735** (2):L33, 1105.5486.

[323] Sunyaev, R.A., Markevitch, M., and Pavlinsky, M. The Center of the Galaxy in the Recent Past: A View from GRANAT. *The Astrophysical Journal* **407** 1993 606.

[324] Sunyaev, R. and Churazov, E. Equivalent width, shape and proper motion of the iron fluorescent line emission from molecular clouds as an indicator of the illuminating source X-ray flux history. *Monthly Notices of the Royal Astronomical Society* **297** (4) 1998 1279, astro-ph/9805038.

[325] Odaka, H., et al. X-Ray Diagnostics of Giant Molecular Clouds in the Galactic Center Region and Past Activity of Sgr A*. *The Astrophysical Journal* **740** (2):103, 1110.1936.

[326] Molaro, M., Khatri, R., and Sunyaev, R.A. Probing the clumping structure of giant molecular clouds through the spectrum, polarisation and morphology of X-ray reflection nebulae. *Astronomy and Astrophysics* **589**:A88, 1511.05125.

[327] Wang, Q.D., et al. Dissecting X-ray-Emitting Gas Around the Center of Our Galaxy. *Science* **341** (6149) 2013 981, 1307.5845.

[328] Corrales, L., et al. The Chandra High-resolution X-Ray Spectrum of Quiescent Emission from Sgr A*. *The Astrophysical Journal* **891** (1):71, 2002.07198.

[329] Ponti, G., Terrier, R., Goldwurm, A., Belanger, G., and Trap, G. Discovery of a Superluminal Fe K Echo at the Galactic Center: The Glorious Past of Sgr A* Preserved by Molecular Clouds. *Astrophysical Journal* **714** (1) 2010 732, 1003.2001.

[330] Ponti, G., et al. On the past activity of sgr a*. *Proceedings of the International Astronomical Union* **9** (S303) 2013 333?343.

[331] Churazov, E., Khabibullin, I., Sunyaev, R., and Ponti, G. Not that long time ago in the nearest galaxy: 3D slice of molecular gas revealed by a 110 yr old flare of Sgr A*. *Monthly Notices of the Royal Astronomical Society* **465** (1) 2017 45, 1610.06699.

[332] Valinia, A., Tatischeff, V., Arnaud, K., Ebisawa, K., and Ramaty, R. On the Origin of the Iron K Line in the Spectrum of The Galactic X-Ray Background. *The Astrophysical Journal* **543** (2) 2000 733, astro-ph/0006202.

[333] Dogiel, V.A., et al. Origin of Thermal and Non-Thermal Hard X-Ray Emission from the Galactic Center. *Publications of the ASJ* **61** 2009 1099, 0906.2247.

[334] Dogiel, V.A., Chernyshov, D.O., Tatischeff, V., Cheng, K.S., and Terrier, R. The Origin of the 6.4 keV Line Emission and H_2 Ionization in the Diffuse Molecular Gas of the Galactic Center Region. *The Astrophysical Journal Letters* **771** (2):L43, 1306.1654.

[335] Dogiel, V., et al. Origin of 6.4keV Line Emission from Molecular Clouds in the Galactic Center. *Publications of the ASJ* **61** 2009 901.

[336] Morlino, G. and Gabici, S. Cosmic ray penetration in diffuse clouds. *Monthly Notices of the Royal Astronomical Society* **451** 2015 L100, 1503.02435.

[337] Evans, I.N., et al. The Chandra Source Catalog 2.0. In *American Astronomical Society Meeting Abstracts #231*, vol. 231 of *American Astronomical Society Meeting Abstracts*, 238.01 (2018).

[338] Turner, M.J.L., et al. The European Photon Imaging Camera on XMM-Newton: The MOS cameras. *Astronomy and Astrophysics* **365** 2001 L27, astro-ph/0011498.

[339] Strüder, L., et al. The European Photon Imaging Camera on XMM-Newton: The pn-CCD camera. *Astronomy and Astrophysics* **365** 2001 L18.

[340] Snowden, S.L., Mushotzky, R.F., Kuntz, K.D., and Davis, D.S. A catalog of galaxy clusters observed by XMM-Newton. *Astronomy and Astrophysics* **478** (2) 2008 615, 0710.2241.

[341] Harrison, F.A., et al. The Nuclear Spectroscopic Telescope Array (NuSTAR) High-energy X-Ray Mission. *The Astrophysical Journal* **770** (2):103, 1301.7307.

[342] Nasa High Energy Astrophysics Science Archive Research Center (Heasarc). HEAsoft: Unified Release of FTOOLS and XANADU (2014), 1408.004.

[343] Krivonos, R.A., et al. First Hard X-Ray Detection of the Non-thermal Emission around the Arches Cluster: Morphology and Spectral Studies with NuSTAR. *The Astrophysical Journal* **781** (2):107, 1312.2635.

[344] Arnaud, K.A. XSPEC: The First Ten Years. In G.H. Jacoby and J. Barnes, eds., *Astronomical Data Analysis Software and Systems V*, vol. 101 of *Astronomical Society of the Pacific Conference Series*, 17 (1996).

[345] Uchiyama, H., Nobukawa, M., Tsuru, T.G., and Koyama, K. K-Shell Line Distribution of Heavy Elements along the Galactic Plane Observed with Suzaku. *Publications of the ASJ* **65**:19, 1209.0067.

[346] Muno, M.P., et al. Diffuse X-Ray Emission in a Deep Chandra Image of the Galactic Center. *The Astrophysical Journal* **613** (1) 2004 326, astro-ph/0402087.

[347] Walls, M., Chernyakova, M., Terrier, R., and Goldwurm, A. Examining molecular clouds in the Galactic Centre region using X-ray reflection spectra simulations. *MNRAS* **463** (3) 2016 2893, 1609.00175.

[348] Jones, P.A., Burton, M.G., Tothill, N.F.H., and Cunningham, M.R. Spectral imaging of the Sagittarius B2 region in multiple 7-mm molecular lines. *Monthly Notices of the Royal Astronomical Society* **411** (4) 2011 2293. ISSN 0035-8711, https://academic.oup.com/mnras/article-pdf/411/4/2293/3046777/mnras0411-2293.pdf, URL https://doi.org/10.1111/j.1365-2966.2010.17849.x.

[349] Hailey, C.J., et al. Evidence for Intermediate Polars as the Origin of the Galactic Center Hard X-ray Emission. *ApJ* **826** (2):160, 1605.06066.

[350] Murphy, K.D. and Yaqoob, T. An X-ray spectral model for Compton-thick toroidal reprocessors. *MNRAS* **397** (3) 2009 1549, 0905.3188.

[351] Yaqoob, T. The nature of the Compton-thick X-ray reprocessor in NGC 4945. *Monthly Notices of the Royal Astronomical Society* **423** (4) 2012 3360, 1204.4196.

[352] Churazov, E., Khabibullin, I., Ponti, G., and Sunyaev, R. Polarization and long-term variability of Sgr A* X-ray echo. *Monthly Notices of the Royal Astronomical Society* **468** (1) 2017 165, 1612.00180.

[353] Rogers, F., Zhang, S., Perez, K., Clavel, M., and Taylor, A. New Constraints on Cosmic Particle Populations at the Galactic Center using X-ray Observations of the Molecular Cloud Sagittarius B2 288, 2108.13399.

[354] Barnes, P.J., et al. The Three-mm Ultimate Mopra Milky Way Survey. I. Survey Overview, Initial Data Releases, and First Results. *The Astrophysical Journal* **812** (1):6, 1507.05095.

[355] Khabibullin, I., Churazov, E., and Sunyaev, R. SRG/eROSITA view of X-ray reflection in the Central Molecular Zone: a snapshot in September–October 2019. *Monthly Notices of the Royal Astronomical Society* **509** (4) 2021 6068. ISSN 0035-8711, https://academic.oup.com/mnras/article-pdf/509/4/6068/41794731/stab3333.pdf, URL https://doi.org/10.1093/mnras/stab3333.

[356] Ishisaki, Y., et al. Resolve instrument on x-ray astronomy recovery mission (xarm). *Journal of Low Temperature Physics* **193** (5) 2018 991, URL https://doi.org/10.1007/s10909-018-1913-4.

[357] Barret, D., et al. The ATHENA X-ray Integral Field Unit (X-IFU). In J.W.A. den Herder, S. Nikzad, and K. Nakazawa, eds., *Space Telescopes and Instrumentation 2018: Ultraviolet to Gamma Ray*, vol. 10699 of *Society of Photo-Optical Instrumentation Engineers (SPIE) Conference Series*, 106991G (2018), 1807.06092.

[358] Yan, Q.Z., et al. Towards a three-dimensional distribution of the molecular clouds in the Galactic Centre. *Monthly Notices of the Royal Astronomical Society* **471** (3) 2017 2523. ISSN 0035-8711, https://academic.oup.com/mnras/article-pdf/471/3/2523/19495163/stx1724.pdf, URL https://doi.org/10.1093/mnras/stx1724.

[359] Gabici, S., Aharonian, F.A., and Blasi, P. Gamma rays from molecular clouds. *Astrophysics and Space Science* **309** (1-4) 2007 365, astro-ph/0610032.

[360] Gabici, S. Cosmic Rays and Molecular Clouds. In D.F. Torres and O. Reimer, eds., *Cosmic Rays in Star-Forming Environments*, vol. 34, 221 (2013), 1208.4979.

[361] Dogiel, V.A., et al. Spectrum of Relativistic and Subrelativistic Cosmic Rays in the 100 pc Central Region. *ApJ* **809** (1):48, 1507.02440.

[362] Owen, E.R., On, A.Y.L., Lai, S.P., and Wu, K. Observational Signatures of Cosmic-Ray Interactions in Molecular Clouds. *The Astrophysical Journal* **913** (1):52, 2103.06542.

[363] Oka, T., Geballe, T.R., Goto, M., Usuda, T., and McCall, B.J. Hot and Diffuse Clouds near the Galactic Center Probed by Metastable $H^+_3$1,. *The Astrophysical Journal* **632** (2) 2005 882, astro-ph/0507463.

[364] van der Tak, F.F.S., et al. APEX mapping of H_3O^+ in the Sgr B2 region. *Astronomy and Astrophysics* **454** (2) 2006 L99, astro-ph/0605582.

[365] Dogiel, V.A., Gurevich, A.V., Istomin, I.N., and Zybin, K.P. On relativistic particle acceleration in molecular clouds. *Monthly Notices of the Royal Astronomical Society* **228** 1987 843.

[366] Istomin, Y.N. and Kiselev, A. Magnetic field generation in Galactic molecular clouds. *Monthly Notices of the Royal Astronomical Society* **436** (3) 2013 2774, 1309.6110.